Light-matter coupling in low-dimensional semiconductors and fiber-based microcavities

Lukas Husel

München 2025

Light-matter coupling in low-dimensional semiconductors and fiber-based microcavities

Dissertation
an der Fakultät für Physik
der Ludwig-Maximilians-Universität
München

vorgelegt von
Lukas Husel
aus Aalen

München, den 30. Januar 2025

Erstgutachter: Prof. Alexander Högele
Zweitgutachter: Prof. Andreas Tittl

Tag der mündlichen Prüfung: 14. März 2025

Zusammenfassung

Die Kopplung zwischen Photonen und Exzitonen, gebundenen Elektron-Loch-Paaren in Halbleitern, ist von zentralem Interesse in der Quantenwissenschaft und -technologie auf Festkörperbasis. Viele Anwendungen erfordern eine verstärkte Licht-Materie-Wechselwirkung, was häufig in optischen Resonatoren mit mikroskopischen Modenvolumina erreicht wird. Eine vielversprechende Plattform sind faserbasierte Fabry-Pérot-Resonatoren, in denen ein Resonatorspiegel an der Spitze einer optischen Faser angebracht ist. Die vorliegende Dissertation befasst sich mit der Kopplung solcher Resonatoren an zwei verschiedene niedrigdimensionale Halbleitermaterialien, die stark gebundene Exzitonen aufweisen.

Übergangsmetall-Dichalcogenid-Monolagen sind zweidimensionale Halbleiter, die sich durch ihre große Exziton-Oszillatorstärke ideal für Untersuchungen der kohärenten Licht-Materie-Kopplung in optischen Resonatoren eignen. In diesem Regime bilden sich Exziton-Polaritonen, hybride Licht-Materie-Quantenzustände. Diese bieten vielversprechende Anwendungen in der nichtlinearen Festkörperoptik und in der Quantensimulation, wenn es gelingt, ihre Energien lokal zu kontrollieren um Potentiallandschaften zu definieren. In dieser Arbeit wurde eine solche Kontrolle über den exzitonischen Anteil von Polaritonen in einer Übergangsmetall-Dichalcogenid-Monolage realisiert. Durch Nanostrukturierung der dielektrischen Halbleiterumgebung wurden Kreisflächen von Exzitonen mit veränderten Resonanzenergien definiert. Dies führte zu einer lokalen Energieverschiebung der Polaritonen, deren Betrag über die Resonatorenergie kontrolliert wurde. Zusätzlich wurde das Regime dispersiver Kopplung demonstriert, in dem eine effektive Wechselwirkung zwischen hochgradig exzitonartigen Polaritonen vermittelt wurde, die in verschiedenen definierten Kreisflächen lokalisiert waren.

Fluoreszierende Defekte in Kohlenstoff-Nanoröhren stellen nulldimensionale Quantensysteme dar, die bei Raumtemperatur Einzelphotonen bei technologisch relevanten Telekommunikationswellenlängen emittieren. In diesen Systemen limitiert starke Dephasierung bei Raumtemperatur die Ununterscheidbarkeit der Photonen. Zur Überwindung dieser Einschränkung wurden in dieser Arbeit einzelne Nanoröhren-Defekte an einen Faserresonator gekoppelt und das Regime inkohärenter Licht-Materie-Kopplung implementiert. In diesem Regime ist die spektrale Linienbreite des Emitters deutlich größer als die des Resonators, was zu einer starken spektralen Bereinigung der emittierten Einzelphotonen führt. Die Messergebnisse zeigen eine entsprechende Erhöhung der Photonen-Ununterscheidbarkeit um zwei Größenordnungen im Vergleich zur Emission ohne Resonator, bei gleichzeitiger Erhöhung der spektralen Emissionsdichte um mindestens einen Faktor vier.

Die Ergebnisse dieser Dissertation eröffnen Perspektiven für die Entwicklung von Polariton-Experimenten auf Grundlage von dielektrisch modifizierten Übergangsmetall-Dichalcogeniden sowie von verbesserten Quantenlichtquellen auf der Basis funktionalisierter Kohlenstoff-Nanoröhren. Die Experimente wurden in verschiedenen Regimes der Resonatorkopplung durchgeführt und zeigen dadurch die Vielseitigkeit von faserbasierten Resonatoren auf.

Abstract

The coupling between photons and excitons, bound electron-hole pairs in semiconductors, is of central interest in solid-state based quantum science and technology. Many applications and experiments require enhanced light-matter interactions, frequently achieved in optical resonators with microscopic mode volumes. A promising platform to emerge from recent miniaturization efforts are open fiber-based Fabry-Pérot cavities, in which one resonator mirror is machined on the tip of an optical fiber. This dissertation reports on the coupling of such cavities to two different low-dimensional semiconductor platforms, where the confinement of charge carriers gives rise to strongly-bound excitons.

Monolayer transition metal dichalcogenides are two-dimensional semiconductors, whose large exciton oscillator strength renders them prime candidates for studies of coherent light-matter coupling in optical resonators. In this regime, exciton-polaritons are formed, hybrid light-matter quantum states with promise for experiments and devices in solid-state nonlinear optics and quantum simulation. In many applications, local control of polariton energies is required, forming the basis for engineered potential landscapes. In this dissertation, we locally control polaritons formed by transition metal dichalcogenide excitons coupled to a cryogenic fiber cavity via their excitonic fraction. By nanostructuring the dielectric semiconductor environment, we define disk-shaped areas of excitons with modified resonance energies. The local modulation in exciton energy translates to shifts in the polariton energy, tunable in magnitude via the cavity-exciton detuning. We also demonstrate the dispersive regime of cavity-coupling, where an effective hopping is mediated between highly exciton-like polaritons localized to different disk-shaped areas in the device.

Fluorescent defects in functionalized carbon nanotubes constitute zero-dimensional quantum systems capable of emitting room-temperature single photons at technologically relevant telecom wavelengths. In these emitters, large room-temperature dephasing limits the photon indistinguishability, an important resource in the design of single photon sources. In this work, we implement a recently proposed strategy to overcome this limitation by coupling individual nanotube defects to a room-temperature fiber cavity operated in the incoherent good cavity regime. Here, the spectral linewidth of the emitter greatly exceeds that of the cavity, resulting in a drastic spectral purification of single photons emitted from the cavity. Our experimental results indicate a corresponding increase of the photon indistinguishability by two orders of magnitude compared to free-space emission, accompanied by an enhancement of the emission spectral density by at least a factor of four.

The results of this dissertation provide perspectives for the design of polaritonic devices based on dielectrically tailored transition metal dichalcogenides, as well as improved sources of quantum light built on functionalized carbon nanotubes. The corresponding experiments are performed in different regimes of cavity-coupling, thus highlighting the versatility of fiber-based cavities for solid-state based studies of light-matter coupling.

Contents

1 Introduction

The interaction between light and matter gives rise to a plethora of phenomena relevant to everyday human life and unsurprisingly, scientific interest is drawn towards understanding this process on a fundamental level. The advent of quantum mechanics at the beginning of the 20th century identified photons as the individual constituents of a light field [1, 2], which can be thought to exchange energy with matter by interacting with other particles. Applied to the fundamental excitations of electrons in semiconductors, this insight is instrumental in the design of many established devices emitting or absorbing light, enabling key technologies such as the distribution of information in optical fiber networks. In addition to providing a fundamental understanding of light-matter interaction, advances in quantum mechanics also inform proposals which promise paradigm shifts in computation [3–5] and cryptography [6, 7]. In the envisioned technologies, photons play a central role as carriers of information in quantum networks [8, 9] and computing [10]. Potential improvements in these applications are expected to arise from engineered photon-photon interactions [11, 12], achieved by dressing with interacting matter particles to form polaritons [13, 14]. These prospects render light-matter coupling a valuable resource for the design of future devices and motivate fundamental research projects based on novel optoelectronic materials with relevance to quantum technologies as explored in this doctoral thesis.

Quantum technologies of central research interest demand implementations in the solid-state, which hold promise for the design of integrated devices and scalability of the fabrication process. In solid-state systems with nanoscopic dimensions such as quantum wells [15, 16] or quantum dots [17] the confinement of electrons and other quasiparticles modifies their interactions as well as their optical response. As such, particle confinement provides a strategy to realize individual quantum systems for the encoding of information [18] or the generation of single photons [19–21]. This perspective motivates research into nanoscale materials, adding to the relentless drive of the semiconductor industry to increase the processing capabilities for classically encoded information by virtue of device miniaturization. In this context, materials with reduced dimensions have attracted significant interest, with particle confinement provided by the system extent near the atomic limit.

Among the low-dimensional solid-state materials which have emerged in recent decades, two platforms stand out due to their exceptional optoelectronic properties. On the one hand, monolayer transition metal dichalcogenides (TMDs) [22], part of the family of layered van der Waals materials introduced with the discovery of graphene about two decades ago [23], constitute two-dimensional direct-bandgap semiconductors with prospects for nanoscale electronic and photonic devices [24–27]. On the other hand, carbon nanotubes (CNTs), considered a building block of future nanotechnology upon their first observation in the 1990s [28, 29], manifest as one-dimensional semiconductors which promise applications in quantum computing [30] and as room-temperature quantum light sources at telecom wavelengths [31]. In both TMDs and CNTs, electron confinement due to reduced dimensionality together with reduced dielectric screening give rise to room-temperature stable excitons, tightly bound pairs of electrons and holes which dominate the optical response owing to their large oscillator strength [32, 33]. The prospect for tailoring exciton properties by strategies such as functionalization [34, 35] or the application of external fields [36–38] renders TMDs and CNTs prime candidates for experiments and devices in which light-matter interaction is controlled at the excitonic level.

Complementary to the confinement of excitons and electrons in nanoscale semiconductors, confining photons provides a constructive strategy for controlling light-matter interactions. In many applications, which prominently include the laser [39, 40], this is enabled by tailored photonic environments in optical cavities. Coherent coupling between cavity photons and excitons in two-dimensional semiconductor systems such as monolayer TMDs gives rise to exciton-polaritons [13], hybrid light-matter quasiparticles with properties tunable via both the exciton and photon fraction and with applications in quantum simulation [41] and nonlinear optics [42]. Cavities coupled to optical transitions in individual quantum systems such as trapped excitons in functionalized CNTs enable the enhancement of crucial emitter properties, including the decay rate by virtue of the Purcell effect [43] or the photon spectral purity [44, 45].

Crucially, maximizing the light-matter coupling strength is required in many experiments, achieved in resonators with minimal optical mode volume, a constraint which continues to drive research into photonic confinement on the micro- or nanoscale. A variety of platforms has emerged in recent decades, including semiconductor Bragg reflector cavities [46], photonic crystal cavities [47] or plasmonic and dielectric nanoresonators and their assemblies into metasurfaces [48–52]. Among these platforms, fiber-based Fabry-Pérot cavities [53–56] constitute a promising candidate for the coupling to low-dimensional semiconductors. In this geometry, at least one resonator mirror is fabricated on the tip of an optical fiber, allowing for microscopic mode volume at full tunability of the relative mirror position. Combined with the possibility to achieve large quality factors with highly reflective mirror coatings, this platform has proven highly suitable for controlling light-matter coupling in a variety of quantum systems such as ultracold atoms [57] and ions [58, 59], defects in diamond [60, 61],

or low-dimensional semiconductors, evidenced by pioneering experiments on CNTs [62–64] and TMDs [65, 66, P3] performed in the last decade.

In this work, we employed fiber-based Fabry-Pérot cavities to enhance and control the light-matter interaction in two-dimensional monolayer TMDs and fluorescent defects in CNTs, which constitute zero-dimensional quantum systems. In Chapter 2, the properties of these material platforms are discussed, followed by an introduction to optical resonators. The chapter also highlights relevant aspects of coupling between cavity photons and excitons confined to two-dimensional structures such as quantum wells or TMDs as well as zero-dimensional quantum emitters. In this context, the theoretical concepts relevant for the analysis of experimental results are introduced.

Chapter 3 details the experimental techniques relevant to this dissertation. A discussion of the fundamental properties of fiber-based Fabry-Pérot cavities is followed by a description of implementations operating at room- and cryogenic temperatures. The chapter also includes details on a cryogenic optical spectroscopy setup used for device characterization, and a fabrication method for van der Waals heterostructures with engineered TMD dielectric environment.

Experimental results obtained on a TMD monolayer are presented in Chapter 4, where coherent coupling between excitons and the optical mode of a cryogenic fiber cavity results in the formation of exciton-polaritons. Asserting local control over these hybrid light-matter quasiparticles is required for their use in photonic simulation and studies of non-equilibrium many-body physics [67]. In the device presented here, this control was achieved by nanostructuring the dielectric semiconductor environment, defining disk-shaped areas of excitons with modified resonance energies. The resulting local modulation in exciton energy [68, 69] translates to the polaritons [70], leading to cavity-tunable energy shifts. In addition, the cavity setup provides access to the dispersive regime of cavity-coupling [71, 72], in which an effective hopping is mediated between excitons localized to different disk-shaped areas coupled to the same cavity mode. Our technique holds promise for the implementation of lattice potentials in future polaritonic devices based on TMDs.

Chapter 5 reports on cavity-coupling of excitons bound to fluorescent CNT quantum defects, emitters of telecom-band single photons at room-temperature [73] and thus promising candidates for novel single photon sources [74, 75]. In these emitters, strong dephasing prevents the emission of photons with high indistinguishability, which is a crucial resource relevant to photonic quantum technologies. The experiments presented in Chapter 5 overcome this limitation by coupling the emitters to a high finesse fiber cavity operated at room-temperature and in the regime of incoherent good cavity-coupling [45]. For this system, cavity-enhancement of the photon spectral purity and hence indistinguishability was demonstrated, enabled by photon emission into the spectrally narrow window of the cavity linewidth. These results establish incoherent good cavity-coupling as a promising approach to the realization of optimized room-temperature single photon sources.

Chapter 4 and Chapter 5 form the basis of manuscripts [P1, P2], published or intended for publication. As such, each of these chapters contains a brief introduction describing the current state of research and the advantages of the respective semiconductor platform, as well as a short summary and outlook. The central results of this thesis are summarized and put into perspective in the final Chapter 6.

2 Fundamental concepts

This chapter introduces the fundamental concepts relevant to the experiments on microcavity-coupled excitons performed in the framework of this thesis. The chapter starts with a discussion of excitons in two-dimensional transition metal dichalcogenides (Section 2.1), followed by an introduction to excitons in fluorescent carbon nanotube quantum defects (Section 2.2). Subsequently, the fundamental spectral properties of optical resonators are derived (Section 2.3). Building on these concepts, the coupling of optical resonator modes to excitons in quantum wells, with confinement in one spatial dimension, and quantum dots, with confinement in three dimensions, are discussed in Section 2.4 and Section 2.5, respectively. Crucial properties as well as differences between the two systems are highlighted. Section 2.5, which treats resonator-quantum dot coupling, includes an introduction to the theoretical analysis of the Hong-Ou-Mandel experiments presented in Chapter 5, as well as a brief review of the properties of solid-state single photon emitters.

2.1. Excitons in two-dimensional transition metal dichalcogenides

Sparked by the discovery of graphene, fundamental research and technological development based on the class of layered van der Waals materials has attracted significant interest in the last two decades [76]. Of particular relevance is the family of transition metal dichalcogenides (TMDs), which manifest as layered crystals of structure X-M-X, in which M and X represent transition metal and chalcogen atoms, respectively [24].

Crystal structure and electronic properties of monolayer transition metal dichalcogenides

In the following, we focus on the subset of $MoSe_2$, MoS_2, WSe_2, WS_2, which most commonly crystallize in the stable 2H phase [25] as illustrated in Fig. 2.1a. In contrast to graphene, these materials are semiconducting, which renders them highly relevant for optoelectronic applications. We discuss some of the unique properties of monolayer crystals, with a particular focus on the A:1s exciton transition in $MoSe_2$, whose experimental optical response is shown in Fig. 2.1b. As we will elaborate based on Refs. [25, 33], large exciton binding energies and

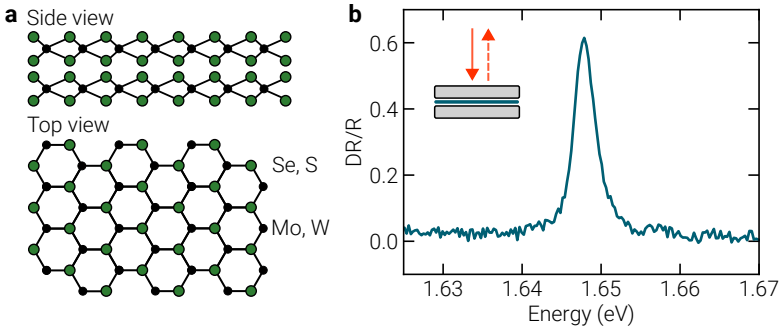

Figure 2.1.: Transition metal dichalcogenide monolayers. a, Illustration of a transition metal dichalcogenide (TMD) crystal in 2H stacking, consisting of layers with structural composition MX_2, in which M denotes the transition metals molybdenum (Mo) or tungsten (W) and X denotes the chalcogens sulfur (S) or selenium (Se). **b**, Optical response of A:1s excitons in a $MoSe_2$ monolayer, encapsulated by thin layers of hexagonal boron nitride and probed in differential reflectivity (DR) at a temperature of 4K as illustrated in the inset. Device and experimental procedure are described in detail in Chapter 3.

oscillator strength of this transition render TMDs a prime candidate for the study of strong exciton-photon coupling in microcavities [77], the central focus of this work. The potential of TMDs for different (opto-) electronic devices based on mono- and multilayer structures is highlighted in the reviews of Refs. [24–27, 78, 79]

In the TMD crystals of interest, the strength of covalent bonds between atoms localized to the individual layers exceeds that of the weak van der Waals bonds between different layers [76]. As a result, individual monolayers can be produced by mechanical exfoliation [80], with alternative fabrication strategies provided by chemical vapor deposition [81–83] or molecular beam epitaxy [84]. While multilayer and bulk TMDs exhibit indirect bandgaps [85, 86], monolayer crystals are semiconductors with direct electronic bandgaps [22, 87] on the order of 2 eV [33].

The Brillouin zone, shown schematically in Fig. 2.2a, exhibits hexagonal shape with high symmetry points denoted by Γ and K/K'. The bandgap is located at the K/K' points, where the band structure approximates parabolic valleys [88, 89], as illustrated in Fig. 2.2b and c. At these high-symmetry points, the large angular momentum of the dominating transition metal orbital contributions to the valence band electronic states leads to a large spin-orbit coupling and hence a valence band splitting of several hundred meV [86, 90]. A small contribution from chalcogen p-orbitals to the conduction band electronic states results in conduction band spin-orbit splittings on the order of a few to ten meV [89]. Notably, this splitting has opposite sign for Mo and W-based monolayers [89, 91], as illustrated in the schematic band structures in Fig. 2.2b. As a consequence of time-reversal symmetry, the spin-orbit splitting is reversed between the K and K' valleys, leading to opposite spin polarizations in the band structure [92] as shown schematically in Fig. 2.2b and c.

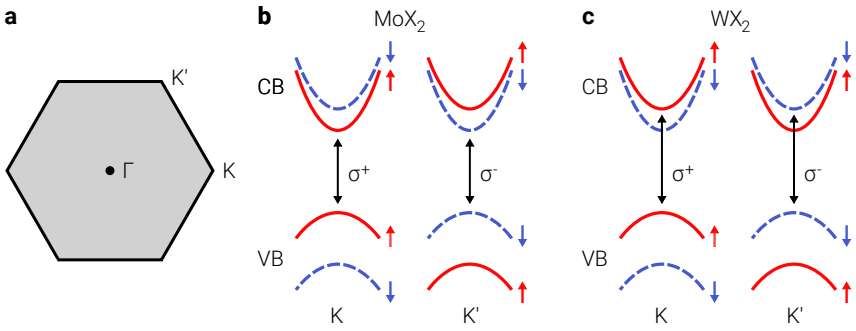

Figure 2.2.: Band structure of TMD monolayers a, Schematic of the first Brillouin zone of a TMD monolayer, with the high-symmetry points indicated by Γ, K and K'. **b**, Band structure schematic of MoX_2 monolayers, with X = S, Se, shown near the K and K' points (left and right panel, respectively). Valence and conduction band (VB and CB, respectively) are split by virtue of spin-orbit coupling, with the splitting in the former exceeding that in the latter by approximately one order of magnitude. The valleys at K and K' feature reversed spin-ordering, as well as energetically lowest optical transitions coupling to opposite circular polarization. **c**, Same as **b** but for WX_2 monolayers. The figure is adapted from Ref. [33].

The properties discussed above have important consequences for the selection rules of the interband optical transitions. Parallel spin alignment renders the energetically lowest transition in Mo-based TMDs spin-bright [93], as illustrated in Fig. 2.2b and c. Broken inversion symmetry and different conduction band orbital angular momentum for the different valleys result in chiral optical selection rules for transitions at the K and K' points, which couple to σ^+ and σ^- polarized light [94–96]. These selection rules enable the optical generation of spin- and valley-polarized electrons, a property which contrasts that of many other semiconductors, such as several III-V systems, whose bandgap is situated at the Γ points, and continues to drive research into TMD-based opto-valleytronic devices [33, 78].

Tightly bound excitons and their optical response

In addition to the electronic band structure, the isolation of TMD mono- and few layer structures greatly influences the properties of excitons, tightly bound electron-hole pairs. Reduced dielectric screening in the monolayer limit, as illustrated in Fig. 2.3a, leads to the formation of Wannier-Mott excitons with binding energies of several hundred meV [33, 97–99], which consequently dominate the optical response in the range from cryogenic to room-temperature. This contrasts many conventional semiconductors such as gallium arsenide with binding energies on the order of a few meV, in which room-temperature exciton formation is infeasible [33].

Monolayer TMD excitons are formed by electrons and holes from different valence and conduction bands, leading to a variety of species with different properties described in

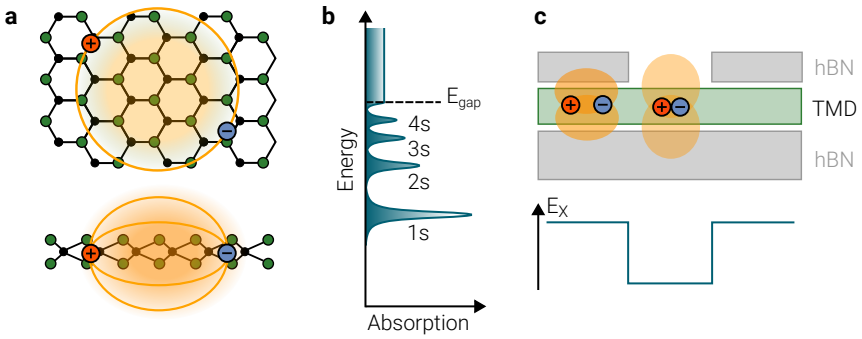

Figure 2.3.: Excitons in TMD monolayers a, Schematic of a Wannier-Mott exciton in a TMD monolayer in top and side view (top and bottom panel, respectively), tightly bound by strong Coulomb interactions, with electric field lines illustrated by solid yellow lines. **b**, Schematic of the TMD monolayer optical absorption. The tightly bound A:1s exciton, as well as higher order Rydberg exciton states, induce optical transitions of considerable oscillator strength at energies below the free-particle bandgap at energy E_{gap}. Additional orbital states, dark states and transitions to different bands are omitted for clarity. **c**, Influence of dielectric environment on exciton energy. Strong Coulomb interactions and two-dimensional quantum confinement render TMD excitons largely susceptible to changes in the dielectric response of the surrounding medium, which influence both binding energy and electronic bandgap. The result is a change in optical transition energy E_{X}, shown schematically for local removal of the hexagonal boron nitride (hBN) encapsulation layer, as implemented in the experiments in Chapter 4. The figure is adapted from Ref. [33].

detail in Ref. [33], with the splittings between different resonances determined by the difference in electronic band energy, as well as electron and hole effective masses and exciton exchange energy [100]. In addition, quantum confinement to two dimensions results in a modification of the Coulomb attraction between electron and hole, which is described by a Rytova-Keldysh potential. This results in a non-hydrogenic Rydberg series of higher excited exciton states [101], as illustrated in Fig. 2.3b, which can also occupy different orbital states. The family of monolayer excitons is further enriched by charged states, most notably trions [102] with a binding energy of around 30 meV in $MoSe_2$ [103], and multi-exciton complexes [104]. In the following, we focus on the bright neutral A:1s exciton in $MoSe_2$, with electron and hole in the energetically lowest conduction band and highest valence band, respectively, which is a bright transition due to parallel spin alignment [33]. Compared to other transitions in the material system, it exhibits maximum oscillator strength, rendering it particularly suitable for studies of strong light-matter coupling in optical cavities.

We consider excitons coupling to a radiation field with wave vectors normal to the crystal plane, which requires conservation of in-plane photon and exciton center-of-mass momenta. This requirement defines the so-called light cone of bright excitons, whose optical response is described by a Lorentzian oscillator model, with an amplitude reflection coefficient [105]

$$r_{\mathrm{TMD}} = \frac{i\gamma_{\mathrm{rad}}/2}{\omega_{\mathrm{x}} - \omega - i\Gamma/2}. \tag{2.1}$$

In this expression, γ_{rad} and Γ are the exciton radiative and FWHM linewidths. Due to the valley-degeneracy of neutral excitons, Eq. (2.1) holds for arbitrary input polarization. Illumination at non-normal incidence or lifted valley-degeneracy, induced e.g. by application of a magnetic field [36], requires a polarization-dependent treatment of the optical response as presented in Ref. [105].

The radiative decay rate γ_{rad} is influenced by the average electron-hole distance, which for A:1s excitons is small due to strong Coulomb interactions and a correspondingly small exciton Bohr radius on the order of 1 nm [33]. As a result, bright 1s excitons exhibit radiative lifetimes $\tau_{\mathrm{rad}} = 1/\gamma_{\mathrm{rad}}$ on the order of a few 100 fs [33, 106–108], corresponding to $\hbar\gamma_{\mathrm{rad}}$ on the order of 1 meV, with fluctuations between reported values likely arising from slight differences in dielectric environment or strain-induced crystal deformations between different samples. When probing the optical response in a differential reflectivity measurement, interference between fields reflected at different dielectric layers in a typical sample modifies the experimental line shape, resulting in a Fano-like spectral response. The Lorentzian reflection profile is retrieved from experimental data by means of the Kramers-Kronig relations [109].

The exciton FWHM linewidth Γ is determined by both homogeneous and inhomogeneous contributions [110], with the former including radiative and non-radiative broadening, induced e.g. by the formation of charged complexes or the trapping at defects [110], as well as dephasing, induced by exciton-phonon coupling and scattering [111]. Sources of inhomogeneous broadening are sample inhomogeneities and contamination with defects, leading to local variations of exciton energy and radiative decay rate on length scales smaller than the optical volume probed in an experiment. The radiative lifetime is about two orders of magnitude smaller than in gallium arsenide quantum wells [33], rendering light-matter coupling highly efficient. Combined with encapsulation in hexagonal boron nitride at reduced disorder, excitons with linewidths approaching the radiative limit have been observed in high quality samples [108]. The respective optical transitions constitute ideal candidates for the formation of exciton-polaritons and are the central focus of this work. A detailed discussion of the optical properties of different exciton species, including dark, charged and multi-particle complexes, exciton response to external electric and magnetic fields, as well as aspects concerning multilayer TMD structures is provided in Refs. [33, 79].

Dielectric screening of Coulomb interactions

Confinement to the two-dimensional monolayer plane renders TMD excitons highly susceptible to the dielectric environment [68]. This can be understood by noting that the electric field between the charged exciton compounds extends into the volume outside the crystal plane, as illustrated schematically in Fig. 2.3a. Since Coulomb interactions between electron

and hole are strong, the resulting susceptibility of the exciton energy to the dielectric constant of the surrounding medium is large, providing a pathway towards engineering of the local exciton potential via the dielectric environment.

The magnitude of the exciton energy shift depends on the dielectric response of the medium surrounding the monolayer [112]. As an example, decreasing the dielectric constant of the surrounding medium by locally removing the hexagonal boron nitride encapsulation layer, as illustrated schematically in Fig. 2.3c, is expected to increase the exciton binding energy by around 200 meV [113, 114]. At the same time, the interaction-induced renormalization shift of the quasiparticle bandgap will experience a reduction of similar magnitude to the increase in binding energy [68]. As a result, the change in optical transition energy upon change of the dielectric environment is typically reported to be on the order of a few meV, differing between samples fabricated by different methods and in different geometries [68–70, 112, 114–116]. In Chapter 4, we harness this effect to translate exciton energy modulation into an engineered polariton energy landscape.

2.2. Excitons in functionalized carbon nanotubes

Since their first description in literature in 1991 [28], carbon nanotubes (CNTs) have been at the center of intensive research activity for a period of roughly two decades due to their intriguing electronic, mechanical and optical properties, enabling applications in a diverse range of fields ranging from the development of novel macroscopic materials to quantum computing platforms [29–32]. Single-walled carbon nanotubes, which are the focus of this work, can be considered as rolled up sheets of monolayer graphite as illustrated in Fig. 2.4a, with typical diameters ranging from around 1 to 10 nm [117, p. 35]. Their reduced dimensionality and nanoscopic shape gives rise to distinct optoelectronic properties which we discuss in the following. We place a particular emphasis on localized excitons for room-temperature single photon emission, which have added the perspective of quantum light-source development to carbon nanotube research in the last decade [31].

Carbon nanotube crystal structure and electronic properties

A single-walled CNT can be imagined to consist of a rectangular graphene sheet, whose geometric properties determine the CNT crystal structure as illustrated in Fig. 2.4c. Graphene manifests in a two-dimensional hexagonal lattice of carbon atoms, bound by σ-bonds from sp^2-hybridized orbitals [119]. Relative to this lattice, different possible CNT unit cells are described by a circumference vector $\mathbf{C}_h$, along which the nanotube is rolled up, as well as a translational vector $\mathbf{T}$. The decomposition of $\mathbf{C}_h$ into the basis vectors $\mathbf{a}_1$ and $\mathbf{a}_2$ of the graphene lattice as shown schematically in Fig. 2.4b, according to $\mathbf{C}_h = n\mathbf{a}_1 + m\mathbf{a}_2$ with integer n and m, is used to characterize CNTs of different structure by means of the chirality

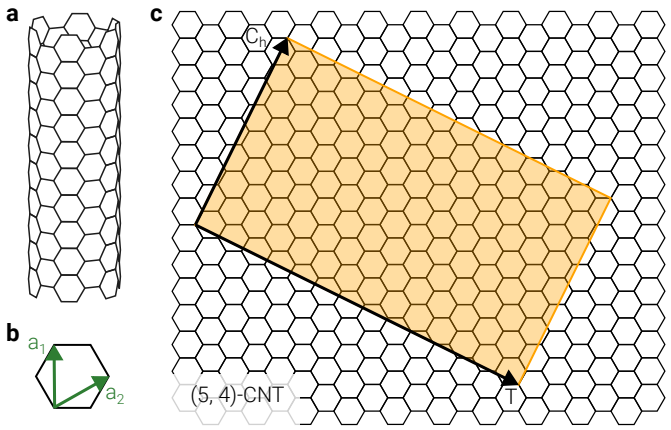

Figure 2.4.: Single-walled carbon nanotubes. **a**, Crystal structure schematic of a chiral single-walled carbon nanotube. **b**, Hexagonal unit cell of the graphene real space lattice, with basis vectors $\mathbf{a}_1$ and $\mathbf{a}_2$. **c**, Unit cell of a chiral (5,4) carbon nanotube, with basis vectors $\mathbf{C}_h$ and $\mathbf{T}$. $\mathbf{C}_h$ is the circumference vector of the nanotube. The figure is adapted from Ref. [118].

(n, m) [117, p. 37]. The chirality determines nanotube diameter and edge type, as evident from Fig. 2.4c. CNTs can be synthesized by arc discharge, laser vaporization or different chemical vapor deposition methods, which are discriminated in their type of catalyst supply [120].

Similar to the crystal structure, it is instructive to discuss the electronic properties of carbon nanotubes in the context of graphene. Graphene is a semimetal, whose band structure near the high-symmetry K and K' points in the hexagonal first Brillouin zone features a linear dispersion determined by electronic π-orbitals [119]. As illustrated in Fig. 2.5a, the CNT reciprocal lattice vectors $\mathbf{K}_1$ and $\mathbf{K}_2$, corresponding to the real space vectors $\mathbf{C}_h$ and $\mathbf{T}$, sample a subspace of the graphene reciprocal lattice. Quantization of the electronic motion along the nanotube circumference results in discrete values for $\mathbf{K}_1$, while the possible values for $\mathbf{K}_2$ are continuous in the limit of a tube of infinite length [117, p. 47]. The CNT band structure is constructed by projecting cuts through the graphene band structure at different values of $\mathbf{K}_1$ into the one-dimensional first Brillouin zone of the nanotube. For about one third of the possible chiralities, selected values of $\mathbf{K}_1$ coincide with the K or K' points in the graphene band structure, at which conduction and valence band are degenerate in energy. The corresponding CNT band structure will therefore also feature a band crossing and hence be of metallic nature [117, p. 60]. By contrast, if the K or K' points do not intersect with any nanotube reciprocal lattice vector, the CNT is semiconducting, featuring an energy gap between valence and conduction band on the order of 1 eV, which roughly scales with the nanotube diameter d_t as $1/d_\mathrm{t}$ [117, p. 69]. In the following, we focus on these semiconducting nanotubes due to their possibility for the creation of room-temperature stable excitons.

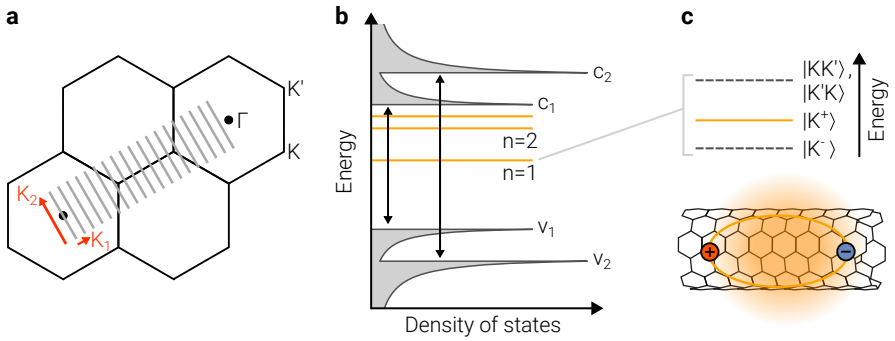

Figure 2.5.: Optical properties of semiconducting carbon nanotubes. a, Reciprocal carbon nanotube basis vectors $\mathbf{K}_1$ and $\mathbf{K}_2$ of a (9,0) CNT, drawn relative to the graphene reciprocal lattice with high symmetry points Γ, K and K'. **b**, Electronic density of states of a semiconducting CNT, illustrated for quasimomenta corresponding to the electronic band edges. Shown are the two lowest and highest energy conduction and valence bands c_1, c_2 and v_1, v_2, respectively. Black arrows indicate the dominant optical transitions. The yellow horizontal lines illustrate transitions corresponding to different states of tightly bound excitons, with the two lowest energy states labeled $n = 1$ and $n = 2$. **c**, Top panel: Schematic of the singlet manifold of the lowest-energy exciton transition. States are labeled $|k_e k_h\rangle$ according to quasimomenta of electron k_e and hole k_h constituting the exciton, indicated by the graphene K and K' valleys. Only the state $|K^+\rangle$, which is an odd parity superposition of $|KK\rangle$ and $|KK'\rangle$ is optically bright. All other states, including the even parity superposition $|K^-\rangle$, are optically dark. The figure is adapted from Ref. [118]. Bottom panel: Schematic of a carbon nanotube exciton.

The band structure of a semiconducting CNT features different conduction and valence bands which we label by indices i and j, respectively, and which have minimum and maximum value, respectively, at the center of the first Brillouin zone. Due to the one-dimensional nature of the system, the density of electronic states exhibits van-Hove singularities and correspondingly maximum values at the band edges [121], as illustrated in Fig. 2.5b. Optical selection rules allow for transitions between valence and conduction bands of identical indices i and j for light of linear polarization oriented parallel to the nanotube axis [122], which dominate the optical response. Transitions between states with indices satisfying $i - j = \pm 1$ are in principle allowed to couple to the orthogonal linear polarization, but are strongly suppressed due a depolarization effect [123].

Tightly bound excitons and their optical response

Reduced CNT dimensionality, accompanied by reduced dielectric screening, greatly enhances the Coulomb interaction between electrons and holes [124–126]. As a result, tightly bound excitons dominate the optical response, with Bohr radius on the order of 1 nm and binding energies on the order of several 100 meV, which renders them stable even at elevated temperatures [126]. Excitons can be formed by electrons and holes in different valence and

conduction bands, which can occupy states of different orbital momenta of the bound two-particle complex [32, 125, 126]. In the following, our focus is on the lowest-energy exciton states labeled by E_{11}, formed by an electron and a hole from the lowest energy conduction band and the highest energy valence band, respectively, corresponding to the c_1 to v_1 transition illustrated schematically in Fig. 2.5b.

The electronic band structure at the band edges is four-fold degenerate due to the degrees of freedom provided by spin and valley, corresponding to single-particle momenta near the K or K' points in the graphene band structure. As a result, 16 exciton states can be distinguished, which are subdivided into twelve triplet states of total spin 1, and four singlet states of spin zero [127]. The degeneracy between different states is lifted due to an interplay between short- and long-range Coulomb interactions. The triplet states are lowest in energy, but optically dark due to their total spin of 1 [127]. Transitions between singlet and triplet manifold are suppressed, such that the singlet states dominate the optical response [128]. The respective manifold, with exciton energies shown schematically in the top panel of Fig. 2.5c, is comprised of states in which electron and hole occupy different valleys, which are optically dark, and states in which electron and hole reside in the same K or K' valley, hybridized as a result of the crystal symmetry [127]. Of the resulting superpositions, only the one of odd parity is optically bright. Lifting of the degeneracy in the singlet manifold gives rise to a characteristic energy ordering in which the dark state is lowest in energy [32, 127]. This dark state forms a population reservoir in photoluminescence experiments, rendering photon emission from CNTs inefficient as compared to other solid-state emitters [31]. The emission efficiency can be further compromised by quenching due to localization at unintended surface defects [129]. The dark-bright splitting is on the order of a few meV, with the precise value depending on the chirality [130–132]. The radiative lifetime of lowest-energy bright excitons near zero center-of-mass momenta is on the order of 1 ns [133, 134], and influenced by the nanotube dielectric environment [135]. The population lifetime, which determines the time-dependent photoluminescence response is dominated by nonradiative decay processes and therefore on the order of 10-100 ps [135, 136].

Luminescent quantum defects in functionalized carbon nanotubes

The low CNT photoluminescence quantum yield, which compares unfavorably with alternative platforms, has triggered interest in increasing the brightness of nanotube exciton emission with the goal of enhanced performance in quantum optoelectronic applications. A successful strategy is provided by the controlled integration of molecular defects such as oxygen or aryl functional groups into the nanotube lattice [31], frequently referred to as functionalization. This process results in the emergence of localized electronic states and corresponding exciton localization at the nanotube defect (NTD) sites, as illustrated in the top panel of Fig. 2.6a. This localization modifies the energy shifts between bright

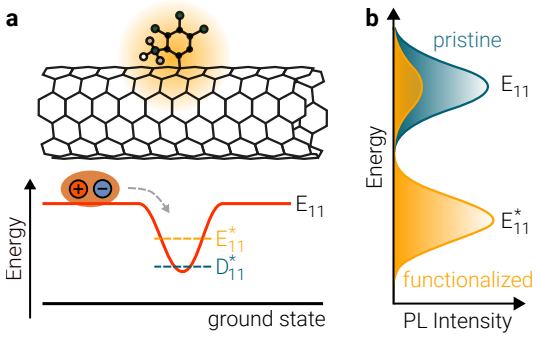

Figure 2.6.: Fluorescent carbon nanotube quantum defects. a, Aryl-functionalized carbon nanotube, with an sp^3 hybridized bond formed between the nanotube lattice and the defect radical. The bottom panel shows a schematic of the resulting exciton energy landscape, with localized bright and dark states E^*_{11} and D^*_{11} forming a trap for mobile excitons E_{11} in the pristine nanotube. The figure is adapted from Ref. [73]. **b**, Schematic of carbon nanotube photoluminescence spectra. Upon functionalization, an emission feature attributed to E^*_{11} excitons localized at the defect site emerges, redshifted by a few hundred meV from the E_{11} transition.

and dark exciton states and suppresses PL quenching due to immobilization. As a result, functionalization enables enhancement of the CNT quantum yield by more than one order of magnitude [34].

In addition to enhancement in PL brightness, trapping of individual excitons at the defect sites results in the emission of single photons, which is of central interest to applications in quantum science and technology [74]. While this effect is also observed at cryogenic temperature for exciton traps created by variations in the dielectric environment [137, 138], the large variation of potential energy in NTDs enables room-temperature trapping [73]. Initial experimental demonstrations were based on the incorporation of oxygen defects [34, 139] at near-infrared emission energies and subject to PL intensity fluctuations [140]. The focus of the present work is on aryl-defects, bound to the nanotube lattice by an sp^3-bond, which enable strong exciton localization with corresponding emission wavelengths in the technologically relevant telecom range and at exceptional room-temperature stability [35, 73].

Aryl-defect sites in the nanotube lattice are generated in a diazonium reaction, which results in the formation of an sp^3-hybridized bond to the aryl group of choice, as well as a second pairing group bonding to a free carbon radical [141]. The electronic configuration of the bonding sites, combined with the electron-hole interaction strength, determines the optical transition energy of the localized exciton. For aryl-defects, a strong modification of the electronic orbitals at the defect site results in redshifts of the exciton emission energy on the order of a few hundred meV, with the precise value determined by the functional group, as well as the carbon nanotube chirality and bandgap [141, 142]. The choice of defect and CNT type therefore allows for tunability of the emission wavelength [143]. The

corresponding strong exciton localization at the defect sites has enabled the operation of room-temperature stable single photon emission with near-unity purity in the telecom wavelength range [73].

The choice of functional group and nanotube chirality also determine the energetic level structure of excitons trapped at the defect sites. For many configurations, a single bright redshifted exciton feature emerges upon functionalization, commonly labeled E_{11}^* as illustrated in Fig. 2.6a and b [142]. In other cases, a second redshifted emission peak is identified, attributed to a different charging geometry of the electronic orbitals. In addition, dark exciton states have also been identified at the defect sites, illustrated schematically in Fig. 2.6a by the state labeled D_{11}^* [144, 145]. The precise level structure depends on the complex interplay of functional group and nanotube lattice geometry during functionalization, and is beyond the scope of the present discussion. Details on the specific functional group employed for experiments in this work are provided in Chapter 5.

In typical experiments, NTD single photon emission is probed in photoluminescence generated by incoherent excitation. In this configuration, defect sites are populated by free E_{11} excitons residing in the surrounding nanotube lattice on timescales on the order of 1 ps [146]. The population lifetimes of the trapped bright exciton states are on the order of 100 ps [73, 144], which is enhanced compared to that of free excitons as expected for reduced nonradiative decay rates due to immobilization at reduced quenching. Population transfer to dark states of localized and free excitons however still influences the photoluminescence decay dynamics, with the detailed response determined by the NTD type [144]. Reported radiative lifetimes range from 1 to 15 ns [73, 144], enhanced compared to free excitons due to strong localization. At room-temperature, individual NTDs feature emission linewidths on the order of 10 meV, dominated by strong dephasing [31, 147]. While single photon emission at telecom wavelengths renders functionalized CNTs excellent candidates for the development of room-temperature sources of quantum light, the broad linewidth limits photon indistinguishability and compromises source performance. A promising strategy to overcome this limitation is provided by NTD-cavity coupling in the incoherent good cavity regime [45], as demonstrated in Chapter 5.

2.3. Optical Fabry-Pérot resonators

Introduced in a seminal work by Fabry and Pérot in 1899 [148, 149], optical interferometers have developed enormous relevance in a diverse range of technological and scientific applications, including the notable examples of laser resonators [40] and a large variety of nanophotonic devices [150]. In this section, we consider an interferometer[1] in the ge-

[1] Depending on the application, the device of interest is frequently referred to as optical interferometer, resonator, cavity or etalon. We will use the relevant terms interchangeably.

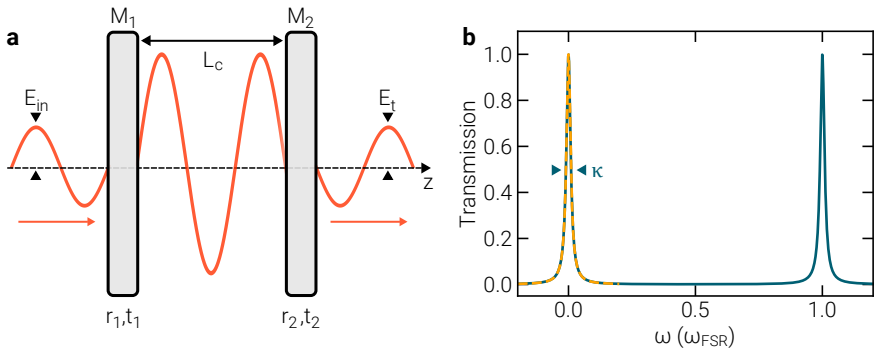

Figure 2.7.: Optical Fabry-Pérot Resonators. a, Schematic side view of an optical resonator, featuring planar mirrors M_1 and M_2 with electric field reflection and transmission coefficients r_1, t_1 and r_2, t_2, respectively. Red arrows indicate the wavevector direction of the incoming and transmitted monochromatic electric fields with amplitudes E_{in} and E_{t}. If the optical frequency ω matches the resonance condition defined by the mirror distance L_{c}, a standing wave is formed inside the resonator. **b**, Transmission of a resonator with identical mirrors and finesse 100 as a function of frequency (teal solid line). Resonances at FWHM linewidth κ are separated by the free spectral range ω_{FSR}. The yellow dashed line is the Lorentzian approximation to the Airy transmission profile.

ometry investigated by Fabry and Pérot, consisting of two parallel plane mirrors as shown schematically in Fig. 2.7a. If light is injected into the resonator at a wavelength that satisfies the condition for constructive interference after a round trip, a standing wave is formed at enhanced field intensity. In the following, we discuss the interferometer properties relevant to studies of coupling between the confined light field and dilute media placed inside the cavity. Due to the wide range of resonator applications, literature on the fundamental properties is abundant. A detailed introduction is given in Refs. [40, 151], on which this section is largely based, a recent discussion on common approximations to the resonance line shapes can be found in [152]. The presentation of parts of this section is adapted from [153].

Resonator transmission

We begin by discussing a scenario frequently encountered in experimental settings, illustrated in Fig. 2.7a: a light field $\mathcal{E}_{\mathrm{in}}(x,t) = 1/2 E_{\mathrm{in}} e^{-i(\omega t - 2\pi/\lambda x)} + \mathrm{c.c.}$ at amplitude E_{in}, wavelength λ and frequency ω impinges on one of the mirrors spaced by a distance L_{c}, and we are interested in the amplitudes of the transmitted field E_{t}. In the following, we assume that the medium between the mirrors has a refractive index $n \approx 1$. The extension to a dispersive intracavity medium is straightforward.

With the phase acquired after one round-trip through the resonator, $\phi_{\mathrm{rt}} = 2\pi \times 2L_{\mathrm{c}}/\lambda$, we find, following the derivations in [40, 152],

$$\frac{E_\mathrm{t}}{E_\mathrm{in}} = \frac{t_1 t_2 e^{i\phi_\mathrm{rt}/2}}{1 - r_0 e^{i\phi_\mathrm{rt}}} \tag{2.2}$$

for the transmission. In this expression, t_k and r_k are the complex coefficients of field transmission and reflection for mirror M_k as labeled in Fig. 2.7a, and $r_0 = r_1 r_2$. Mirror transmission and reflection coefficients of power are given by $T_k = |r_k|^2$ and $R_k = |r_k|^2$, respectively.

From the expression for the transmitted field, we derive the coefficient of transmitted power, T_c, which is readily accessible in many experiments and whose measurement allows to determine fundamental resonator properties. Use of Eq. (2.2) yields

$$T_\mathrm{c} = \frac{|E_\mathrm{t}|^2}{|E_\mathrm{in}|^2} = \frac{T_\mathrm{max}}{1 + \left(\frac{2}{\pi}\mathcal{F}\right)^2 \sin^2\left(\phi_\mathrm{Airy}\right)}, \tag{2.3}$$

which is the Airy-formula with $\phi_\mathrm{Airy} = \frac{1}{2}\phi_\mathrm{rt} + \frac{1}{2}\arg r_0$. It entails the definition of two relevant resonator characteristics, the resonant transmission

$$T_\mathrm{max} = \frac{|t_1 t_2|^2}{(1 - |r_0|)^2} \tag{2.4}$$

and the finesse

$$\mathcal{F} = \frac{\pi\sqrt{|r_0|}}{1 - |r_0|}, \tag{2.5}$$

which is a measure for the mirror reflectivity as evident from this equation, as well as for the cavity linewidth as discussed below.

Distributed Bragg reflectors

Before discussing the cavity resonances described by Eq. (2.3) in more detail, we focus on a common experimental implementation, which is also used in the present work: resonators based on distributed Bragg reflectors (DBRs) as cavity mirrors. Consisting of alternating layers of dielectric materials with different refractive indices, DBR mirrors with reflectivity as large as 0.9999984 have been achieved in the optical domain [154], rendering them highly suitable for quantum optical applications based on, e.g., semiconductor quantum dots [155] and wells [13], individual atoms [156] and ultracold atomic ensembles [157].

Fig. 2.8a and b show a schematic of an exemplary DBR mirror, as used in the setups described in Chapter 3. The transmission, shown in Fig. 2.8c as calculated from a transfer matrix formalism as outlined in Chapter A assuming negligible scattering and absorption loss, reaches minimum values in the wavelength range near the vertical dashed line. The corresponding near-unity reflectivity is a result of constructive interference between the light field reflected at each dielectric surface and the field transmitted through this surface from

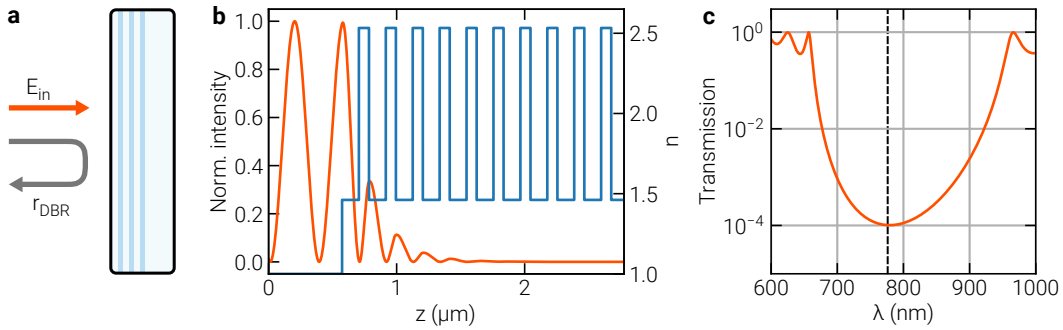

Figure 2.8.: Distributed Bragg reflectors. a, Schematic of a distributed Bragg reflector (DBR) coating consisting of alternating layers of dielectrics with different refractive index n, giving rise to a complex field reflection coefficient r_{DBR}. **b**, Refractive index profile (blue) and electric field intensity of a plane wave impinging on the mirror (red) for an exemplary DBR coating at the stopband center wavelength $\lambda_{\mathrm{s}} = 765\,\mathrm{nm}$, featuring ten pairs of SiO_2 and TiO_2 layers at thickness $\lambda_{\mathrm{s}}/(4n)$. The computation is based on the transfer matrix formalism described in Chapter A. **c**, Transmission $1 - |r_{\mathrm{DBR}}|^2$ of the DBR coating shown in **b**, with the stopband center wavelength indicated by the vertical dashed line.

the neighboring dielectric layer. Since the phase difference between the two fields depends on the optical frequency, high reflectivity is achieved only in a given range of frequencies, which is referred to as the stopband. By varying layer thickness, number and materials, the reflectivity and stopband width can be tuned to match experimental requirements.

Due to non-unity reflectivity at the individual dielectric interfaces, a fraction of the light field impinging on a DBR penetrates into the mirror, as illustrated in Fig. 2.8b. In an optical resonator, this penetration at a depth L_{DBR} extends the cavity length by as much as several µm, an effect with particularly strong influence on the spectral properties of microcavities at mirror distances L_{c} on the order of an optical wavelength [13]. We account for this effect in the following discussion by employing the DBR reflection coefficient for a mirror labeled k [158]

$$r_{\mathrm{DBR,k}} = r_k e^{i(L_{\mathrm{DBR},k}/c)(\omega-\omega_{\mathrm{s}})}, \tag{2.6}$$

in which ω_{s} is the stopband center frequency of maximum DBR reflectivity and c is the speed of light. This description is valid for frequencies close to ω_{s} [158]. While analytical expressions for L_{DBR} can be found in the limiting cases of highly periodic structures [158], more complex mirror designs rely on numerical calculations as presented in Chapter A to determine this quantity. We note that the phase of the DBR transmission coefficient t_k, which is also dependent on the dielectric structure, is irrelevant for the following derivations.

Resonator spectral characteristics

Based on the previous discussion, we investigate the resonances of a cavity with two DBR mirrors. Resonant enhancement of the intra-cavity field occurs if ϕ_{Airy} in Eq. (2.3) is equal to $q\pi$, with q a positive integer denoting the longitudinal mode order. The corresponding cavity resonance frequency is

$$\omega_{\mathrm{c,q}} = c/L_{\mathrm{c}}\left(q\pi + 1/2\arg r_0\right). \tag{2.7}$$

In the following, we assume mirror reflectivities $r_{\mathrm{DBR,1}}$ and $r_{\mathrm{DBR,2}}$ as in Eq. (2.6) and cavity operation at high finesse and frequencies close to the center of the mirror stopband, $\omega_{\mathrm{c,q}} \approx \omega_{\mathrm{s}}$. These assumptions apply to the experimental settings in this work, unless otherwise indicated. The phase determining the resonance condition becomes

$$\phi_{\mathrm{Airy}} = \pi\frac{\omega - \omega_{\mathrm{c,q}}}{\Delta\omega_{\mathrm{FSR}}} + \pi q, \tag{2.8}$$

in which $\omega_{\mathrm{c,q}}$ has to satisfy Eq. (2.7) upon accounting for the fact that $r_0 = r_{\mathrm{DBR,1}}\, r_{\mathrm{DBR,2}}$. In Eq. (2.8),

$$\Delta\omega_{\mathrm{FSR}} = 2\pi\frac{c}{2L_{\mathrm{eff}}} \tag{2.9}$$

is the free spectral range of the resonator, with $L_{\mathrm{eff}} = L_{\mathrm{c}} + L_{\mathrm{DBR,1}}/2 + L_{\mathrm{DBR,2}}/2$ the effective cavity length, which exceeds L_{c} due to the field penetration into the mirrors.

In the case of large cavity finesse $\mathcal{F} \gg 1$, the expression for cavity transmission Eq. (2.3) at frequencies close to a resonance can be simplified considerably. The derivation, which is given in [153], relies on using Eq. (2.8) to substitute ϕ_{rt} in Eq. (2.2), and expanding the exponentials around the resonance frequency as $e^{i2\pi q + x} \approx 1 + x$. Computing the cavity transmission yields

$$T_{\mathrm{c}} \approx \frac{|t_1\, t_2|^2}{(1-|r_0|^2)}\,\frac{(\kappa/2)^2}{(\omega-\omega_{\mathrm{c,q}})^2 + (\kappa/2)^2}, \tag{2.10}$$

which is the well-known Lorentzian line shape with FWHM linewidth $\kappa = \Delta\omega_{\mathrm{FSR}}/(\sqrt{|r_0|}\mathcal{F})$. For $\mathcal{F} \gg 1$, which implies $|r_0| \approx 1$, the linewidth can be expressed as

$$\kappa \approx \frac{\Delta\omega_{\mathrm{FSR}}}{\mathcal{F}} \tag{2.11}$$

to a very good approximation. Eq. (2.11) is also the FWHM linewidth of the resonances of the Airy-formula in Eq. (2.3).

In Fig. 2.7b, we plot the cavity transmission Eq. (2.3) for identical mirrors and $\mathcal{F} = 100$. If the resonance condition $\phi_{\mathrm{Airy}} = q\pi$ is satisfied, the cavity exhibits maximum transmission. The respective resonance frequencies are spaced by $\Delta\omega_{\mathrm{FSR}}$. At these frequencies, the condition for constructive interference after one round trip through the cavity is satisfied by

the light field, such that a standing wave is formed at an intensity which can be drastically enhanced compared to the input field. In the simple case of two mirrors with real reflectivity coefficients, the mirror distance has to match an integer multiple of half the optical wavelength to satisfy this condition.

As evident from Eq. (2.11), the resonance linewidth decreases for increasing finesse. This is readily understood by considering the cavity as a dissipative system, in which the loss channel is transmission through the mirrors. Large finesse then implies small dissipation, large storage times of the field inside the cavity and correspondingly a small linewidth. Finally, the validity of the Lorentzian approximation to the cavity line shape is confirmed by the plot of Eq. (2.10) shown in Fig. 2.7b by the yellow dashed line.

Similar to the finesse, the quality factor $Q = \omega_{\mathrm{c,q}}/\kappa$ is a measure for the dissipation of a given resonance. For an optical resonator, it is calculated as

$$Q \approx q\mathcal{F}, \tag{2.12}$$

which is easily derived from Eq. (2.11). It is evident that for optical resonators, the distinction between finesse and quality factor is of little relevance, since both quantities are directly proportional to each other. In many experiments, the finesse is reported to characterize the resonator, quantifying the mirror reflectivities which are crucial design parameters. The Q-factor is relevant for comparison with different cavity platforms in which no mirrors are employed, such as plasmonic cavities [P4] or whispering gallery resonators [150].

Besides mirror transmission, loss of optical power during a resonator round trip may occur from other sources, such as scattering or absorption in a medium placed between the mirrors. To demonstrate how this affects the transmission profile, we denote the fraction of power which is lost during a single pass through such a medium as B, such that a fraction $(1-2B)$ is transmitted during a cavity round trip. In addition, we account for power loss A_k through scattering and absorption in the mirror labeled k, such that $1 = R_k + T_k + A_k$. Under these conditions, the transmitted field is described by Eq. (2.2) with $|r_0| = \sqrt{(1-2B)\,(1-T_2-A_2)\,(1-T_1-A_1)}$. Defining $L_{\mathrm{tot}} = T_1 + T_2 + A_1 + A_2 + 2B$, and assuming that $T_1, T_2, A_1, A_2, 2B \ll 1$, which holds for typical DBR mirrors, we find $|r_0| \approx \sqrt{1-L_{\mathrm{tot}}}$. Plugging this expression into Eq. (2.4) and Eq. (2.5) and expanding for small L_{tot} yields

$$T_{\max} \approx \frac{4T_1T_2}{(T_1+T_2+A_1+A_2+2B)^2} \qquad \text{and} \qquad \mathcal{F} \approx \frac{2\pi}{T_1+T_2+A_1+A_2+2B}, \tag{2.13}$$

for the maximum transmission and the finesse, respectively. As evident from these expressions, the introduction of loss other than mirror transmission will reduce cavity transmission and finesse, a principle which is at the heart of cavity-enhanced absorption microscopy [159, P5].

Finally, we point to two properties of experimental resonators relevant to the discussion in the following sections. First, while the case of planar mirror resonators discussed here

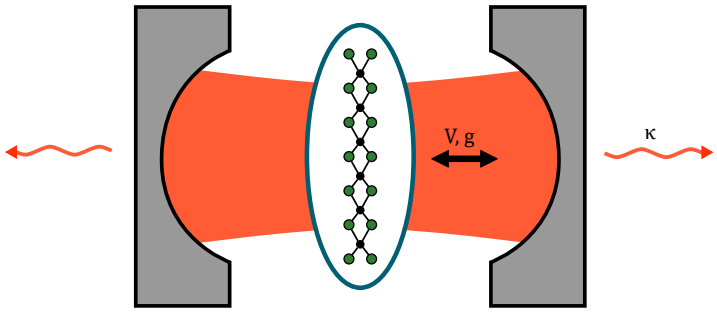

Figure 2.9.: Cavity-coupled monolayer semiconductor. Illustration of a semiconducting TMD monolayer coupled to a single mode of an optical resonator with spectral linewidth κ. The cavity is assumed to couple to a single TMD exciton transition, with similar optical response to that of an epitaxially grown quantum well. The strength of cavity-exciton coupling is denoted by V and g in the semiclassical and quantum mechanical theoretical frameworks presented in the main text, respectively. For illustration purposes, concave mirror profiles are shown, which result in confinement of the resonator mode in the direction orthogonal to the optical axis.

will result in plane-wave intra-cavity fields, the use of spherical mirrors leads to additional transverse field confinement, typically at Gaussian transverse field distributions [40]. As we will show in Section 2.4, this distinction is of relevance when discussing strongly coupled exciton-photon states. Second, it is important to note that the field within the resonator is confined to the mode volume V_c, a parameter which crucially determines the exciton-photon coupling strength [13]. V_c is calculated in Section 5.3 for the case of an experimental cavity used in this work. For the following sections, a simple rule of thumb is sufficient: $V_c \propto L_c$.

2.4. Light-matter coupling in quantum wells

Coupling between quantum well excitons and the modes of an optical resonator is at the heart of experiments and devices in fields such as solid-state nonlinear optics [42] and quantum simulation [160]. In a quantum well, which can be realized in various semiconductor systems, excitons are confined along one spatial direction, strongly altering their intrinsic properties as well as their interaction with light. For a detailed investigation into the physics of quantum wells, which exceeds the scope of this thesis, we refer to Ref. [16], in which the introduction provides an overview of quantum wells in epitaxially grown semiconductors, as well as to Section 2.1, in which the quantum wells constituted by monolayer semiconductors are discussed.

In the following, we consider a single generic transition in the quantum well exciton spectrum, assuming that the resonance of interest is spectrally well resolved such that its

linewidth is greatly smaller than the spectral distance to other resonances arising e.g. from transitions to different electronic bands [16] or the interaction with charges [161]. We discuss the coupling of excitons to a single mode of an optical resonator with FWHM linewidth κ, as illustrated in Fig. 2.9. The presented theoretical treatments were established to describe epitaxially grown quantum well microcavities, and we provide extensions wherever necessary to ensure that the theory captures cavity-coupled TMD monolayer semiconductors. The given expressions provide the basis for the analysis of the experimental results presented in Chapter 4, in which the present discussion is also extended to include cavity-coupling to multiple excitonic transitions.

2.4.1. Semiclassical description

We begin by giving a description of cavity-exciton coupling in a semiclassical framework, which in the last three decades has been successfully applied to microcavity-coupled epitaxially grown quantum wells [158, 162–164] and more recently to describe cavity-exciton coupling in TMD heterostructures [165, 166]. The semiclassical treatment allows for a straightforward definition of the regimes of strong and weak light-matter coupling, which is of fundamental interest to many experiments. In this section, we reproduce the main results of the theoretical analysis based on Refs. [158, 164].

In the semiclassical framework, the optical field confined inside the resonator is treated as a classical electromagnetic wave at frequency ω_c governed by Maxwell's equations. The optical response induced by the exciton transition of interest is described by the reflection and transmission coefficients of an electric field impinging on the quantum well, r_{QW} and t_{QW}, which are given by [167]

$$r_{QW} = \frac{i\gamma_{rad}/2}{\omega_x - \omega - i\Gamma/2} \qquad \text{and} \qquad t_{QW} = 1 + r_{QW}. \tag{2.14}$$

This expression describes a Lorentzian exciton response at frequency ω_x, with FWHM and radiative linewidths[2] Γ and γ_{rad}, which relates to the radiative lifetime as $\tau_{rad} = 1/\gamma_{rad}$. We emphasize that Eq. (2.14) applies to TMD monolayer excitons [105] (c.f. Eq. (2.1)), the central interest of the present work. In this case, the FWHM linewidth can be expressed as $\Gamma \approx \gamma_{rad} + \gamma'$, in which γ' includes contributions to the linewidth from nonradiative decay, dephasing and inhomogeneous broadening [110].

In the following, we consider a quantum well placed at the field antinode of a microcavity consisting of DBR mirrors with identical amplitude reflection coefficients r described by Eq. (2.6), as illustrated in Fig. 2.9. The optical response of the coupled cavity-exciton system is analyzed using a transfer matrix formalism [158, 167], which allows to compute

[2] In the present discussion, linewidths are defined in units of angular frequency. Experimental results for these quantities are reported in eV in Chapter 4, where the conversion factor $\hbar$ is omitted for the sake of brevity.

reflectivity and transmission as well as the system's resonance frequencies[3]. The formalism is introduced in detail in Refs. [158, 163, 164], the relevant transfer matrices are given in Chapter A.

As shown in Ref. [158], the resonance frequencies of the coupled cavity-quantum well system satisfy the equation

$$\left(\omega - \omega_\mathrm{x} + i\gamma'/2\right)\left(\omega - \omega_\mathrm{c} + i\kappa/2\right) = V^2, \tag{2.15}$$

with

$$V = \sqrt{\frac{1+r}{r}\frac{c\gamma_\mathrm{rad}}{L_\mathrm{eff}}} \approx \sqrt{\frac{2c\gamma_\mathrm{rad}}{L_\mathrm{eff}}}, \tag{2.16}$$

where the last approximation holds in the case $r \approx 1$. In this expression, L_eff is the effective cavity length defined in Eq. (2.9), accounting for field penetration into the mirrors, and $\kappa/2 = c\left(1-\sqrt{|r_0|}\right)/\left(\sqrt{|r_0|}L_\mathrm{eff}\right)$ is the HWHM cavity linewidth, with $|r_0| = |r|^2$ in the case of identical DBR reflectivity r. We note that the expression for κ in Eq. (2.15) approximates to the linewidth in Eq. (2.11) derived from the Airy transmission profile in the case of near-unity mirror reflectivity.

Eq. (2.15) provides a pictorial interpretation of light-matter coupling in microcavities. Exciton and cavity are described as oscillators with Lorentzian line shapes, coupled by an interaction of strength V. The complex resonance frequencies of the coupled system are obtained from Eq. (2.15) as [158]

$$\omega = \frac{\left(\omega_\mathrm{c} + \omega_\mathrm{x} - i\left(\gamma' + \kappa\right)/2\right)}{2} \pm \sqrt{V^2 + \frac{1}{4}\left(\omega_\mathrm{c} - \omega_\mathrm{x} - i\frac{\gamma' - \kappa}{2}\right)^2}. \tag{2.17}$$

This equation entails a clear definition of the regimes of strong and weak light-matter coupling in quantum well-microcavity systems. Before discussing this distinction in more detail, we introduce the equivalent quantum-mechanical description of light-matter coupling in the following section.

2.4.2. Quantum-mechanical description

Complementary to the semiclassical description, a quantum-mechanical treatment of cavity-exciton coupling allows for an intuitive analysis of the system's eigenstates in the framework of hybridized light-matter states, which is particularly useful in the regime of strong light-matter coupling. Here, the formalism gives rise to the frequently encountered polariton picture, in which the eigenstates are interpreted as quasiparticles with emerging

[3] For a comparison of different semiclassical approaches, in particular modifications to Eq. (2.2) treating the quantum well as a dispersive intra-cavity medium [46, 168], see Ref. [158]

properties. Quantum and semiclassical treatments yield identical results for the eigenstates as well as cavity transmission and reflectivity [162]. In the following discussion, we follow Refs. [13, 164].

We consider a quantized cavity field, with the bosonic creation operators $\hat{a}^\dagger$ and $\hat{b}^\dagger$ for intracavity photons and excitons at energies $\hbar\omega_\mathrm{c}$ and $\hbar\omega_\mathrm{x}$, respectively. The time-independent Hamiltonian of the system is given in the rotating wave approximation by [164]

$$H = \hbar\omega_\mathrm{c}\hat{a}^\dagger\hat{a} + \hbar\omega_\mathrm{x}\hat{b}^\dagger\hat{b} + \hbar g\left(\hat{a}\hat{b}^\dagger + \hat{b}\hat{a}^\dagger\right), \tag{2.18}$$

with the light-matter coupling strength g. As described above, we consider a single excitonic mode coupled to a single cavity mode, neglecting multiplicities in the exciton and cavity spectra. An extension of the present Hamiltonian accounting for such multiplicities is presented in Chapter 4.

In its generic form, the Hamiltonian of Eq. (2.18) provides a phenomenological description of light-matter interaction. For comparison with experimental results, a suitable expression for the light-matter coupling strength g has to be employed, which depends sensitively on material properties such as the electron hole overlap and the cavity mode volume. For TMD monolayer excitons in a high-finesse cavity, we identify g with the semiclassical result of Eq. (2.15), such that

$$g = \sqrt{\frac{2c\gamma_\mathrm{rad}}{L_\mathrm{eff}}}. \tag{2.19}$$

This identification yields satisfactory agreement with experimental results [165]. Using $\gamma_\mathrm{rad} \propto f$, with the oscillator strength f [105], we find $g \propto \sqrt{f/L_\mathrm{eff}}$. For derivations of g from first principles, see [169, 170].

To diagonalize the Hamiltonian of Eq. (2.18), we evoke the transformation

$$\hat{p} = X\hat{b} + C\hat{a} \qquad \hat{q} = -C\hat{b} + X\hat{a}, \tag{2.20}$$

which yields

$$H = E_\mathrm{LP}\hat{p}^\dagger\hat{p} + E_\mathrm{UP}\hat{q}^\dagger\hat{q}. \tag{2.21}$$

The coefficients X and C are referred to as the Hopfield coefficients [171], and will be discussed below. The eigenenergies are given by

$$E_\mathrm{LP/UP} = \frac{\hbar\omega_\mathrm{x} + \hbar\omega_\mathrm{c}}{2} \pm \sqrt{g^2 + \Delta^2/4}, \tag{2.22}$$

in which we have defined the exciton-cavity detuning $\Delta = \hbar\omega_\mathrm{x} - \hbar\omega_\mathrm{c}$. It is evident that if cavity and exciton are resonant, the spectrum of the coupled system splits into two eigenstates. This splitting of magnitude $2g$ is a hallmark of the regime of strong light-matter coupling, which is discussed in the subsequent section.

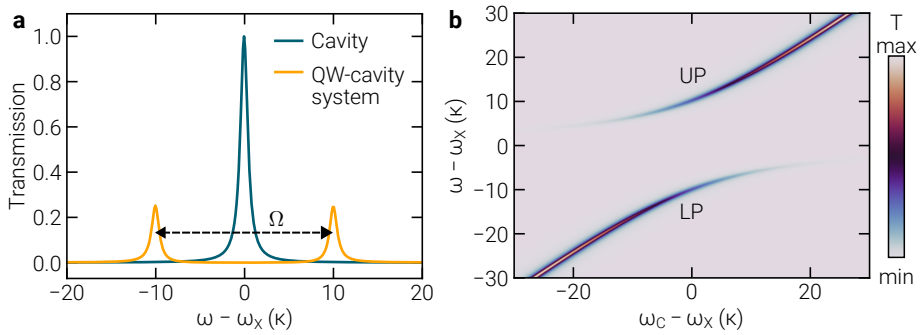

Figure 2.10.: Strong exciton-photon coupling. a, Transmission of an empty cavity (teal line) and upon coupling to a quantum well exciton transition with linewidth $\Gamma = \kappa$ (yellow line) as a function of laser frequency. The coupled system operates in the regime of strong light-matter coupling, where two resonance frequencies are split by the Rabi splitting Ω. The computation is based on the dissipative transmission model introduced in Section 4.3. **b**, Transmission map of the strongly coupled exciton-cavity system investigated in **a**, featuring an avoided crossing of upper (UP) and lower (LP) polariton branches.

Finally, we emphasize the crucial difference between the Hamiltonian of Eq. (2.18) and the Jaynes-Cummings Hamiltonian describing cavity-coupling of a single quantum emitter (c.f. Section 2.5). Bosonic quantum well excitons (and hence operators $\hat{b}$) enable the transformation into the polariton Hamiltonian of Eq. (2.21) and give rise to fundamentally different behavior if multi-particle excitations are considered. This difference is briefly discussed in Section 2.5.

2.4.3. Strong coupling regime

The optical response of the coupled cavity-quantum well system depends on the ratio of light-matter coupling strength and the rates of dissipation from the coupled system: photon loss through the mirrors κ and nonradiative exciton broadening γ', including nonradiative decay and dephasing. If g is large enough, the so-called normal mode splitting of the cavity resonance is observed if the cavity energy is resonant with the exciton transition, as illustrated in Fig. 2.10. The resonances of the coupled system, labeled upper and lower polariton (LP and UP), are split by the Rabi frequency Ω. At zero detuning between cavity and exciton, their linewidth is given by $(\kappa + \gamma')/2$ [158].

Based on the semiclassical treatment presented above, a strict condition for the emergence of strong coupling is [158][4]

$$4g > \left|\gamma' - \kappa\right|, \tag{2.23}$$

for which the square root in Eq. (2.15) becomes real, yielding two distinct eigenfrequencies.

[4] In the following, we will use the identification $V = g$ of Eq. (2.19)

In addition to Eq. (2.23), a second condition is frequently established to observe the strong coupling regime: the experimental splitting Ω should exceed the resonance linewidth. In its most simple form, this condition can be expressed using the splitting derived from the quantum-mechanical Hamiltonian of Eq. (2.18), which yields

$$4g > \gamma' + \kappa. \tag{2.24}$$

In the case of high finesse microcavities, however, different Rabi splittings are observed in measurements of cavity transmission, reflectivity and absorption [158]. Some authors therefore argue that in order to claim strong light-matter coupling, the resonance linewidth $(\kappa + \gamma')/2$ should not exceed the smallest of these splittings [164], which is the one observed in absorption, $\Omega_A = 2\sqrt{g^2 - \left(\gamma' + \kappa\right)^2/8}$ [158]. For the experimental results of this thesis, this distinction is irrelevant: both discussed conditions are fulfilled wherever strong coupling is reported.

Eq. (2.24) allows for an interpretation of the strong coupling regime in the time domain: the rate of energy exchange between cavity mode and quantum well exceeds the total rate of dissipation by photon loss through the mirrors and nonradiative exciton decay. This renders the light-matter coupling coherent: (damped) Rabi oscillations in the exciton and photon population occur, in which excitons are subsequently created and annihilated by the absorption and emission of cavity photons [164]. This process is repeated until the excitation dissipates from the system.

Further insight into the system's coherently hybridized exciton-photon eigenstates, split in resonance energy by $\hbar\Omega$, is provided by the Hopfield coefficients of Eq. (2.20). The exciton and photon fraction of the LP resonance, which depend on the detuning Δ, are given by [13]

$$|X|^2 = \frac{1}{2}\left(1 + \frac{\Delta}{\sqrt{\Delta^2 + g^2}}\right) \qquad \text{and} \qquad |C|^2 = \frac{1}{2}\left(1 - \frac{\Delta}{\sqrt{\Delta^2 + g^2}}\right). \tag{2.25}$$

For the UP branch, $|X|^2$ and $|C|^2$ give photon and exciton fraction, respectively. The Hopfield coefficients are plotted in Fig. 2.11a as a function of cavity-exciton detuning. As expected from Eq. (2.25), the eigenstates on resonance are a balanced superposition of photon and exciton.

The diagonal Hamiltonian of Eq. (2.21) is the basis for a widespread interpretation of the strong light-matter coupling regime: the system's eigenstates, coherent superpositions of photons and excitons, constitute quasiparticles referred to as upper and lower polariton at energies $E_{\mathrm{LP/UP}}$, with corresponding bosonic creation operators $\hat{p}$ and $\hat{q}$. The quasiparticle framework is of particular relevance in the case of planar cavities, for which the eigenenergies exhibit a parabolic dispersion as a function of the wavevector $k_{||}$ parallel to the quantum well plane [13] as shown in Fig. 2.11b - similar to the dispersion of free particles. Cavities

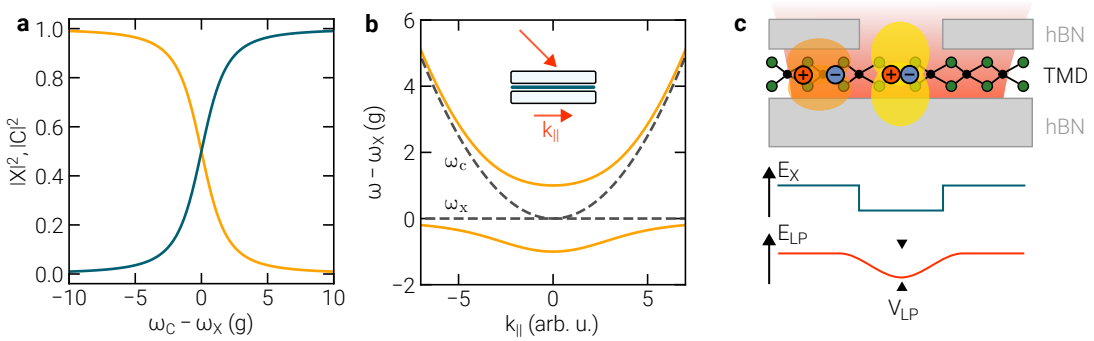

Figure 2.11.: Exciton-polaritons. a, Hopfield coefficients $|X|^2$ (teal line) and $|C|^2$ (yellow line) as a function of cavity-exciton detuning, quantifying exciton and photon fraction in the lower polariton branch, respectively. **b**, Eigenstates of a planar cavity coupled to a quantum well exciton transition (yellow lines), probed as a function of in-plane wavevector $k_{||}$ defined as illustrated in the inset. The dashed lines are the exciton and cavity frequency for the uncoupled system. **c**, Schematic of polariton potential well formation based on engineering the dielectric environment of a cavity-coupled TMD monolayer. Local reduction of the exciton energy in the absence of the top hBN encapsulation layer results in a lower polariton potential well, as shown in the bottom panel of the figure. Combining multiple wells offers a pathway towards polariton lattices of flexible geometries.

with transverse mode confinement, such as the fiber cavity employed for the experiments in Chapter 4, result in corresponding transverse polariton confinement [172].

The strong coupling regime in a solid-state quantum well was first observed for epitaxially grown gallium arsenide microcavities in 1992 [46], laying the foundation for research on exciton-polaritons which is ongoing to this date. Among the intriguing properties of these quasiparticles are their low effective mass, which stems from the photonic fraction of the hybridized state, and the emergence of effective interparticle interactions arising from the excitonic fraction [13], which have enabled the demonstration of bosonic condensation in a solid-state system [13, 173, 174]. In the last three decades, polariton formation has been demonstrated in a large variety of material platforms, including different inorganic [175–177] and organic semiconductors [178, 179], two-dimensional perovskite layers [180], carbon nanotube thin films [181, 182] and van der Waals magnets [183–185], with each platform providing different advantages such as small inhomogeneous and nonradiative broadening in high quality samples, large bandgap or exciton binding energy enabling room-temperature experiments, access to charged exciton complexes or ease of integration with different cavity geometries. A long standing goal is the engineering of effective interactions at sufficient strength to realize nonlinearities at the single photon level in a bosonic system [186], as briefly discussed in Section 2.5.

Large exciton binding energies and light-matter coupling strength render TMD excitons a prime candidate for the investigation of exciton-polariton physics. Initial demonstrations

of strong light-matter coupling of monolayer A:1s excitons in 2015 [187, 188] were soon followed by polariton formation in different TMD materials [165, 189]. These results provided the basis for intensive and diverse research activity on TMD polaritons, exemplified by observations of valley coherence [190–192], providing the basis for the optical valley Hall effect [193], the optical stark effect [194], enhancement of the effective exciton Zeeman splitting [195], bosonic condensation at ambient conditions [196], the demonstration of light-emitting diodes [197], and implementations in different resonator geometries such as plasmonic resonators [198, 199], bound states in the continuum [200] with potential for self-hybridization [52] and topological metasurfaces [201, 202]. Recent reviews are given in [77, 203]. The field continues to attract interest, with a promising perspective provided by coupling to different exciton species at enhanced nonlinearity such as trions [161, 204], Rydberg excitons [205] and excitons in homo- and heterobilayers [206, 207], as well as the implementation of polariton lattices in flexible geometries.

The hybridized character of exciton-polaritons allows for engineering of potentials via both photonic and excitonic potentials [67], since spatially dependent modulations of exciton and photon energies translate to the energy of polaritons, as evident from Eq. (2.22). A possible mechanism to achieve controlled potentials is local modulation of the TMD exciton energy via engineered dielectric environment, resulting in the formation of attractive potential wells as illustrated in Fig. 2.11c and implemented in the experiments described in Chapter 4. In epitaxially grown quantum wells, a common strategy is the fabrication of coupled micropillar cavities, which has enabled polariton-based quantum simulation [41] of Josephson oscillations [208], flat bands in honeycomb lattices [209], topological insulators [210] and Kardar-Parisi-Zhang universality [211]. Examples for different potential engineering strategies are induced local changes in cavity energy by microstructured mirrors [212] and strain [213], with a full review of implemented techniques presented in [67]. As discussed in detail in Chapter 4, subjecting TMD polaritons to lattice potentials in flexible geometries remains a challenge en route towards polariton-based quantum simulation based on this platform.

2.4.4. Weak coupling regime

Complementary to the previous discussion, the weak coupling regime holds if the resonance linewidth exceeds the observable normal mode splitting. This implies that the light-matter coupling strength g is small compared to the total dissipation from the system. In this regime, small eigenstate splittings induced by cavity-coupling are negligible [164]. If g is sufficiently small, $4g < \left|\gamma' - \kappa\right|$ holds, for which the semiclassical result of Eq. (2.15) yields degenerate resonance frequencies and hence vanishing normal mode splitting.

In the weak coupling regime, dissipation inhibits the coherent exchange of energy between quantum well excitons and the cavity mode. However, the cavity still has the potential to

drastically influence the exciton decay dynamics: the modification of the photonic density of states can yield an enhancement of the radiative decay rate [214], rendering the cavity mode an efficient decay channel. This effect is further enhanced by the build-up of an intracavity field, stimulating exciton emission. The enhancement of the radiative decay rate by cavity-coupling is referred to as the Purcell effect. This hallmark property of the weak-coupling regime is quantified by the (ideal) Purcell factor [43] (c.f. Section 2.5), which for quantum well excitons is given by $F_{\mathrm{P,2D}} = \lambda Q / (4\pi L_{\mathrm{eff}})$ [164], such that the intracavity radiative decay rate becomes $F_{\mathrm{P,2D}}\gamma_{\mathrm{rad}}$ for zero exciton-cavity detuning. The Purcell effect is most clearly evidenced in a photoluminescence experiment, where weak cavity-coupling can enhance the emission efficiency.

For the TMD (quantum well) excitons investigated in this work, the weak coupling regime is of little relevance. Upon coupling to microcavities, large exciton oscillator strengths result in large values of g, which exceed the total dissipation even in the case of exciton linewidths broadened by room-temperature dephasing [165, 187] and small values of cavity finesse [190]. As a result, the strong coupling regime holds for many experiments, in particular those presented in Chapter 4 for a cryogenic cavity at large finesse. Purcell enhancement of the TMD exciton radiative lifetime has been observed in resonators with very low Q-factors [110], such as the dielectric cavity formed by two hBN layers [108, 215] or the photonic crystal constituted by a single DBR-mirror [216]. In the framework of this thesis, the weak coupling regime is relevant to the experiments performed on CNT-based quantum defects, such that it is discussed in more detail in the following Section 2.5.

2.5. Light-matter coupling in quantum emitters

In quantum science and technology, single photon sources play a key role as emitters of flying quantum bits, with which information encoded in quantum states can be transmitted over potentially long distances [217]. Notably, emission into a single photon state generates a light field with non-classical (i.e. quantum mechanical) properties, motivating the term "quantum emitter". After first demonstrations in atoms [218, 219] and ions [220], implementations of solid-state based single photon sources are of central interest in ongoing technological development, due to the promise for facilitated device integration and large-scale fabrication.

2.5.1. Solid-state quantum emitters

Quantum emitters capable of generating single photons have been identified in a large variety of solid-state systems. The first demonstration in 1992 based on a dye molecule in an organic crystal [221], was followed by groundbreaking experiments in the year 2000

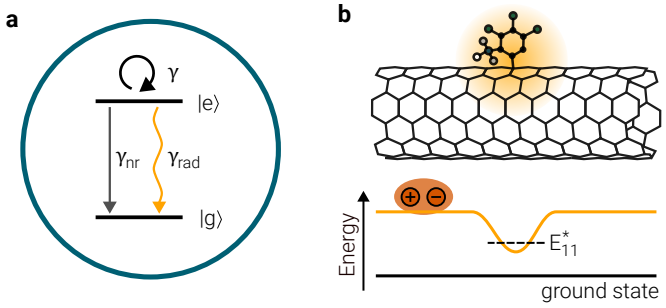

Figure 2.12.: Solid-state quantum emitters. a, Energy level diagram of a generic two-level solid-state quantum emitter. Transitions from excited state $|e\rangle$ to ground state $|g\rangle$ occur via radiative and nonradiative processes at rates γ_{rad} and γ_{NR}, respectively. The system is subject to pure dephasing at a rate γ^*. **b**, Schematic of the quantum emitter formed by functional carbon nanotube defects. Local reduction of exciton energy at the defect sites results in trapping of individual excitons in localized states and single photon emission, as detailed in Section 2.2.

on colloidal and epitaxially grown quantum dots [19, 20] and nitrogen vacancy centers in diamond [222, 223]. Motivated by applications in quantum information processing and communication, these platforms have seen great improvements towards technological maturity in the last two decades, while a plethora of other solid-state systems capable of hosting quantum emitters have been discovered and developed. A non-exhaustive list includes different defects in diamond [224–227], nitrides [228–231], bulk silicon [232], carbon nanotubes [73, 137] and two-dimensional van der Waals materials such as graphene [233], TMDs [234–237] and hBN [238], as well as rare earth ions [239–241] and perovskite nanocrystals [242]. The research field is very active, and a full review by far exceeds the scope of this work, which has its emphasis on fluorescent carbon nanotube defects (NTDs). The properties of this quantum emitter, along with a comparison to alternative platforms, are discussed in Chapter 5. Recent reviews of solid-state single photon sources are given in Refs. [75, 243–247]

In the present section, we illustrate the fundamental properties of a generic solid-state quantum emitter: a quantum-mechanical two-level system, in which transitions between ground and excited state occur by emission or absorption of a photon, as illustrated in Fig. 2.12a. In solids, such artificial atoms are formed by local modification of the electron energy, induced e.g. by epitaxial growth of quantum dots or defects in the crystal lattice, where the resulting quantum-confined electron states exhibit discrete energy levels. If sufficiently strong Coulomb interactions between electrons and holes are present, a two-level system can also be formed by a localized exciton state as illustrated in Fig. 2.12b for the relevant case of NTDs (see Section 2.2 for details). The simplified energy level structure of Fig. 2.12a neglects the presence of additional energy levels, which is relevant to many quantum emitters. For NTDs, the extension to a more realistic level scheme is discussed in Section 5.4. The minimal system chosen for the present discussion serves to introduce the

fundamental characteristics of a single photon source, as well as the mathematical tools to analyze the two-photon interference experiments presented in Section 5.4.

We consider the two-level system illustrated in Fig. 2.12a, with ground and excited states $|g\rangle$ and $|e\rangle$, respectively. The treatment of light-matter interaction in such a system in semi-classical and fully quantum mechanical frameworks is a textbook classic [248]. The system is subject to population decay at a rate $\gamma = \gamma_{\mathrm{rad}} + \gamma_{\mathrm{NR}}$, with radiative and nonradiative decay rates γ_{rad} and γ_{NR}, respectively, as well as (Markovian) dephasing at a rate γ^*.

In what follows, we assume periodic pulsed excitation with a temporal pulse distance Δ which greatly exceeds the life- and coherence time of the system. We assume that at time $t = 0$ during each pulse cycle, the system is instantaneously projected into its excited state, neglecting any delay induced by the excitation. This scenario corresponds to the case of incoherent excitation with negligible delay compared to life- and dephasing time, which is relevant to the NTD experiments discussed in Chapter 5. Transitions between the energy levels are described by the lowering and raising operators $\hat{\sigma}_{\mathrm{ge}}$ and $\hat{\sigma}_{\mathrm{eg}} = \hat{\sigma}_{\mathrm{ge}}^{\dagger}$, while projection operators for ground and excited state are labeled $\hat{\sigma}_{\mathrm{ee}}$ and $\hat{\sigma}_{\mathrm{gg}}$.

The time-dependence of the system during each pulse cycle in the presence of radiative dissipation is described by a density matrix $\hat{\rho}$, whose relevant components evolve according to

$$\rho_{\mathrm{ee}}(t) = \exp\left(-t/T_1\right) \qquad \text{and} \qquad \rho_{\mathrm{ge}}(t) = \exp\left(-t/T_2\right), \tag{2.26}$$

with the population lifetime defined as $T_1 = 1/(\gamma)$ and the coherence time T_2, which depends on T_1 and the dephasing time $T_2^* = 2/(\gamma^*)$ as

$$\frac{1}{T_2} = \frac{1}{2T_1} + \frac{1}{T_2^*}. \tag{2.27}$$

With the previous definitions, the FWHM of the emitter spectral profile is given by $\Gamma = \gamma + \gamma^* = 2/T_2$. Eq. (2.26) are derived under the assumption $\rho_{\mathrm{ee}}(0) = \rho_{\mathrm{ge}}(0) = 1$ from the optical Bloch equations in the absence of a driving field [164, p. 181], which can be obtained from a Lindblad master equation. As expected for a two-level system, population and coherences decay exponentially.

Single photon purity and Hanbury-Brown-Twiss experiment

We now discuss a central characteristic of the quantum emitter under study: the single photon purity, which is quantified by the second order coherence function of the emitted light field. The established method to benchmark this quantity is the Hanbury-Brown-Twiss (HBT) experiment [74, 219, 221], in which correlations between the output port of a beam splitter are measured [249] and which was originally devised to determine the radius of extraterrestrial objects in radio astronomy [250].

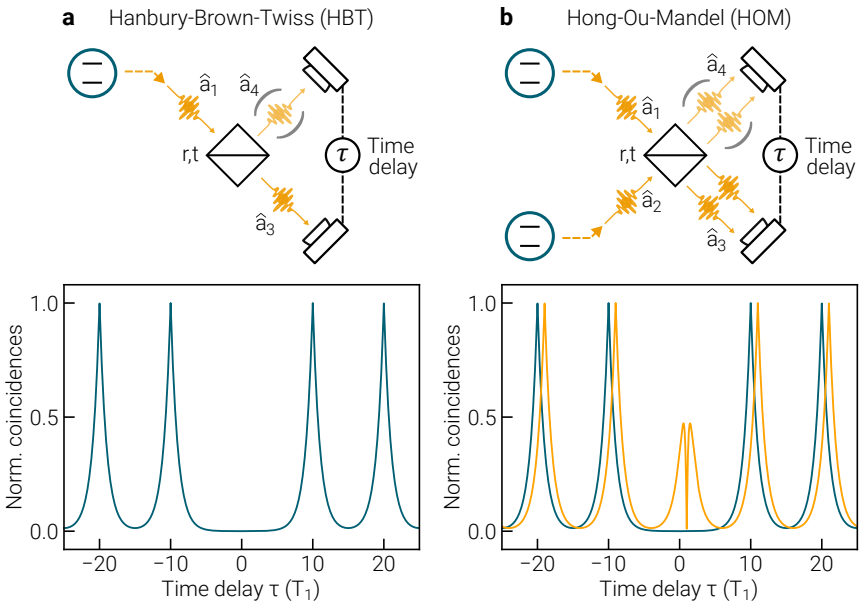

Figure 2.13.: Benchmarking of single photon sources. a, Top panel: Schematic of a Hanbury-Brown-Twiss (HBT) experiment used to benchmark single photon purity. Photons generated by a quantum emitter impinge on a beam splitter with amplitude reflection and transmission coefficients r and t, and detection events at the output ports are time-correlated. The bosonic photon annihilation operators for input and output modes are denoted by $\hat{a}_1$ and $\hat{a}_{3/4}$, respectively. Bottom panel: Normalized coincidences between the beam splitter output ports as a function of time delay, computed for pulsed excitation of an ideal, simplified two-level system as described in the main text. **b**, Top panel: Schematic of a Hong-Ou-Mandel (HOM) experiment used to benchmark photon indistinguishability. Photons emitted by two quantum emitters impinge on the input ports of a beam splitter with characteristics as defined in **a**. Bottom panel: Normalized coincidences between the beam splitter output ports as a function of time delay, computed for identical copies of the two-level system considered in **a** as described in the main text, with lifetime limited coherence $T_2 = 2T_1$ (teal line) and $T_2 = 0.5T_1$ (yellow line).

We consider the HBT experiment shown schematically in the top panel of Fig. 2.13a, and follow the formalism established in [251] to derive expressions for the experimentally accessible coherence functions. In the experiment, photons emitted from the two-level system are guided to one input port of a beam splitter. Photons emerging at the output ports are detected by single photon detectors, and detection events between the output ports are time-correlated as a function of time delay τ to obtain the (non-normalized) cross-correlation function

$$\tilde{G}^{(2)}_{\mathrm{HBT}}(\tau) = \int_0^\infty \mathrm{d}t \langle \hat{a}_3^\dagger(t)\hat{a}_4^\dagger(t+\tau)\hat{a}_4(t+\tau)\hat{a}_3(t)\rangle. \tag{2.28}$$

In this expression, $\hat{a}_3$ and $\hat{a}_4$ are the photon annihilation operators in the two output modes of the beam splitter as illustrated in the top panel of Fig. 2.13a, for which we assume single-

mode operation. An extension to multimode operation, including details on the quantization of the light field, is treated in [252]. The detectors' integration time is much longer than the population lifetime, which motivates the integration performed over t.

The effect of the beam splitter on its input modes $\hat{a}_1$ and $\hat{a}_2$ is described by [251]

$$\begin{pmatrix} \hat{a}_3 \\ \hat{a}_4 \end{pmatrix} = \begin{pmatrix} t_{\mathrm{BS}} & r_{\mathrm{BS}} \\ -r_{\mathrm{BS}} & t_{\mathrm{BS}} \end{pmatrix} \begin{pmatrix} \hat{a}_1 \\ \hat{a}_2 \end{pmatrix}, \tag{2.29}$$

with the complex coefficients of amplitude reflection and transmission r_{BS} and t_{BS}, respectively. In the HBT experiment, photons in the beam splitter input mode $\hat{a}_1$ originate from the two-level system, which in the far field results in the linear relation $\hat{a}_1 \propto \hat{\sigma}_{\mathrm{ge}}$ [248, 251][5]. Combined with Eq. (2.29), the cross-correlation function is calculated as

$$\tilde{G}^{(2)}_{\mathrm{HBT}}(\tau) \propto R_{\mathrm{BS}} T_{\mathrm{BS}} \int_0^\infty \mathrm{d}t \langle \hat{\sigma}_{\mathrm{eg}}(t) \hat{\sigma}_{\mathrm{eg}}(t+\tau) \hat{\sigma}_{\mathrm{ge}}(t+\tau) \hat{\sigma}_{\mathrm{ge}}(t) \rangle, \tag{2.30}$$

with $R_{\mathrm{BS}} = |r_{\mathrm{BS}}|^2$ and $T_{\mathrm{BS}} = |t_{\mathrm{BS}}|^2$.

Since the excitation pulse separation Δ by far exceeds the life- and coherence time of the emitter, the cross-correlation function can be expressed as a sum of the contributions from each excitation cycle $n \in \mathbb{Z}$,

$$\begin{aligned} \tilde{G}^{(2)}_{\mathrm{HBT}}(\tau) &\propto \sum_n \int_0^\infty \mathrm{d}t \langle \hat{\sigma}_{\mathrm{eg}}(t) \hat{\sigma}_{\mathrm{eg}}(t+n\Delta+\tau) \hat{\sigma}_{\mathrm{ge}}(t+n\Delta+\tau) \hat{\sigma}_{\mathrm{ge}}(t) \rangle \\ &= \sum_{n\neq 0} \int_0^\infty \mathrm{d}t \langle \hat{\sigma}_{\mathrm{eg}}(t) \hat{\sigma}_{\mathrm{ge}}(t) \rangle \langle \hat{\sigma}_{\mathrm{eg}}(t+n\Delta+\tau) \hat{\sigma}_{\mathrm{ge}}(t+n\Delta+\tau) \rangle \\ &\quad + \int_0^\infty \mathrm{d}t \langle \hat{\sigma}_{\mathrm{eg}}(t) \hat{\sigma}_{\mathrm{eg}}(t+\tau) \hat{\sigma}_{\mathrm{ge}}(t+\tau) \hat{\sigma}_{\mathrm{ge}}(t) \rangle. \end{aligned} \tag{2.31}$$

The second equality is obtained from the fact that for photons emitted during different excitation cycles, the cross-correlators separate due to $\Delta \gg T_1, T_2$.

We compute the correlators in Eq. (2.31) using the time evolution of the density matrix components of Eq. (2.26), combined with the relation $\langle \hat{\sigma}_{\mathrm{eg}}(t) \hat{\sigma}_{\mathrm{ge}}(t) \rangle = \langle \hat{\sigma}_{\mathrm{ee}}(t) \rangle = \rho_{\mathrm{ee}}(t)$. The correlator at $\tau \approx 0$ is computed using the quantum regression theorem [251, 254] [248, p. 333], which yields $\langle \hat{\sigma}_{\mathrm{eg}}(t) \hat{\sigma}_{\mathrm{eg}}(t+\tau) \hat{\sigma}_{\mathrm{ge}}(t+\tau) \hat{\sigma}_{\mathrm{ge}}(t) \rangle = 0$. The cross-correlation function evaluates to

$$\tilde{G}^{(2)}_{\mathrm{HBT}}(\tau) \propto \sum_{n\neq 0} \exp\left(-|\tau + n\Delta| / T_1\right). \tag{2.32}$$

In in the bottom panel of Fig. 2.13a, we plot the result of Eq. (2.32), which describes an expected experimental histogram. The cross-correlation function exhibits a peak at each possible time delay between two excitation cycles, $\tau = n\Delta$. Correlations near $\tau = 0$ are absent,

[5] For an alternative approach to the derivation presented in the following, see Refs. [252, 253].

the central hallmark indicating the emission of single photons, which due to their particle-like nature exit the beam splitter on a single output port [218].

A frequently used experimental benchmark is the coincidence probability between the beam splitter output ports p_{HBT} at zero time delay, which under pulsed excitation is obtained by integrating coincidence events in the cross-correlation peak at $\tau = 0$ and normalizing by the values obtained for pulses at $|\tau| \gg 0$. Using Eq. (2.31), we find

$$p_{\mathrm{HBT}} = \frac{\int \mathrm{d}\tau \int_0^\infty \mathrm{d}t \langle \hat{\sigma}_{\mathrm{eg}}(t)\hat{\sigma}_{\mathrm{eg}}(t+\tau)\hat{\sigma}_{\mathrm{ge}}(t+\tau)\hat{\sigma}_{\mathrm{ge}}(t)\rangle}{\int \mathrm{d}\tau \int_0^\infty \mathrm{d}t \langle \hat{\sigma}_{\mathrm{eg}}(t)\hat{\sigma}_{\mathrm{ge}}(t)\rangle \langle \hat{\sigma}_{\mathrm{eg}}(t+\tau)\hat{\sigma}_{\mathrm{ge}}(t+\tau)\rangle}. \tag{2.33}$$

This expression is equal to the normalized second order coherence function of the radiation field with annihilation operator $\hat{a}$

$$g^{(2)}_{\mathrm{HBT}}(\tau) = \frac{\langle \hat{a}^\dagger(t)\hat{a}^\dagger(t+\tau)\hat{a}(t+\tau)\hat{a}(t)\rangle}{\langle \hat{a}^\dagger(t)\hat{a}(t)\rangle \langle \hat{a}^\dagger(t+\tau)\hat{a}(t+\tau)\rangle} \tag{2.34}$$

evaluated at $\tau = 0$, such that $g^{(2)}_{\mathrm{HBT}}(0) = p_{\mathrm{HBT}}$. It is frequently referred to as the single photon purity and used to benchmark the performance of a quantum emitter. For the ideal two-level system considered here, $g^{(2)}_{\mathrm{HBT}}(0) = 0$, indicating the emission of pure single photons.

In realistic experimental settings, different mechanisms such as emitter re-excitation or the presence of multiple emitters in the investigated optical volume can lead to a non-vanishing probability for multi-photon emission during an excitation cycle and increase $g^{(2)}_{\mathrm{HBT}}(0)$. In these cases, a measurement of $g^{(2)}_{\mathrm{HBT}}(0)$ can yield insight into the photon number statistics of the emitted radiation field, which however frequently requires additional knowledge or assumptions about the origin of multi-photon emission [255]. In general, $g^{(2)}_{\mathrm{HBT}}(0) < 0.5$ indicates the presence of a single quantum emitter in the optical volume probed in an experiment, while $g^{(2)}_{\mathrm{HBT}}(0) < 1$ indicates a non-classical distribution of photon number states in the radiation field [75, 256].

If additional energy levels contribute to the emitter's decay dynamics, the second order coherence function of Eq. (2.34) can exhibit values $g^{(2)}_{\mathrm{HBT}}(\tau) > 1$ for time delays $\tau \neq 0$, even in the case of a single photon emitter [222]. In the pulsed experiment considered here, this time dependence can be probed by integrating coincidence counts in peaks centered at time delays $\tau = n\Delta$ similar to Eq. (2.33), such that the resulting binned histogram peaks then have a height of $g^{(2)}_{\mathrm{HBT}}(n\Delta)$. An alternative strategy is provided by continuous-wave excitation, which probes the full time-dependence of $g^{(2)}_{\mathrm{HBT}}(\tau)$ in a steady state of the system [222].

Two-photon interference and Hong-Ou-Mandel experiment

Along with large degree of single photon purity, a central requirement for many applications in quantum information processing is a large degree of photon indistinguishability, which enables the observation of two-photon interference [257]. This mechanism is frequently

probed in a Hong-Ou-Mandel experiment, whose general idea is to impinge two photons on different input ports of a beam splitter as sketched in the top panel of Fig. 2.13b. The experiment was originally performed on photon pairs generated by spontaneous parametric downconversion [258–260], where it was used to determine the photon coherence length at unprecedented temporal precision [258]. The potential of this method to quantify the indistinguishability of single photons was first demonstrated using semiconductor quantum dots [21].

To investigate how the quantum emitter properties influence the outcome of the Hong-Ou-Mandel experiment, we consider the scenario shown in the top panel of Fig. 2.13b: identical copies of the ideal two-level system introduced above are assumed to be projected into the excited state at the beginning of each excitation cycle, and the emitted photons are coupled into different input ports of the beam splitter[6]. Detection events in the output ports are time-correlated, which corresponds to a measurement of the non-normalized cross-correlation function [251, 261]

$$\tilde{G}^{(2)}_{\mathrm{HOM}}(\tau) = \int_0^\infty \mathrm{d}t \langle \hat{a}_3^\dagger(t)\hat{a}_4^\dagger(t+\tau)\hat{a}_4(t+\tau)\hat{a}_3(t)\rangle. \tag{2.35}$$

Using the beam splitter input-output relations of Eq. (2.29), we find

$$\begin{aligned}\tilde{G}^{(2)}_{\mathrm{HOM}}(\tau) = \int_0^\infty \mathrm{d}t & R_{\mathrm{BS}}^2 \langle \hat{a}_2^\dagger(t)\hat{a}_1^\dagger(t+\tau)\hat{a}_1(t+\tau)\hat{a}_2(t)\rangle + T_{\mathrm{BS}}^2 \langle \hat{a}_1^\dagger(t)\hat{a}_2^\dagger(t+\tau)\hat{a}_2(t+\tau)\hat{a}_1(t)\rangle \\ & + R_{\mathrm{BS}}T_{\mathrm{BS}} \langle \hat{a}_1^\dagger(t)\hat{a}_1^\dagger(t+\tau)\hat{a}_1(t+\tau)\hat{a}_1(t)\rangle + R_{\mathrm{BS}}T_{\mathrm{BS}} \langle \hat{a}_2^\dagger(t)\hat{a}_2^\dagger(t+\tau)\hat{a}_2(t+\tau)\hat{a}_2(t)\rangle \\ & - R_{\mathrm{BS}}T_{\mathrm{BS}} \langle \hat{a}_2^\dagger(t)\hat{a}_1^\dagger(t+\tau)\hat{a}_2(t+\tau)\hat{a}_1(t)\rangle - R_{\mathrm{BS}}T_{\mathrm{BS}} \langle \hat{a}_1^\dagger(t)\hat{a}_2^\dagger(t+\tau)\hat{a}_1(t+\tau)\hat{a}_2(t)\rangle,\end{aligned} \tag{2.36}$$

in which we have neglected correlators associated with the presence of more than two photons in the beam splitter input ports, since these events are identically zero for the ideal single photon emitter under study and unlikely in the case of the experiments in Chapter 5.

Under the assumption that the emitters in Fig. 2.13c are identical and their time-dependent decay is governed by Eq. (2.26), Eq. (2.36) evaluates to

$$\begin{aligned}\tilde{G}^{(2)}_{\mathrm{HOM}}(\tau) \propto & \left(R_{\mathrm{BS}}^2 + T_{\mathrm{BS}}^2\right)\sum_n \int_0^\infty \mathrm{d}t \langle \hat{\sigma}_{\mathrm{eg}}(t)\hat{\sigma}_{\mathrm{ge}}(t)\rangle \langle \hat{\sigma}_{\mathrm{eg}}(t+n\Delta+\tau)\hat{\sigma}_{\mathrm{ge}}(t+n\Delta+\tau)\rangle \\ & + 2R_{\mathrm{BS}}T_{\mathrm{BS}} \int_0^\infty \mathrm{d}t \langle \hat{\sigma}_{\mathrm{eg}}(t)\hat{\sigma}_{\mathrm{eg}}(t+\tau)\hat{\sigma}_{\mathrm{ge}}(t+\tau)\hat{\sigma}_{\mathrm{ge}}(t)\rangle \\ & - 2R_{\mathrm{BS}}T_{\mathrm{BS}} \int_0^\infty \mathrm{d}t \left|\langle \hat{\sigma}_{\mathrm{eg}}(t)\hat{\sigma}_{\mathrm{ge}}(t+\tau)\rangle\right|^2 \\ \propto & \left(R_{\mathrm{BS}}^2 + T_{\mathrm{BS}}^2\right)\sum_n \exp\left(-|\tau+n\Delta|/T_1\right) - 2R_{\mathrm{BS}}T_{\mathrm{BS}}\exp\left(-2|\tau|/T_2\right).\end{aligned} \tag{2.37}$$

[6] This ideal scenario is chosen for illustration purposes, and to introduce the theoretical concepts relevant for the analysis of Hong-Ou-Mandel type experiments presented in Chapter 5, which were performed on quantum emitters with imperfect single photon purity in an imbalanced Mach-Zehnder interferometer.

The first line in this expression describes coincidences arising from photons which exit the beam splitter on different output ports, which give rise to identical histogram peaks at $\tau \neq 0$. The second line are coincidences near $\tau = 0$ arising due to multiphoton emission, which are zero for the ideal two-level system considered here. The third line describes a reduction of the coincidence counts near $\tau = 0$ due to two-photon interference. To illustrate this effect, we plot Eq. (2.37) in the bottom panel of Fig. 2.13b for a balanced beam splitter and different values of the coherence time. In a lifetime-limited decay with $T_2 = 2T_1$, i.e. in the absence of dephasing, any coincidences near $\tau = 0$ are absent. This signifies that photons at large coherence exit the beam splitter on the same output port, which is the Hong-Ou-Mandel effect.

Similar to the HBT experiment, we compute the normalized correlation function near zero time delay by normalizing to a peak height at $\tau \neq 0$, which yields

$$g^{(2)}_{\mathrm{HOM}}(0) = 1 - \frac{2R_{\mathrm{BS}}T_{\mathrm{BS}}}{R^2_{\mathrm{BS}} + T^2_{\mathrm{BS}}} \frac{\int \mathrm{d}\tau \int_0^\infty \mathrm{d}t \left|\langle \hat{\sigma}_{\mathrm{eg}}(t)\hat{\sigma}_{\mathrm{ge}}(t+\tau)\rangle\right|^2}{\int \mathrm{d}\tau \int_0^\infty \mathrm{d}t \langle \hat{\sigma}_{\mathrm{eg}}(t)\hat{\sigma}_{\mathrm{ge}}(t)\rangle \langle \hat{\sigma}_{\mathrm{eg}}(t+\tau)\hat{\sigma}_{\mathrm{ge}}(t+\tau)\rangle}. \tag{2.38}$$

This expression describes the reduced coincidence probability due to two-photon interference, motivating the definition of the Hong-Ou-Mandel visibility for the photonic mode with annihilation operator $\hat{a}$ [45],

$$v_{\mathrm{HOM}} := \frac{\int \mathrm{d}\tau \int_0^\infty \mathrm{d}t \left|\langle \hat{a}^\dagger(t)\hat{a}(t+\tau)\rangle\right|^2}{\int \mathrm{d}\tau \int_0^\infty \mathrm{d}t \langle \hat{a}^\dagger(t)\hat{a}(t)\rangle \langle \hat{a}^\dagger(t+\tau)\hat{a}(t+\tau)\rangle}. \tag{2.39}$$

For the identical two-level systems under study, we find using Eq. (2.26) and the quantum regression theorem

$$v_{\mathrm{HOM}} = \frac{\int \mathrm{d}\tau \int_0^\infty \mathrm{d}t \left|\langle \hat{\sigma}_{\mathrm{eg}}(t)\hat{\sigma}_{\mathrm{ge}}(t+\tau)\rangle\right|^2}{\int \mathrm{d}\tau \int_0^\infty \mathrm{d}t \langle \hat{\sigma}_{\mathrm{eg}}(t)\hat{\sigma}_{\mathrm{ge}}(t)\rangle \langle \hat{\sigma}_{\mathrm{eg}}(t+\tau)\hat{\sigma}_{\mathrm{ge}}(t+\tau)\rangle} = \frac{T_2}{2T_1}. \tag{2.40}$$

As expected, Eq. (2.38) describes the behavior observed in Fig. 2.13b: for a balanced beam splitter and lifetime-limited photon coherence, the probability $g^{(2)}_{\mathrm{HOM}}(0) = 1 - v_{\mathrm{HOM}}$ for a coincidence event between the beam splitter output ports is zero.

v_{HOM} is sometimes referred to as the photon indistinguishability [262]. In the case of identical, ideal two-level systems considered here, it constitutes a measure of the first order coherence function [251]. Other works have linked its measurement to a determination of the photon wavepacket overlap [21, 253, 256, 262]. Such interpretations of v_{HOM} are valid in the limiting case of photon emission into a pure state [263]. This requirement is not fulfilled in all experimental settings, rendering the extraction of emitter properties from a Hong-Ou-Mandel experiment an ongoing field of research [264–266], with potential additional insights provided by continuous wave excitation [266–268]. In the experiments presented in

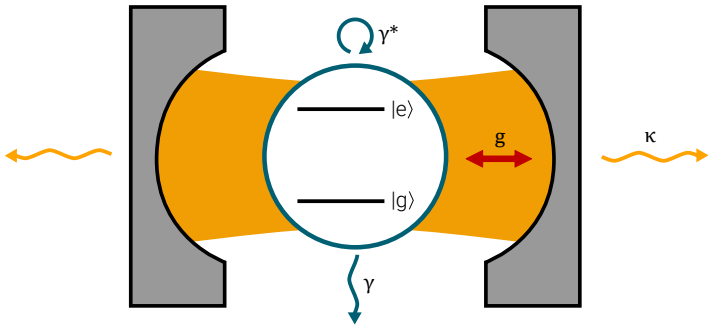

Figure 2.14.: Cavity-coupled solid-state quantum emitter. Schematic of a two-level solid-state quantum emitter coupled to a single mode of an optical cavity with linewidth κ. The light-matter coupling strength is denoted by g, emitter population decay and dephasing rates are given by γ and γ^*, respectively. A resonator with concave mirror profiles is considered, which results in confinement of the resonator mode in the direction orthogonal to the optical axis.

Chapter 5, we refrain from assumptions about the purity of the photonic quantum state and interpret a non-zero HOM visibility as signature of cavity-enhanced photon coherence [45]. To this end, we extend the discussion presented in this section to the case of two-photon interference probed in a Mach-Zehnder interferometer with a cavity-coupled quantum emitter with non-vanishing probability for multiphoton emission.

2.5.2. Quantum emitter-cavity coupling

The previous discussion focused on an individual quantum emitter radiating into free space. If the same emitter is placed inside a resonator, the density of optical states available for radiative decay is modified. This modification can have drastic consequences on light-matter coupling, similar to the case of quantum wells discussed in Section 2.4. In the following, we will discuss the fundamental optical properties of a coupled cavity-quantum emitter system. Motivated by the experiments presented in Chapter 5, the focus will be on the properties relevant to single photon emission in the regime of incoherent coupling, probed in photoluminescence experiments[7].

We consider the system shown schematically in Fig. 2.14. A two-level quantum emitter with resonance frequency ω_x is coupled to a single mode of an optical cavity with frequency ω_c and FWHM Lorentzian linewidth κ. The cavity photon annihilation operator is $\hat{a}$. As before, we describe transitions between the energy levels $|g\rangle$ and $|e\rangle$ by the lowering and raising operators $\hat{\sigma}_{ge}$ and $\hat{\sigma}_{eg} = \hat{\sigma}_{ge}^{\dagger}$. The population decay rate $\gamma = \gamma_{rad} + \gamma_{NR}$, including

[7] Motivated by applications in the development of sources of single photons as long-distance carriers of quantum information, the present discussion is focused on emitters and resonators operating at optical and telecom wavelengths. A treatment of cavity quantum electrodynamics in the microwave domain is beyond the scope of this chapter.

radiative and nonradiative contributions, is defined such that $\gamma = 1/T_1$ with the population lifetime T_1. Combined with the dephasing rate $\gamma^* = 2/T^*$, the quantum emitter's FWHM (Lorentzian) linewidth is $\Gamma = \gamma + \gamma^*$. The probability for radiative emission of a photon is quantified by the quantum yield

$$\eta_{\mathrm{QY}} = \frac{\gamma_{\mathrm{rad}}}{\gamma}. \tag{2.41}$$

The coupled system is described by the Jaynes-Cummings Hamiltonian [269], which reads based on Ref. [270]

$$H_{\mathrm{JC}} = \hbar\omega_{\mathrm{c}}\hat{a}^\dagger\hat{a} + \hbar\omega_{\mathrm{x}}\hat{\sigma}_{\mathrm{ge}}^\dagger\hat{\sigma}_{\mathrm{ge}} + \hbar g\left(\hat{a}\hat{\sigma}_{\mathrm{eg}} + \hat{\sigma}_{\mathrm{ge}}\hat{a}^\dagger\right), \tag{2.42}$$

with the light-matter coupling strength g. Evidently, this Hamiltonian resembles the one for a cavity-coupled quantum well of Eq. (2.18). The difference lies in the fermionic commutation relation obeyed by the annihilation and creation operators σ_{i}, which contrasts that of the bosonic quantum well exciton operators. This distinction has important consequences: it reflects the possibility for single photon emission from a cavity-coupled quantum emitter and influences the Hamiltonian spectrum in the coherent coupling regime, as discussed below.

The light-matter coupling strength g is derived from the electronic dipole transition in a two-level atom in vacuum, for which it is given by [271] $g_{\mathrm{atom}} = \sqrt{\mu_{\mathrm{eg}}^2\omega_{\mathrm{x}}/(2\epsilon_0\hbar V_{\mathrm{c}})}$, with the dipole matrix element squared μ_{eg}^2 and the dielectric constant ϵ_0. For a solid-state two-level quantum emitter, accounting for the refractive index n in the surrounding medium is required when computing the dipole matrix element. Using μ_{eg}^2 as obtained for a quantum emitter [272], the light-matter coupling strength reads

$$g = \sqrt{\frac{3\lambda^2 c\gamma_{\mathrm{rad}}}{8\pi n^3 V_{\mathrm{c}}}}, \tag{2.43}$$

with the emission wavelength λ and the radiative decay rate $\gamma_{\mathrm{rad}} = 1/\tau_{\mathrm{rad}}$.

Eq. (2.43) motivates a central cavity design criterion for the coupling to quantum emitters. Large light-matter coupling strength, which is crucial for many applications in quantum science and technology, is obtained by making the cavity mode volume as small as possible. This observation continues to drive cavity miniaturization, and has resulted in the development of various micro- and nanocavity platforms in the last decade. Open Fabry-Pérot resonators offer a large degree of tunability and enable the coupling to various types of emitters [61, 62, 155, 273–275], with mode volumes as small as λ^3 achieved in fiber cavities [274]. Epitaxially grown monolithic Fabry-Pérot cavities allow for the direct integration of quantum dots during the fabrication process [19, 21] at a small degree of optical losses, but penetration into the DBR mirrors can limit the achievable mode volume to a few $\mu\mathrm{m}^3$ [150].

Comparable or smaller mode volumes are provided by photonic crystal cavities, which have also been combined with various quantum emitters [276–279]. In this monolithic platform, the position of the cavity mode with respect to the emitter is not tunable, which can make emitter placement during the fabrication process challenging. Further monolithic geometries include whispering gallery resonators [20], which can feature large quality factors, as well as waveguides [280], bullseye structures [281], and dielectric metasurfaces based on bound states in the continuum [282], all of which allow for sub-microscopic mode volumes. Another monolithic platform to allow for nanoscopic mode volumes are plasmonic resonators [147, 283–285], which however can provide undesired additional nonradiative dissipation channels limiting photon emission efficiencies [286]. The development of novel microcavity geometries and their coupling to individual quantum emitters of different types is a very active field of research, a full review of which is far beyond the scope of the present work. Some summaries are given in Refs. [150, 286–288]. The specific advantages of fiber-based Fabry-Pérot resonators for coupling to individual quantum emitters are discussed in detail in Section 3.1.

In the following, we will present central characteristics of cavity-coupled quantum emitters, both in the regime of coherent and incoherent coupling. This system has been studied extensively in the past, such that we refrain from lengthy derivations and merely reproduce relevant results from existing literature. The focus of the presentation is on radiative decay rate, coherence time and emission efficiency of photons from the coupled systems. Cavity-coupling offers different strategies for enhancement of these parameters, which as we will show are crucial for the development of optimized single photon sources.

2.5.3. Coherent coupling regime

If the light-matter coupling strength exceeds the sum of all dissipation rates, such that $2g > \gamma + \gamma^* + \kappa$, the system operates in the regime of coherent coupling [45, 289]. In this case, the spontaneous emission spectrum exhibits two peaks, split by the normal mode splitting $2\sqrt{g^2 - (\kappa^2 + \gamma^2)/2}$ [290]. This result can be derived by computing the eigenstates of the Hamiltonian Eq. (2.42) in the eigenstate manifold with only a single photon present in the cavity, obtained in the basis $\{|g,n\rangle, |e,n\rangle\}$ with $n \in \{0,1\}$. We note that in contrast to coherent coupling, for which this splitting exceeds the peak FWHM linewidth $\left(\gamma + \gamma^* + \kappa\right)/2$, Ref. [289] defines the condition for strong coupling as $2g > \left|\gamma + \gamma^* - \kappa\right|$, for which a splitting is present but potentially not resolved in experimental spectra. Other sources use the terms interchangeably, or define slightly different conditions [271, 291]. The distinction is irrelevant to the present discussion, which is focused on illustrating the fundamental properties of systems with coherent energy exchange between cavity and emitter. In this case, the system undergoes Rabi oscillations, with damping determined by emitter nonradiative decay and photon loss from the cavity [290].

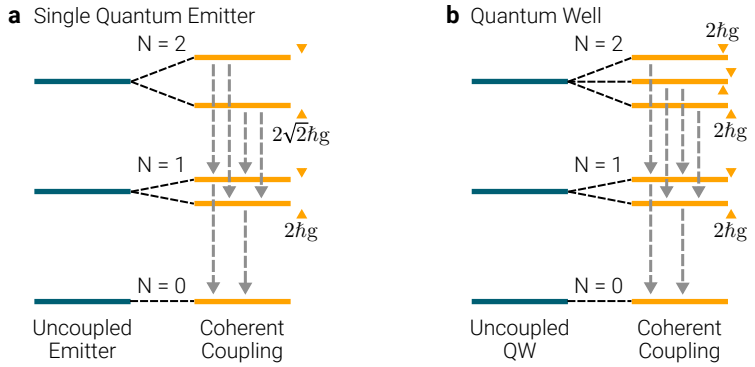

Figure 2.15.: Coherent cavity-coupling regime. **a**, Spectrum of an individual quantum emitter (left), and of the same emitter coupled to a single mode of an optical cavity (right) for different total number of emitter and cavity excitations N. The eigenstates of the coupled system are split by $2\sqrt{N}g$, and the energy differences of the allowed optical transitions in the excitation manifold indicated by dashed arrows result in an anharmonic spectrum. **b**, Same but for the case of a quantum well featuring a bosonic exciton transition. Neighboring eigenstates in an excitation manifold are split by $2g$, which combined with the allowed optical transitions results in a spectral splitting of $2g$, independent of the total excitation number N. The figure is adapted from Ref. [164].

Of experimental interest is the efficiency of photon emission from the cavity, which in the absence of dephasing is given by[8] [292]

$$\beta_{\mathrm{coh}} = \frac{\kappa}{\kappa+\gamma}\frac{2C}{2C+1}, \tag{2.44}$$

with the cooperativity $C = 2g^2/(\kappa\gamma)$ [155]. This parameter quantifies the enhancement of the emitter lifetime by cavity-coupling, which is evident from the equality $2C = F_{\mathrm{p,ideal}}\eta_{\mathrm{QY}}$, with the ideal Purcell factor $F_{\mathrm{p,ideal}}$ as defined in Eq. (2.51) and discussed below. The fraction $2C/(2C+1)$ in Eq. (2.44) can therefore be identified as the probability for photon coupling to the intracavity mode. To obtain the emission efficiency, this probability has to be multiplied with the outcoupling efficiency $\kappa/(\kappa+\gamma)$. As evident from Eq. (2.44), large photon emission efficiency in the coherent coupling regime requires large cooperativity and small cavity linewidths. If the emitter undergoes dephasing, the emission efficiency is reduced [290].

To this point, the discussed properties of the cavity-emitter system resemble those of a strongly coupled quantum well discussed in Section 2.4. The difference between the two platforms manifests if more than one photon is present in the cavity. If the light-matter coupling is strong, the eigenstates of the Jaynes-Cummings-Hamiltonian separate into manifolds associated with a fixed number N of excitations in the system [164, p. 191], as

[8] In our labeling for β, we follow the convention of Ref. [45]. In different works [155, 292], the photon emission efficiency is sometimes labeled η, while β is referred to as the probability for emission into the intracavity mode [155].

illustrated in Fig. 2.15a. Each manifold consists of two eigenstates, which are split in energy by $2\hbar\sqrt{N}g$. The result is an anharmonic spectrum, evidenced by the different transition energies between states of different manifolds, which can induce nonlinear optical behavior of the coupled system [293].

In contrast to a quantum emitter, excitons in quantum wells are of bosonic character. As a result, the coupled quantum well-cavity system described by Eq. (2.18) features a manifold of $N+1$ eigenstates split by $2g$ if N excitations are present in the system [164, p. 188], as illustrated in Fig. 2.15b. Notably, each excitation is an upper or lower polariton as defined in Section 2.4. Dissipation can only occur by removing a polaritonic excitation from the system, which suppresses certain transitions between eigenstates in different manifolds, as illustrated in Fig. 2.15b. The resulting optical spectrum features exactly two resonance frequencies with a splitting given by $2g$ (in the absence of dissipation), which is independent of the number of photons in the cavity. Achieving optical nonlinearities in bosonic polariton systems therefore requires excitonic interactions, which translate to effective interactions of the hybrid exciton-photon eigenstates [13]. A long-standing goal in the field is the realization of polariton blockade [186, 294, 295], a nonlinearity on the single photon level in a system of coupled bosons.

The coherent coupling regime for individual quantum emitters in the optical domain was first observed for atoms in cavities [156], where it forms the basis for single photon sources [296], photonic quantum gates [297, 298] and nonlinear optical behavior on the single- and few photon level induced by the Jaynes-Cummings anharmonic spectrum [299, 300]. Similar results have been obtained with individual ions [301]. In the solid-state, coherent coupling has been observed for quantum dots in epitaxially grown microcavity structures [302] and photonic crystal cavities [303] at spectrally narrow cavity linewidth, operated at cryogenic temperatures at minimal dephasing and incoherent broadening. This platform has enabled the observation of nonlinear phenomena related to the Jaynes-Cummings anharmonic spectrum [304, 305], and recent results offer a promising perspective towards a photonic quantum gate in the solid-state [155]. In many other solid-state quantum emitters including nanotube defects, limitations such as low quantum yields or reduced photon-cavity coupling efficiencies due to large refractive index of the host material prevent the observation of coherent coupling. However, as we will show in the following section, the regime of incoherent coupling offers promising approaches for optimized single photon sources based on these emitters.

2.5.4. Incoherent coupling regime

If the total dissipation exceeds the coupling strength such that $2g < \gamma + \gamma^* + \kappa$, the system operates in the incoherent coupling regime. This regime is at times also referred to as weak coupling [45, 293], and slightly different definitions for its distinction from coherent and

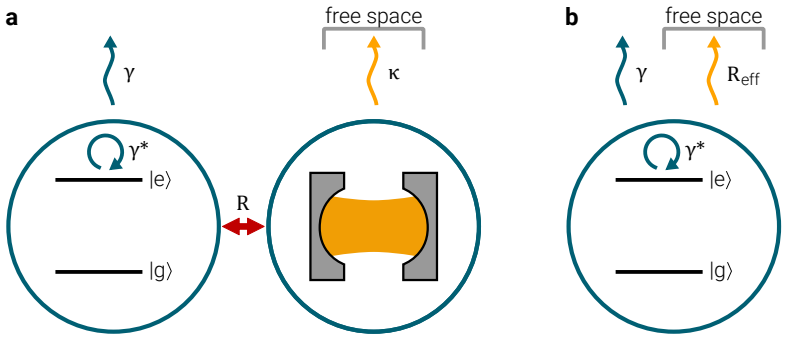

Figure 2.16.: Incoherent cavity-emitter coupling. a, Schematic of a quantum emitter-cavity system in the regime of incoherent coupling. Emitter and cavity exchange energy at a rate R, dissipation occurs via emitter population decay and dephasing at rates γ and γ^* and photon decay into free space through the cavity mirrors at rate κ. **b**, Equivalent description of the coupled system, in which the cavity provides an additional channel for emitter dissipation into the free space reservoir at an effective rate R_{eff}. The figure is adapted from Ref. [289].

strong coupling exist in the literature, as pointed out in Section 2.4. In the present section, we focus on the case $2g \ll \gamma + \gamma^* + \kappa$, which is relevant to the experiments presented in Chapter 5. We follow the derivation in Ref. [45], from which we also adapt the definitions of different coupling regimes.

We focus on single photon emission from a cavity-coupled quantum emitter, such that we consider the process of spontaneous (and stimulated) emission with the emitter projected into the excited state $|e\rangle$ at time $t = 0$ by incoherent excitation. In the relevant subspace $\{|g,1\rangle, |e,0\rangle\}$, the system's density matrix has time-dependent components $\rho_{\mathrm{cc}}(t) = \langle \hat{a}^\dagger(t)\hat{a}(t)\rangle$, $\rho_{\mathrm{ec}}(t) = \langle \hat{\sigma}^\dagger_{\mathrm{ge}}(t)\hat{a}(t)\rangle$, $\rho_{\mathrm{ce}}(t) = \langle \hat{a}^\dagger(t)\hat{\sigma}_{\mathrm{ge}}(t)\rangle$ and $\rho_{\mathrm{ee}}(t) = \langle \hat{\sigma}^\dagger_{\mathrm{ge}}(t)\hat{\sigma}_{\mathrm{ge}}(t)\rangle$ [45]. The time-dependence of the density matrix is computed from a Lindblad master equation in Markovian approximation [44]. In the incoherent coupling regime, the coherences can be eliminated, yielding the time-dependence for the populations [289]

$$\begin{aligned} \frac{\mathrm{d}\rho_{\mathrm{cc}}}{\mathrm{d}t} &= -(\kappa + R)\rho_{\mathrm{cc}} + R\rho_{\mathrm{ee}} \\ \frac{\mathrm{d}\rho_{\mathrm{ee}}}{\mathrm{d}t} &= -(\gamma + R)\rho_{\mathrm{ee}} + R\rho_{\mathrm{cc}}, \end{aligned} \tag{2.45}$$

with the rate

$$R = \frac{4g^2}{\kappa + \gamma + \gamma^*} \frac{1}{1 + 4\left(\frac{\omega_{\mathrm{c}} - \omega_{\mathrm{x}}}{\kappa + \gamma + \gamma^*}\right)^2}. \tag{2.46}$$

These equations yield the interpretation of the system's decay dynamics illustrated schematically in Fig. 2.16a. In the incoherent coupling regime, emitter and cavity exchange energy at a rate R, with dissipation from the emitter by nonradiative processes and radiative decay into free space at a rate γ, and photon loss from the cavity at rate κ. We note that the

presence of the cavity mode reduces the rate of radiative decay into free space compared to emission into the full solid angle [306]. In fiber-based microcavities, the cavity mode volume is small, however, such that the effect is negligible and the rate for free-space emission is given by γ to a good approximation [307].

From the perspective of the emitter, photons are emitted into the outcoupling mode of the cavity (i.e. into the mode outside of the mirrors) at an effective rate [289]

$$R_{\mathrm{eff}} = \frac{\kappa R}{\kappa + R}. \tag{2.47}$$

This observation motivates an additional interpretation of the dynamics in the incoherent cavity regime, illustrated in Fig. 2.16b. From the perspective of the emitter, the cavity outcoupling mode provides a reservoir for dissipation at a rate R_{eff}, in addition to decay at a rate γ. Consistent with this interpretation, the efficiency of photon emission from the cavity upon initial excitation of the emitter as derived from Eq. (2.45) reads [45]

$$\beta = \frac{R\kappa/(R+\kappa)}{\gamma + R\kappa/(R+\kappa)} = \frac{R_{\mathrm{eff}}}{R_{\mathrm{eff}} + \gamma}. \tag{2.48}$$

By modification of the optical density of states and induced stimulated emission, the presence of the cavity can enhance the emitter decay rate and hence the efficiency of single photon emission. This observation motivates the definition of the Purcell factor

$$F_{\mathrm{p}} = \frac{R}{\gamma_{\mathrm{rad}}}, \tag{2.49}$$

which quantifies the enhancement of the emission rate into the cavity mode compared to the free space radiative decay rate. Enhancement as compared to the free space population decay rate is quantified by the effective Purcell factor

$$F_{\mathrm{p}}^{*} = \frac{R}{\gamma}. \tag{2.50}$$

From these expressions, it is evident that Purcell factors and emission efficiency depend on the light-matter coupling strength and on the ratio between the rates of dissipation induced by cavity and emitter, respectively. Based on this consideration, two distinct sub-regimes of incoherent coupling can be identified, whose properties we discuss in the following. Note that again, different conventions exist for labeling and defining these regimes, with the present discussion following Ref. [45].

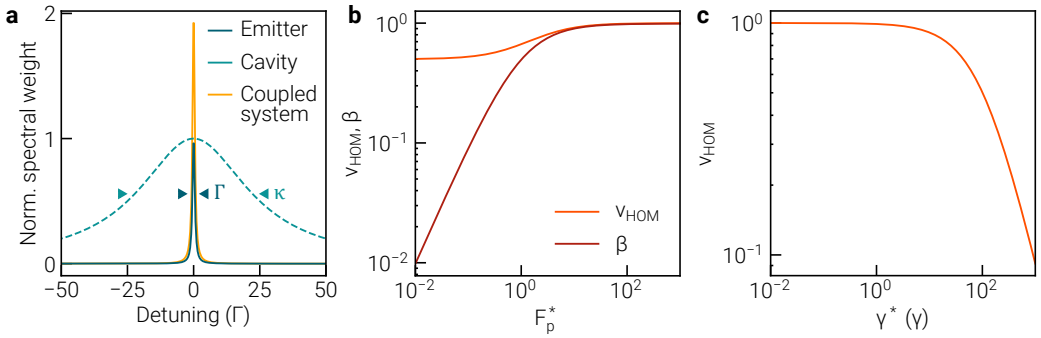

Figure 2.17.: Regime of incoherent bad cavity-coupling. a, Illustration of spectral profiles in the regime of incoherent bad cavity-coupling, in which the linewidth κ of the cavity transmission profile (light green dashed line) greatly exceeds that of the emitter, Γ (teal line). The linewidth of the coupled system approximates that of the emitter, with enhanced emission efficiency in case of a large Purcell factor (yellow line). **b**, Two-photon interference visibility v_{HOM} (orange) and photon emission efficiency β (dark red) as a function of effective Purcell factor F_{P}^*, calculated for $\kappa = 100\gamma$ and $\gamma^* = \gamma$. **c**, v_{HOM} as a function of dephasing rate, calculated for $F_{\mathrm{P}}^* = 100$.

Incoherent bad cavity-coupling regime

If photon loss from the cavity is the dominant decay channel such that $\kappa \gg \gamma + \gamma^*$, the coupled system operates in the bad cavity regime. In this regime, the cavity linewidth exceeds that of the emitter as illustrated in Fig. 2.17a, such that any photon emitted into the cavity mode is efficiently transmitted through the mirrors. On resonance, the rate of energy exchange between cavity and emitter approximates to $R \approx 4g^2/\kappa$, which yields the effective Purcell factor $F_{\mathrm{p}}^* \approx 4g^2/(\kappa\gamma)$. The population decay rate of the cavity-coupled emitter $\gamma_{\mathrm{c}} = \gamma + R$ is enhanced compared to the free space rate γ by the factor $1 + F_{\mathrm{p}}^*$ (see Eq. (2.50)). This enhancement of emitter decay rate by cavity-coupling is frequently referred to as Purcell effect.

The rate of radiative decay into the cavity mode is enhanced compared to the free space radiative decay by the factor defined in Eq. (2.49), which in the bad cavity regime is at times referred to as the ideal Purcell factor [308], given by

$$F_{\mathrm{p,ideal}} \approx \frac{4g^2}{\gamma_{\mathrm{rad}}\kappa} = \frac{3}{4\pi^2}\left(\frac{\lambda}{n}\right)^3 \frac{Q_{\mathrm{c}}}{V_{\mathrm{c}}}, \tag{2.51}$$

with the cavity Q-factor $Q_{\mathrm{c}} = \omega_{\mathrm{c}}/\kappa$. This result is identical to the expression given by Purcell [43] to quantify the enhancement of radiative decay rate in microwave cavities, and can also be derived by computing the decay rate from Fermi's golden rule [271, 309].

The photon emission efficiency in the bad cavity regime computes to

$$\beta_{\mathrm{bc}} \approx \frac{\kappa}{\kappa + \gamma}\frac{F_{\mathrm{p}}^*}{F_{\mathrm{p}}^* + 1}. \tag{2.52}$$

This expression is similar to the one obtained in the coherent coupling regime, Eq. (2.44), with the cooperativity replaced by the effective Purcell factor. In the incoherent bad cavity regime, extraction of emitted photons via the cavity can be highly efficient and greatly exceed the free space quantum yield if large effective Purcell factors are achieved. A frequently employed strategy towards this goal is the use of emitters with reduced radiative decay or dephasing, coupled to cavities with small mode volume at correspondingly large values of light-matter coupling strength.

The coherence time of the emitted photons is given by $2/(\gamma^* + \gamma + R)$ [45]. Combined with the cavity-shortened lifetime $1/(\gamma + R)$, this yields a HOM-visibility of

$$v_{\mathrm{HOM,bc}} = \frac{\gamma + R}{\gamma^* + \gamma + R} = \frac{F_{\mathrm{p}}^* + 1}{F_{\mathrm{p}}^* + 1 + \gamma^*/\gamma} \tag{2.53}$$

in the bad cavity regime. This result is derived from computing the relevant HOM cross-correlation functions for the coupled system [45].

As evident from plots of β_{bc} and $v_{\mathrm{HOM,bc}}$ shown in Fig. 2.17b, large photon emission efficiency and indistinguishability in the incoherent bad cavity-coupling regime require large effective Purcell factors. In many experiments, this is achieved by maximizing R using cavities with small mode volumes and large quality factors. At the same time, dephasing should be minimized, since it imposes drastic limitations on the two-photon interference visibility as illustrated in Fig. 2.17c, a requirement which places constraints on the choice of emitter and experiment design.

Based on these considerations, simultaneous values of large emission efficiency and indistinguishability in the regime of incoherent bad cavity-coupling have to date relied on operation at cryogenic temperatures at reduced dephasing. Under these conditions, the strategy has proven extremely successful in the realization of optimized, bright sources of indistinguishable photons based on quantum dots coupled to different microcavity platforms operating in the near-infrared wavelength domain [21, 281, 310]. Combined with the benefit of near lifetime-limited linewidths in high quality samples, values of v_{HOM} as large as 0.9956 have been reported [311], with recent count rates as large as 40 MHz at comparable visibility [312]. Recently, promising implementations at telecom wavelengths have been realized with nanotube defects [147], erbium ions [240], quantum dots [313, 314], color centers in silicon [315]. However, the maximum value of v_{HOM} obtained in all of these experiments was 0.8, motivating further development. At room-temperature, many solid-state emitters are subject to strong dephasing, limiting the indistinguishability in the bad cavity-coupling regime. Here, an alternative strategy is provided by the incoherent regime of cavity-coupling discussed in the following.

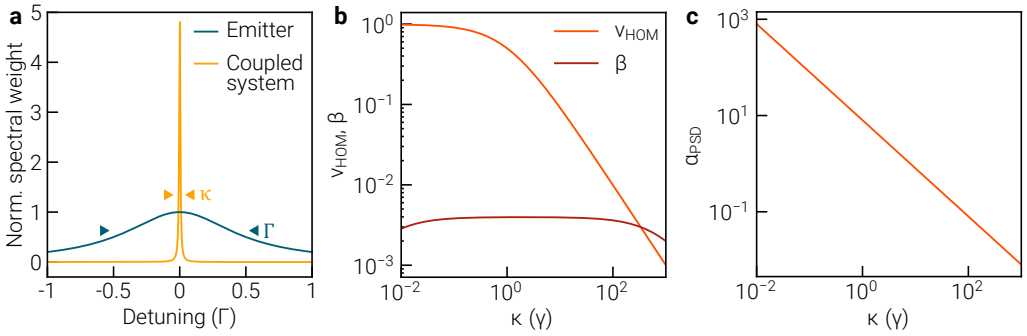

Figure 2.18.: Regime of incoherent good cavity-coupling. a, Spectral profiles of a free-space quantum emitter at linewidth Γ (teal) and emitter-cavity system in the regime of incoherent good cavity-coupling at linewidth κ (yellow). **b**, Two-photon interference visibility v_{HOM} (orange) and photon emission efficiency β (dark red) as a function of cavity linewidth, calculated for $g = \gamma$ and dephasing $\gamma^* = 10^3\gamma$. **c**, Enhancement factor α_{PSD} of the emission spectral density upon cavity-coupling as a function of cavity linewidth, calculated for the same parameters as in **b**.

Incoherent good cavity-coupling regime

If emitter dissipation dominates over photon loss, i.e. $\gamma + \gamma^* \gg \kappa$, the system operates in the incoherent good cavity regime. The rate of energy exchange between cavity and emitter approximates to $R \approx 4g^2/(\gamma + \gamma^*)$. The Purcell factor quantifying cavity-enhancement of the radiative decay rate approximates to

$$F_{\mathrm{p}} \approx \frac{4g^2}{\gamma_{\mathrm{rad}}(\gamma + \gamma^*)} = \frac{3}{4\pi^2}\left(\frac{\lambda}{n}\right)^3 \frac{Q_{\mathrm{em}}}{V_{\mathrm{c}}}, \tag{2.54}$$

with the emitter quality factor $Q_{\mathrm{em}} = \omega_{\mathrm{x}}/(\gamma + \gamma^*)$. Again, if enhancement of the radiative decay rate is desired in this regime, small mode volume cavities are beneficial. Similar to the bad cavity regime, Eq. (2.54) can also be derived from Fermi's golden rule [271, 309].

In the incoherent good coupling regime, the narrow cavity linewidth has important consequences for the coherence time of the system. Upon emission into the cavity at rate R, photons spend a time $\approx 1/\kappa$ in the cavity before being emitted, which defines the coherence time of the system. In the spectral domain, this corresponds to a drastic purification of the emission profile, whose linewidth is given by κ as illustrated in Fig. 2.18a. The enhancement in coherence time is reflected in the expression for the HOM-visibility, which in the incoherent good cavity regime reads [45]

$$v_{\mathrm{HOM}} = \frac{\gamma + \frac{\kappa R}{\kappa + R}}{\gamma + \kappa + 2R}. \tag{2.55}$$

A detailed interpretation of this expression is provided in Ref. [45]. At large dephasing and correspondingly small R, it is evident that minimizing κ maximizes the indistinguisha-

bility, as expected for the cavity-limited coherence time. This behavior is confirmed by a plot of v_{HOM} shown in Fig. 2.18b, calculated for an emitter subject to strong dephasing with $\gamma^* = 10^3\gamma$. Evidently, near-unity values of v_{HOM} are attainable in the incoherent good cavity-coupling regime in the presence of strong dephasing. In the bad cavity regime, this achievement would require giant Purcell factors, which have to date remained elusive.

Since the cavity linewidth is much smaller than the emitter linewidth, as illustrated in Fig. 2.18a, the efficiency of photon emission from the cavity into the spectrally narrow window defined by κ is much smaller than the free space quantum yield for emission at full emitter linewidth $\gamma + \gamma^*$, evidenced by the small values of β in Fig. 2.18b. However, incoherent good cavity-coupling increases the power spectral density of the emission [45]. This enhancement by a factor α_{PSD} computes to

$$\alpha_{\mathrm{PSD}} = \frac{\beta/\kappa}{\eta_{\mathrm{QY}}/\gamma^*} = \frac{F_{\mathrm{p,ideal}}}{1 + F_{\mathrm{p}}^*(1+\gamma/\kappa)} \approx F_{\mathrm{p,ideal}}, \tag{2.56}$$

with the ideal Purcell factor defined in Eq. (2.51). The last approximation holds in the case of small R, caused e.g. by large room-temperature dephasing. Cavity-enhancement of the power spectral density was first observed for vacancy centers in diamond [60, 308]. Eq. (2.56) provides an interpretation for the origin of this enhancement: due to the large mismatch between cavity and emitter linewidth, only the fraction of the emitter spectrum which overlaps with the cavity spectrum experiences full Purcell enhancement of the emission efficiency [308].

The incoherent good cavity regime provides a strategy for obtaining large indistinguishability in the presence of strong dephasing, which is relevant to many room-temperature solid-state systems. Alternative methods to obtain similar indistinguishability are spectral or temporal filtering at corresponding spectral bandwidths κ. However, as evident from a calculation of α_{PSD} shown in Fig. 2.18c, the efficiency of the cavity-coupled system can drastically outperform filtering due to the enhancement in power spectral density at sufficiently small cavity linewidth. This renders incoherent good cavity-coupling a promising approach for realizing optimized room-temperature single photon sources, as we will show in detail in the experiments on cavity-coupled carbon nanotube defects presented in Chapter 5.

3 Experimental techniques

The present chapter provides details on the experimental techniques relevant to this dissertation. A brief introduction of fiber-based Fabry-Pérot resonators along with definitions of experimentally relevant quantities (Section 3.1) is followed by a description and characterization of implementations in setups operating at ambient conditions (Section 3.2) and in a cryogenic environment (Section 3.3). The description of the room-temperature cavity system is accompanied by a characterization of the optical setups used for Hanbury-Brown-Twiss and Hong-Ou-Mandel experiments. In addition, a description of cryogenic confocal spectroscopy is provided (Section 3.4). The chapter closes by reporting on a fabrication technique for van der Waals heterostacks consisting of transition metal dichalcogenide monolayer semiconductors with engineered dielectric environment (Section 3.5).

3.1. Optical fiber-based Fabry-Pérot resonators

The investigation of cavity-coupled low-dimensional semiconductors presented in this thesis places three main requirements on the optical resonator: First, microscopic mode volume to enable large light-matter coupling strength as discussed in Section 2.5. Second, an open cavity design with full tunability in all three lateral spatial directions to control cavity resonance energy and mode position. This property enables maximizing spectral and spatial overlap with individual CNT quantum defects in Chapter 5, as well as spatial mapping of cavity-exciton coupling in two-dimensional TMDs in Chapter 4. Third, the potential to realize high finesse cavities at spectrally narrow linewidths.

The resonator implementation of choice, shown schematically in Fig. 3.1a, meets all three requirements: a fiber-based Fabry-Pérot microcavity [53–56]. Alternative cavity platforms, together with their potential to meet the above requirements, are briefly discussed in Section 2.5.

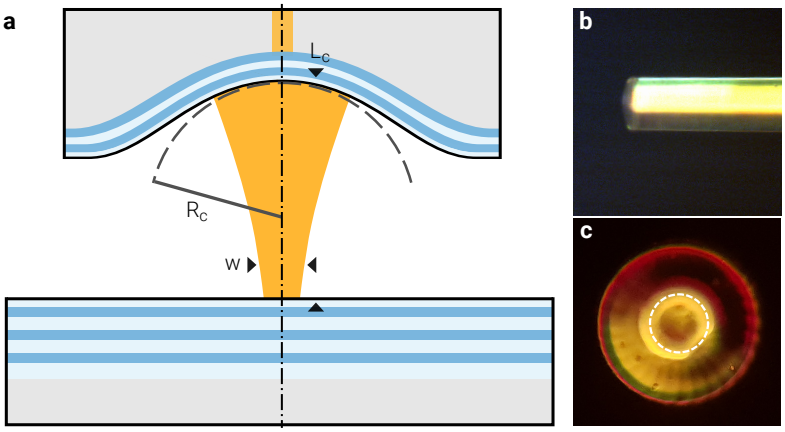

Figure 3.1.: Fiber-based Fabry-Pérot resonators. a, Schematic of a fiber-based resonator, consisting of a planar mirror and a mirror formed by a concave indentation in the tip of an optical fiber, which can be approximated by a spherical profile at radius of curvature R_c. Both mirrors at a distance L_c feature DBR-coatings. The area of the fundamental Gaussian mode containing a $1/e^2$ fraction of the intensity, as defined by the beam waist w, is shown schematically in orange. The vertical dashed line marks the optical axis z. **b**, **c**, Optical microscope images of a fiber cavity mirror in side and top view, respectively. The fiber diameter is 125 µm.

3.1.1. Fundamental concepts

In the plano-concave geometry chosen here, a fiber-based Fabry-Pérot cavity consists of a macroscopic planar mirror and a microscopic mirror formed by an indentation in the tip of an optical fiber. With typical fiber diameters of 125 µm, this open resonator geometry enables the realization of microscopic mirror distances at small mode volumes [274]. Both mirrors can be coated with dielectric DBR-coatings to allow for large values of cavity finesse.

The indentation on the fiber tip is typically machined by laser ablation at near-infrared wavelengths [55, 316], which allows to create profiles with low surface roughness compared to alternative methods [317]. As shown in in Fig. 3.1a, the resulting mirror features a Gaussian height profile, which near its center approximates to a half-sphere [318]. In addition, the fiber tip is frequently machined into a conic shape to enable the smallest possible mirror distance, limited by the depth of the mirror profile [307]. Fig. 3.1b and c show optical microscope images of a fiber mirror used for the experiments presented in Chapter 5. The side view reveals the conic shape of the fiber tip, while the mirror indentation is visible as a near-circular area in the top view.

With present machining technology, profile depths smaller than 100 nm have been demonstrated [274]. Reported values for the radius of curvature range from 10 µm [319] to 2 mm [59]. For cavities with a large mirror distance, the fabrication of homogeneous near-spherical mirror profiles at radius of curvature exceeding a few 100 µm using laser ablation is challenging [320], with an alternative strategy provided by 3D laser writing [321]. At small radius of

curvature near 10 µm, DBR-structures coated on the fiber tip tend to deviate from a spherical shape, inducing diffraction losses which reduce the finesse [307]. For the resonators used in this work, which feature small radius of curvature at finesse ≈ 1000, this effect is irrelevant.

3.1.2. Optical properties

The cavity mode formed inside a plano-concave fiber cavity needs to satisfy the roundtrip condition of constructive interference for all positions of the wavefront. For spherical mirrors, this requirement is fulfilled by a Gaussian mode, whose intensity profile is shown schematically in Fig. 3.1a with the optical axis z indicated by the vertical dashed line. For this mode, the electric field $\mathcal{E}_0(\boldsymbol{x},t) = 1/2 E_0 u_0(\boldsymbol{x}) e^{-i(\omega t - 2\pi/\lambda z)} + \text{c.c.}$ in two spatial dimensions $\boldsymbol{x} = (x,z)^T$ exhibits a complex amplitude [151]

$$u_0(\boldsymbol{x}) = \frac{w_0}{w(z)} e^{-\frac{x^2}{w(z)^2}} e^{-i\frac{2\pi x^2}{\lambda 2R(z)} + i\Psi(z)}. \tag{3.1}$$

This expression contains three main characteristics of the Gaussian mode: the transverse $1/e^2$ radius of intensity, which equals the beam waist w_0 at the focal point, given by $w(z) = w_0\sqrt{1+(z/z_\mathrm{r})^2}$, with the Rayleigh range $z_\mathrm{r} = \pi w_0^2/\lambda$; the radius of curvature of the wavefront, $R(z) = z(1+(z_\mathrm{r}/z)^2)$; and the Guoy phase $\Psi(z) = \arctan(z/z_\mathrm{r})$. From these expressions, we find that a cavity with mirror distance L_c and mirror radius of curvature R_c exhibits a mode waist

$$w_\mathrm{c} = \sqrt{\frac{\lambda L_\mathrm{c}}{\pi}\sqrt{\frac{R_\mathrm{c}}{L_\mathrm{c}} - 1}} \tag{3.2}$$

on the planar mirror. The Guoy-phase Ψ_0 of the mode adds to the cavity roundtrip phase in Eq. (2.3), which has to be accounted for when computing the cavity resonance frequency from Eq. (2.7).

It is evident from Eq. (3.1) that the introduction of a spherical mirror results in confinement of the cavity mode in the transverse spatial directions (i.e. orthogonal to the optical axis), which contrasts the plane-wave eigenmodes of the planar resonator discussed in Section 2.3. This field confinement to potentially small mode volumes V_c is crucial for obtaining large values of light-matter coupling strength, as detailed in Section 2.5. To estimate the mode volume, we approximate the cavity field as a cylinder of radius $w_\mathrm{c}/2$ [274], which yields

$$V_\mathrm{c} \approx \frac{\pi w_\mathrm{c}^2}{4} L_\mathrm{c}. \tag{3.3}$$

For DBR-mirrors, corrections to the mode volume accounting for large penetration into the coating, as discussed in Section 2.3, are sometimes required to account for experimental

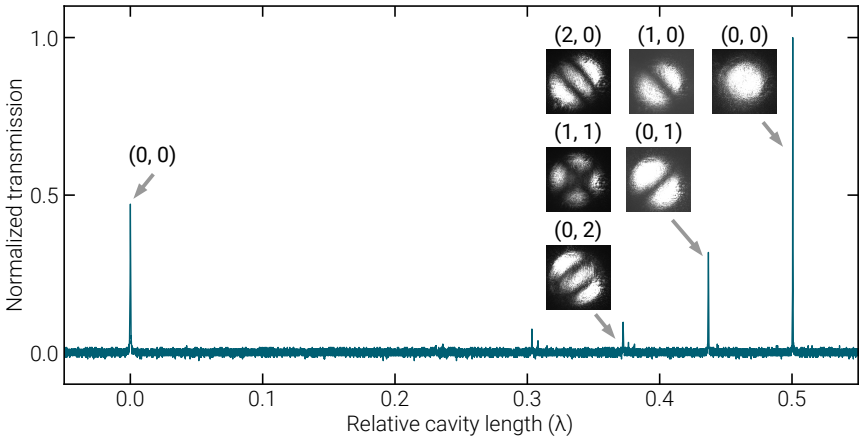

Figure 3.2.: Spectrum of a fiber-based Fabry-Pérot cavity. Experimental transmission of the fiber cavity described in Section 3.2 as a function of cavity length, featuring resonances of two fundamental Gaussian modes of different longitudinal order, as well as $\mathrm{TEM}_{\mathrm{mn}}$ resonances of higher order (m,n). Experimental transverse intensity profiles of modes with $m+n \leq 2$ are shown in the insets.

observations [62]. For the experiments performed with the setups described in the present chapter, Eq. (3.3) provides satisfactory agreement with experimental results.

In many fiber cavities, imperfections in the fabrication process cause a small degree of ellipticity in the mirror profile [159, 318, 322], breaking the cylindrical symmetry of the cavity modes which separate in the transverse directions $\boldsymbol{r} = (x,y)^T$. Their complex amplitude is given by the product of two Hermite-Gaussian modes $u_m(x,z)u_n(y,z)$ of order (m,n) [322]. These transverse electromagnetic modes, labeled $\mathrm{TEM}_{\mathrm{mn}}$, satisfy the condition for constructive interference after a cavity roundtrip. The fundamental TEM_{00}-mode is of Gaussian shape, described by Eq. (3.1). For the fiber mirrors employed in this work, the degree of ellipticity is small, such that the fundamental mode is well-approximated by a cylindrical Gaussian.

Hermite-Gaussian modes of order (m,n) exhibit a Guoy-phase of $(1+2m)\Psi_{0,\mathrm{x}} + (1+2n)\Psi_{0,\mathrm{y}}$, with $\Psi_{0,\mathrm{x,y}}$ the Guoy-phases of the fundamental mode in the transverse directions [151]. As a result, they are shifted in resonance frequency from the fundamental mode of order q by [322]

$$\Delta\omega_{\mathrm{mn}} = \frac{m}{\pi}\Psi_{0,\mathrm{x}} + \frac{n}{\pi}\Psi_{0,\mathrm{y}}. \tag{3.4}$$

This shift is evidenced in the experimental transmission of the fiber cavity shown in Fig. 3.2, in which the higher order TEM modes contribute additional resonances to the spectrum. Their transverse intensity profiles, measured with a camera placed in the transmission path for selected resonances, exhibit additional nodes in the transverse directions. The number of these nodes is given by the transverse mode order.

In addition to the transverse mode profiles, the ellipticity in the fiber profile also deter-

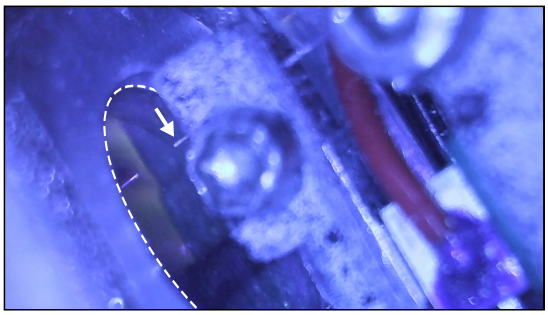

Figure 3.3.: Room-temperature fiber cavity setup. Optical image of the fiber cavity device. The visible edge of the planar mirror is marked by the dashed white line. The fiber mirror in its mount is marked by the white arrow. The fiber with a diameter of 125 µm is retracted such that its reflection is visible on the planar mirror.

mines the polarization of the eigenmodes. Deviations from the paraxial approximation to Maxwell's equations, which are particularly pronounced for small mirror radius of curvature, result in polarization eigenmodes with lifted degeneracy, linearly polarized along the principal axes of the elliptical mirror profile [318]. This splitting is on the order of 100 MHz, corresponding to 0.4 µeV, in representative experimental implementations [56, 159]. For the results of this work, the effect is negligible: cavity and/or exciton linewidth exceed the polarization splitting, such that the polarization eigenmodes are considered to be effectively degenerate.

As evident from the discussion above, mirror geometry and alignment determine if and at which frequency a cavity mode will form. Resonators which exhibit eigenmodes are called stable, with the criteria for stability derived in Ref. [151] for common resonator geometries. In particular, a plano-concave fiber resonator with a perfectly spherical mirror and suitably chosen cavity length will in principle be stable for any orientation of fiber and planar mirror, as long as losses by clipping on the edges of the mirror profile are negligible. The situation differs for typical experimental fiber cavities: deviations from spherical mirror profiles induce diffraction losses to the intra-cavity field [322], which reduce the finesse and can render the resonator unstable in the worst-case scenario. This effect is enhanced if the fiber is tilted from parallel orientation with the optical axis, such that tilts should be minimized in experimental setups.

3.2. Room-temperature fiber cavity setup

3.2.1. Experimental setup

The experiments presented in Chapter 5 investigate cavity-coupling of carbon nanotube defects (NTDs) at ambient conditions. The cavity platform used to implement this system

is Qlibri Quantum, recently developed by Qlibri GmbH to allow for ultra-stable fiber cavity operation at minimal fluctuations of the cavity length[1]. The heart of the device, which consists of kinematic mounts for the two mirrors, is shown in the optical image of Fig. 3.3, a schematic of the cavity is shown in the top panel of Fig. 3.4a. The planar mirror with a diameter of 12.7 mm is fixed inside a tube-shaped mount. The mirror features a polystyrene (PS) spacer with functionalized carbon nanotubes placed on top, fabricated as described in Section 5.2.

The position of the planar mirror is tunable in the transverse directions relative to the fiber mirror. The fiber is mounted on a lever arm, tunable along the optical axis to control the cavity length. Stepper motors allow for coarse displacement over the range of several mm along all three spatial dimensions with a resolution on the order of 100 nm. Fine tuning of relative mirror position at a resolution of 60 pm is enabled by piezoelectric actuators over a range of several 10 µm in transverse directions and several µm along the cavity length axis.

The cavity platform is equipped with controllers for the stepper motors and voltage amplifiers to actuate the piezoelectric transducers, as well as a digital analog converter to read out the signal of a photodiode used to measure the cavity transmission. Actuation and data acquisition rely on a field-programmable gate array operating at a bandwidth of 80 MHz. A Python software framework enables control of the mirror position and acquisition of the photodiode signal. Setup and software are designed to enable scanning cavity absorption measurements [159] at high speeds. In this approach, the planar mirror is raster scanned in an area of interest, and the cavity transmission is measured at each position as a function of cavity length, which is scanned across a resonance. In the present realization, data from a sample area of 28 × 40 µm can be acquired in 40 s at a resolution of 256 × 409 pixels. For the experiments presented in Chapter 5, a different measurement is of interest: spatial maps of NTD photoluminescence (PL) at telecom wavelengths near 1460 nm, measured with superconducting nanowire single photon detectors. Accordingly, the software framework was modified to enable acquisition of detector counts as a function of position via the Python interface of the time correlator (TimeTagger Ultra, see below for a description of the single photon detection system).

The optical setups used for measurements of cavity transmission and photoluminescence are shown schematically in Fig. 3.4. Light was injected into the cavity through the mirror fiber, and transmission or photoluminescence emission through the planar mirror were analyzed with different methods. To this end, the cavity mode was collimated using an aspheric lens (Thorlabs AC127-019-C-ML) mounted on a kinematic stage for translation along the optical axis, as illustrated in the central panel of Fig. 3.4a. For NTD photoluminescence experiments, we placed a combination of longpass filters (Thorlabs FELH1400, Semrock BLP02-1319R)

[1] The experiments on cavity-coupled carbon nanotube defects using the setup described in the following were performed in collaboration with Julian Trapp, who also reports on some of the characterization results in his Master's thesis [323].

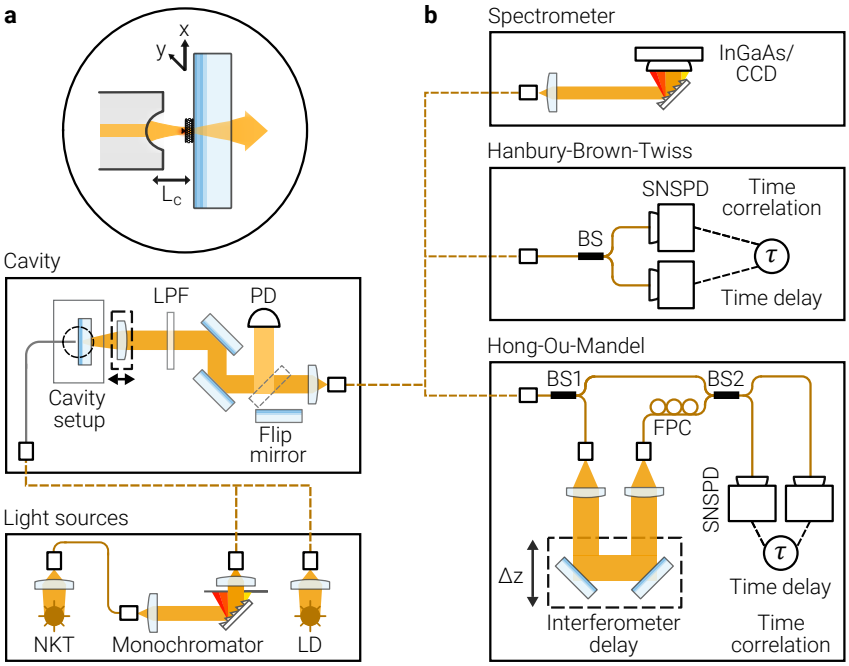

Figure 3.4.: Optical setups for room-temperature cavity operation. a, Top: schematic of the fiber cavity marked by the dashed circle in the center panel, featuring functionalized carbon nanotubes on the planar mirror. Drawing not to scale. Center: schematic of the optical setup in the cavity periphery. LPF, longpass filter. PD, photodiode. Bottom: illustration of light sources for photoluminescence (PL) excitation and cavity characterization. LD, laser diode. NKT, white light source, spectrally filtered by a monochromator as described in the main text. **b**, Schematics of setups for analysis of cavity transmission and PL. Top: grating spectrometer with Indium Gallium Arsenide (InGaAs) or silicon charge coupled device (CCD) detector. Center: Hanbury-Brown-Twiss setup for measurements of second order correlation functions based on optical fibers, indicated by orange solid lines. BS, beam splitter. SNSPD, superconducting nanowire single photon detectors. Bottom: Mach-Zehnder interferometer for Hong-Ou-Mandel type experiments to quantify photon indistinguishability. FPC, fiber polarization controller. Individual optical setups in **a** and **b** can be connected using optical fibers, as illustrated by dashed lines.

in the transmission path to suppress excitation light at wavelengths near 1185 nm with a specified optical density of 11. Additional optical elements such as polarizers were placed in the transmission path if required. The transmitted cavity mode was either coupled into a single mode fiber or redirected by a flip mirror to impinge on a photodiode (model specified below).

The different types of light sources are illustrated in the bottom panel of Fig. 3.4a. Fiber-coupled laser diodes provided monochromatic light at different wavelengths: a continuous-wave diode (Roithner RLT1450-10MGS-B, controlled by Thorlabs LDC200C) operated resonant with the NTD exciton at a wavelength of 1466.12 nm, measured with a grating spec-

trometer (see below for details). A pulsed diode (legacy equipment of the Kotthaus chair) operated at a wavelength of 785 nm inside the near-infrared stopband of the mirror coating, see Fig. 3.5 for details.

A supercontinuum fiber laser (NKT SuperK Extreme) provided pulsed light with tunable repetition rates in the range 2–78 MHz and a power of 4 W in the wavelength range 400–2000 nm. To operate as a white light source in the relevant telecom range at wavelengths larger than 1100 nm, a hard-coated spectral filter was employed (Semrock TLP01-1116). To avoid damage to this component, additional long- and shortpass filters were placed upstream in the beam path. For pulsed incoherent excitation of NTD photoluminescence at a wavelength of 1185 nm (see Section 5.2 for details), the telecom-band white light was injected into a home-built monochromator, which provided additional spectral filtering at a bandwidth $\Delta\lambda \approx 2$ nm [323].

The fiber-coupled cavity transmission and photoluminescence were analyzed with the devices and setups illustrated schematically in Fig. 3.4b. We performed spectroscopy using a fiber-coupled grating spectrometer (Roper Scientific Acton SP2500) in which the detector could be switched between a silicon charge-coupled device (CCD, Roper Scientific Spec-10:100BR/LN) for operation at near-infrared wavelengths and an Indium Gallium Arsenide (InGaAs) array (Roper Scientific OMA V:1024-1.7 LN) operating at telecom wavelengths larger than 1000 nm. Both detectors were cooled to liquid nitrogen temperatures. Gratings with 300 and 1200 grooves/mm were used depending on the experimental requirements.

We measured second order coherence functions in a Hanbury-Brown-Twiss (HBT) experiment (see Section 2.5 for details), implemented using a balanced fiber beam splitter as shown in the central panel of Fig. 3.4b. Each beam splitter output was injected into one of two fiber-coupled superconducting nanowire single photon detectors (SNSPDs, Scontel TCOPRS-CCR-SW-85), which were housed inside a closed-cycle cryostat at a temperature of 2.1 K. We correlated detection events in the two channels using a time correlator (PicoHarp 300, replaced by TimeTagger Ultra in the later stages of the experiment). To measure time-dependent photoluminescence, we used a single SNSPD channel, with the second channel of the time correlator synced to a periodic sequence of electronic pulses generated by the NKT laser, with the period matching the excitation pulse frequency. The characterization of the SNSPDs and the time correlation systems is presented below, along with a description of the Hong-Ou-Mandel experiment shown in the lower panel of Fig. 3.4b.

3.2.2. Cavity characteristics

Both fiber and planar mirror featured identical DBR coatings consisting of alternating layers of TiO_2 and Ta_2O_5, fabricated by ion beam sputtering (Laseroptik GmbH). The coating transmission, computed from a transfer matrix formalism as described in Chapter A, is shown by the red line in Fig. 3.5a. The coating enables high finesse at low transmission

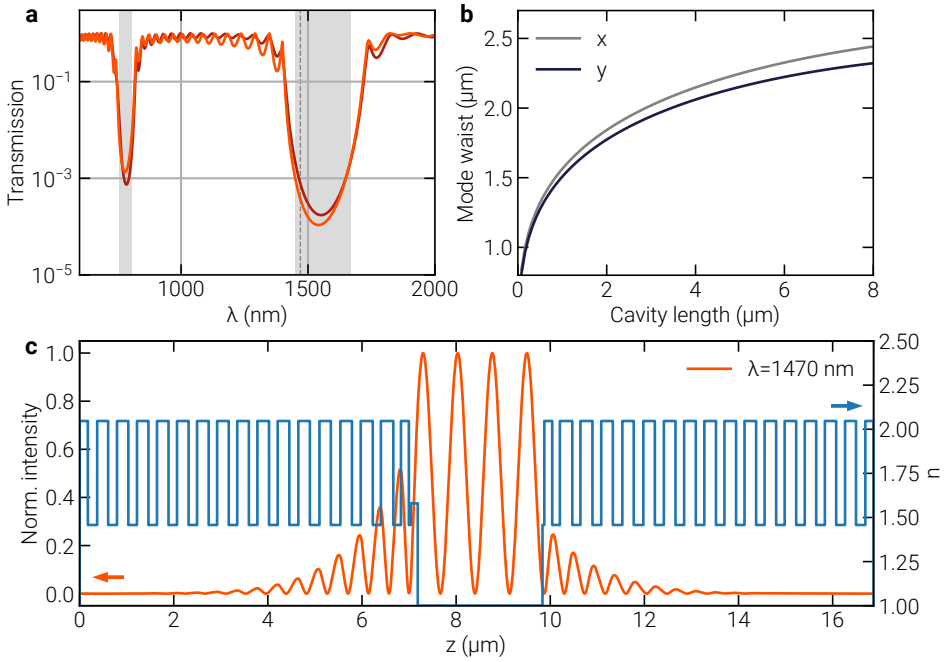

Figure 3.5.: Characteristics of the room-temperature cavity. a, Transmission of DBR-coatings on the fiber (red solid line) and planar mirror (gray solid line), computed from a transfer matrix simulation. Both mirrors feature identical coatings, a 150 nm thick polystyrene spacer was added to the planar mirror to place carbon nanotube defects close to an antinode of the intracavity field. The mirror coating features two stop bands at near-unity reflectivity, marked by the gray areas. The vertical dashed line indicates the resonance of the carbon nanotube defects at a wavelength of 1470 nm. **b**, Cavity mode waist as a function of mirror distance, computed for the fiber mirror used in the experiments. **c**, Refractive index profile (blue line) and intra-cavity field profile (orange line) along the optical axis z from transfer matrix simulations. The mode order is $q = 4$ at the nanotube defect resonance wavelength of 1470 nm.

in the telecom band near wavelengths of 1550 nm. As a result, a second stop band of low transmission emerges at half this wavelength, near 775 nm in the near-infrared domain. The polystyrene spacer included to place nanotube defects at an antinode of the intracavity field leads to a slight modification of the mirror transmission, shown by the gray line in Fig. 3.5a.

The fiber mirror, fabricated and characterized in the group of David Hunger, featured an elliptical profile, a common property of fiber based microcavities as described above. From a measurement of the height profile in white light interferometry, radii of curvature of 28.3 µm and 24.6 µm along the principal axes x and y of the ellipse were obtained. The resulting mode waist along these directions, computed from Eq. (3.2), is plotted in Fig. 3.5b as a function of mirror distance L_c. At typical operating lengths $L_c \approx 2\,\mu$m, the cavity exhibits mode waists of $\approx 2\,\mu$m. The difference in mode waist along the two transverse directions is smaller than 5 % at relevant cavity lengths, which is negligible for computations of light-

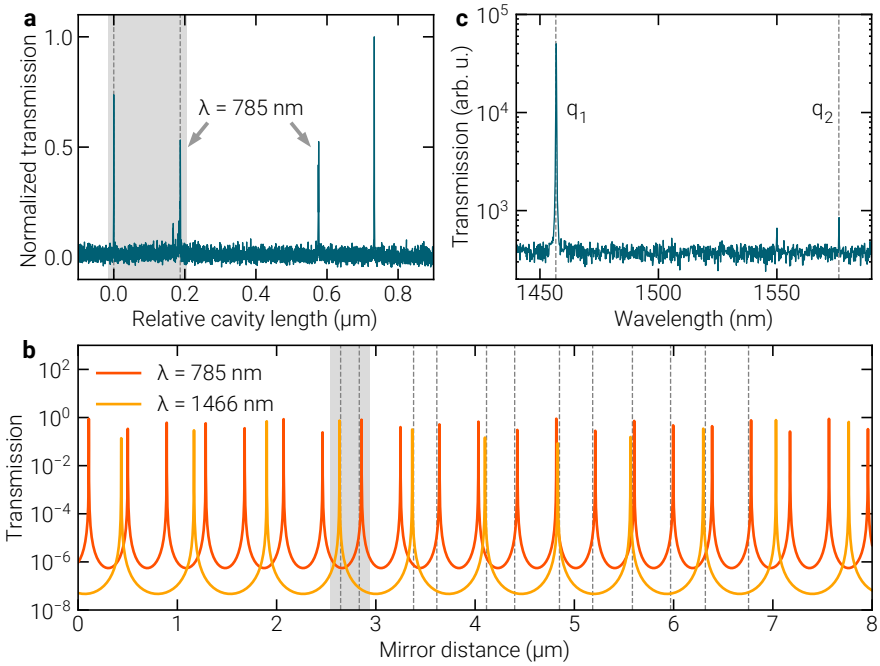

Figure 3.6.: Mode order and cavity length. a, Experimental cavity transmission as a function of cavity length, with two lasers at different wavelengths injected into the cavity. The resonances marked by the arrows stem from a laser with a wavelength $\lambda = 785$ nm. All other resonances originate from a laser with $\lambda = 1466$ nm. **b**, Cavity transmission as a function of mirror distance for two different wavelengths, 785 nm (orange) and 1466 nm (yellow), obtained from transfer matrix simulations. Differences in maximum transmission of the individual resonances are a numerical artifact. The dashed vertical lines indicate pairs of resonances of the 785 nm and 1466 nm lasers, obtained from measurements as in **a**. The gray areas in **a** and **b** mark an identical range of mirror distances. **c**, Experimental cavity transmission as a function of wavelength, measured with a white light source. The dashed vertical lines indicate two fundamental resonances of neighboring longitudinal mode orders q_1 and q_2, respectively.

matter coupling strength from the mode volume presented in Section 5.3. The fiber profile depth was 1.95 μm.

In Fig. 3.5c, we show by the solid orange line the intracavity field along the optical axis z, obtained from transfer matrix simulations described in Chapter A. The refractive index profile of the cavity mirrors is shown in blue. The calculation was performed for the NTD resonance wavelength of 1470 nm and the lowest accessible mode order $q = 4$ as determined below. As expected, a standing wave forms inside the cavity, with the number of antinodes given by the mode order. The PS spacer at $z \approx 7\,\mu$m places the NTDs close to such an antinode. All characterization measurements presented in the following were performed with the cavity mode positioned on the PS spacer but away from any NTDs.

To compute the mode volume, a measurement of the mirror distance is required, for which we harness the open geometry of the cavity. We simultaneously inject light from two laser

diodes at wavelengths $\lambda = 785\,\text{nm}$ and 1466 nm, respectively, and scan the cavity length. The resulting photodiode transmission measurement, shown in Fig. 3.6a for the lowest experimentally accessible mode order, features resonances stemming from both lasers. In particular, the two resonances at maximum transmission are fundamental cavity modes of neighboring longitudinal order at $\lambda = 1466\,\text{nm}$. From their distance, which corresponds to half the wavelength, we calculate the change in cavity length as a function of time, which we use in turn to calibrate the x-axis. We measure the difference between one resonance at $\lambda = 785\,\text{nm}$ to the lowest energy resonance at $\lambda = 1466\,\text{nm}$ in the length sweep, with both resonances marked by vertical dashed lines in Fig. 3.6a.

To determine the mirror distance, we compute the expected cavity transmission for both experimental laser wavelengths from a transfer matrix simulation, with the result shown in Fig. 3.6b. The experimental resonance frequencies, obtained as described above, are shown by vertical dashed lines. For comparison with the simulation, the distance between the resonances at $\lambda = 1466\,\text{nm}$ is set to exactly half a wavelength, with the $\lambda = 785\,\text{nm}$ resonances spaced by the experimental distance. The mirror distance corresponding to the lowest experimentally accessible mode order, marked by the gray shaded area, was adjusted to yield agreement between the experimental and simulated cavity resonances. From the good agreement between experiment and simulation, we conclude that for the lowest experimentally accessible resonance at $\lambda = 1466\,\text{nm}$ the mirror distance is 2.65 µm. This corresponds to a mode order $q = 4$, evidenced from the fact that the cavity exhibits three additional resonances as the mirror distance is reduced towards zero. Achieving smaller mirror distances is prevented by physical contact between fiber and planar mirror, consistent with the mirror profile depth of 1.95 µm.

To measure the cavity linewidth, knowledge of the effective cavity length is required, which differs from the mirror distance due to field penetration into the mirror coatings as evident from Eqs. (2.9) and (2.11). We determine this parameter by measuring the cavity transmission of a white light source with a grating spectrometer. A representative spectrum is shown in Fig. 3.6c, with two fundamental modes of neighboring longitudinal mode orders q_1 and q_2 marked by vertical dashed lines. Their distance in resonance frequency is given by the free spectral range, such that $\Delta\omega_{\text{FSR}} = \omega_{\text{c,q1}} - \omega_{\text{c,q2}}$, with $\omega_{\text{c,q1}} > \omega_{\text{c,q2}}$. Using Eq. (2.9), we find

$$L_{\text{eff}} = \frac{\lambda_1 \lambda_2}{2\,(\lambda_2 - \lambda_1)}, \tag{3.5}$$

with λ_1 and λ_2 the wavelengths corresponding to the respective mode orders. From the two resonance wavelengths in Fig. 3.6c, we obtain $L_{\text{eff}} = 9.7\,\mu\text{m}$. Assigning an effective mode order q_{eff} as

$$L_{\text{eff}} = q_{\text{eff}}\lambda/2, \tag{3.6}$$

we find $q_{\text{eff}} \approx 13$. From measurements based on the injection of two lasers as described

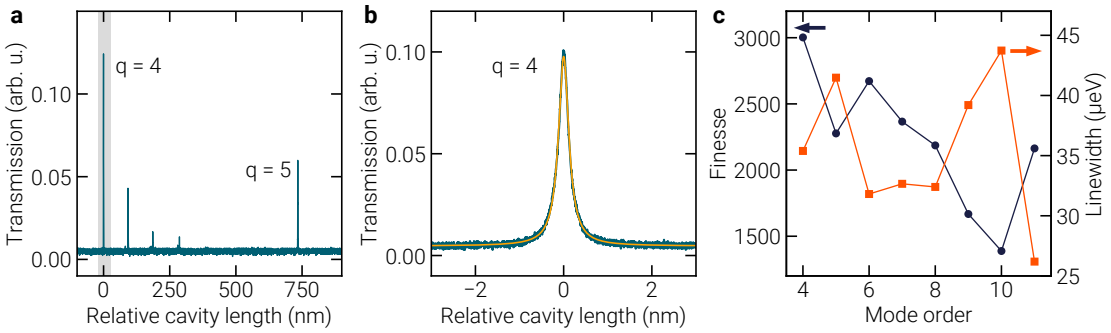

Figure 3.7.: Cavity finesse and linewidth. **a**, Cavity transmission of a laser diode with a wavelength of 1466 nm as a function of cavity length, which is tuned by approx. one free spectral range. The resonances at maximum transmission are fundamental modes of orders $q = 4$ and 5, respectively. **b**, Same measurement as in **a**, but for cavity lengths in a narrow range around the $q = 4$ resonance marked by the gray area in **a**. The solid yellow line is the fit of a Lorentzian profile. **c**, Finesse (dark blue dots) and linewidth (orange squares) as a function of mode order, obtained as described in the main text from measurements as shown in **a** and **b**. Parts of the figure are adapted from [P2].

above, we find that the difference between q_{eff} and the mode order q as obtained from the mirror distance is 4, illustrating the influence of field penetration into the mirror coatings. In the remainder of this section, we refer to q as the mode order, and use q_{eff} to compute the cavity linewidth from the measured finesse, as derived from Eq. (2.11).

We obtained the cavity linewidth from the measured transmission of the laser diode at 1466 nm wavelength through the cavity for varying mirror distance. In this measurement, cavity length fluctuations occur at frequencies of up to approx. 10 kHz, which can lead to broadening of measured linewidths (see Section 3.3 for details). Correspondingly, the length scan speed was adjusted such that the measurement bandwidth exceeded the bandwidth of the mechanical noise. A photodiode with maximum bandwidth of 10 MHz (Thorlabs PDA400) was read out with an oscilloscope with a bandwidth of 1 GHz and maximum sampling rate 8 Gs/s (LeCryo WavePro 954). At the same time, the scan speed was kept low enough to prevent ring-down effects of the field stored inside the cavity [324, 325], which occur in high finesse cavities at sufficiently large scan speeds. The measurement of the laser linewidth was limited by the spectrometer resolution of 24 μeV, such that the spectrally narrow laser diode did not contribute to the measured cavity linewidths.

To calculate time-dependent change in cavity length, we scanned the cavity length over one free spectral range, with data shown in Fig. 3.7a for mode orders $q = 4$ and 5. Subsequently, FWHM linewidths δL are obtained from Lorentzian fits to the transmission profile at the respective mode order, as shown in Fig. 3.7b for $q = 4$. From the fit result, we compute the finesse as $\mathcal{F} = \lambda / (2\delta L)$, an expression which is straightforwardly obtained by approximating the length dependent cavity transmission of Eq. (2.3) as a Lorentzian. Using Eq. (2.11), we

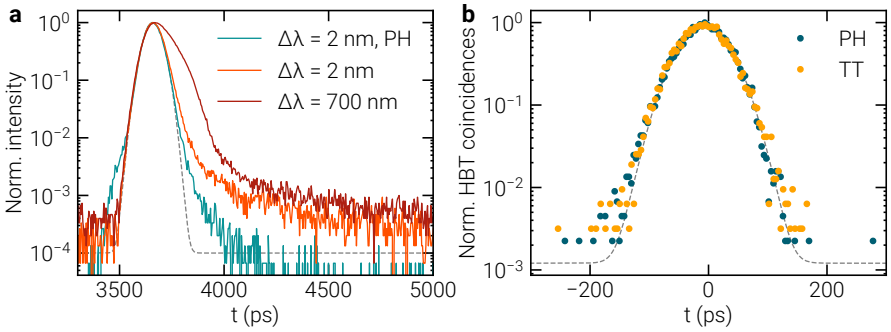

Figure 3.8.: Characteristics of the single photon detection system. a, Time-dependent laser pulse intensity, measured with a single channel of the superconducting nanowire single photon detectors (SNSPDs). The measurement was performed for different spectral widths $\Delta\lambda$ of the superconducting fiber laser system as indicated in the legend. Data shown by the light green line were obtained using the PicoHarp (PH) time correlator, for all other datasets the TimeTagger time correlator was used. The dashed line is a Gaussian profile with $1/e^2$ half width of 40 ps. **b**, Normalized coincidences in a Hanbury-Brown-Twiss (HBT) experiment, obtained for a laser pulse with spectral width $\Delta\lambda \approx 2$ nm using the TimeTagger (TT, yellow dots) and PicoHarp (PH, teal dots) time correlators, respectively. The dashed line is a Gaussian profile with $1/e^2$ half width 40 ps.

compute the linewidth as $\kappa = L_{\text{eff}}\mathcal{F}/(2\pi c)$, accounting for the field penetration into the mirrors by using $L_{\text{eff}} = (q+4)\lambda/2$ as obtained from the measurements presented above. From ten repetitions of the measurement, we obtain the results shown in Fig. 3.7c. At the lowest accessible mode order, which is used for the measurements in Chapter 5, we find $\kappa = 35.4 \pm 0.1\,\mu$eV. The finesse changes as function of mode order, likely due to diffraction loss arising at small mirror radius of curvature [322].

3.2.3. Single photon detection system and Hong-Ou-Mandel setup

To characterize the SNSPDs and time correlation systems, we measured the time-dependent intensity of supercontinuum fiber laser pulses. Results are shown in Fig. 3.8a for different laser spectral bandwidths $\Delta\lambda$, controlled using different filters as described above. For $\Delta\lambda = 2$ nm, centered at $\lambda = 1185$ nm, both TimeTagger (orange line) and PicoHarp time correlator (PH, light green line) yield temporal profiles well described by a Gaussian with $1/e^2$ half width of 40 ps, which we extract as the instrument response time of the single photon detection system. This response is limited by the SNSPD response, in agreement with specifications.

White light generation inside the supercontinuum fiber results in chirped laser pulses, such that the pulse length will depend on the selected spectral width. Increasing the spectral filtering range to $\Delta\lambda = 200$ nm, a repetition of the measurement yields the same instrument-limited temporal profile as for $\Delta\lambda = 2$ nm (data not shown). We conclude that the instrument

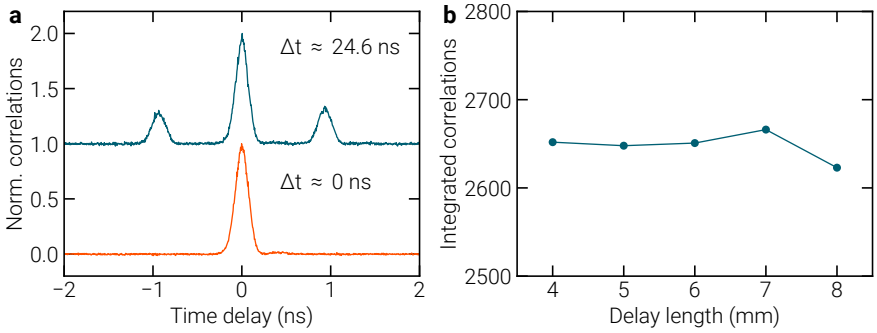

Figure 3.9.: Alignment of the Mach-Zehnder interferometer. **a**, Normalized coincidence counts at the output of the Mach-Zehnder interferometer used in Hong-Ou-Mandel type experiments. The light source is a pulsed superconducting fiber laser. Shown are the cases of near-zero interferometer delay Δt (orange line) and interferometer delay $\Delta t \approx 24.6$ ns (teal line), offset vertically for illustration purposes. **b**, Integrated coincidence counts from data as in **a** for varying interferometer delay near $\Delta t \approx 0$. The investigated range of interferometer delay is the same as in the two-photon interference experiments as discussed in Section 5.4.

response time of 40 ps greatly exceeds the pulse length for these spectral windows. This is of relevance to the single photon purity measurements presented in Section 5.3, where the pulse length should be smaller than the nanotube defect lifetime of 90 ps to avoid emitter reexcitation. Increasing the pulse spectral width to $\Delta\lambda = 700$ nm results in an increase in pulse duration, as expected for a chirped pulse.

The timing jitter is characterized by measuring coincidences in the HBT experiment as the pulsed laser with $\Delta\lambda = 2$ nm is injected into the beam splitter. The resulting temporal profile for both time correlation systems is well described by a Gaussian with $1/e^2$ half width of 40 ps, in agreement with the instrument response measured as described above.

To quantify photon indistinguishability in Section 5.4, we perform two-photon interference measurements in a Hong-Ou-Mandel type experiment (see Section 2.5 for details). We employ an imbalanced Mach-Zehnder interferometer in fiber-based configuration as shown schematically in the bottom panel of Fig. 3.4b, similar to the technique used in first demonstration of photon indistinguishability on semiconductor quantum dots [21]. An incoming sequence of light pulses is split at a beam splitter, after which one arm of the interferometer is coupled to a free space delay stage. This arm is delayed by one pulse separation of 12.8 ns at 78 MHz laser repetition rate, with an additional delay Δx adjustable via the delay stage, corresponding to a time delay Δt [326]. The second interferometer arm is an optical fiber. Both arms are recombined at a second beam splitter, whose output ports are fed into different SNSPD channels.

The polarization in the interferometer arms was aligned using fiber polarization controllers to yield maximum classical interference visibility. The visibility was measured with the laser at wavelength 1466 nm injected into the transmission path of the cavity, which was

coupled into the interferometer using optical fibers. Due to laser coherence, small changes in interferometer delay induced e.g. by thermal drifts were sufficient to induce fringes with full visibility at the beam splitter output ports, which were monitored during alignment using a photodiode. Details on relevant interferometer parameters such as the visibility and the beam splitter split ratios are given in Section 5.4, where their influence on the measured photon indistinguishability is discussed.

To determine the stage position corresponding to zero interferometer delay, we injected laser pulses at a central wavelength of 1470 nm into the interferometer and measured coincidences between the output ports of the second beam splitter. Measurement results are shown in Fig. 3.9a. Near zero interferometer delay, pulses from both interferometer arms are in temporal overlap at the interferometer outputs, resulting in a single Gaussian profile of the coincidence counts. The situation is drastically different if an additional fiber of length 5 m is inserted into one of the interferometer arms. The corresponding interferometer delay is $\Delta t \approx 24.5$ ns, which deviates from twice the pulse separation by $\approx$1 ns. As a result, the coincidence count histogram for this interferometer delay exhibits two additional peaks, as evidenced in Fig. 3.9a. In coarse alignment of the interferometer delay, the three peaks were brought into best possible temporal overlap.

To characterize the interferometer alignment, we performed coincidence histogram measurements as in Fig. 3.9a near $\Delta t \approx 0$ ns for varying interferometer delay, tuned via the delay stage. From fits of Gaussian profiles to the histogram peaks, we extracted the peak width as a function of interferometer delay. The delay range in which the peaks featured widths near the minimum value was investigated in the experiments in Section 5.4. For this range, we also determined the coincidences integrated over the full peak, which corresponds to a measurement of the optical mode matching in the delay stage with data shown in Fig. 3.9b. In the investigated range, deviations in peak intensity are on the order of a few percent, indicating excellent optical alignment of the delay stage and rendering delay-dependent corrections to the Hong-Ou-Mandel coincidences measured in Section 5.4 negligible.

3.3. Cryogenic fiber cavity setup

The experiments presented in Chapter 4 investigate cavity-coupling of different transition metal dichalcogenide (TMD) exciton resonances with spectral detunings on the order of a few meV. To resolve these energy shifts, a minimization of phonon-induced broadening of the exciton linewidth is beneficial [111], for which cavity operation at cryogenic temperatures near 4 K is required. While many pioneering experiments on cavity-coupled solid-state samples were performed in liquid helium bath cryostats [155, 319, 327], closed-cycle cryostats provide an alternative platform at increased scalability and potential cost efficiency. However, the cyclic compression required for cooling in these systems leads to

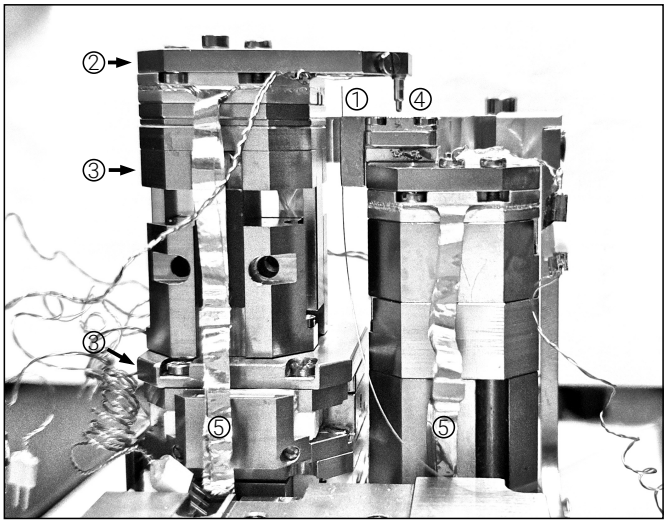

Figure 3.10.: Fiber cavity setup for operation at cryogenic temperatures. Optical image of the fiber cavity device, acquired with the setup removed from the cryostat. (1) Cavity fiber, fixed to a piezoelectric transducer. The fiber diameter is 125 µm. (2) Mount for the planar mirror, fixed to (3) a stack of nanopositioners. (4) Spring-loaded pin for mechanical coupling of mirror and fiber mounts at reduced reciprocal displacement. (5) Thermal links.

an increased level of mechanical vibrations, which translate to undesired fluctuations of the cavity length and hence the spectral emitter-cavity detuning. The central challenge in experimental design is therefore to reduce the influence of cryostat vibrations on the cavity length, which has been addressed in a number of experiments by introducing active and passive mechanical stabilization systems [275, 328–332], with an overview of recent progress in this field provided in [332].

3.3.1. Experimental setup

In our experiments, we employ a cryogenic fiber cavity platform, developed by Samarth Vadia in cooperation with attocube systems AG[2]. Design, development and properties of the setup are described in detail in Refs. [328, 334], with crucial emphasis on optimized mechanical stability of the cavity mirrors. In the present section, only the features relevant to the experiments in Chapter 4 are described. In particular, we present a characterization of the mechanical properties after moving the setup to a new cryostat, accompanied by slight modifications, and the implementation of lateral position scans to enable investigations of light-matter coupling as a function of cavity mode position.

The heart of the cavity setup is shown in Fig. 3.10. The planar mirror is mounted on a stack

[2] In the experimental campaign relevant to this thesis, the cryogenic cavity system was implemented and characterized in collaboration with Johannes Scherzer, who also reports on some of the characterization results in his dissertation [333].

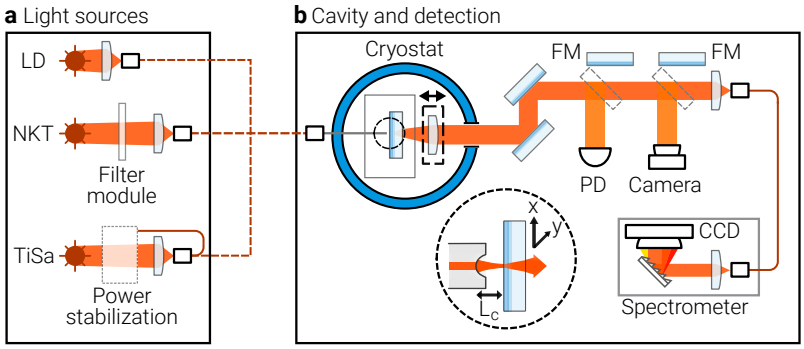

Figure 3.11.: Optical setups for cryogenic cavity operation. a, Schematic of the light sources used for cavity characterization and transmission measurements. LD, laser diode. NKT, pulsed supercontinuum laser. TiSa, Titanium sapphire laser. **b**, Schematic of the optical setups used to analyze cavity transmission. FM, flip mirror. PD, photodiode.

of nanopositioners (attocube systems ANPx311 and ANPz102) for lateral displacement of the sample with respect to the fiber mirror, and coarse step-wise positioning of fiber and mirror distance over a range of 4.8 mm. The planar mirror, not visible in Fig. 3.10, is fixed to a tube-shaped mount, with the DBR-coated surface with sample on top facing the fiber mirror.

The cavity fiber, fabricated in the group of David Hunger, is fixed to a piezoelectric transducer (UHU Endfest glue), which allows for fine-tuning of the cavity length. The transducer is mounted on a titanium stack, with the height adjusted to place the fiber tip within the range of vertical positions accessible by the planar mirror. A spring-loaded pin provides mechanical contact at sufficient rigidity to reduce relative displacement between cavity mirrors, while still allowing for tuning of the mirror distance [328, 334]. This pin provides the only mechanical connection between fiber and planar mirror stacks, the additional metal beam visible in the background of Fig. 3.10 is attached to a different setup component. The cavity fiber is spliced to a fiber feed-through port in the cryostat housing for optical connection.

The two mirror stacks shown in Fig. 3.10 are mounted on a stage designed to passively isolate the cavity from mechanical vibrations of the cryostat cold plate. The vibration isolation system is based on mechanical springs and magnetic damping, as described in detail in [328, 334]. The characterization of its mechanical properties is presented below. Thermal links to the cryostat cold plate made from copper lamella enable thermalization of the relevant cavity components with the reservoir. Electrical connections are established via break-out ports of the cryostat. Control electronics for nanopositioners (attocube systems ANC350 and ANC300) and piezoelectric transducer (attocube systems ANC300 with ANM200, amplifying the voltage output of National Instruments USB-6363) are controlled via a Python software, with the measurement protocol outlined below.

The optical setup used for cavity transmission and characterization measurements is

shown schematically in Fig. 3.11. The cavity system, with tunability along all three spatial directions as illustrated in the inset, is mounted inside a closed cycle cryostat connected to an optical table (attocube systems attoDRY800). The cavity mode transmitted through the planar mirror was collimated using an aspheric lens (Thorlabs AL1210), whose position along the optical axis was controlled with a nanopositioner (attocube systems ANPx311-HL). After transmission through an optical window in the cryostat housing, the cavity mode was coupled into a single-mode fiber for analysis with a grating spectrometer (Roper Scientific Acton SP2500) and CCD cooled to liquid nitrogen temperatures (Roper Scientific Spec-10:100BR). If required, the detection system was switched to a photodiode (see the discussion below for details) or optical camera.

The required light sources are shown schematically in Fig. 3.11a. A laser diode operated at a wavelength $\lambda = 532\,\text{nm}$, outside the stopband of the DBR-coating (see below for details). By detecting its transmission through the cavity with a camera at large mirror distance, this diode was used for coarse positioning of the sample with respect to the cavity mode. A supercontinuum pulsed laser (NKT SuperK Extreme) served as a white light source, spectrally filtered to bandwidths in the range $\Delta\lambda = 10$–$100\,\text{nm}$ using a commercially available module (NKT Varia). A titanium sapphire laser (M Squared SolsTis), operated in continuous wave mode and power stabilized using an acusto-optic modulator, provided tunable monochromatic laser light in the near-infrared wavelength range. The light source of choice was coupled into the cavity via the mirror fiber.

Fiber and planar mirror featured an identical DBR-coating made from alternating layers of SiO_2 and TiO_2 (Laseroptik GmbH), whose transmission as calculated from a transfer matrix simulation is shown by the orange line in Fig. 3.12a (see Chapter A for details on the calculation). The coating features a stopband minimum at a wavelength $\lambda = 740\,\text{nm}$, close to the exciton resonance of interest at $\lambda = 755\,\text{nm}$. The van der Waals-heterostack featured hexagonal boron nitride (hBN) layers for encapsulation of the TMD monolayer at reduced inhomogeneous broadening, and to place the quantum well close to the antinode of an intracavity field. This spacer introduced a slight modification to the coating reflectivity, evidenced by the red line in Fig. 3.12a.

3.3.2. Cavity characteristics

To determine the cavity finesse, we measured the transmission of the titanium sapphire laser tuned to a wavelength $\lambda = 755\,\text{nm}$ for varying cavity length, with data shown in Fig. 3.12b. For this measurement, the cavity was operated at the lowest accessible effective mode order $q_{\text{eff}} = 6$, determined based on Eq. (3.6) and limited by the depth of the mirror profile. The experiments in Chapter 4 were performed at identical mode order. The time-dependent change in cavity length was computed by scanning the mirror distance over one free spectral range. Similar to the linewidth measurements presented in Section 3.2, the scan speed

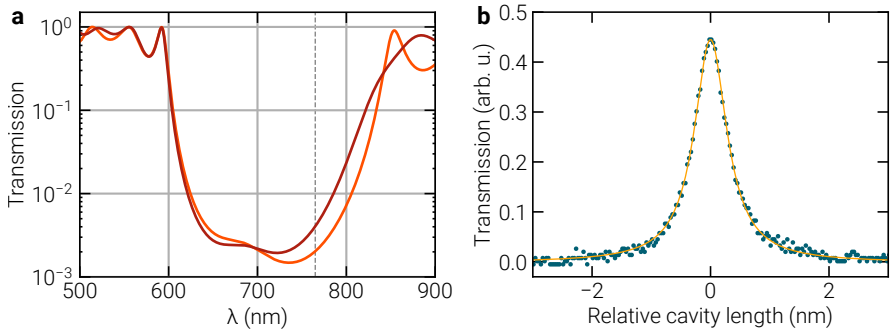

Figure 3.12.: Cavity finesse. a, Transmission of the DBR-coating on the cavity mirrors from a transfer matrix calculation (orange line), and transmission for the case a 90 nm thick spacer of hexagonal boron nitride placed on top of the planar mirror (red line). The vertical dashed line indicates the resonance wavelength of the A:1s-exciton in $MoSe_2$. **b**, Experimental cavity transmission as a function of mirror distance, measured at effective mode order $q_{\mathrm{eff}} = 6$ and wavelength $\lambda = 755$ nm. The yellow line is the fit of a Lorentzian profile.

was set fast enough to achieve a measurement bandwidth which exceeded the maximum bandwidth of cavity length fluctuations of around 1 kHz. Likewise, photodiode (Vishay BPW34, amplified by Femto DLPCA-200) and detection system (LeCroy WavePro 954) were chosen to provide a sufficiently large measurement bandwidth. From fits of a Lorentzian profile to the data, we determined the cavity finesse as described in Section 3.2, resulting in $\mathcal{F} = 576 \pm 12$, with the standard error obtained from ten repetitions of the measurement. This result is smaller than the theoretically expected value $\mathcal{F} \approx 1500$, likely a result of diffraction loss caused by a tilt between fiber and planar mirror. The corresponding measured cavity linewidth is $\kappa = 480 \pm 10\,\mu\mathrm{eV}$.

Cavity operation inside a closed-cycle cryostat, as explained above, induces an increase in mechanical vibrations, which can lead to an enhancement of fluctuations in the mirror distance, thereby reducing the mechanical stability of the cavity. Prior to the measurement campaign performed in the framework of this thesis, the cavity setup was moved to a new cryostat, which made a reassessment of the stability necessary.

We employed the method used in [328] to characterize cavity length fluctuations, which is based on measuring the transmission of a power-stabilized titanium sapphire laser through the resonator. First, we measured a mirror distance-dependent transmission profile as shown in Fig. 3.13a, to which we fit an Airy formula of Eq. (2.3) to determine the cavity finesse and the photodiode voltage at maximum transmission $V_{\mathrm{c,max}}$. Next, we detuned the cavity length from the resonance by one half width at half maximum of the transmission profile and recorded the time-dependent cavity transmission. Near the chosen mirror distance, the Airy profile features a near-linear slope, as illustrated by the black line in Fig. 3.13a.

We use the linear slope approximation to convert the measured time-dependent transmission to mirror displacement. For cavity lengths L_{c} near half width half maximum, the

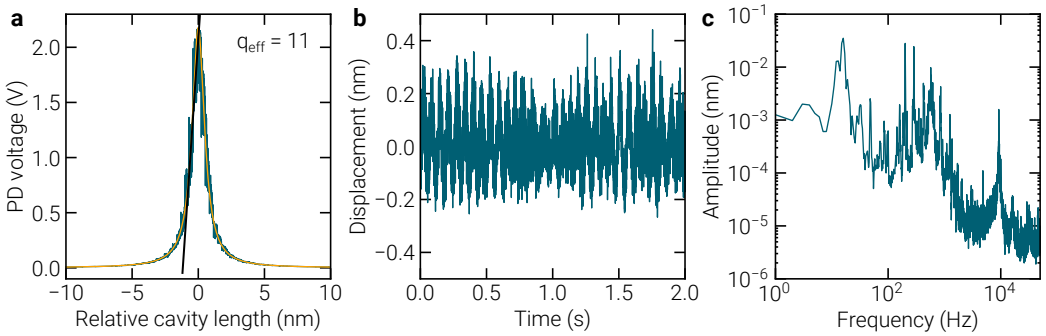

Figure 3.13.: Passive cavity stability at room-temperature. a, Cavity transmission at a wavelength of 800 nm and effective mode order $q_{\mathrm{eff}} = 11$ for varying mirror distance, measured with a photodiode (PD). The yellow line is the fit of an Airy formula. Near half-maximum, the transmission profile exhibits a linear slope, as illustrated by the black line. **b**, Mirror displacement as a function of time, measured as described in the main text. **c**, Fourier transform amplitude for a displacement time trace as shown in **b**.

voltage measured with the transmission photodiode is given by $V(L_{\mathrm{c}}) = aL_{\mathrm{c}} + V_{\mathrm{c,max}}/2$, such that the cavity length can be determined as $L_{\mathrm{c}} = (V - V_{\mathrm{c,max}}/2)/a$ from a measured voltage V. In these expressions, a is the slope of the transmission profile, which we computed using two different methods. For comparison with mirror displacement data obtained for the old cryostat, we employed the same approach as used in the respective measurement campaign. We computed the slope from the minimum and maximum voltages $V_{\mathrm{tr,min/max}}$ of the transmission time trace as $a = (V_{\mathrm{tr,max}} - V_{\mathrm{tr,min}})/(L_{\mathrm{c,max}} - L_{\mathrm{c,min}})$, in which the lengths $L_{\mathrm{c,max/min}}$ corresponding to maximum and minimum cavity transmission were determined by solving the Airy formula for L_{c}. For all other data, we used a simplified approach, approximating $a \approx 2\mathcal{F}/\lambda$, which is easily obtained from the Lorentzian approximation to the cavity transmission.

The time-dependent mirror displacement, obtained as described above, is shown in Fig. 3.13b for room-temperature cavity operation. We operated the laser at a wavelength $\lambda = 800$ nm and effective mode order $q_{\mathrm{eff}} = 11$, where cavity linewidth was sufficiently large (i.e. the finesse was sufficiently low) for the linear slope approximation to remain valid for the measured values of cavity transmission. Insight into the mechanical properties of the setup is provided by computing the Fourier transform of such a time trace, with the amplitude of Fourier transform coefficients shown in Fig. 3.13c. Maxima near 10 Hz and 300 Hz indicate mechanical resonances at the respective frequencies.

From a time-dependent displacement measurement with a duration of 10 s, we obtained a root mean square (rms) displacement of 90 pm, which is increased compared to the value of 30 pm obtained for room-temperature operation with the setup placed in the old cryostat. Comparing Fourier transform amplitudes of cavity length fluctuations for both cryostats, with data shown in Fig. 3.14a, we find increased displacements for frequencies in the ranges

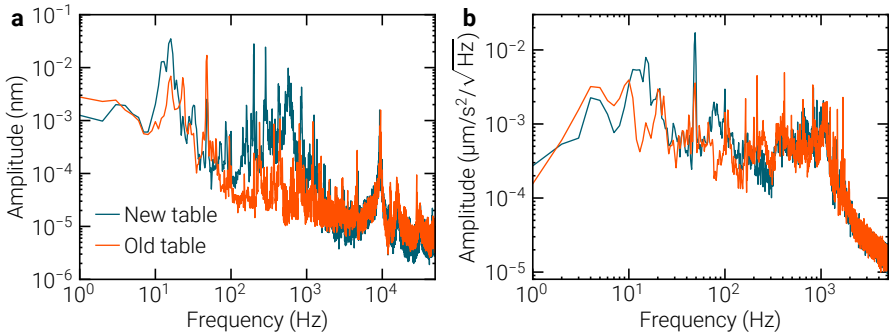

Figure 3.14.: Cavity operation in different cryostats. **a**, Fourier transform amplitudes of cavity length fluctuations, with the setup placed in the cryostat used for development (old table, orange line), and the cryostat used for the experiments presented in this thesis (new table, teal line). **b**, Fourier transform amplitude of accelerometry measurements performed in vertical direction, with the measurement device placed on the old and new optical tables (orange and teal line, respectively).

10–30 Hz and 100–1000 Hz. To elucidate the origin of this increase, we performed accelerometry measurements (TableStable VA-2C) on both optical tables, with Fourier transform amplitudes of table accelerations in the vertical direction shown in Fig. 3.14b. In the frequency range 10–30 Hz, the optical table of the new cryostat exhibits an increased acceleration amplitude, which likely explains the observed increase in cavity length fluctuations in the respective frequency range. The cavity setup features a mechanical resonance at approximately 15 Hz defined by the springs [328], which enables efficient mechanical coupling to the table vibrations near this frequency. The increased vibrational level of the new table was observed to be largely independent of the weight distribution on the table and the air pressure at which the table's damping system was operated.

The origin of increased cavity vibrations in the range 100–1000 Hz proved difficult to identify. We investigated the setup for any loose or broken components, removed and reapplied the glue fixing cavity fiber and springs, exchanged the spring-loaded pin, and investigated the influence of different devices such as cryostat compressors on cavity stability. None of these changes to the setup caused a significant decrease in the cavity length fluctuations. Possible remaining origins of mirror displacement are thus an increased level of mechanical noise of the new cryostat cold plate, and increased environmental noise during measurements on the new cryostat, induced by construction works in the building at the time of the measurement campaign.

Cryostat operation further decreases the cavity stability due to additional mechanical vibrations introduced to the system. Fig. 3.15a shows time-dependent mirror displacement measured at a temperature of 4 K, obtained for wavelength $\lambda = 840$ nm at effective mode order $q_{\mathrm{eff}} = 6$. Periodic cryostat compression at a frequency of 1 Hz results in large mirror displacements. We find that a histogram of measured displacement values, shown in Fig. 3.15b,

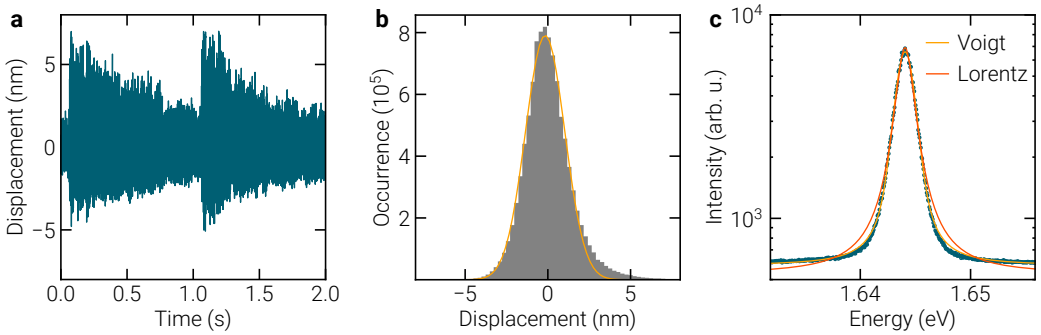

Figure 3.15.: Cavity stability at cryogenic temperatures. a, Mirror displacement time trace, acquired during cavity operation at a temperature of 4 K. **b**, Occurrence of mirror displacements in a time trace of 10 s. The yellow line is the fit of a Gaussian. **c**, Cavity transmission of a white light source, measured with a grating spectrometer, along with fits of a Lorentzian (orange line) and the Voigt model derived in the main text (yellow line).

is approximated by Gaussian function with $1/e^2$ half width $\sigma_\mathrm{L} = 1.19\,\mathrm{nm}$. The observed asymmetry with respect to zero displacement is likely caused by a deviation from the linear slope approximation used to compute the displacements.

The observed mirror displacements result in a broadening of the energy-dependent cavity transmission profile, which is of central interest in the experiments presented in Chapter 4. To investigate this broadening, we note that a displacement ΔL results in an energy shift $\Delta E = E_\mathrm{c}\Delta L/L_\mathrm{c}$, in which E_c is the cavity photon energy at mirror distance L_c. The energy-dependent transmission of a cavity with Lorentzian line shape (i.e. $\mathcal{F} \gg 1$), time-averaged over multiple compression cycles, is therefore given by a convolution of the transmitted cavity field with the displacement distribution. This consideration yields

$$T_\mathrm{c}(E) \propto \left| \int_{-\infty}^{\infty} d(\Delta L) \frac{\kappa/2}{(E - E_\mathrm{c} + E_\mathrm{c}\Delta L/L_\mathrm{c}) + i\kappa/2} \exp\left(-\frac{\Delta L^2}{2\sigma_\mathrm{L}^2}\right) \right|^2 , \tag{3.7}$$

which is a Voigt profile.

An experimental cavity transmission spectrum, obtained for an integration time of 2 s for the lowest accessible effective mode order $q_\mathrm{eff} = 6$, is shown in Fig. 3.15c. A fit of Eq. (3.7) (yellow line) is in good agreement with the data, in particular compared to best fit of a Lorentzian profile (orange line). From the fit of the Voigt profile, we find $\kappa = 405\,\mu\mathrm{eV}$, close to the value $480 \pm 10\,\mu\mathrm{eV}$ obtained from the measurement of length-dependent cavity transmission as in Fig. 3.12b. The fit also yields $\sigma_\mathrm{L} = 0.84\,\mathrm{nm}$, which deviates from the $1/e^2$ half width of the histogram in Fig. 3.15b by around 30 %. The deviation is likely the result of an increased noise background in the stability measurement, caused by construction work in the building, and deviations of the displacement distribution from a Gaussian. Despite the deviation, the Voigt model of Eq. (3.7) provides an estimate for the order of magnitude of the rms mirror displacements.

As evident from the previous discussion and the data in Fig. 3.15c, the cavity FWHM linewidth of 1.6 meV at cryogenic temperatures is limited by fluctuations in the mirror distance. While in the new cryostat, the passive mechanical stability of the cavity system is decreased compared to the previous implementation reported in [328], the linewidth is suitable for experiments on cavity-coupled TMD excitons, whose linewidth is on the order 2 meV, similar to that of the cavity. As a result, we observe pronounced Rabi splittings in the experiments in Chapter 4, which clearly fulfill the conditions for strong coupling given in Section 2.4.

In Chapter 4, cavity-exciton coupling is investigated as a function of lateral position of the cavity mode, which requires a characterization of the setup's transverse scanning capability. In Fig. 3.16a, we show a map of cavity transmission at cavity energy $E_c = 1.668$ eV, obtained by raster-scanning the planar mirror with respect to the cavity fiber using the nanopositioners. The data was obtained from a hyperspectral measurement, for which at each position, cavity transmission spectra of a white light source were measured with a spectrometer for multiple values of the cavity length, which was tuned via the fiber piezoelectric transducer. From the cavity length sweep at each position, the spectrum corresponding to a cavity energy $E_c = 1.668$ eV was selected, and the transmission maximum was plotted to obtain the map of Fig. 3.16a. Typical length sweeps in the experiments in Chapter 4 featured 50 steps covering a range of approx. 100 meV in cavity energy, such that the cavity energy was changed by approximately one linewidth between each spectrum. The integration time for each spectrum was chosen to exceed the cryostat compression period of 1 s to average over fluctuations in mirror distance. The step size in the lateral direction, tuned via nanopositioner voltage and frequency, was chosen as small as possible while keeping the measurement duration within a reasonable time frame.

Raster-scanning the lateral position of the planar mirror resulted in small shifts of the cavity length between different positions, likely caused by the mechanical coupling between the two mirrors via the spring-loaded pin. We found that the position-dependence of this shift was reproducible along the fast axis of the position scan. In hyperspectral measurements, we therefore compensated the position-dependent length shift prior to sweeping the cavity length by applying a pre-calibrated voltage to the vertical nanopositioner with the planar mirror attached. This approach corresponds to a feed forward drift compensation, implemented in the experiment control software.

In the inset of Fig. 3.16a, we show an optical micrograph of the sample area covered by the cavity transmission map. Air-holes in the top hBN encapsulation layer with a diameter of 600 nm (see Section 3.5 for details) are visible as white dots in the micrograph. Inside the cavity, these holes induce additional optical loss through scattering and are thus clearly visible in the spatial cavity map at reduced transmission. In the same manner, a small circular defect, also visible in the micrograph, and a crack in the top hBN-layer, visible in the confocal measurement of Fig. 3.21, are identified.

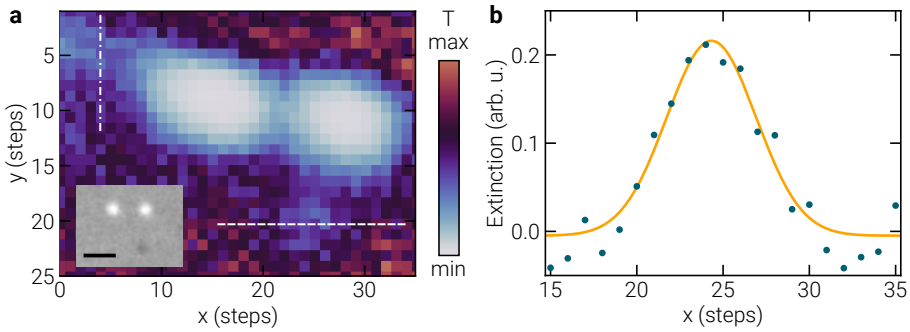

Figure 3.16.: Scanning capability of the cryogenic cavity setup. **a**, Map of cavity transmission at cavity energy $E_c = 1.668$ eV and effective mode order $q_{\text{eff}} = 6$, measured for the device area shown in the optical micrograph in the inset. The inset scale bar is 2 µm. **b**, Optical extinction along the dashed white line in **a**, computed from the measured transmission as detailed in the main text. The yellow solid line is the fit of a Gaussian profile.

We use the transmission map to determine the cavity mode waist from the spatially dependent optical extinction loss B (i.e. absorption and scattering), induced by sources of loss placed inside the cavity. Using Eq. (2.13), we find $B \propto \sqrt{T_{c,0}/T_c} - 1$, in which T_c and $T_{c,0}$ are the measured transmission at the position of and away from the source of loss, respectively. In Fig. 3.16b, we show the optical extinction computed along the dashed horizontal line in Fig. 3.16a. The lateral dimensions of the sample defect, which is the source of optical loss, are much smaller than the expected cavity waist, indicated by its diffraction-limited point spread function in the optical micrograph. As a result, the extinction profile is given by the Gaussian cavity point spread function, whose $1/e^2$ half width corresponds to the cavity mode waist. From a fit to the extinction data, with the result shown by the yellow line in Fig. 3.16b, we find $w_c = 1.07 \pm 0.08$ µm, with the error determined by repeating the analysis for multiple line cuts in the transmission map. This result is in excellent agreement with the expected value of 1 µm, computed from Eq. (3.2) for the fiber radius of curvature of 10 µm. In the vertical scan direction, we determined the waist from the extinction of the crack in the hBN encapsulation, indicated by the dash-dotted line in Fig. 3.16a. The result $w_c = 0.83 \pm 0.02$ µm indicates a slight ellipticity of the cavity mode, negligible for the analysis of the experiments presented in Chapter 4.

3.4. Cryogenic confocal spectroscopy

Prior to cavity-coupling, TMD-devices fabricated as described in Section 3.5 were characterized using cryogenic confocal spectroscopy [335] to assess the device quality and to determine the resonance energies of individual exciton species. A schematic of the optical spectroscopy setup is shown in Fig. 3.17. Lasers at wavelength $\lambda = 633$ nm and $\lambda = 675$ nm

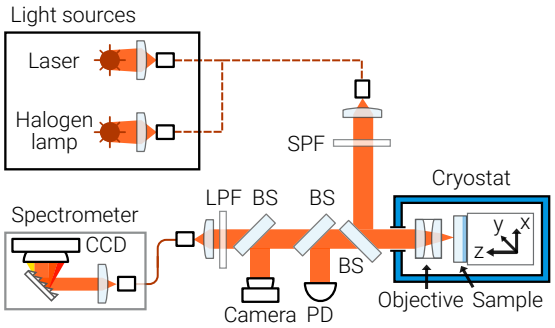

Figure 3.17.: Optical setup for cryogenic confocal spectroscopy. Schematic of the relevant components for confocal optical spectroscopy: Fiber-coupled light sources, injected into the setup via a single-mode fiber; cryostat housing objective and sample; devices for detection and analysis, including spectrometer with charge-coupled device (CCD), photodiode (PD) and camera. BS, beam splitter. SPF, short pass filter. LPF, long pass filter.

provided offresonant excitation light for photoluminescence (PL) experiments. A halogen lamp (Ocean optics HL-2000-HP) served as a white light source. All light sources were coupled into a single mode fiber referred to as excitation fiber and guided to the optical setup in the periphery of the cryostat (attocube systems attoDRY800).

The excitation fiber output was collimated using a broadband collimator (attocube systems RT-APO/NIR-IR/0.13) and guided into the cryostat via a beam splitter (reflectivity 10 %), where it was focused on the sample surface using an achromatic objective (attocube systems LT-APO/VISIR/0.82). Piezoelectric nanopositioners (attocube systems ANPx101, ANPz102 and ANSxy100) enabled displacement of the sample with respect to the objective. Light emitted or reflected from the sample and transmitted through the beam splitter was coupled into a single mode fiber, referred to as detection fiber, using a broadband collimator (attocube systems RT-APO/NIR-IR/0.13). The output of this fiber was coupled into a grating spectrometer (Princeton Instruments IsoPlane SCT320) and, upon dispersion, analyzed with a silicon CCD (Princeton Instruments Pixis 1024), cooled using a Peltier element. Additional pick-up beam splitters in the detection path (transmission 90 %) guided light to a camera for localization of the sample and a photodiode for measurements of optical power. For PL experiments, short- and longpass filters were placed in the excitation and detection path in order to suppress the pump laser and Raman photons generated in the excitation fiber. In white-light measurements, confocal differential reflectivity was computed from the measured reflected intensity I_{meas} as $\mathrm{DR} = (I_{\mathrm{meas}} - I_{\mathrm{b}})/I_{\mathrm{b}}$, with I_{b} a background determined with the focal spot positioned away from the sample region of interest. The setup was controlled with a Python software, allowing for fully automated measurements.

Figure 3.18.: Device geometry and components. a, Schematic side view of the fabricated device. A monolayer of molybdenum diselenide ($MoSe_2$), encapsulated by two layers of hexagonal boron nitride (hBN) is placed on a distributed Bragg reflector (DBR). Local removal of the hBN encapsulation by dry etching locally modifies exciton properties. **b**, Optical micrograph of triangular monolayer crystals of $MoSe_2$, grown by chemical vapor deposition. **c**, Optical micrograph of thin layers of hBN, obtained by mechanical exfoliation. The flake marked by the dashed white rectangle has a height of 44 nm and was used for the final device in Fig. 3.21. The scale bars in **b** and **c** are 100 µm.

3.5. Nanofabrication of van der Waals heterostacks

Among the intriguing properties of monolayer transition metal dichalcogenides (TMDs) is the possibility for their assembly into van der Waals heterostacks. This approach, at times referred to as "van der Waals Lego" [76], enables the tailored design of devices with novel properties, with the emergence of moiré physics in TMD heterostructures [79] and graphene multilayers [336–338] as a prominent example. Combined with established nanofabrication techniques, van der Waals heterostacks offer a route towards local control over TMD exciton properties [69]. Leveraging this concept, we developed a fabrication technique which we present in the following, with the final device employed in the experiments in Chapter 4[3]. We emphasize that a broader review of TMD-based nanofabrication by far exceeds the scope of this dissertation, such that we briefly describe the methods relevant to the present work, providing references for contextualization wherever possible. Parts of the section are adapted or reproduced verbatim from the publication [P1].

The device, illustrated in Fig. 3.18a, is based on a monolayer of molybdenum diselenide ($MoSe_2$). Encapsulation between two layers of hexagonal boron nitride (hBN) yields near-homogeneous exciton linewidths [340] due to monolayer interfaces at reduced strain and surface charges compared to other dielectrics, which is desired in many optoelectronic experiments. Local removal of the hBN encapsulation enables dielectric control over TMD exciton properties (see Section 2.1), the central interest of the experiments in Chapter 4. The heterostack is placed on a distributed Bragg reflector (DBR) mirror, enabling strong exciton-photon coupling upon assembly into a fiber-based microcavity (see Chapter 4).

[3] The fabrication method was developed with contributions by Lukas Krelle, who also reports on the technique in his Master's thesis [339], for which the concept was extended to realize plasmonic lattices coupled to TMD excitons [P4].

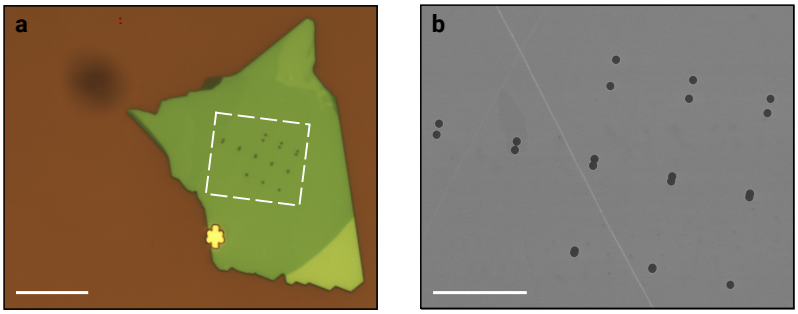

Figure 3.19.: Dry etching of hexagonal boron nitride. **a**, Optical micrograph of a flake of hexagonal boron nitride, with a pattern of 600 nm-diameter air-holes produced via reactive ion etching. The yellow star is a gold alignment mark for lithography. The scale bar is 25 µm. **b**, Scanning electron microscopy image of the area marked by the dashed white rectangle in **a**, showing a close-up of the air-hole pattern. The scale bar is 7 µm.

Prior to heterostack assembly, we identified and processed the individual device constituents. Monolayers of $MoSe_2$ were grown by chemical vapor deposition [81–83], performed by Ismail Bilgin. A typical growth run results in triangular $MoSe_2$ monolayer crystals with edge lengths of several tens of µm, as shown in Fig. 3.18b for growth on a silicon substrate covered by a 90 nm thick SiO_2 oxide layer. For device fabrication, we selected monolayers with near-constant optical contrast to ensure homogeneity of the exciton host material. Crystals featuring multilayer nuclei, visible by increased contrast in the optical microscope, were discarded. We performed heterostack assembly as early as possible after crystal growth, since we found that storage for several weeks frequently prevented monolayer transfer with the method described below, potentially due to oxidization-induced surface contamination [341].

We produced hBN layers on a silicon substrate covered by SiO_2 by mechanical exfoliation [23] with adhesive tape, resulting in flakes with spatial extents of up to 100 µm and thicknesses ranging from a few nm to several µm (see [339, 342, 343] for a detailed description of the exfoliation procedure). A typical exfoliation result is shown in Fig. 3.18c, with the bottom flake of the device used for the experiments presented in Chapter 4 marked by the white dashed rectangle. We selected flakes featuring constant thickness in areas of at least 30 µm × 30 µm to ensure large-area homogeneity. The bottom layer requires a thickness of around 90 nm to place the $MoSe_2$ monolayer close to an antinode of the intracavity field at maximum light-matter coupling strength, calculated as the optical path length $d = \lambda/(4n)$ of an hBN layer with refractive index $n = 2.12$ [344] at a wavelength $\lambda = 765$ nm. For the top layer, a thickness in the range 20–50 nm was selected, which we found to enable successful transfer after processing as described below. Optical contrast provided a rough estimate for flake pre-selection based on the thickness, which was subsequently determined in atomic force microscopy.

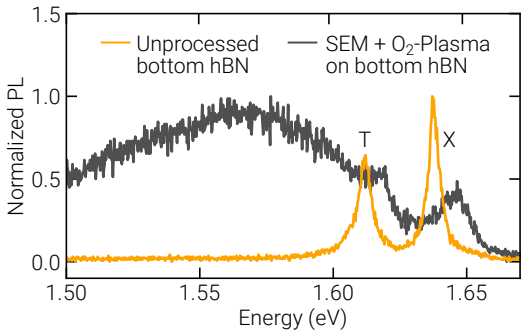

Figure 3.20.: Device contamination. Cryogenic photoluminescence spectra of hBN-encapsulated $MoSe_2$ monolayers (pump wavelength 675 nm, see Section 3.4 for a description of the experiment). The spectrum shown by the yellow line is obtained for a heterostack in which the bottom hBN surface in contact with the TMD monolayer was not exposed to any processing, except cleaning with acetone and isopropanol, featuring distinct exciton (X) and trion (T) resonances with near-Lorentzian line shapes. The gray line shows a spectrum obtained for a device in which the bottom hBN layer was exposed to scanning electron microscopy (SEM) and oxygen plasma prior to heterostack assembly.

To locally remove the dielectric encapsulation of the TMD as illustrated in Fig. 3.18a, we performed dry etching on the top hBN layer [345] prior to heterostack assembly. We fabricated a pattern of air-holes with a diameter of 600 nm, grouped in pairs with varying distance, as shown in optical and scanning electron microscopy (SEM) of a processed flake in Fig. 3.19a and b, respectively. The pattern geometry is motivated by the experiments presented in Chapter 4.

For patterning, a polymer mask with the desired geometry was created on the top hBN layer using electron beam lithography. 4 % polymethyl methacrylate 950K dissolved in anisole was used as resist, with typical electron beam doses and acceleration voltages of 500 µC/cm^2 and 20 kV, respectively. Air-holes were etched using inductively coupled plasma-based reactive ion etching (Oxford PlasmaLab 100 ICP-RIE). We used a plasma of argon and sulfur hexafluoride, which were injected at flowrates of 5 and 10 sccm, respectively, as the chamber pressure was kept at 10 mTorr. Inductively coupled plasma and radio frequency powers were 70 and 6 W, respectively. The achieved etch rate was 0.6 nm/s. After etching and resist removal, the hBN flake was cleaned using oxygen plasma. From SEM images as shown in Fig. 3.19b, we determined the side wall slope to typically deviate by 20° from vertical. Hole diameter and standard error were 611.3 ± 0.9 nm, measured from SEM images for a test sample featuring 19 holes. This result is very close to the nominal value of 600 nm used in the mask design, indicating accuracy in the fabrication process.

By investigating test stacks of hBN-encapsulated TMD monolayers, we found that exposing the top surface of the bottom hBN layer to SEM and oxygen plasma prior to device assembly resulted in a drastic modification of the exciton resonance. Cryogenic confocal

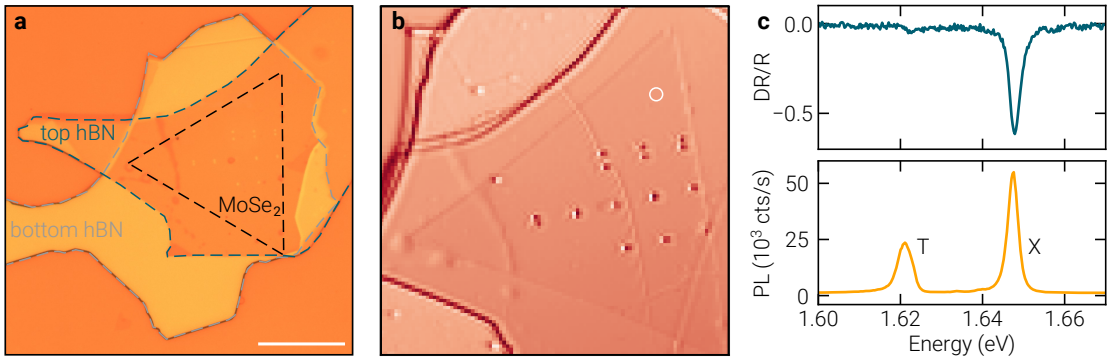

Figure 3.21.: Fabricated device. **a**, Optical micrograph of the device employed in the experiments presented in Chapter 4. The scale bar is 25 µm. **b**, Map of cryogenic confocal differential reflectivity (DR), integrated in the spectral range 1.670 to 1.809 eV (see Section 3.4 for a description of the measurement). The triangular area is the $MoSe_2$ monolayer crystal marked by the dashed black triangle in **a**. **c**, Cryogenic DR (top panel) and PL (bottom panel, pump wavelength 632 nm), obtained at the position marked by the white circle in **b**. *X* and *T* denote exciton and trion resonances, respectively.

photoluminescence (PL) measurements, with data shown in Fig. 3.20, demonstrate that in addition the exciton and trion resonances observed in a high-quality heterostack (yellow line in Fig. 3.20) a broad, redshifted shoulder emerges from the trion upon processing of the bottom hBN-layer. A potential origin is hydrocarbon contamination of the surface, which upon exposure to the electron beam results in the generation of defect radicals [346], thereby modifying the exciton dielectric environment. The strongly broadened line shape would render the devices unsuitable for the intended experiments. As a consequence, we avoided exposing the bottom layer surfaces to any processing steps or solvents, except for acetone and isopropanol used to remove exfoliation tape residues. We also refrained from performing SEM-imaging on the processed top layer of the final device.

For heterostack assembly, we employed the hot pick-up technique [347, 348], which relies on the fact that the relatively weak van der Waals-forces between device components and substrate can be overcome by adhesion to a suitably chosen polymer or other device components, if heated to the correct temperature. Based on this effect, a thin layer of polymer is used to subsequently pick up the individual components of the device, starting from the top layer. The technique, along with the employed setups, is described in detail in [342, 343] such that we only report the key parameters in the following.

We fabricated stamps based on spherical polydimethylsiloxane (PDMS) droplets, covered with thin polymer films. For initial pick-up of the processed top hBN layer, we employed the polycaprolactone (PCL) polymer [349, 350] to ensure sufficient adhesion, since transfer attempts based on the widely used polycarbonate [351] were unsuccessful. After pick-up, the top hBN layer was released onto the TMD monolayer crystal and PCL residues were removed

using tetrahydrofuran. Subsequently, the stack was assembled and released on the DBR mirror using the established method based on polycarbonate films. After release, devices were annealed for 12 hours at 180 °C under high vacuum (chamber pressure $< 1 \times 10^{-7}$ mbar).

A microscope image of the final device is shown in Fig. 3.21a. Top and bottom hBN layers exhibit thicknesses of 44 and 87 nm, respectively. The fabricated air-hole pattern in the top hBN layer, visible by white dots, covers the triangular $MoSe_2$ monolayer. In Fig. 3.21b, we show a map of integrated cryogenic confocal differential reflectivity, measured in the monolayer area. This measurement reveals additional line and point defects in the device due to increased sensitivity of the measurement method to photonic scattering and absorption loss. Overall, the device exhibits large homogeneous TMD areas, which is desired for polariton-based experiments. Representative differential reflectivity and PL spectra are shown in Fig. 3.21c. The presence of a trion resonance is most likely the result of a small degree of native doping. FWHM exciton linewidths of around 3 meV in PL are close to reported near-homogeneous linewidths of 1.1 [108] and 2 meV [352], indicating satisfactory device quality at small inhomogeneous broadening.

Microcavity-coupling of excitons in a two-dimensional semiconductor

4

In this chapter, we demonstrate control over cavity-coupled excitons in a monolayer semiconductor, achieved by engineering the dielectric environment. Exciton-polaritons, coherently hybridized states of excitons and photons, manifest in our system, which is operated at cryogenic temperatures and in the regime of strong light-matter coupling. Modulating the exciton energy by nanopatterning the semiconductor encapsulation layer, we realize mesoscopic domains of excitons with distinct properties defined by their dielectric environment. Upon cavity-coupling, the local modulation of the exciton energy results in polariton energy shifts, which we control in magnitude via the cavity-exciton detuning. We further demonstrate operation of our system in the regime of dispersive cavity-coupling, where an effective hopping is mediated between different mesoscopic exciton domains weakly dressed by the same cavity mode. Our results represent a step towards polaritonic lattices and quantum simulators based on dielectrically tailored two-dimensional semiconductors.

Device fabrication and confocal cryogenic spectroscopy were performed as described in Section 3.5 and Section 3.4 with contributions by Farsane Tabataba-Vakili and Lukas Krelle. Johannes Scherzer contributed to the implementation of the cavity setup, discussed in Section 3.3.

THIS CHAPTER IS BASED ON THE PUBLICATION [P1]:

Husel, L., Tabataba-Vakili, F., Scherzer, J., Krelle, L., Bilgin, I., Vadia, S., Watanabe, K., Taniguchi, T., Carusotto, I., and Högele, A.: "Cavity-mediated exciton hopping in a dielectrically engineered polariton system."
arXiv.org, 2506.05561 (2025)

Parts of this publication are reproduced verbatim in the following, the figures from the manuscript have been adapted and extended.

4.1. Introduction: Dielectric control of exciton-polaritons in two-dimensional semiconductors

Coherently hybridized states of cavity photons and semiconductor excitons, commonly referred to as exciton-polaritons, underpin phenomena of non-equilibrium quantum many-body physics [13], nonlinear optics [42] and quantum simulations [160] in conventional quantum well microcavity structures. In two-dimensional semiconductors and related van der Waals heterostructures as introduced in Section 2.1, large exciton binding energies and oscillator strengths enable robust polariton formation and condensation at elevated temperatures [77, 196] with unique features provided by spin-valley locking [193, 353], novel quasiparticles with enhanced nonlinearities upon doping [66], or moiré exciton-polaritons in heterostructures [P3, 206]. These properties establish semiconductor monolayers and heterostructures as prime candidates for studies of strong light-matter coupling in the solid-state.

Control over the polariton degrees of freedom via the excitonic fraction is the key to recent developments in device design [67] and has enabled demonstrations of topological insulators [210] or Kardar-Parisi-Zhang universality [211] in conventional semiconductor quantum wells. Within this framework, excitons in monolayer TMDs with high sensitivity to their dielectric environment provide means of additional engineering, taking advantage of sizable changes in the bandgap and binding energy induced by proximal dielectrics [68, 69, 115]. As such, local disorder in TMD devices facilitates trapping of polaritons with enhanced coherence [196, 354]. Complementary approaches have demonstrated polariton trapping by additional monolayers [355, 356], laser-induced disorder [357] and local strain [358]. Despite this progress, deterministic, scalable and tunable control over local exciton-polariton interactions and energies, a prerequisite for potential formation, remains challenging.

In this chapter, we demonstrate local control of the exciton-polariton energy via environmental dielectric engineering, and show how the spatially confined cavity mode can be used to mediate coupling between highly exciton-like polaritons. To define local exciton sites, we use a nanopatterned encapsulation layer of hBN, which consolidates disk-shaped exciton domains with energies distinct from excitons in the surrounding monolayer regions with unpatterned hBN. Strong coupling of one or multiple exciton domains to the optical mode of a fiber-based microcavity results in distinct polariton states, with properties determined by both the locally defined dielectric environment and the actively controlled spectral cavity-coupling. Moreover, we demonstrate the regime of dispersive cavity-coupling [71] to mediate an effective hopping between distant domains of excitons weakly dressed by cavity photons as a premise to quantum simulation architectures already established for superconducting qubits [359], ultracold atoms [360], solid-state quantum emitters [72] and optomechanical systems [361].

4.2. Experimental concept and implementation

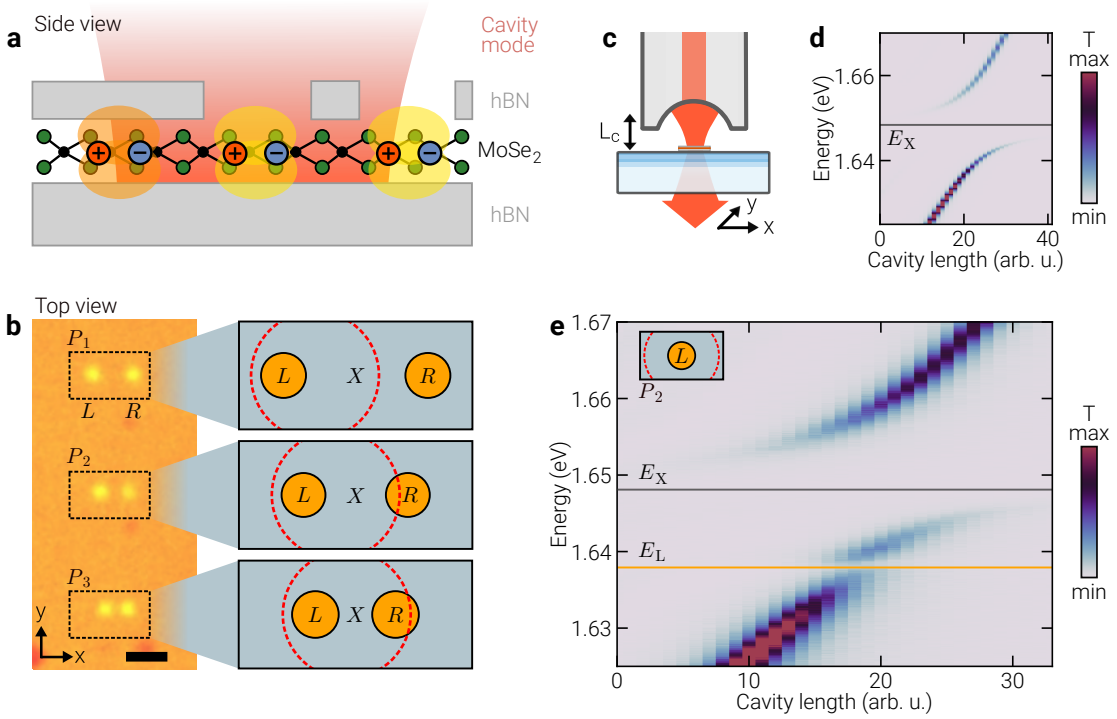

Figure 4.1.: Dielectric engineering of polariton domains. a, Schematics of a $MoSe_2$ monolayer encapsulated by planar bottom and patterned top hBN layers with spatially distinct regions of exciton-polaritons formed by strong coupling to the mode of an open cavity. **b**, Left panel: optical micrograph of the van der Waals heterostructure, with pairs of holes in the top hBN layer P_1, P_2 and P_3 visible as yellow circles of nominally identical left (L) and right (R) disks with variable separation, surrounded by fully encapsulated monolayer. The scale bar is 2 μm. Right panel: The red dashed circle shows the waist diameter of the cavity mode on the scale of the diameters and distances of disk-shaped domains surrounded by regions of monolayer excitons (X) in unpatterned hBN. **c**, Schematic of the cryogenic fiber-based open microcavity, with piezoelectrically actuated lateral translation in the $x-y$ plane and cavity length (L_C) tuning along z. **d**, Cavity transmission as a function of the cavity length tuned via the z-piezo voltage, recorded away from structured hBN for the exciton energy E_X indicated by the horizontal solid line. **e**, Same but with the cavity mode positioned near the center of a single exciton disk of etched pair P_2 as illustrated in the inset. The solid horizontal lines indicate the energy of monolayer and disk-localized excitons E_X and E_L, respectively.

Our approach, illustrated schematically in Fig. 4.1a, is based on a van der Waals heterostack with a monolayer of molybdenum diselenide ($MoSe_2$) encapsulated by a planar bottom hBN layer and a patterned top hBN layer with through-holes defined by reactive-ion etching (see Section 3.5 for details). The resulting modification of the dielectric environment on the scale of a few hundred nanometers affects both the monolayer bandgap and the

exciton binding energy [68, 112, 115], yielding a spatially modified exciton resonance energy which in turn determines local properties of exciton-polaritons upon strong coupling to an optical microcavity with photonic modes confined in all spatial directions. The left panel in Fig. 4.1b shows an optical micrograph of the corresponding sample, with two holes in the top hBN layer of same diameter and variable distance as pairs of yellow circles. The right panel illustrates schematically the resulting exciton landscape: left (L) and right (R) disk-shaped exciton domains at each etch site are surrounded by monolayer excitons (X) in the unpatterned area. Due to fabrication imperfections such as interfacial bubbles and unintentional strain, the exciton energies E_{L} and E_{R} differ between the two nominally identical domains, and both differ from the surrounding exciton energy E_{X} by virtue of different dielectric environments.

In the following, we focus on three etch-site pairs P_1, P_2 and P_3 in Fig. 4.1b with 2.0, 1.4 and 1.1 μm distances between the centers of the left and right holes with identical diameters of 0.6 μm. The finite extent of the fundamental Gaussian cavity mode with a waist of ~ 1 μm (shown by the red dashed circle in the schematics of Fig. 4.1b) and the tunability of the open cavity along all three spatial degrees of freedom (as indicated in Fig. 4.1c) allows us to study different limits of polaritons in strong light-matter coupling. First, by placing the cavity mode over the left site of the pair P_1 or P_2 that is sufficiently distant from its right counterpart, we study the local formation of polaritons in the left disk as well as their coupling to the surrounding exciton-polariton continuum (top panel of the schematics in Fig. 4.1b). In the second setting (central panel in Fig. 4.1b), the cavity mode creates and samples both left and right polariton disks, yet at a distance too large for intersite coupling. The third configuration (bottom panel in Fig. 4.1b), finally, is used to demonstrate effective cavity-mediated coupling between the left and right sites of polariton pairs.

Coupling between TMD excitons and our tunable cryogenic fiber-based microcavity system, operated at a base temperature of 4.3 K, is achieved according to the experimental schematics in Fig. 4.1c. The setup, described in detail in Section 3.3 and [328], was operated in a closed-cycle cryostat, with the cavity mounted on a passive vibration isolation system to suppress changes in cavity length induced by mechanical vibrations of the cryostat cold plate. The nanopatterned heterostack is placed on a macroscopic planar mirror, whose vertical separation L_{C} from the microscopic mirror of the micromachined fiber facet is controlled by piezoelectric actuators, which also allow for lateral displacement of the sample with respect to the cavity mode. The thickness of the bottom hBN used to encapsulate the $MoSe_2$ monolayer grown by chemical vapor deposition was 87 nm, placing the TMD monolayer close to an antinode of the intracavity field.

A Gaussian-shaped indentation with radius of curvature of ~ 14 μm on the fiber tip served as concave cavity mirror. Fiber and planar mirror had identical dielectric coatings, forming highly reflective distributed Bragg reflectors. The cavity transmission was measured with a white-light source in a spectral bandwidth of 10 nm. The cavity mode transmitted through

the planar mirror was collimated using an aspheric lens, before being coupled into a single mode fiber, dispersed in a grating spectrometer and detected with a CCD camera. Coupling of the fundamental Gaussian mode into the single mode fiber was maximized. The cavity also featured higher order Hermite-Gaussian modes [P5], whose influence on the transmission measurements is discussed in Section 4.3. The cavity was operated at longitudinal mode order $q = 6$ as the lowest accessible without physical contact between the fiber and the planar mirror. Typical integration times for transmission measurements were chosen between one and two seconds in order to average over multiple cryostat compressor cycles. As a result, the measured cavity transmission profiles are broadened by mechanical vibrations. With the cavity mode positioned away from the monolayer, we determined a full-width at half-maximum cavity linewidth $\kappa = 1.52$ meV from the fit of a Voigt profile, with Lorentzian and Gaussian contributions of 1.15 and 0.70 meV stemming from broadening by mirror loss and mechanical vibrations, respectively.

We calibrate the coupling strength between the exciton domains and our tunable microcavity by changing the spectral resonance condition between the exciton and cavity energy, E_X and E_C, via the cavity length. The result is a clear signature of strong coupling in the cavity transmission of Fig. 4.1d on a region away from structured hBN. The avoided crossing is a hallmark of polariton formation, with light-matter coupling strength $g_X = 9.6$ meV at longitudinal cavity mode order $q = 6$ as determined from the dissipative model analysis described in Section 4.3. This coupling strength is characteristic for cavity-coupling of monolayer excitons [328, 362], and places the system together with polariton linewidths of ~ 2.5 meV and the cavity linewidth $\kappa \simeq 1.5$ meV in the regime of strong light-matter coupling [158].

We observe a strong modification of the characteristic exciton-polariton splitting as we position the cavity over the left hole-etched site of P_2, with cavity transmission shown in Fig. 4.1e. As a function of the cavity length detuning, we observe an additional polariton branch related to the disk-localized exciton fraction with energy E_L, redshifted from E_X by 10 meV due to effectively reduced screening below the hole in hBN [68–70, 115]. As the area of the local exciton domain is smaller than the cavity spot, the corresponding light-matter coupling strength is reduced to $g_L = 2.65 \pm 0.04$ meV as compared to the coupling of spatially unconfined monolayer excitons in regions with both-sided hBN encapsulation (see Section 4.3 for details on the measurement of g_L). This scaling of the light-matter coupling with the spatial extent of exciton-confining domains with redshifted transition energy indicates the formation of local polariton disks.

4.3. Analysis of cavity transmission spectra

To gain a more detailed insight into the properties of dielectrically defined exciton and polariton domains, we determine exciton resonance energies and light-matter coupling

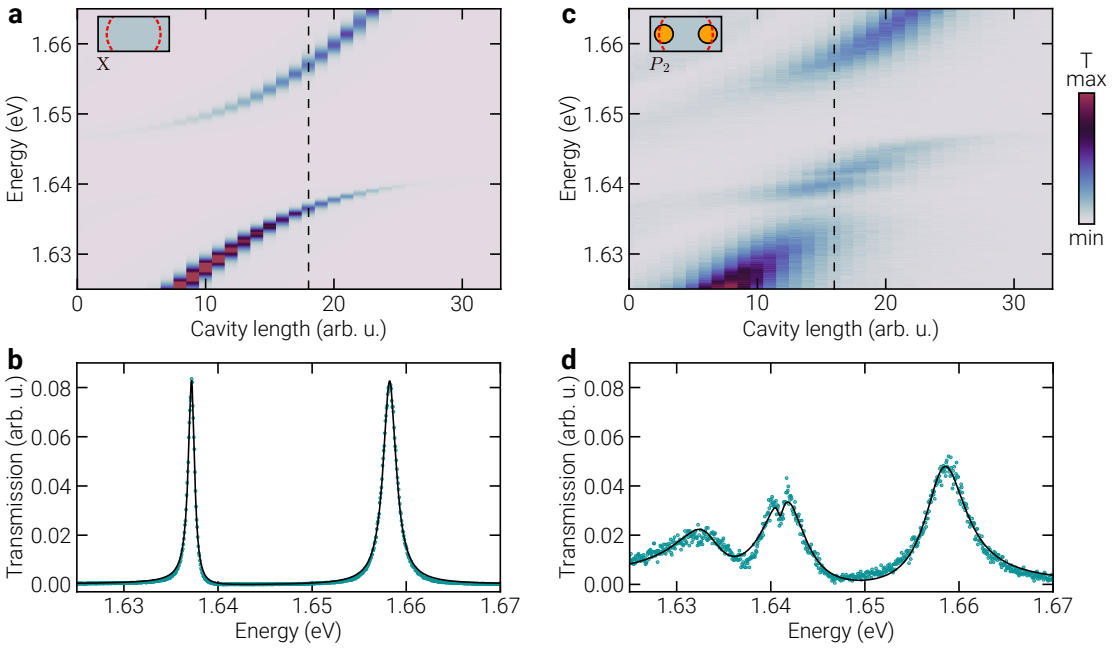

Figure 4.2.: Analysis of cavity transmission spectra. a, Cavity transmission as function of cavity length, tuned via piezoelectric actuator voltage. The cavity mode is positioned on a TMD area fully encapsulated by hBN, coupling to X excitons as defined in Fig. 4.1b. **b**, Experimental transmission spectrum obtained for the voltage marked by the vertical dashed line in **a** (green dots), along with a fit of the model of Eq. 4.2 for a single cavity-coupled exciton resonance. **c**, Cavity length sweep with the cavity positioned at the etch site pair P_2, resulting in additional cavity-coupled excitonic resonances originating from the etch site domains. **d**, Same as **b**, but with a model fit for three cavity-coupled exciton resonances of different energies and coupling strengths. All data in the figure are normalized to the maximum transmission measured in the respective cavity length sweep.

strengths from cavity-based measurements via a dissipative model for the cavity transmission. The starting point is the time-independent Hamiltonian of the system as introduced in Section 2.4, which describes excitons of different energies E_i localized to non-overlapping areas of the device labeled i as individual quantum wells coupled to a single cavity mode, each with a light-matter coupling strength g_i,

$$H = E_C a^\dagger a + \sum_i E_i b_i^\dagger b_i + \hbar g_i (b_i^\dagger a + a^\dagger b_i). \tag{4.1}$$

In this expression, b_i is the bosonic annihilation operator of excitons in area i, while a is the bosonic annihilation operator for cavity photons at energy E_C. Combining Eq. (4.1) with the dissipative input-output formalism of Refs. [72, 363], we find the cavity transmission at energy E

$$T(E) = \eta\kappa_m \left| \mathrm{i}(E_C - E) + \hbar\kappa/2 + \sum_i \frac{(\hbar g_i)^2}{\mathrm{i}(E_i - E) + \hbar\Gamma_i/2} \right|^{-2}, \tag{4.2}$$

in which κ and Γ_i are the cavity and exciton FWHM linewidths, respectively and η is a proportionality constant. $\kappa_m = \kappa_{m,in}\kappa_{m,out}$ is the product of decay rates through the in- and outcoupling mirror, $\kappa_{m,in}$ and $\kappa_{m,out}$, respectively.

In the experiment, we measure cavity transmission as a function of cavity length as described above and in Section 3.3, with a typical result shown in Fig. 4.2a for the cavity mode positioned on the fully encapsulated TMD area. All spectra are background-corrected for a constant CCD offset and normalized with respect to the maximum measured transmission for a given length sweep. From transmission measurements of the empty cavity (covering only two hBN layers), we found that κ varied by about 20% in the investigated spectral range, a result of wavelength-dependent mirror reflectivity. To account for this effect, we normalized the measured transmission spectra $T_{meas}(E)$ by the values $\kappa_{m,meas}(E)$ measured for the empty cavity, which we found to improve the results of the fit procedure described in the following. We note that while the cavity linewidth in experimental spectra is broadened by residual cryostat vibrations, the light-matter coupling dynamics are dominated by the Lorentzian contribution κ to the cavity linewidth as the frequency of the mechanical vibrations was orders of magnitude slower than the energy exchange rate between the cavity and excitons. Vibration broadening is therefore negligible when extracting exciton energies and light-matter coupling strengths from the model of Eq. (4.2).

To determine E_i and g_i, we fit Eq. (4.2) to normalized transmission spectra at different cavity lengths. Data and a representative fit result are shown in Fig. 4.2b by green dots and the black line, respectively. The fit yields good agreement between model and data, also in the case of multiple exciton domains coupled to the cavity, for which representative data and fit results are shown in Fig. 4.2c and d, respectively.

For each excitonic resonance i (identified by the presence of corresponding polariton branches), we compute mean values $\bar{E}_i$, $\bar{g}_i$ and standard error δE_i, δg_i from fit results for E_i and g_i obtained at different cavity lengths. $\bar{E}_i \pm \delta E_i$ and $\bar{g}_i \pm \delta g_i$ constitute our measurement results and uncertainty. To obtain good fit quality, we ensured that the fit results obtained for individual cavity lengths complied with three criteria: First, the fit results for the cavity energy should be a linear function of cavity length. Fits for which the obtained cavity energy deviated strongly from this linear dependence were discarded in the analysis. Second, only fits in which the cavity energy was in or near resonance with the exciton energy were used, a condition which we found to minimize the errors in the fit parameters of interest. Third, fits whose cost functions deviated largely from those obtained for similar cavity lengths were discarded. In the fits, all parameters in Eq. (4.2) were kept free, except for exciton energies associated with polariton branches subject to strong incoherent broadening, relevant only to a small number of spectra investigated. Fit results for different cavity lengths were used to compute $\bar{E}_i \pm \delta E_i$ and $\bar{g}_i \pm \delta g_i$, with the precise number of spectra available for analysis determined by the signal to noise ratio in the respective polariton branches.

Due to an ellipticity in the fiber mirror profile, the cavity exhibits non-degenerate higher

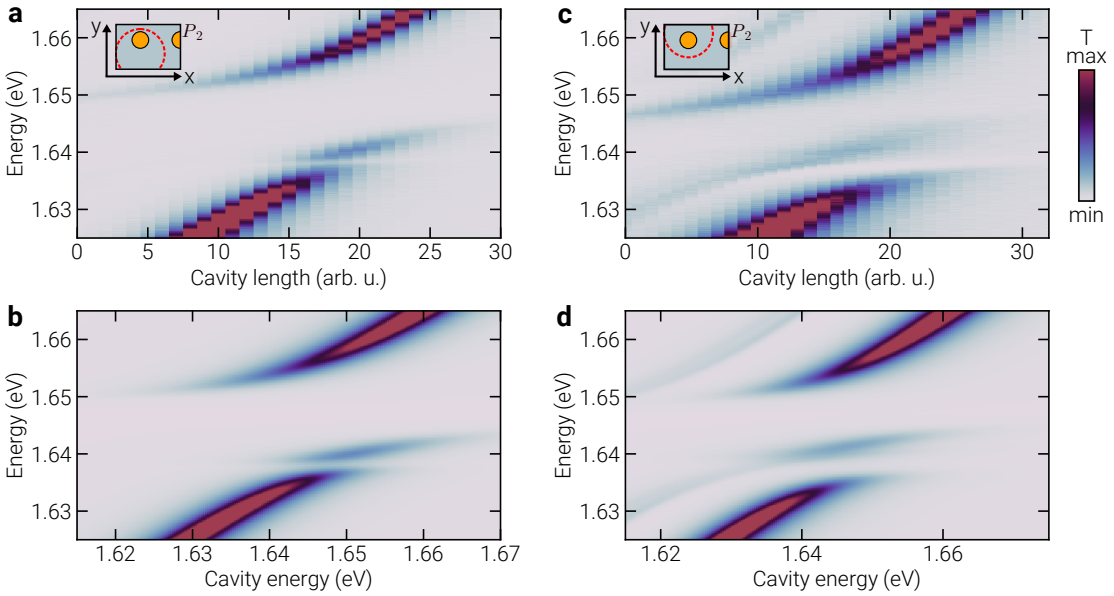

Figure 4.3.: Higher transverse order cavity modes. **a**, Measured cavity transmission for a sweep of the cavity length. The position of the cavity mode with respect to the exciton domain pair P_2 is illustrated in the inset. Excitons in the left domain and the encapsulated monolayer couple to the cavity, resulting in three polariton branches. **b**, Plot of theoretical cavity transmission (Eq. 4.2), with parameters obtained from a fit to the data in in **a**. **c**, Same as in **a**, with a different cavity mode position as illustrated in the inset. Higher transverse order cavity modes contribute additional cavity resonances to the spectra. **d**, Plot of theoretical cavity transmission, with the model of Eq. 4.2 extended to the case of three cavity modes coupling to the excitonic resonances. The model parameters were adjusted to yield agreement with the data in **c**.

order Hermite-Gaussian modes [322] as introduced in Section 3.1, which contribute to the measured transmission spectra. We found this contribution to depend on the position of the cavity mode relative to the etch sites, a finding we illustrate in Fig. 4.3. If the center of the cavity mode was placed near the bottom of the etch site center (coordinate system defined in the inset of Fig. 4.3a), the transmission spectra were typically dominated by a single cavity resonance associated with the fundamental Gaussian cavity mode, as illustrated by the data shown in Fig. 4.3a. Results of the theoretical model of Eq. (4.2), plotted in Fig. 4.3b, yield excellent agreement with the data.

If the cavity mode was moved close to the etch site center, with representative data shown in Fig. 4.3c, higher order modes contributed cavity resonances to the measured spectra, blueshifted with respect to the fundamental mode. To support this assignment, we extend the model of Eq. (4.2) to describe exciton-coupling to three different cavity modes. The result is shown in Fig. 4.3d and agrees well with the measurement result.

The contribution of the higher order modes to the measured spectra persisted as the cavity mode was moved towards the top of the etch site center. This asymmetry, which was

also observed for the etch site pairs P1 and P3, is likely a result of asymmetric transversal mode profiles caused by a tilted cavity fiber. For several positions close to the etch site centers, the higher order modes were resonant with the middle polariton branches, adding uncertainty to the fit procedure described above. To determine exciton coupling strengths and resonance energies, we therefore restricted our measurements to cavity mode positions with negligible higher order mode contributions.

4.4. Mesoscopic domains of excitons and polaritons

We investigate the properties of dielectrically engineered exciton domains by performing spatially resolved measurements of exciton energy and light-matter coupling strength, enabled by the tunability of our open cavity system. The top panel in Fig. 4.4a shows a raster-scan map of cavity transmission for the etch site pair P_2, obtained at a fixed cavity energy spectrally detuned from any exciton resonance. At this energy, the etch site induces mainly photonic scattering loss to the cavity mode, resulting in the observed decrease in cavity transmission.

Positioning the cavity mode along the dashed line in the transmission map of Fig. 4.4a, we recorded cavity transmission spectra similar to the ones shown in Fig. 4.2a and c for varying cavity-exciton detuning. Using the analysis procedure described in Section 4.3, we determined resonance energy E_i and light-matter coupling strength g_i of all exciton resonances i which contributed polariton branches to the transmission spectra. The results for E_i and g_i are shown in the middle and bottom panels of Fig. 4.4a, respectively. Results for E and g at each position were labeled according to the corresponding exciton resonances X, L and R.

As the cavity is placed at the left side of the etch site ($x = 0$ μm, left side in Fig. 4.4a), only X-excitons in the TMD area fully encapsulated with hBN couple to the cavity with light-matter coupling strength $g_X = 9.7$ meV. Their resonance energy experiences a blueshift as the cavity mode is moved towards the etch site centers, which likely originates from local strain [364] induced during fabrication.

As expected, we find two exciton domains defined by the through-holes in the hBN encapsulation layer, giving rise to resonances L and R with maximum values of light-matter coupling strength at the respective etch site centers. The maximum coupling strength $g_{L/R}$ for these domains is expected to scale as $g_{L/R} \propto \sqrt{\eta_A}$ [65, 365] with η_A the overlap between exciton domain and cavity mode. Using the domain area A_S and the $1/e^2$ area of the transverse cavity field A_C, we estimate $\max(g_L)\sqrt{A_S/A_C} = 2.91$ meV, close to the maximum measured value $g_L = 2.65 \pm 0.04$ meV in Fig. 4.4b. The difference in energy and coupling strengths between the L and R domains reflect typical inhomogeneities in TMD-based van der Waals heterostructures. Repeating measurements and analysis for the etch site pair P_3,

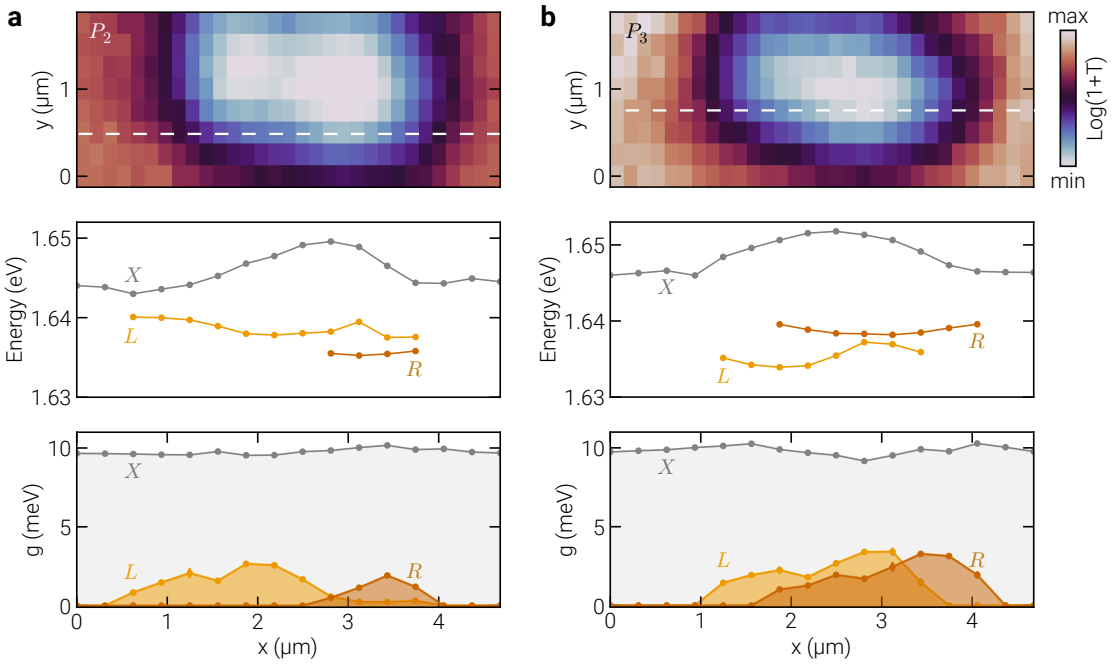

Figure 4.4.: Cavity-coupled mesoscopic exciton domains. a, Top panel: Cavity transmission map at fixed cavity energy (E_C = 1.612 eV) of the etch site pair P_2. Axes of the coordinate system are the same as in Fig. 4.1b. Middle panel: Exciton resonance energies along the white dashed line in the top panel, identified from cavity length sweeps and originating from X, L and R domains as defined in Fig. 4.1b. Bottom panel: Exciton light-matter coupling strengths g for the resonances identified in the middle panel. At positions where polariton branches associated with the individual resonances were absent in the transmission spectra, no data points are shown for the energies, and the values of g have been set to zero. **b**, Same as **a** but for the etch site pair P_3. The cavity transmission map was obtained at E_C = 1.666 eV.

with data shown in Fig. 4.4c, yields similar results as for P_2. Again, we find different excitonic domains L and R defined by the air-holes, whose coupling strength maxima are observed at smaller distance than for P_2 due to the reduced etch site distance.

Our observation of redshifted exciton resonances at reduced dielectric screening is in agreement with recent results on dielectrically screened TMD excitons [70, 112]. Notably, it contrasts the case of graphene-encapsulated TMD monolayers [68], for which the exciton energy is known to blueshift at reduced dielectric screening, an effect which has been linked to the difference in dielectric response of graphene and hBN [112]. For the sake of completeness, we note that at several etch sites, we observed spectrally broad exciton resonances, near-resonant or blueshifted compared to the energy X excitons, which coupled weakly to the cavity and are irrelevant to the measurements presented in the following. A possible origin for this complex exciton energy landscape is inhomogeneous strain in the device.

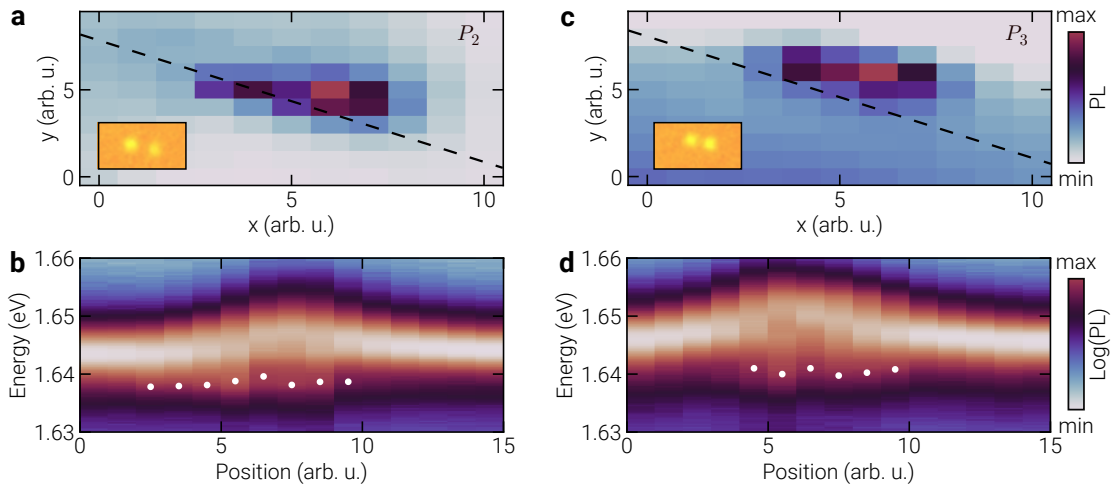

Figure 4.5.: Exciton domains in confocal photoluminescence spectroscopy. a, Raster-scan map of etch site pair P_2 in cryogenic confocal PL, integrated in the spectral range 1.61 to 1.72 eV. The inset shows a microscope image of the investigated device area. **b**, Spectrally resolved PL-line cut along the dashed line in **a**. The white dots are energetic positions of a redshifted shoulder, obtained from the fit of double Gaussian profiles to the PL spectra at each position. **c**, **d**, Same as **a** and **b**, respectively, but for the etch site pair P_3.

The exciton resonance energies obtained from measurements of cavity transmission are consistent with the results of confocal cryogenic photoluminescence (PL) spectroscopy, performed with the device mounted in backscattering geometry inside a closed-cycle cryostat held at 4.3 K (see Section 3.4 for details). A raster-scan map of integrated PL for the etch site area P_2 is shown in Fig. 4.5a, obtained for a CW pump laser wavelength of 675 nm and with a spatial resolution in the transverse direction of approx. 1 μm. In Fig. 4.5b, we plot a spectrally resolved PL line cut across the etch site pair, measured along the dashed line in Fig. 4.5a, at similar positions to the cavity-based measurements of exciton energy and light-matter coupling strength shown in Fig. 4.4a. The PL spectra are dominated by the resonance of X excitons in the encapsulated monolayer region at maximum intensity, which exhibits a pronounced blueshift at the etch site position, consistent with data obtained from cavity transmission spectroscopy shown in Fig. 4.4a and likely a result of strain as explained above. Excitons localized to the through-hole domains give rise to a redshifted shoulder, with energetic positions indicated by white dots. While inhomogeneous broadening at the investigated positions prevents a precise extraction of exciton energies from PL data, the spectral shoulder arising as a consequence of dielectric domain engineering is in qualitative agreement with resonance energies obtained from cavity-based measurements shown in Fig. 4.4. Similar results are obtained for the etch site area P_3, as shown in Fig. 4.5c and d, with the line cut in Fig. 4.5c performed at a position similar to the one in Fig. 4.4b.

4.5. Local modulation of polariton energies

Cavity-coupling of dielectrically defined exciton domains results in local shifts of the polariton energy, which we map out by spatial and spectral cavity tuning with data shown in Fig. 4.6. Displacing the cavity laterally at a constant cavity length with cavity energy 1.647 eV across one domain of the pair P_1, the cavity transmission in Fig. 4.6a maps out the evolution of the upper and lower polariton energies, with an energetic minimum of the lower polariton at the center of the etch site. We emphasize that this redshift of ~ 2 meV is expected to directly translate to an attractive polariton potential well for the disk-confined lower polaritons, if our device is coupled to a two-dimensional cavity [366]. The Gaussian cavity mode of our fiber cavity prevents the formation of localized polariton states at the etch site. The superimposed near-linear blueshift, also evidenced in the upper polariton branch, stems from the unintentional spatial inhomogeneity of the exciton energy E_X around this site.

The effect of the nanostructured dielectric environment on the polariton energy is even more pronounced for the pair P_2 with transmission data in Fig. 4.6b. Upon spatial displacement across the left and right disk of the pair for a constant cavity energy of 1.661 eV, we observe in the left panel of Fig. 4.6b two local energy minima for both the upper and lower polariton branches, each one originating from excitons localized to a single etch site. The difference in energy at the left and right disk is related to the aforementioned unintentional disk imperfections. Surprisingly, for a reduced cavity energy of 1.640 eV, the energy shift of the upper polariton at the etch sites changes its sign, as evidenced in the right panel of Fig. 4.6b. The dependence of the upper and lower polariton energies on the cavity energy is illustrated for five discrete values in Fig. 4.6c.

To systematically investigate the local polariton energy shifts induced by our nanofabrication technique, we normalized the cavity transmission spectra in Fig. 4.6 at each position to the maximum transmission of the lower polariton branch. The polariton energies were determined as the energies of maximum cavity transmission of lower and upper polariton branch for each position. Polariton energies were fit with the double Gaussian profile

$$E(x) = c - a_{\mathrm{L}} \exp(-(x - x_{\mathrm{L}})^2 / s_{\mathrm{L}}^2) - a_{\mathrm{R}} \exp(-(x - x_{\mathrm{R}})^2 / s_{\mathrm{R}}^2), \tag{4.3}$$

where the fit results for a_{L} and a_{R} are the energy shifts at the left and right etch site, respectively. For the single etch site in Fig. 4.6a, we modified Eq. (4.3) to describe a single Gaussian well with the offset c a linear function of position. The cavity energy E_C was determined from a fit of the dissipative model of Eq. (4.2) at a position away from any etch site (e.g. $x = 0$ μm). The result of this analysis is the dependence of polariton energy shift on cavity energy shown in Fig. 4.6d and e, in agreement with polariton energies shown in Fig. 4.6c.

The dependence of the upper polariton energy shift on the cavity resonance condition, and its surprising sign reversal, can be understood by noting that the dominant exciton contribution to the upper polariton branch arises from X excitons in the encapsulated

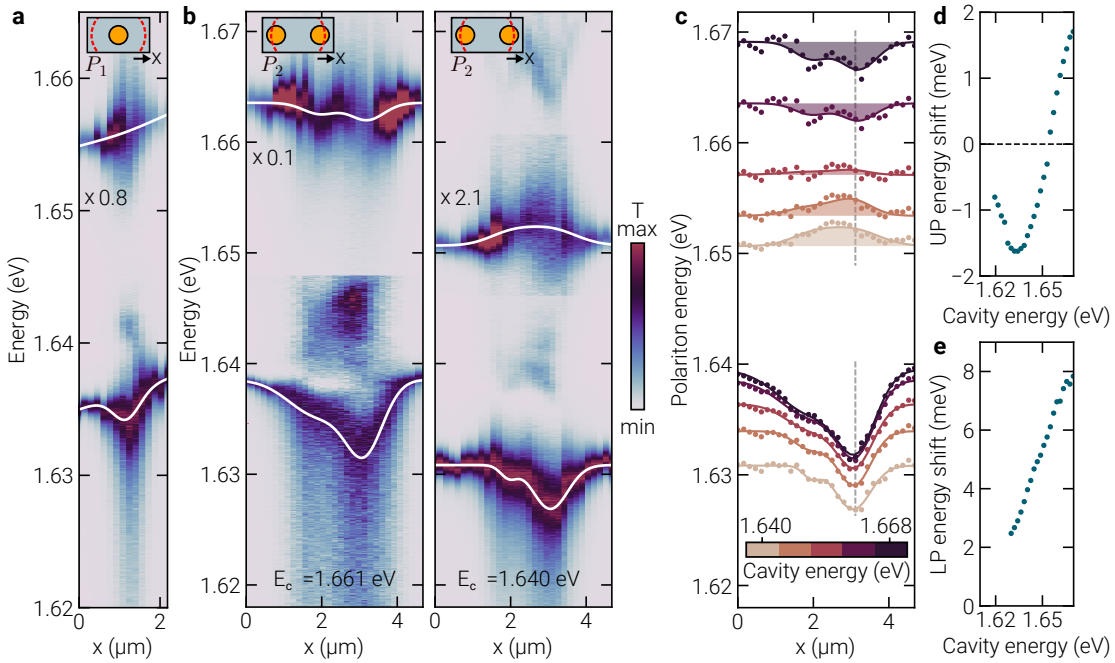

Figure 4.6.: Dielectrically engineered polariton disks with cavity-controlled energy shifts. a, Cavity transmission for a fixed cavity energy of 1.647 eV and lateral cavity translation across the right exciton domain of pair P_1, as illustrated in the inset. The white solid lines show best fits of polynomial and Gaussian profiles to maximum transmission of the upper and lower polariton branches, respectively. **b**, Same but for the domain pair P_2, recorded at cavity energies of 1.661 and 1.640 eV in the left and right panel, respectively. The spectra at each position were normalized to the maximum transmission of the lower polariton branch and rescaled for the upper polariton branch by a factor of 0.8, 0.1 and 2.1 as indicated in the respective sub-panels. **c**, Energy profiles of the lower and upper polaritons (corresponding to the transmission maxima in **b**) as a function of the lateral cavity displacement for five cavity energies indicated by the color-bar. The solid lines show best fits of two Gaussians for both the upper and lower polariton energy profiles at different cavity energies. **d**, **e**, Local energy shift of upper and lower polariton as a function of the cavity energy for the right polariton disk of P_2 at position $x \approx 3\mu$m.

monolayer. Local removal of the encapsulation modifies relevant exciton properties, giving rise to two competing effects on polariton formation. On the one hand, the light-matter coupling strength of this exciton transition is expected to be reduced at the etch site position due to reduced overlap between cavity mode and X area, resulting in a local decrease in Rabi splitting and hence polariton energy. On the other hand, the pronounced blueshift of the X resonance observed at the etch site in Figs. 4.4 and 4.5 as a result of unintentional strain directly translates to a local increase in polariton energy. The interplay of both effects leads to the observed dependence in Fig. 4.6d. The difference in the energy shift between the left and right domain in Fig. 4.6b therefore reflects differences in the effective dielectric

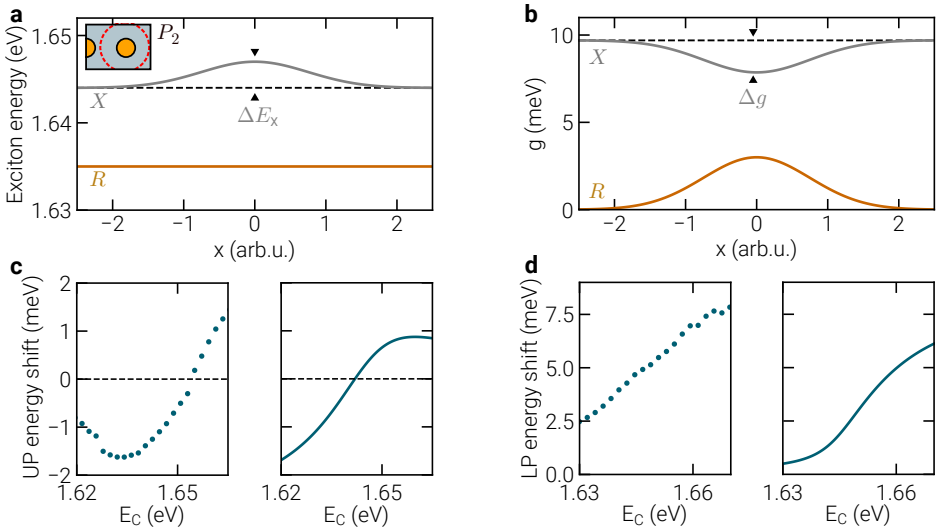

Figure 4.7.: Model for local polariton energy modulation. a, b, Exciton energy and light-matter coupling strength, respectively, used to model the polariton energies for the right exciton domain of P_2 illustrated in the inset. X and R excitons stem from the encapsulated monolayer and right etch site domain, respectively. **c, d**, Upper and lower polariton energy shift, respectively, for the exciton domain R of P_2 as obtained from experiment (left panel) and model calculations (right panel).

environment and strain between nominally identical upper polariton disks.

To develop a more quantitative understanding for the polariton states in our system, we compute energy shifts for the right etch site of P_2 as shown schematically in the inset of Fig. 4.7a. Energy and light-matter coupling strength of the relevant exciton resonances are shown in Fig. 4.7a and b, respectively. Their spatial dependence, based on the data shown in Fig. 4.4a, is approximated by Gaussian profiles with the etch site center positioned at $x = 0$ for illustration purposes. The maximum local blueshift in X exciton energy, $\Delta E_X = 3$ meV, is close to the one obtained from the data in Fig. 4.4a. The value of local reduction in light-matter coupling strength, $\Delta g = 2$ meV, is expected from a computation of the mode overlap η_A between cavity mode and etch site area, accounting for the Gaussian cavity mode profile (see the discussion in Section 4.4 for details). While such a reduction is not observed in Fig. 4.4a, the use of this value for Δg in the calculation is justified: in contrast to the measurements presented in Fig. 4.4a, all measurements of polariton energy shifts were carried out near the etch site centers, where the maximum value $\Delta g = 2$ meV is expected.

From the exciton energies and light-matter coupling strengths shown in Fig. 4.7a and b, we calculate the upper polariton energy $E_{\mathrm{UP}}(x)$ as a function of cavity energy from the eigenstates of Eq. (4.1), with two cavity-coupled exciton resonances X and R. The energy shift induced by the etch site domain is given by $E_{\mathrm{UP}}(x = \infty) - E_{\mathrm{UP}}(x = 0)$. The result of this calculation, shown in the right panel of Fig. 4.7c, is in reasonable agreement with the

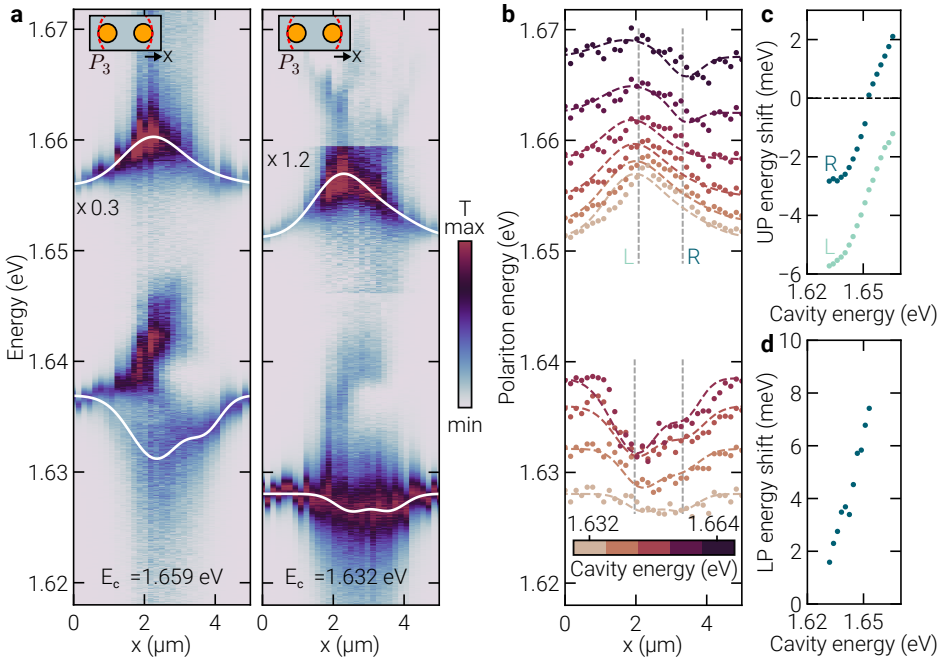

Figure 4.8.: Dielectrically engineered polariton disks for P_3. a, Cavity transmission for lateral cavity translation across the exciton domain pair P_3, obtained in similar fashion to the data shown in Fig. 4.6a and b. The white solid lines show best fits of double Gaussian profiles to maximum transmission of the upper and lower polariton branches, respectively. **b**, Energy profiles of the lower and upper polaritons as a function of the lateral cavity displacement for different cavity energies as indicated by the color-bar, along with best fits of two Gaussians (solid lines). **c**, **d**, Local upper and lower polariton energy shift as a function of the cavity energy for the polariton disks as labeled in **b**.

data obtained for P_2, reproduced in the left panel. The deviation between data and model prediction observed for $E_C < 1.63$ eV could stem from a slightly reduced value of ΔE_X at the investigated cavity mode position. Adjusting the model parameters in our analysis reveals that sign and magnitude of the upper polariton energy shift at a given cavity energy sensitively depend on the exact values of ΔE_X and Δg. In the present device, the value of ΔE_X is determined by unintended strain and other inhomogeneities. Consistently, we did not observe a cavity-controlled sign reversal of the upper polariton energy shift in all investigated etch sites, with an example provided by the left exciton domain of pair P_3 as shown in Fig. 4.8b and c.

The dependence of the local lower polariton energy shift on the cavity energy is understood by noting that for large cavity energy, the lowest polariton energy in the system is dictated by the lowest-energy exciton. By virtue of dielectric engineering, the exciton energy at the etch-site center is reduced from its monolayer value in fully hBN-encapsulated regions. Thus, in the limit of large cavity energies, the local energy shift for the lower polariton

corresponds to the energy difference imprinted by different dielectric environments. The monotonous increase of lower polariton energy shift observed in the left panel of Fig. 4.6d is in good agreement with the model results shown in the right panel of Fig. 4.7d, calculated for the lower polariton branch with a similar approach as outlined above. As before, the difference in energy shift between the left and right domains in the pair P_2 arises from differences in the effective dielectric environment and strain between lower polariton disks. For the pair P_3, we also observe lower polariton redshifts in Fig. 4.8b and d, similar in magnitude to the ones obtained for P_2. This behavior is expected from the similarity in redshifted exciton domains between the two pairs evident from Fig. 4.4. These observations manifest local control over the polariton energy in our cavity system as one key result, which as explained above is expected to directly translate to tunable polariton potential wells upon implementation of our approach in a two-dimensional cavity.

4.6. Cavity-mediated exciton hopping

The second key feature of our system is the ability to establish site-to-surrounding and site-to-site coupling in the dispersive cavity regime, mediating an effective long-range hopping. From a theoretical perspective, this interaction follows from the time-independent Hamiltonian for multiple cavity-coupled exciton domains i with light-matter coupling strengths g_i, energies E_i and detunings $\Delta_i = E_i - E_C$ from the cavity energy E_C. Expansion to second order in g_i/Δ_i via a Schrieffer-Wolff transformation [71, 359] yields:

$$\tilde{H} \simeq \left(E_C - \sum_i \frac{g_i^2}{\Delta_i}\right) a^\dagger a + \sum_i \left(E_i + \frac{g_i^2}{\Delta_i}\right) b_i^\dagger b_i + \sum_i \sum_{j\neq i} \frac{g_i g_j}{2\Delta_i} \left(b_i^\dagger b_j + b_j^\dagger b_i\right), \tag{4.4}$$

with the respective bosonic annihilation operators for cavity photons and excitons, a and b_i. The result is a system described by multiple exciton resonances which are weakly dressed by cavity photons. In addition, excitons associated with different resonances i and j are coupled via an effective beam-splitter type coupling of strength $J_{ij} = g_i g_j \left(\Delta_i^{-1} + \Delta_j^{-1}\right)/2$, mediated by dispersive exchange of cavity photons. We note that the resulting effective coupling of strength J_{ij} has been studied for two or multiple individual fermionic two-level systems coupled to the same cavity mode, such as superconducting qubits [359] and defects in diamond [72], and more recently in bosonic quantized motional modes of levitated nanoparticles [361]. These experiments contrast the case of bosonic excitons studied in our work.

The effective coupling between disk-localized excitons and their surrounding monolayer excitons is sizable when the cavity mode is positioned close to the edge of a single etch site. This effect is shown conceptually in Fig. 4.9a: by imbalanced cavity dressing, the difference in the respective energies of the bare excitons (left panel) can be tuned into resonance (central

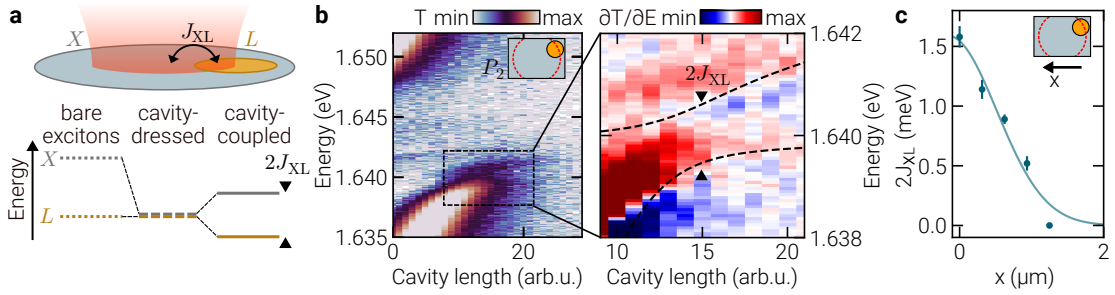

Figure 4.9.: Cavity-mediated long-range exciton hopping. a, Top: Schematic of excitons L and X, coupled via an effective cavity-mediated hopping of strength J_{XL}. Bottom left: exciton energies in the absence of a cavity mode. Bottom center: exciton energies tuned into resonance due to weak cavity-dressing. Bottom right: System eigenstates as observed in experiment, split due to the effective interaction J_{XL}. **b**, Left panel: cavity transmission as a function of cavity length, with the cavity mode positioned at the edge of a single domain L as illustrated in the inset. Right panel: derivative of cavity transmission with respect to energy, computed for data in the dashed rectangle in the left panel. The dashed lines are the eigenstates of the effective system Hamiltonian, Eq. (4.4). **c**, J_{XL} as a function of cavity mode position, which is moved away from the etch site center. $x = 0$ μm corresponds to the mode position illustrated in the inset.

panel), where dispersive coupling induces an effective splitting given by $2J_{XL}$ (right panel). The corresponding experiment on the left disk in pair P_2 shows in Fig. 4.9b the avoided crossing due to dispersive cavity-dressing and coupling, with a maximum coupling strength of $2J_{XL} = 1.5$ meV for optimal conditions.

In the dispersive cavity-coupling regime, the spectral resonances observed in transmission spectra correspond to the eigenstates of the system as given by the Hamiltonian of Eq. (4.4), with the strict requirement for the approximation to hold being $\left|g_i^2/\Delta_i\right|^2 \ll 1$ for each excitonic species. In practice, we verified by numerical analysis that the deviation between the full cavity-coupling model of Eq. (4.1) and the dispersive model are dependent on the precise values of coupling strengths and energies of the individual exciton resonances. For the data shown in Fig. 4.9b, two exciton resonances differing in energy by approximately 3 meV and with values of g_i differing by a factor of approximately 6 coupled to the cavity at a detuning $\Delta_X \approx 15$ meV. For these parameters, we found that deviations between full model and dispersive approximation were well within the typical linewidths observed in the experiments, underlining the validity of the approximation. We note that the regime of dispersive cavity-coupling investigated here could only be accessed at selected positions on the sample. For different positions, broadening and reduced transmission of the polariton branches induced by disorder resulted in reduced signal-to-noise ratio, preventing the extraction of the system's eigenstates at satisfactory experimental confidence.

In Fig. 4.9b, two exciton resonances X and L are coupled via the cavity mode, a setting for which we calculated the eigenstates of the system from the Hamiltonian Eq. (4.4) using

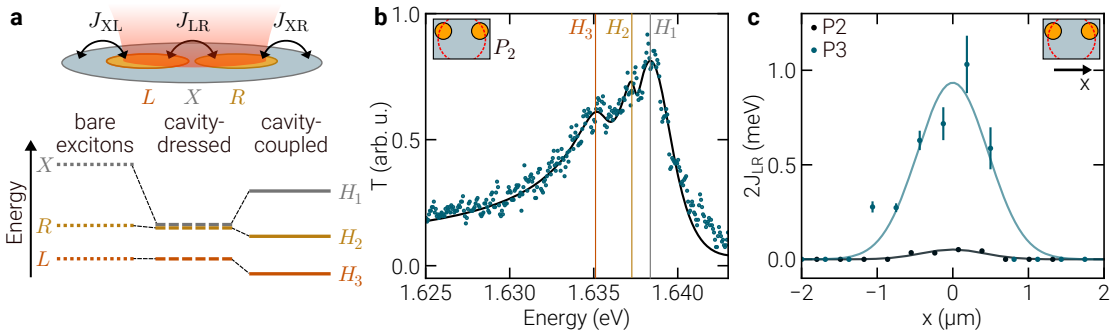

Figure 4.10.: Effective inter-site and site-to-surrounding hopping. a, Interaction J_{LR} between excitons of left and right domain L and R, mediated by the cavity in addition to the respective interactions J_{XL} and J_{XR} with the surrounding exciton reservoir X. **b**, Cavity transmission spectrum (teal data) for a cavity energy of 1.659 eV and mode position as illustrated in the inset with best fit (black solid line) according to the dissipative model analysis. The vertical lines indicate the eigenenergies of the coupled system. **c**, Coupling strength J_{LR} at cavity energy 1.670 eV for the etch site pairs P_2 and P_3 (black and teal data, respectively, with error bars of one standard deviation and Gaussian fits as solid lines) as the cavity is moved across the etch site pair, as obtained from exciton light-matter coupling strengths and resonance energies as shown in Fig. 4.4. $x = 0$ μm corresponds to the cavity mode centered between both sites.

the following set of parameters: $E_X = 1.6436$ eV, $g_X = 9.5$ meV, $E_L = 1.6399$ eV, $g_L = 1.6$ meV. These values are in agreement with the results obtained from fits of Eq. (4.2) to the transmission spectra for different cavity lengths measured at the same cavity mode position: $E_X = 1.64358 \pm 0.00002$ eV, $g_X = 9.577 \pm 0.004$ meV, $E_L = 1.63999 \pm 0.00003$ eV, $g_L = 1.5 \pm 0.1$ meV. From the same fits, we obtained the cavity energy as a function of piezoelectric actuator voltage used in the theoretical computation. The resulting eigenenergies are shown by the black dashed lines in the right panel of Fig. 4.9b, in agreement with experimental resonances. Unavoidably, the coupling of strength J_{XL} as obtained from cavity transmission spectra vanishes as the cavity is moved away from the etch-site, as confirmed in Fig. 4.9c.

Finally, we demonstrate effective long-range coupling mediated by the cavity between excitons of two distant sites, as shown conceptually in Fig. 4.10a: we use cavity-dressing to tune the surrounding excitons X and the right disk R into resonance while leaving the exciton energy in the left disk L mainly unaffected. With dispersive coupling, we obtain hybrid eigenstates H_1, H_2 and H_3 of the coupled system, with energies defined by effective interactions J_{XL}, J_{XR} and J_{LR} among all three constituents. The corresponding spectral signature is shown in Fig. 4.10b, for a maximal intersite coupling strength $2J_{LR}$ of ~ 0.1 meV for the sites of pair P_2. In the framework of dispersive cavity-coupling, these exciton resonance energies differ from the bare eigenstates of the system as a direct result of the cavity-induced interaction. Spatial cavity-imbalance results in the reduction of such coupling, as confirmed

in Fig. 4.10c for P_2, as well as for P_3 with more closely spaced sites and thus a factor of ten stronger coupling $J_{LR} \simeq 1$ meV for a cavity energy of 1.670 eV.

4.7. Summary and outlook

To conclude, we have implemented a fabrication method for deterministic dielectric engineering of mesoscopic exciton domains in a two-dimensional semiconductor, with resonance energy redshifted by up to 10 meV from excitons in the surrounding semiconductor area. Employing a fiber-based microcavity system, we demonstrated cavity control of exciton domains and their effective long-range coupling. These results, obtained in the dispersive cavity-coupling regime which has scarcely been explored in the domain of quantum well polaritons, highlight a promising approach to quantum simulations in exciton-based lattices and circuits. Upon strong hybridization between excitons and cavity photons, our engineered exciton domains directly translate to polariton energy shifts, with magnitudes on the order of several meV tunable via the energy of the cavity resonance.

We anticipate the locally controlled polariton energy shifts obtained in the Gaussian mode of our cavity to directly translate to potential wells in a two-dimensional cavity geometry. This could be implemented by combining the present device with a recently demonstrated micro-mechanical assembly technique [366]. Our approach to dielectric engineering is based on a scalable fabrication method, which we expect to readily allow for implementations of potential well arrays with flexible geometries, a premise for polariton-based quantum simulation [210, 211]. As an initial demonstration of this concept, we recently employed our technique in the controlled fabrication of gold nanodisks arranged to form a lattice, giving rise to collective plasmonic resonances which coherently coupled to TMD excitons [P4]. In the present device, unintended variations in the polariton energy landscape arise from local disorder such as strain, which can be eliminated with more dedicated fabrication. Alternatively, the energy variations associated with local strain could serve as a parameter to tailor polariton potentials in addition to dielectric environmental engineering or active gate control with nanostructured electrodes [37, 38]. Combined with cavity-coupling to Rydberg excitons [205] or hybrid moiré excitons [109, 367] with enhanced nonlinearities, our technique could serve as a building block for advanced polaritonic devices.

Microcavity-coupling of fluorescent carbon nanotube quantum defects

5

In this chapter, we report on cavity-coupling of fluorescent carbon nanotube quantum defects with photon emission at room-temperature and telecom wavelengths. Operating our system in the regime of incoherent good cavity-coupling, enabled by spectrally narrow linewidth of the fiber-based microcavity and large emitter dephasing, we demonstrate telecom-band single photon emission, with cavity-enhancement of the emission spectral density compared to spectral or temporal filtering. We find experimental signatures of two-photon interference in Hong-Ou-Mandel type experiments performed in an imbalanced Mach-Zehnder interferometer, which result from spectral purification upon coupling to the cavity at narrow spectral bandwidth. In our system, the photon indistinguishability as quantified by the two-photon interference visibility is increased by more than two orders of magnitude compared to the expected free-space limit. A model for time-dependent coupling between cavity and quantum defect, accounting for the presence of optically dark exciton states, yields qualitative agreement with the experimental observations. The results highlight a promising strategy to attain optimized non-classical light sources.

The experiments presented in this chapter were performed in close collaboration with Julian Trapp, who also reports on some of the results in his Master's thesis [323]. Johannes Scherzer contributed to the operation of the cavity setup. The synthesis of aryl-functionalized carbon nanotubes was performed in the group of YuHuang Wang at the university of Maryland.

THIS CHAPTER IS BASED ON THE PUBLICATION [P2]:

Husel, L.*, Trapp, J.*, Scherzer, J., Wu, X., Wang, P., Fortner, J., Nutz, M., Hümmer, T., Polovnikov, B., Förg, M., Hunger, D., Wang, Y., and Högele, A.: "Cavity-enhanced photon indistinguishability at room temperature and telecom wavelengths."; *equal contribution
Nature Communications **15**, 3989 (2024)

Parts of this publication are reproduced verbatim in the following, the figures from the publication have been adapted and extended.

5.1. Introduction: Indistinguishable single photons in the regime of incoherent good cavity-coupling

The capability of two indistinguishable single photons to interfere on a balanced beam splitter and exit jointly on either one of its output ports is a premise to quantum photonic applications [257] such as quantum teleportation [368], quantum computation [10] or quantum optical metrology [369]. Solid-state based sources of indistinguishable single photons have witnessed tremendous progress in the past decades [243], and among them semiconductor quantum dots stand out as they enable the generation of pure and indistinguishable single photons [370, 371] when coupled to optical microcavities [281, 311, 312]. However, their operation is so far restricted to cryogenic temperatures and wavelengths in the near-infrared. These limitations motivate alternative platforms operating at ambient conditions and telecom wavelengths to facilitate long-distance quantum communication in optical fibers at reduced loss. Various quantum emitters have proven capable of emitting pure telecom-band single photons at room-temperature, including color centers in silicon carbide [229] and gallium nitride [372]. Recently, the realm of such emitters has been expanded by luminescent nanotube defects (NTDs) in sp^3-functionalized single-wall carbon nanotubes [31], described in detail in Section 2.2. Unlike other emitters, NTDs allow for precise control over the emission wavelength via covalent side-wall chemistry [73, 143, 373]. Moreover, carbon nanotubes are straightforward to integrate with gated structures [374], microcavities [62–64, 276, 375] or plasmonic cavities [147]. These properties, combined with high single photon purity [73, 147], render NTDs excellent candidates for the development of sources of quantum light.

As common to solid-state quantum emitters, NTDs are subject to strong dephasing at room-temperature. As a result, the coherence time T_2 of the emitted photons is orders of magnitude smaller than the population lifetime T_1. The respective photon indistinguishability, which can be quantified by $T_2/(2T_1)$ [252, 376] as derived in Section 2.5, is therefore limited to vanishingly small values. This limitation represents a major challenge in the development of single photon sources based on NTDs and other solid-state quantum emitters. The strategy of reducing T_1 to enhance the photon indistinguishability via Purcell enhancement [370], has been successfully applied to quantum dots and Erbium ions in various cavity geometries [240, 281, 310–312, 377, 378] as well as to NTDs by coupling to a plasmonic nanocavity [147]. However, all these experiments were operated in the regimes of coherent or incoherent bad cavity-coupling [289], where strong dephasing at ambient conditions limits both photon coherence time and Purcell enhancement, and thus all experiments to date crucially relied on operation at cryogenic temperatures with reduced dephasing. Although at ambient conditions spectral or temporal filtering of mainly incoherent photons would increase the photon coherence in principle, it would come at the cost of drastically

reduced collection efficiency. Therefore, enhancement of T_2 at efficiencies exceeding those attainable through spectral or temporal filtering has remained elusive for quantum emitters subject to strong dephasing.

In this chapter, we demonstrate enhancement of photon indistinguishability for telecom-band single photons from individual NTDs coupled to an optical microcavity. Motivated by a recent theoretical proposal, we operate the NTD-cavity system in the regime of incoherent good cavity-coupling [45], where the photon coherence time is determined by the cavity linewidth. By choosing a cavity with a spectrally narrow linewidth, we enhance T_2 and thus the photon indistinguishability of the coupled NTD-cavity system. At the same time, the cavity enhances the emission spectral density, thus yielding simultaneous increase of both indistinguishability and efficiency unattainable by spectral or temporal filtering. As a consequence, the efficiency of our system outperforms spectral or temporal filtering within the same bandwidth by at least a factor of four with an estimated increase of photon indistinguishability by two orders of magnitude as compared to free-space NTDs. Our results experimentally establish the regime of incoherent good cavity-coupling as a powerful strategy for optimized sources of quantum light.

5.2. Experimental concept and implementation

Our experiment, shown schematically in Fig. 5.1a, is based on room-temperature NTDs with telecom-band emission wavelengths, coupled to the fundamental mode of a high finesse fiber-based Fabry-Pérot cavity [56]. In this setting, cavity-coupling strongly modifies the photonic spectral bandwidth, which is illustrated in Fig. 5.1b. At ambient conditions, the spectral width of the NTD emission profile is dominated by pure dephasing at rate γ^*, with $\Gamma = 2\gamma^*$ on the order of ten nanometers or 10 meV. This is orders of magnitude larger than the experimental cavity linewidth κ, with a value of approximately 60 pm in the wavelength domain. The small value of κ enables operation of our system in the regime of incoherent good cavity-coupling, where $2g \ll \gamma + \gamma^* + \kappa$ and $\kappa < \gamma + \gamma^*$ holds for the light-matter coupling strength g, the population decay rate γ, κ and γ^* (see Section 2.5 for details). In this regime, the cavity is incoherently pumped upon initial (incoherent) excitation of the NTD at a rate $R \approx 4g^2/\gamma^*$ [45], which in our system is smaller than the population decay rate. Any photon that is coupled into the resonator will be emitted via the cavity mode on a timescale $1/\kappa$. Since the emission process from the cavity is coherent [45], this constitutes a giant increase in the photon coherence time compared to the free-space limit of $1/\gamma^*$. In the spectral domain, the effect corresponds to a drastic spectral purification as illustrated in Fig. 5.1b, similar to spectral filtering. This effect is a key feature of the incoherent good cavity-coupling regime and is instrumental for enhanced photon indistinguishability.

In addition to the coherence time, the cavity also enhances the emission spectral density,

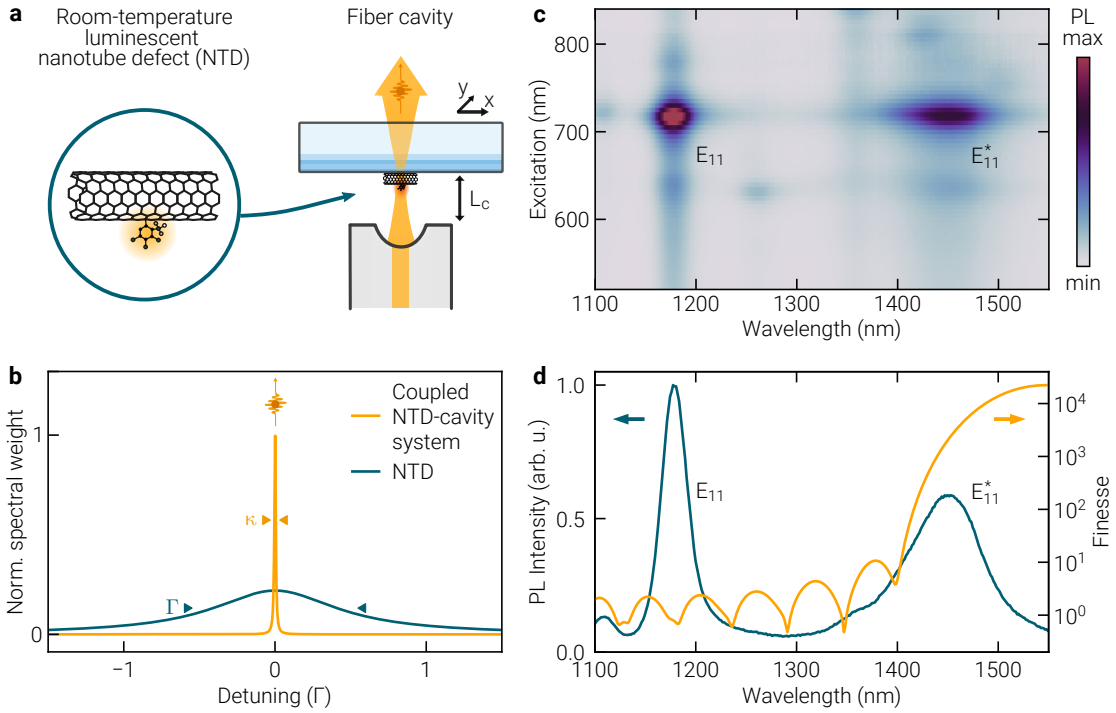

Figure 5.1.: Functionalized carbon nanotubes in an open micro-cavity. a, Schematic of luminescent nanotube defects (NTDs) coupled to the fiber-based open micro-cavity system with tunable cavity length L_c and lateral displacement degrees of freedom of the macroscopic mirror x and y. **b**, Schematic spectral weight of strongly dephased free-space NTD luminescence (teal) subjected to incoherent cavity-coupling (orange). **c**, Photoluminescence (PL) excitation of functionalized (8,6) carbon nanotubes with emission band of fundamental excitons (E_{11}) and NTD states (E_{11}^*). **d**, Ensemble PL spectrum (teal) and cavity finesse in transfer-matrix simulations (orange). The NTD luminescence spectrally close to maximal cavity finesse was excited at the E_{11} transition at near-unity transmission of the cavity mirrors.

with the enhancement quantified by the ideal Purcell factor $F_{\mathrm{p,ideal}} \propto g^2$ [308] as defined in Eq. (2.51) in Section 2.5. Increasing $F_{\mathrm{p,ideal}}$ via the light-matter coupling strength g increases the single photon efficiency, i.e. the probability that a photon is emitted into the cavity mode. In the incoherent good cavity regime, this probability is smaller than the free-space quantum yield due to the large mismatch in the spectral bandwidths of the emitter and the cavity. However, as we demonstrate in the following, maximizing g (achieved in our case by minimizing the microcavity mode volume) results in an efficiency which by far exceeds that obtained by filtering at a spectral bandwidth κ or an equivalent temporal bandwidth.

The NTDs used in this work, shown schematically in the left panel of Fig. 5.1a, were obtained by functionalizing (8,6) carbon nanotubes by diazonium reaction [27, 35], with the synthesis performed in the group of YuHuang Wang at the University of Maryland. Briefly, raw HiPco SWCNT material (NoPo Nanotechnologies, India) was dissolved in chloro-

sulfonic acid (99%, Sigma-Aldrich) at a concentration of 0.5 mg/mL, followed by adding 2-amino-4,5,6-trifluorobenezen-1-sulfonyl chloride, which was synthesized from 3,4,5-trifluoeoaniline, and NaNO2 (ReagentPlus® > 99.0%, Sigma-Aldrich) to concentrations of 0.24 mg/mL and 0.2 mg/mL, respectively. After fully mixed, the acid mixture was then added drop-by-drop to Nanopure water with vigorous stirring, resulting in the formation of NTD functionalized carbon nanotubes that precipitated from the solution as black precipitates. The precipitates were filtered and rinsed with an excessive amount of Nanopure water. The synthesized NTDs were dissolved in 2% (wt/v) sodium deoxycholate (DOC, Sigma-Aldrich, ≥ 97%) solution and centrifuged at 16400 rpm for 1 h to remove any bundles. The nanotubes with NTDs were then sorted by aqueous two-phase extraction [27, 379] in a solution of 2% (w/v) DOC in deuterium oxide (D2O, Cambridge Isotope Laboratories, Inc. 99.8%) to obtain NTDs on (8,6) chirality enriched nanotubes.

The photoluminescence (PL) excitation map of an aqueous suspension with covalently functionalized carbon nanotubes is shown in Fig. 5.1c, with an excitation resonance at 718 nm corresponding to the E_{22} transition and emission via E_{11} around 1170 nm, characteristic of (8,6) chiral tubes [380]. The red-shifted emission peak, labeled as E_{11}^* and centered at 1470 nm, corresponds to the luminescence from excitons localized at nanotube side-wall defects with emission wavelength tuned to the telecom S-band [381] by the choice of the functional group [27]. For microcavity integration, the nanotubes were dispersed onto a planar macroscopic mirror with a polystyrene layer on top to ensure optimal coupling near the antinode of the intra-cavity field. To this end, a macroscopic planar mirror was spin-coated with a 10 μL solution of 3% (wt/v) polystyrene/toluene, at 2000 RPM for 1 minute, resulting in the formation of a polystyrene spacer layer with estimated thickness of 150 nm. The coated mirror was then vacuum-dried at room-temperature for 24 hours before being deposited with 5 μL of the NTDs containing solution by spin-coating at 3000 RPM for 1 minute.

The experiments were conducted in an ultra-stable fiber-based open-cavity platform (*Qlibri Quantum*, Qlibri GmbH), with the setup and its characterization described in detail in Section 3.2. The cavity is formed by a microscopic concave fiber mirror with a radius of curvature of 25 μm, fabricated by CO_2 laser ablation [56, 316], and a macroscopic planar mirror with functionalized carbon nanotubes on top. Three translational degrees of freedom are accessible through piezoelectric positioners, allowing for lateral scans and length-tuning of the cavity with sub-nanometer precision, which were used to optimize spectral and spatial overlap between individual NTDs and the fundamental Gaussian cavity mode. For the lowest accessible longitudinal mode order $q = 4$, corresponding to a mirror distance of $L_c = 2.6$ μm, we calculated a mode waist of $\omega_0 = 2$ μm and a cavity mode volume of $V_c = 8.2$ μm^3 [56].

To implement the regime of incoherent NTD-cavity coupling, we employed a distributed Bragg reflector (DBR) mirror coating on fiber and planar mirror for spectrally narrow cavity linewidth at the target wavelength of telecom-band emission. Fig. 5.1d shows jointly the

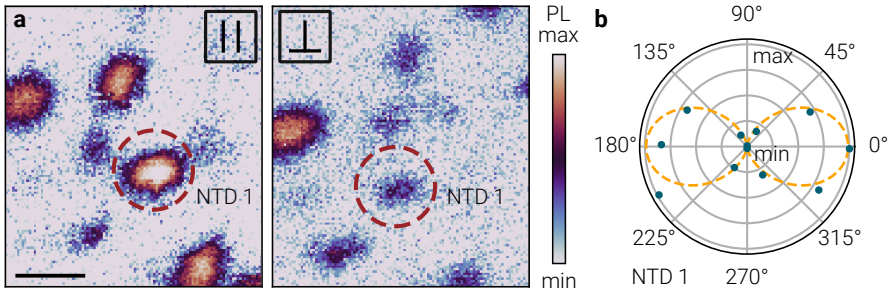

Figure 5.2.: Identification of cavity-coupled carbon nanotube defects. a, Cavity-enhanced PL raster-scan maps recorded for two orthogonal linear polarizations. The detection basis is chosen parallel (left) and perpendicular (right) to the axis of the emitter NTD 1 marked by the dashed circle. The scale bar is 5 μm. **b**, PL intensity for rotating linearly polarized detection basis. The cavity was tuned into spectral and spatial overlap with NTD 1 marked in **a**. 0° corresponds to parallel alignment with the nanotube axis.

ensemble PL spectrum and the cavity finesse obtained from a transfer matrix simulation of the DBR coating. In the cavity, the NTD states were excited resonantly through the E_{11} transition at near-unity DBR mirror transmission and thus independent of the cavity resonance condition using a pulsed supercontinuum white light source at a repetition rate of 78 MHz, spectrally filtered to a linewidth of 2 nm. With a measured finesse value of 3010 ± 10 at a wavelength of 1468 nm, close to the E_{11}^* peak maximum, the cavity mode provided the primary radiative decay channel for the NTD emission. Photons emitted by the NTD-cavity system were coupled into a single mode fiber upon transmission through the planar mirror, and a combination of long-pass filters was used to suppress the excitation laser and other emission at wavelengths below 1400 nm before detection.

5.3. Telecom-band single photons from cavity-coupled nanotube defects

Individual NTDs were identified in the cavity from maps of PL intensity as in Fig. 5.2a, recorded upon lateral raster-scan displacement of the macroscopic mirror for a fixed cavity length. The two maps of Fig. 5.2a were acquired for two orthogonal linear polarizations in the detection path and feature bright PL spots with lateral extent given by the point spread function of the Gaussian fundamental cavity mode with a waist of 2 μm. The left (right) map in Fig. 5.2a was obtained for parallel (orthogonal) orientation of the polarization axis with respect to the nanotube with NTD 1. The contrast in the brightness between the two maps for most PL hot-spots indicates a large degree of linear polarization at the emission sites, a hallmark of the well-known antenna effect in individual carbon nanotubes [137, 382]. The

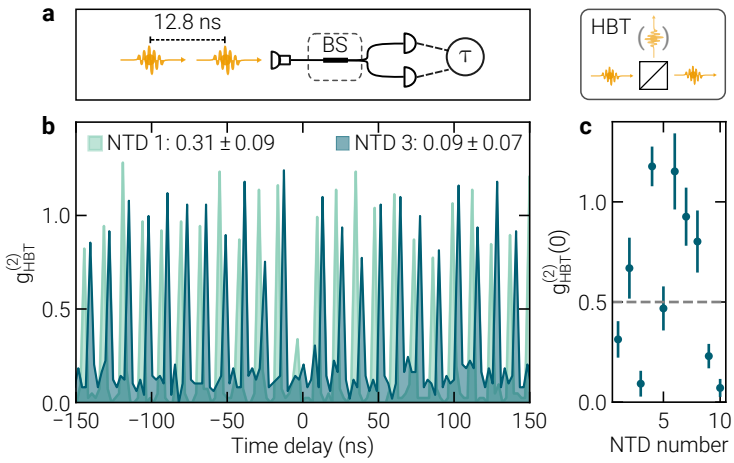

Figure 5.3.: Telecom-band room-temperature single photons from the coupled NTD-cavity system. **a**, Schematic of a Hanbury-Brown-Twiss (HBT) setup based on a fiber beam splitter (BS). **b**, HBT autocorrelation function of cavity-coupled NTD 1 (light green) and NTD 3 (dark green), with second order coherence at zero time delay $g^{(2)}_{\mathrm{HBT}}(0) = 0.31 \pm 0.09$ and 0.09 ± 0.07, respectively. **c**, HBT autocorrelation function at zero time delay, $g^{(2)}_{\mathrm{HBT}}(0)$, as obtained for ten different NTDs. The error bars correspond to the standard uncertainty, obtained as described in the text.

effect is evidenced more clearly in Fig. 5.2b, which shows PL measured for varying linear detection polarization axis for the cavity mode tuned into spectral and spatial overlap with NTD 1.

Operating the coupled NTD-cavity system at the lowest accessible mode order, we determined second-order correlations in photon emission events with a fiber-based Hanbury-Brown-Twiss (HBT) setup, shown schematically in Fig. 5.3a and described in detail in Section 3.2. In the experiments, photons generated via pulsed laser excitation were coupled into a fiber beam splitter, and detection events at the output ports were time-correlated and integrated in 2.5 ns wide windows. The resulting histograms feature prominent peaks separated by the delay between the excitation pulses. To obtain the normalized second-order autocorrelation function $g^{(2)}_{\mathrm{HBT}}(\tau)$, we normalized the histograms with respect to the average height of histogram peaks N_∞ at large time delays. The standard uncertainty of the measured peak height N_0 at $\tau = 0$ is given by $\sqrt{N_0}$ [261] and is the dominant uncertainty in the measurement of N_0. Accordingly, the normalized second-order correlation at zero time delay $g^{(2)}(0)$ was obtained from the measured histograms as $g^{(2)}(0) = N_0/N_\infty(1 \pm 1/\sqrt{N_0})$ [261] including dark count and background correction [311]. The uncertainties in N_∞ and background were found to have negligible influence on this measurement.

The shot-noise limited results of the HBT experiment on two distinct NTDs are shown in Fig. 5.3b, with the corresponding antibunching values $g^{(2)}_{\mathrm{HBT}}(0) = 0.31 \pm 0.09$ and 0.09 ± 0.07 as measures of the single photon purity. These results indicate single photon emission and

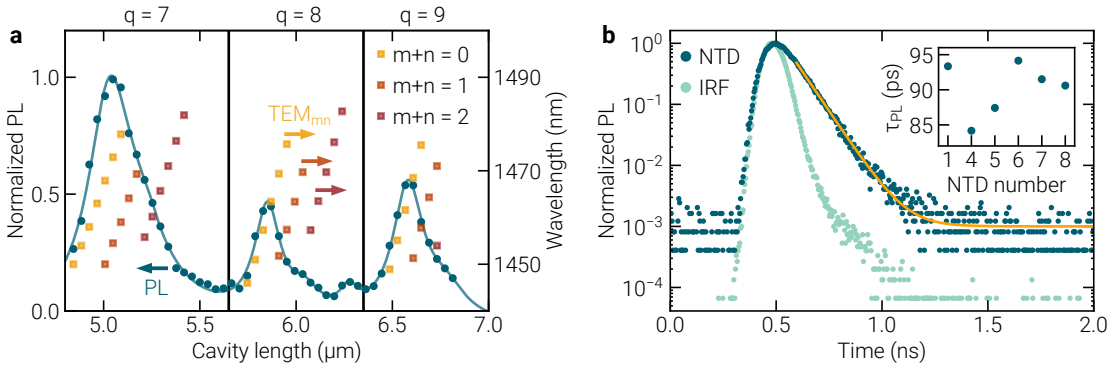

Figure 5.4.: Characteristics of cavity-coupled carbon nanotube defects. a, Normalized PL of NTD 1 as a function of the cavity length, tuned over three longitudinal mode orders (blue circles). The emission spectrum is probed at the resonance wavelengths of the transverse electromagnetic (TEM) cavity modes (yellow, orange and red squares). The solid line was obtained from the fit described in the main text. The colored arrows indicate the respective y-axis **b**, Time-dependent PL intensity of NTD 4 (teal data) along with instrument response (light green data). The orange line is the fit result of a monoexponential decay. The inset shows the decay time τ_{PL} obtained for the investigated NTDs, labeled as in Fig. 5.3c.

the cavity-coupling of individual NTDs. In Fig. 5.3c, we show values of $g^{(2)}_{\mathrm{HBT}}(0)$ obtained for ten emission sites investigated in the course of this work, about half of which complied with the common criterion for single photon emission, $g^{(2)}_{\mathrm{HBT}}(0) < 0.5$.

To determine the NTD spectral bandwidth, we harnessed the tunability of the open cavity geometry. In Fig. 5.4a, we show the normalized PL intensity of NTD 1 as the cavity length is tuned over three longitudinal mode orders $q = 7$, 8 and 9. For each mode order, we observe an asymmetric emission profile, stemming from higher order transverse electromagnetic (TEM) modes. Since the cavity linewidth κ is much smaller than the emitter PL linewidth Γ, the NTD emission spectrum is probed at the resonance wavelength of each TEM-mode [44] with resonance wavelengths given explicitly on the right axis of Fig. 5.4a. We fitted the data by the sum of three Lorentzians for each longitudinal mode order, with the result shown as the solid line in Fig. 5.4a (TEM$_{mn}$ mode orders with $n + m > 2$ were neglected due to vanishing contributions). From the fit, we obtained the emission wavelength 1465 ± 3 nm, and a FWHM linewidth of 28 ± 5 nm, corresponding to $\gamma^* = 8 \pm 2$ meV.

Room-temperature dephasing γ^*, combined with the spectrally narrow cavity linewidth $\kappa = 35.4 \pm 0.1$ μeV measured for the lowest accessible longitudinal mode order, places our experiment in the regime of incoherent good cavity-coupling. To demonstrate this, we compute the NTD light-matter coupling strength g from Eq. (2.43), varying the radiative lifetime τ_{rad} within the range $1 - 15$ ns found for the type of NTDs investigated in this work [73, 144]. Using a refractive index $n = 1$ in our estimate and neglecting the refractive index of the polystyrene spacer, we find an expected upper bound for g in the range of

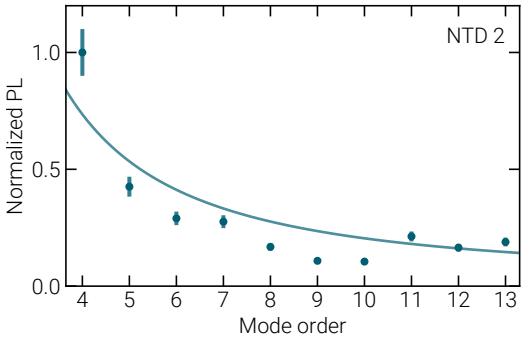

Figure 5.5.: Cavity-tuning of the photon emission efficiency. Maximum PL intensity of emitter NTD 2 as a function of the longitudinal mode order, normalized by the coupling efficiency into the single mode fiber. Cavity-enhancement of the PL intensity is inversely proportional to the mode volume V_c, as evident from best-fit (solid line). The error bars give the standard uncertainty, dominated by experimental uncertainty in fiber coupling.

$17-64$ μeV. Since the population decay rate γ is larger than zero, the defining requirements for the incoherent good cavity regime $2g \ll \gamma+\gamma^*+\kappa$ and $\kappa < \gamma+\gamma^*$ hold in our system [45].

As a result of incoherent cavity-coupling, an enhancement of the PL decay rate γ due to the Purcell effect is negligible in our system. This is evidenced by considering the enhancement of the radiative decay rate $\gamma_{\mathrm{rad}} = 1/\tau_{\mathrm{rad}}$, which is quantified by the Purcell factor F_{p} as defined in Eq. (2.49), which in the limit of incoherent coupling approximates to $F_{\mathrm{p}} \approx 3\lambda^2 c/(4\pi V_{\mathrm{c}}\gamma^*)$ [62], with c the speed of light and λ the emission wavelength. For our system, we find $F_{\mathrm{p}} = 1.6$. The expected enhancement of the population decay rate γ is much smaller, since NTD PL dynamics are dominated by nonradiative decay as detailed in Section 2.2. Consistently, the time-resolved PL for NTD 4 shown in Fig. 5.4b features a monoexponential decay with a time constant $\tau_{\mathrm{PL}} = 84.2 \pm 0.3$ ps in the typical range of free-space NTD population decay times [73, 144], obtained from the fit result shown by the solid orange line. Similar results are obtained for different investigated NTDs as evident from the inset of Fig. 5.4b. An expected short lifetime component on the order of a few picoseconds [144] is not resolved in the instrument-response limited data of Fig. 5.4b, but dominates the two-photon interference timescale as demonstrated below.

Due to the absence of Purcell enhancement and the large mismatch between emitter and cavity spectral bandwidth, the probability for photon emission from the coupled NTD-cavity system is smaller than the free space quantum yield η_{QY}. However, incoherent cavity-coupling enhances the emission spectral density by enabling efficient radiative coupling to the photonic environment defined by the cavity mode upon maximizing the light-matter coupling strength. In our system, this is achieved by minimizing the cavity mode volume, as we demonstrate by showing in Fig. 5.5 the normalized PL for varying mode order. We measured the collected PL intensity for NTD 2, comparable in brightness to NTD 1 and

NTD 3, for ten consecutive longitudinal mode orders, normalized to the largest value and corrected for the variation of the measured fiber coupling. The fiber coupling efficiency depends on the mode waist, which in turn changes with cavity length.

In Fig. 5.5, we observe an increase in the PL intensity by a factor of six as the cavity is tuned to the lowest accessible longitudinal mode order $q = 4$. This mode order corresponds to an intermirror separation of 2.6 μm, mainly limited by the profile depth of the fiber mirror of 2 μm. The increase in the PL intensity stems from an enhancement in light-matter coupling strength g as the cavity length and hence the mode volume V_c is decreased. For our regime of low Purcell enhancement, where the NTD population lifetime is mainly unaffected by the cavity, the emission intensity is proportional to g^2, which in turn is inversely proportional to V_c, as derived from Eq. (2.48). A fit of αV_c^{-1}, with V_c calculated from the cavity length $L_c = q\lambda/2$ [56] and the amplitude α as a free fit parameter, yields a good correspondence with the data (solid line in Fig. 5.5c).

Operating the coupled NTD-cavity system at maximum cavity-enhancement of the PL intensity, we determined the single photon emission efficiency β_c, which gives the probability that a photon is emitted into the spectral window of the cavity linewidth κ given an initial excitation of the emitter. Each excitation pulse generates a photon in the cavity with probability $\beta_c\eta_{em}$, where η_{em} is the probability for population of the defect state by free E_{11} excitons. The rate of photons registered by the detector I_{em} is then given by $I_{em} = f_{exc}\eta_{out}\eta_{sys}\eta_{em}\beta_c$, where f_{exc} is the repetition rate of the excitation source, $\eta_{out} = 0.52$ is the probability for a photon to exit the cavity through the flat mirror obtained from transfer matrix simulations as described in Chapter A and $\eta_{sys} = (1.3 \pm 0.4) \cdot 10^{-2}$ is the combined transmission and detection efficiency of the setup. From the maximum measured value $I_{em} = 1840 \pm 30$ counts/s for NTD1 and the upper bound $\eta_{em} = 1$, we obtain a lower bound of $\min(\beta_c) = (3.9 \pm 0.1) \cdot 10^{-3}$. A measurement of η_{em} would require excitation near or above the saturation threshold. This in turn requires high excitation powers, which can lead to NTD degradation and limit single photon purity and indistinguishability, such that we refrained from these measurements.

The measured lower bound for β_c already is a factor of four larger than the estimated upper bound $\beta_{fs} = \kappa/(\pi\gamma^*) = 1 \cdot 10^{-3}$ for spectrally filtered free-space decay, a competing strategy to obtain indistinguishable single photons from spectrally broad emitters. We expect the actual value of the free space photon emission efficiency $\eta_{QY}\beta_{fs}$ to be at least one order of magnitude smaller when taking into account the non-unity NTD quantum yield η_{QY} on the order of 0.1 [73]. Our measurements therefore indicate a drastic enhancement of the emission spectral density as compared to free space emission. As detailed in Section 2.5 and [308], this enhancement is quantified by the ideal Purcell factor $F_{P,ideal}$ as defined in Eq. (2.51), which can be understood by noting that only the fraction of the broad emitter spectrum which is in overlap with the cavity linewidth experiences full Purcell enhancement. For our system, we expect $F_{P,ideal} = 91$ taking into account the refractive index of polystyrene,

constituting a large enhancement of spectral density by virtue of incoherent good cavity-coupling.

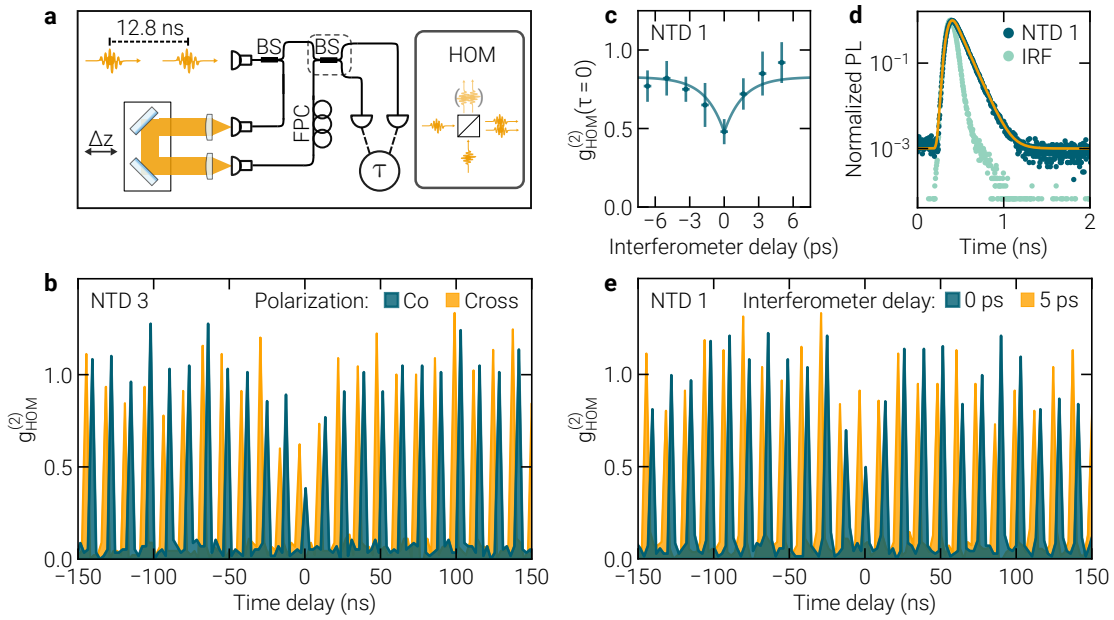

Figure 5.6.: Demonstration of cavity-enhanced photon indistinguishability. a, Schematic of the imbalanced Mach-Zehnder interferometer to probe the photon indistinguishability in Hong-Ou-Mandel (HOM) type experiments based on fiber beam splitters (BS). The time delay between the interferometer arms was tuned via the displacement Δz, and their relative polarization by the fiber polarization controller (FPC) in one arm. **b**, HOM cross-correlation function of NTD 3 for co-polarized (teal) and cross-polarized (orange) interferometer arms with delay of one excitation pulse. The difference in the coincidence probabilities at zero-delay is a hallmark of two-photon interference with visibility $v = 0.51 \pm 0.21$. **c**, HOM cross-correlation function at time delay $\tau = 0$ for NTD 1 as a function of the interferometer delay, with visibility $v = 0.65 \pm 0.24$. Zero interferometer delay again corresponds to delay by one excitation pulse separation. The solid line is an empirical fit to the HOM dip described in the main text. The horizontal error bars correspond to the standard uncertainty in the interferometer delay; the vertical error bars correspond to the standard uncertainty determined as described in the main text. **d**, Temporal PL decay of NTD 1 (teal data) and instrument response (light green data). The orange line shows the result of a biexponential decay model. **e**, HOM cross-correlation function of NTD 1, measured in co-polarized interferometer configuration for interferometer delays 0 ps (teal) and 5 ps (orange).

5.4. Cavity-enhanced photon indistinguishability

5.4.1. Experimental results

We quantified the photon indistinguishability in Hong-Ou-Mandel (HOM) type experiments using an imbalanced Mach-Zehnder interferometer shown schematically in Fig. 5.6a and described in detail in Chapter 3. The train of single photon pulses generated by the source was first split in a fiber beam splitter. The time delay Δt in the interferometer was tuned by the path difference Δz with an adjustable delay stage to enable two-photon interference between consecutively emitted photons at the second beam splitter. In this setting, a delay of zero implies a separation by one excitation pulse. The relative polarization between the interferometer arms was set by fiber polarization controllers, and the detection events at the output ports were time-correlated to obtain the HOM-cross-correlation function $g^{(2)}_{\mathrm{HOM}}(\tau)$, which was calculated similar to the HBT-autocorrelation function as described above.

First, we initialized the interferometer at zero delay and performed a two-photon interference experiment for co- and cross-polarized interferometer arms on NTD 3, with the cavity operated at the lowest accessible mode order at maximum enhancement of the PL efficiency. The shot-noise limited results are shown in Fig. 5.6b. For the co-polarized configuration, we observe a reduction of the measured correlations at zero time delay. This is a hallmark of quantum coherent two-photon interference: the (partially) indistinguishable single photons arriving simultaneously at different input ports of the beam splitter are likely to exit at the same output port, resulting in reduced correlations at zero time delay [21, 281, 311].

Successively, we performed the HOM interference experiment for varying interferometer delays on NTD 1, with cross-correlation histograms for interferometer delays of 0 and 5 ps shown in Fig. 5.6e. The observed reduction in correlations at zero time delay is again a hallmark of two-photon interference, where tuning between the two interferometer delay settings is approximately equivalent to switching the polarization configuration as in Fig. 5.6b. In Fig. 5.6c, we show the measured value of the HOM cross-correlation function at zero time delay for varying interferometer delay. Upon transition through zero-delay, we observed the characteristic HOM dip due to reduced cross-channel correlations by two-photon interference, described by the empirical formula $c[1 - a\exp(-|\Delta t|/\tau_{\mathrm{HOM}})]$, where a is an amplitude, c is an offset at large interferometer delays Δt, and τ_{HOM} is the characteristic timescale of the HOM interference [21]. From the best fit to the data shown by the solid line in Fig. 5.6c, we determined $\tau_{\mathrm{HOM}} = 2 \pm 2$ ps.

5.4.2. Two-photon interference visibility

We quantify the respective degree of photon indistinguishability by the two-photon interference visibility v_{HOM} that one would detect in an interferometer with balanced beam

splitters (BS) and unity classical visibility [312]. We obtain this quantity by careful analysis of the HOM-cross-correlation function, accounting both for imbalanced interferometer arms and non-ideal single photon purity of each NTD. The starting point for the analysis is the additional schematic of the interferometer used to perform two-photon interference experiments shown in Fig. 5.7a. The stream of photons entering the interferometer was divided at BS 1 with transmission and reflection $T_{\mathrm{BS},1}$ and $R_{\mathrm{BS},1}$, respectively, and recombined after a tunable delay Δt at BS 2 with transmission and reflection $T_{\mathrm{BS},2}$ and $R_{\mathrm{BS},2}$. In our interferometer, the transmission of the delay arm is $\mu < 1$. The delay time equals the excitation pulse separation, and is orders of magnitude larger than the coherence time and population lifetimes in our system. We therefore treat the reduced transmission in the delay arm as an effect of imbalanced transmission and reflection of BS 1, and use the effective values $\tilde{T}_{\mathrm{BS},1} = T_{\mathrm{BS},1}/(T_{\mathrm{BS},1} + \mu R_{\mathrm{BS},1})$ and $\tilde{R}_{\mathrm{BS},1} = \mu R_{\mathrm{BS},1}/(T_{\mathrm{BS},1} + \mu R_{\mathrm{BS},1})$ for its transmission and reflection.

Our experimental histograms, obtained by integrating correlation events in a 2.5 ns time window, feature peaks separated by the delay Δ between the excitation pulses, as exemplified by the histogram obtained for NTD 3 in co-polarized interferometer configuration shown in Fig. 5.7b. Using effective transmission and reflection values, we obtain expressions for the height $N_{n\Delta}$ of coincidence peaks at time delays $\tau = n\Delta$ with integer n from the non-normalized cross-correlation function $G^{(2)}_{\mathrm{HBT}}(\tau)$. The computation is based on the formalism in Ref. [251], which is introduced in detail in Section 2.5. We consider the case in which the interferometer delay equals exactly one excitation pulse separation, which is the setting relevant for the measurement of ν_{HOM}.

Based on the derivation in Section 2.5, we find the HOM cross-correlation function between the output ports of the second beam splitter at $\tau = n\Delta$,

$$\begin{aligned} G^{(2)}_{\mathrm{HBT}}(n\Delta) \propto \int_0^\infty \mathrm{d}t \int_0^\infty \mathrm{d}\tau\, & R^2_{\mathrm{BS},2} \langle \hat{a}_2^\dagger(t)\hat{a}_1^\dagger(t+\tau+n\Delta)\hat{a}_1(t+\tau+n\Delta)\hat{a}_2(t)\rangle \\ & + T^2_{\mathrm{BS},2} \langle \hat{a}_1^\dagger(t)\hat{a}_2^\dagger(t+\tau+n\Delta)\hat{a}_2(t+\tau+n\Delta)\hat{a}_1(t)\rangle \\ & + R_{\mathrm{BS},2}T_{\mathrm{BS},2} \langle \hat{a}_1^\dagger(t)\hat{a}_1^\dagger(t+\tau+n\Delta)\hat{a}_1(t+\tau+n\Delta)\hat{a}_1(t)\rangle \\ & + R_{\mathrm{BS},2}T_{\mathrm{BS},2} \langle \hat{a}_2^\dagger(t)\hat{a}_2^\dagger(t+\tau+n\Delta)\hat{a}_2(t+\tau+n\Delta)\hat{a}_2(t)\rangle \\ & - R_{\mathrm{BS},2}T_{\mathrm{BS},2} \langle \hat{a}_2^\dagger(t)\hat{a}_1^\dagger(t+\tau+n\Delta)\hat{a}_2(t+\tau+n\Delta)\hat{a}_1(t)\rangle \\ & - R_{\mathrm{BS},2}T_{\mathrm{BS},2} \langle \hat{a}_1^\dagger(t)\hat{a}_2^\dagger(t+\tau+n\Delta)\hat{a}_1(t+\tau+n\Delta)\hat{a}_2(t)\rangle, \end{aligned} \tag{5.1}$$

with photon annihilation operators $\hat{a}_1$ and $\hat{a}_2$ for the two interferometer arms as labeled in Fig. 5.7a. The integration over τ accounts for binning in the experimental histograms, which is taken to infinity since the bin size greatly exceeds any population and coherence decay times in the system.

We account for the Mach-Zehnder geometry of the interferometer by computing the cross-correlation function for a stream of photons impinging on the first beam splitter, BS1,

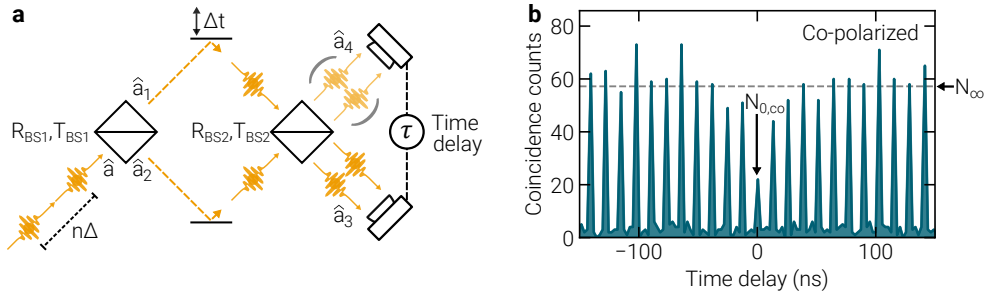

Figure 5.7.: Analysis of HOM cross-correlation histograms. a, Schematic of the imbalanced Mach-Zehnder interferometer used for measurements of the two-photon interference visibility as illustrated in Fig. 5.6a, including relevant parameters for the theoretical analysis. An input stream of single photons, separated by integer multiples n of the excitation pulse separation Δ is split at the first beam splitter (reflection and transmission R_{BS1} and T_{BS1}). Upon interferometer delay Δt, the interferometer arms are recombined at a second beam splitter (reflection and transmission R_{BS2} and T_{BS2}), whose output ports are time-correlated. Photon annihilation operators in the relevant input and output beam splitter modes i are labeled $\hat{a}_i$. **b**, Experimental HOM coincidences for NTD 3 in co-polarized interferometer configuration with delay of one excitation pulse, binned in 2.5 ns time windows. Peak heights $N_{0,\mathrm{co}}$ and N_{∞} were used to compute the two-photon interference visibility as detailed in the text.

as illustrated in Fig. 5.7a. Using Eq. (2.29), we find $\hat{a}_1 = t_{\mathrm{BS},1}\hat{a}$ and $\hat{a}_2 = r_{\mathrm{BS},1}\hat{a}$. Plugging these expressions into Eq. (5.1), we find the cross-correlation function for our imbalanced Mach-Zehnder interferometer. In this step, we also account for the fact that for a given time delay $n\Delta$, only incoming photons separated by a limited number of multiples of Δ lead to higher order correlation events in the output ports of the second beam splitter. These input configurations are illustrated in detail the supplement of Ref. [326]. All other intensity-type correlators in Eq. (5.1) separate into the form $\langle\hat{a}^\dagger(t_1)\hat{a}(t_2)\rangle\langle\hat{a}^\dagger(t_3)\hat{a}(t_4)\rangle$ with times t_1, t_2, t_3 and t_4, which greatly simplifies the expression for $G^{(2)}_{\mathrm{HBT}}(n\Delta)$. In the computation, we also identify the normalized HBT-correlation function at zero time delay based on the expression in Eq. (2.34),

$$g^{(2)}_{\mathrm{HBT}}(0) = \frac{\int_0^\infty \mathrm{d}\tau \int_0^\infty \mathrm{d}t \langle\hat{a}^\dagger(t)\hat{a}^\dagger(t+\tau)\hat{a}(t+\tau)\hat{a}(t)\rangle}{\int_0^\infty \mathrm{d}\tau \int_0^\infty \mathrm{d}t \langle\hat{a}^\dagger(t)\hat{a}(t)\rangle\langle\hat{a}^\dagger(t+\tau)\hat{a}(t+\tau)\rangle} \tag{5.2}$$

explicitly accounting for the effect of non-unity single photon purity on two-photon interference measurements in our interferometer. We further identify the HOM-visibility v_{HOM} [45],

$$v_{\mathrm{HOM}} = \frac{\int_0^\infty \mathrm{d}\tau \int_0^\infty \mathrm{d}t \left|\langle\hat{a}^\dagger(t)\hat{a}(t+\tau)\rangle\right|^2}{\int \mathrm{d}\tau_0^\infty \int_0^\infty \mathrm{d}t \langle\hat{a}^\dagger(t)\hat{a}(t)\rangle\langle\hat{a}^\dagger(t+\tau)\hat{a}(t+\tau)\rangle}, \tag{5.3}$$

as introduced in Eq. (2.39).

Based on the result for the non-normalized HOM cross-correlation function, we compute the expected correlation histogram peak height $N_{n\Delta}$ at time delay $n\Delta$ using the relation

$N_{n\Delta} \propto G^{(2)}_{\mathrm{HBT}}(n\Delta)$, which we successively use to determine the two-photon interference visibility from our measurements. For the height of the peak at $\tau = 0$ for co-polarized interferometer arms (indicated in Fig. 5.7b), we find

$$N_{0,co} = H\left[\tilde{R}_1\tilde{T}_1\left[1-2R_2T_2-2R_2T_2(\epsilon_P)^2 v_{\mathrm{HOM}}\right] + g^{(2)}_{\mathrm{HBT}}(0)R_2T_2(1-2\tilde{R}_1\tilde{T}_1)\right], \tag{5.4}$$

with an integration constant H and accounting for the overlap between the polarization modes of the interferometer arms ϵ_P [312]. The height of the central histogram peak for cross-polarization $N_{0,\mathrm{cross}}$ is obtained by setting $v_{\mathrm{HOM}} = 0$ in Eq. (5.4), which yields

$$N_{0,\mathrm{cross}} = H\left[\tilde{R}_1\tilde{T}_1(1-2R_2T_2) + g^{(2)}_{\mathrm{HBT}}(0)R_2T_2(1-2\tilde{R}_1\tilde{T}_1)\right]. \tag{5.5}$$

For large $|\tau|$, we find

$$N_\infty = H\left[\tilde{R}_1\tilde{T}_1(R_2^2+T_2^2) + R_2T_2({\tilde{R}_1}^2+{\tilde{T}_1}^2)\right], \tag{5.6}$$

which is also indicated in Fig. 5.7b

To determine v_{HOM} for NTD 3, we first extracted the raw visibility v_{raw} from the data shown in Fig. 5.6b as $v_{\mathrm{raw}} = 1 - g^{(2)}_{\mathrm{HOM,co}}(0)/g^{(2)}_{\mathrm{HOM,cross}}(0)$. Next, we calculated $v_{\mathrm{raw}} = 1 - N_{0,\mathrm{co}}/N_{0,\mathrm{cross}}$ from Eq. (5.4) and Eq. (5.5) and solved for v_{HOM}, yielding an expression which depends on v_{raw}, $g^{(2)}_{\mathrm{HBT}}(0)$ and the interferometer parameters $\tilde{T}_1$, $\tilde{R}_1$, T_2, R_2 and ϵ_P. Using experimental values for these quantities ($\tilde{T}_1 = 0.4$, $\tilde{R}_1 = 0.6$, $T_2 = 0.49$, $R_2 = 0.51$ and $\epsilon_P = 0.96$), we finally obtained $v_{\mathrm{HOM}} = 0.51 \pm 0.21$ for NTD 3. Based on the experimental values $\tilde{T}_1$, $\tilde{R}_1$, T_2, R_2, ϵ_P and $g^{(2)}_{\mathrm{HBT}}(0)$ for NTD 3, we estimate $g^{(2)}_{\mathrm{HOM,cross}}(0) = N_{0,\mathrm{cross}}/N_\infty = 0.53 \pm 0.04$ for cross-polarized interferometer arms, in good agreement with the experimental value of 0.61 ± 0.12. The uncertainty in measured peak heights is computed in identical fashion to the HBT experiments. The standard uncertainty in all quantities derived from measured peak heights was obtained by Gaussian error propagation, considering the uncertainties in all input parameters.

For NTD 1, we obtained the raw visibility $v_{\mathrm{raw}} = a$ from the amplitude a of the best-fit to the HOM dip in Fig. 5.6c, and calculated v_{HOM} from v_{raw}, $g^{(2)}_{\mathrm{HBT}}(0)$, and the interferometer parameters as described above to obtain $v_{\mathrm{HOM}} = 0.65 \pm 0.24$. The asymmetric increase in the visibility towards large positive delays observed in Fig. 5.6c is the result of a degradation-induced decrease in the single photon purity during the measurement. For large interferometer delays, we expect $g^{(2)}_{\mathrm{HOM}}(0) = N_{0,\mathrm{cross}}/N_\infty = 0.64 \pm 0.05$ as an estimate for the offset c in the data of in Fig. 5.6c. This value is smaller than the best-fit value $c = 0.80 \pm 0.08$, which could stem from the degradation observed during the measurement resulting in an overall increase in $g^{(2)}_{\mathrm{HOM}}$. In Chapter B, we show for completeness the cross-correlation histograms obtained for all investigated interferometer delays, with the reduction of correlation events at zero time delay τ again providing evidence for two-photon interference for NTD 1. Each

data point in Fig. 5.6c was obtained by computing $g^{(2)}_{\mathrm{HOM}}(0)$ from the respective experimental histogram as described above.

For completeness, we also calculate the values of the HOM cross-correlation function at time delays corresponding to one excitation pulse separation, $\tau = \pm 12.5$ ns. As outlined e.g. in the supplement of Ref. [326], $g^{(2)}_{\mathrm{HOM}}$ is smaller than one for these delays. For the respective histogram peak heights, we find

$$N_{12.5} = H\left[\tilde{R}_1\tilde{T}_1T_2^2 + R_2T_2(1-2\tilde{R}_1\tilde{T}_1) + g^{(2)}_{\mathrm{HBT}}(0)\tilde{R}_1\tilde{T}_1R_2^2\right] \tag{5.7}$$

and

$$N_{-12.5} = H\left[\tilde{R}_1\tilde{T}_1R_2^2 + R_2T_2(1-2\tilde{R}_1\tilde{T}_1) + g^{(2)}_{\mathrm{HBT}}(0)\tilde{R}_1\tilde{T}_1T_2^2\right]. \tag{5.8}$$

We note that these expressions are valid for both co- and cross-polarized interferometer arms since the excitation pulse separation greatly exceeds the photon coherence time, leading to vanishing contributions of quantum interference at these time delays. From our measured values of the interferometer parameters, we calculate the expected value $g^{(2)}_{\mathrm{HOM}}(-12.5\ \mathrm{ns}) = N_{-12.5}/N_\infty = 0.77 \pm 0.02$, in agreement with the value 0.87 ± 0.13 measured in co-polarized configuration and close to the value 0.58 ± 0.12 measured in cross-polarized configuration. We also expect $g^{(2)}_{\mathrm{HOM}}(12.5\ \mathrm{ns}) = N_{12.5}/N_\infty = 0.79 \pm 0.02$, in agreement with the values 0.71 ± 0.12 and 0.75 ± 0.13 measured for co- and cross-polarized interferometer arms, respectively. Overall, these results confirm the good correspondence between our measurements and our theoretical description of the interferometer.

5.4.3. Two-photon interference timescale

Summarizing the analysis of our HOM measurements, we obtain consistent experimental two-photon interference visibilities of $v_{\mathrm{HOM}} = 0.51 \pm 0.21$ for NTD 1 and $v_{\mathrm{HOM}} = 0.65 \pm 0.24$ for NTD 3 from the data shown in Fig. 5.6b and c, orders of magnitude larger than the values expected for room-temperature dephasing. To gain theoretical insight into this observation, we develop a model for time-dependent NTD-cavity coupling. The starting point for the investigation is the characteristic two-photon interference time scale $\tau_{\mathrm{HOM}} = 2 \pm 2$ ps determined from the fit in Fig. 5.6c. This timescale is given by the jitter in the photon arrival time at the beam splitter, which in turn is determined by the NTD population lifetime [252].

To briefly motivate the assignment of the HOM interference timescale, which informs the theoretical model introduced subsequently, we consider a two-level emitter with lifetime T_1 and coherence time T_2 as described in detail in Section 2.5. Each data point of the HOM-dip in Fig. 5.6c is obtained from a correlation histogram as shown in Fig. 5.6b. When probing two independent emitters with unity single photon purity on a beam splitter, the peak around

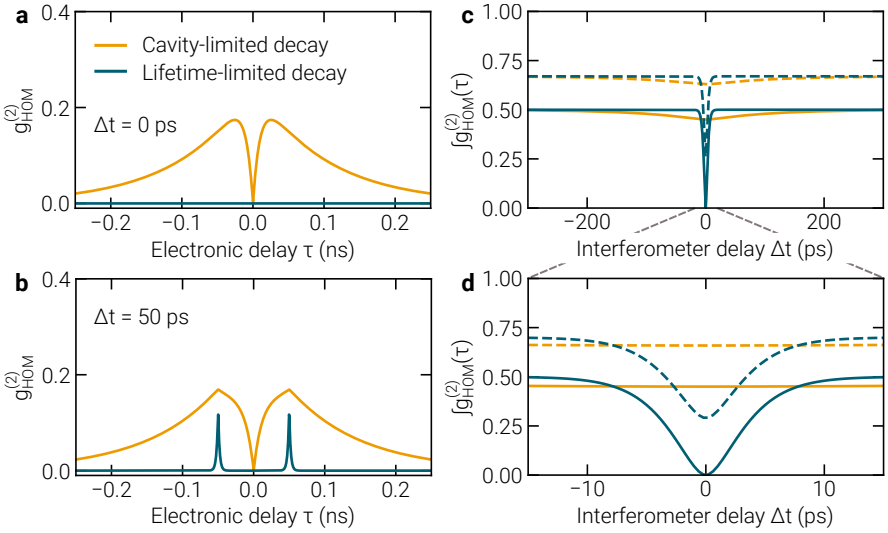

Figure 5.8.: Two-photon interference timescale. **a**, **b**, HOM cross-correlation function as a function of electronic delay τ, for interferometer delay $\Delta t = 0$ ps (**a**) and $\Delta t = 50$ ps (**b**). **c**, **d**, Integrated HOM cross-correlation function as a function of interferometer delay Δt. In all panels, the limiting cases of a fast, lifetime limited decay with lifetime 2 ps (teal lines), and a slow decay with lifetime 100 ps and cavity-limited coherence time 20 ps are considered (orange lines). The solid lines are the results for a single source with unity single photon purity probed in a Mach-Zehnder interferometer with balanced beam splitters. The dashed lines are results for a single source with non-unity single photon purity (NTD 1) probed in our experimental Mach-Zehnder interferometer with imperfect beam splitters.

time delay $\tau = 0$ in such a histogram is described by [252]:

$$g^{(2)}_{\mathrm{HOM}}(\tau) = \frac{1}{4}e^{-|\tau-\Delta t|/T_1} + \frac{1}{4}e^{-|\tau+\Delta t|/T_1} - \frac{1}{2}e^{-|\tau|(2/T_2-1/T_1)-|\tau-\Delta t|/(2T_1)-|\tau+\Delta t|/(2T_1)}. \tag{5.9}$$

If a single emitter is probed in a Mach-Zehnder interferometer with balanced beam splitters, a prefactor of 1/2 has to be included to account for reduced coincidence probability around $\tau = 0$ [265, 326].

We now consider the limiting cases of a lifetime-limited fast decay ($T_1 = 2$ ps, $T_2 = 4$ ps) and a cavity-limited slow decay ($T_1 = 100$ ps, $T_2 = 20$ ps given by the measured cavity lifetime), featured by a single emitter probed in a Mach-Zehnder interferometer. We plot the results of Eq. (5.9) for each of these cases in Fig. 5.8a and b, with interferometer delay $\Delta t = 0$ ps and $\Delta t = 50$ ps, respectively. The lifetime-limited coherence of the fast decay enables two-photon interference, which results in vanishing correlation counts for the lifetime-limited decay in Fig. 5.8a. If the interferometer delay exceeds the coherence time, two-photon interference is suppressed, as evident from Fig. 5.8b.

As obvious from Eq. (5.9) and Fig. 5.8a and b, the coherence time T_2 can in principle be probed by varying the electronic delay τ. By contrast, tuning of the interferometer delay

changes the photon arrival time at the beam splitter, such that this measurement probes the emitter population lifetime. In our experiment, the histogram bin size is much larger than the population lifetime and coherence time, and thus the HOM cross-correlation function at $\tau = 0$ is given by [252]:

$$\begin{aligned} g^{(2)}_{\mathrm{HOM}}(\tau = 0) &= \int_{N_0} g^{(2)}_{\mathrm{HOM}}(\tau)\mathrm{d}\tau \\ &= \frac{1}{2}\left[1 - \frac{T_2}{2T_1}e^{-2|\Delta t|/T_2} - \frac{1}{2T_1/T_2 - 1}\left(e^{-|\Delta t|/T_1} - e^{-2|\Delta t|/T_2}\right)\right], \end{aligned} \tag{5.10}$$

where integration is carried out over all counts in the histogram bin N_0 at $\tau = 0$. For highly indistinguishable photons with $T_2 \approx 2T_1$, this expression simplifies to

$$g^{(2)}_{\mathrm{HOM}}(\tau = 0) \approx \frac{1}{2}\left(1 - \frac{T_2}{2T_1}e^{-|\Delta t|/T_1}\right). \tag{5.11}$$

The function used to fit to the HOM-dip in Fig. 5.6c has the same functional form.

In Fig. 5.8c and d, we plot Eq. (5.10) by solid lines for the limiting cases of lifetime- and cavity limited coherence times introduced above. In addition, we also show by dashed lines the case of NTD 1 (as a single source with non-unity single photon purity) probed in our experimental Mach-Zehnder interferometer with imperfect beam splitters described above, for which the values of $g^{(2)}_{\mathrm{HOM}}(\tau = 0)$ are offset due to interferometer imbalance and nonzero $g^{(2)}_{\mathrm{HBT}}(0)$. As evident from these results, a cavity-limited (slow) decay will have an associated HOM timescale of 100 ps at two-photon interference visibility of around 0.1. By contrast, a lifetime-limited decay process will have an associated HOM timescale of 2 ps, and unity interference visibility. In the case of nonzero $g^{(2)}_{\mathrm{HBT}}(0)$, HOM correlations are nonzero at $\Delta t = 0$ ps.

Comparing the theoretical plot of Fig. 5.8d with the experimental data in Fig. 5.6c implies a fast population decay within a few picoseconds for NTD 1. At the same time, the instrument-limited PL decay shown in Fig. 5.6d indicates the presence of an additional slow decay channel with time constant of approximately 90 ps. Both time scales can be associated with the decay components of the biexponential PL decay characteristic for NTDs [73, 144]. The fast and slow decay channels with time constants τ_{fast} and τ_{slow} arise from an interplay of bright and dark exciton reservoirs, with τ_{fast} as short as a few picoseconds and relative decay amplitudes close to unity in larger-diameter nanotubes [144].

5.4.4. Model for defect-cavity coupling dynamics

To investigate the effect of the biexponential emitter decay on the measured two-photon interference visibility, we model the time-dependent NTD-cavity coupling. We first consider a two-level emitter coupled to a single mode of an optical cavity. This setting was studied

in Ref. [45], where the time-dependent density operator $\hat{\rho}(t)$ of the coupled emitter-cavity system was obtained from a Lindblad master equation in Markovian approximation. As discussed in Section 2.5, the influence of the density operator coherences on the system dynamics is negligible in the regime of incoherent cavity-coupling. The coupled system is therefore fully described by the populations of cavity and emitter, which exchange photons at a rate R given by [44]:

$$R = 4g^2/(\kappa + \gamma + \gamma^*). \tag{5.12}$$

In order to model cavity-coupling of an NTD with biexponential population decay, we first focus on the value of R in our system. Given incoherent cavity-coupling, the denominator in Eq. (5.12) is dominated by the pure dephasing rate γ^*, such that $R \approx 4g^2/\gamma^*$. From the measured value $\gamma^* = 8 \pm 2$ meV and the range for g estimated above ($17-64$ μeV), we expect R to range between 0.14 and 2.04 μeV.

We now extend the model of Ref. [45] to an NTD exhibiting dark and bright exciton states. The dark state has no effect on the limit of incoherent coupling due to its vanishingly small coupling to the cavity. The bright state, on the other hand, will exchange photons with the cavity at rate R, analogous to a radiative two-level system. Based on these considerations, we describe our system with the set of partial differential equations

$$\frac{\partial \rho_\mathrm{c}}{\partial t} = -(\kappa + R)\rho_\mathrm{c} + R\rho_\mathrm{b} \tag{5.13}$$

$$\frac{\partial \rho_\mathrm{d}}{\partial t} = -\gamma_d \rho_\mathrm{d} + \gamma_\mathrm{bd}\rho_\mathrm{b} - \gamma_\mathrm{db}\rho_\mathrm{d} \tag{5.14}$$

$$\frac{\partial \rho_\mathrm{b}}{\partial t} = -(\gamma_b + R)\rho_\mathrm{b} + R\rho_\mathrm{c} - \gamma_\mathrm{bd}\rho_\mathrm{b} + \gamma_\mathrm{db}\rho_\mathrm{d} \tag{5.15}$$

with the populations of the cavity ρ_c, dark state ρ_d and bright state ρ_b. Here, $\gamma_\mathrm{bd/db}$ is the population exchange rate between ρ_b and ρ_d, and $\gamma_\mathrm{b/d}$ are the sum of radiative and nonradiative decay rates of ρ_b and ρ_d. We neglect the effect of initial trapping of E_{11} excitons at the defect site on a picosecond timescale [146], since the associated additional time-jitter in bright state population can be captured in our model by adequately chosen decay rates for the two considered energy levels.

Before analysis of the coupled system, we first focus on the decay dynamics of the bright state of free-space NTDs. In our model, this is achieved by setting the coupling rate in Eq. (5.13) – Eq. (5.15) to zero, $R = 0$, resulting in the time-dependent bright state population

$$\rho_\mathrm{b}(t) = \rho_b(0)\left(A_\mathrm{fast}e^{-t/\tau_\mathrm{fast}} + A_\mathrm{slow}e^{-t/\tau_\mathrm{slow}}\right). \tag{5.16}$$

In this expression, $A_\mathrm{fast/slow} \in 0,1$ are amplitude factors which obey $A_\mathrm{fast} + A_\mathrm{slow} = 1$. The relation between the time constants $\tau_\mathrm{fast/slow}$ and the decay rates in Eq. (5.13) – Eq. (5.15) is given in [383]. As expected, Eq. (5.16) describes a biexponential NTD decay. The fraction of

the population which decays via the fast and slow process, respectively, is quantified by the relative fractional amplitudes $\tilde{A}_{\mathrm{fast/slow}}$ given by [383]:

$$\tilde{A}_{\mathrm{fast/slow}} = \frac{A_{\mathrm{fast/slow}}\tau_{\mathrm{fast/slow}}}{A_{\mathrm{fast}}\tau_{\mathrm{fast}} + A_{\mathrm{slow}}\tau_{\mathrm{slow}}}. \tag{5.17}$$

To compare predictions of our model with experimental data, we solve Eq. (5.13) – Eq. (5.15) for the time-dependent cavity population ρ_{c}. The parameters $\gamma_{\mathrm{b/d}}$, $\gamma_{\mathrm{bd/db}}$ and $\rho_b(0)$ are determined by two requirements on our model prediction. First, the predicted time-dependent PL intensity, which is proportional to the cavity population ρ_{c} convoluted with the instrument response function, should agree with the measured time-dependent PL for NTD 1 shown in Fig. 5.6d. Second, the resulting biexponential bright state decay described by Eq. (5.16) should have a short population lifetime $\tau_{\mathrm{short}} = 2$ ps, as indicated by the HOM interference timescale in Fig. 5.6c. The result of this parameter adaptation is a free-space decay with $\tau_{\mathrm{fast}} = 2$ ps, $\tau_{\mathrm{slow}} = 91$ ps, $\tilde{A}_{\mathrm{fast}} = 0.34$ and $\tilde{A}_{\mathrm{slow}} = 0.66$, which fix the values for $\gamma_{\mathrm{b/d}}$, $\gamma_{\mathrm{bd/db}}$ and $\rho_b(0)$. The corresponding result for the PL decay is shown by the solid line in Fig. 5.6d and agrees well with the measured data.

In order to calculate the expected two-photon interference visibility v_{HOM} for cavity-coupled NTDs, we evaluate [45]

$$v_{\mathrm{HOM}} = \frac{\int_0^\infty \mathrm{d}t\rho_{\mathrm{c}}^2(t)\int_0^\infty \mathrm{d}\tau e^{-\Gamma_{\mathrm{c}}\tau}}{\frac{1}{2}\left|\int_0^\infty \mathrm{d}t\rho_{\mathrm{c}}(t)\right|^2} \tag{5.18}$$

using the result for ρ_{c}. In this equation, $\Gamma_c = \kappa + R$, with $\Gamma_c \approx \kappa$ in our system. With this expression, we find $v_{\mathrm{HOM}} = 0.3$ for the theoretically expected visibility without significant dependence on R within the previously estimated range ($0.13 - 2.0\ \mu$eV).

The model results for the expected two-photon interference visibility, combined with the identification of the fast decay timescale τ_{fast} with the HOM timescale τ_{HOM} as justified above, yield a plausible explanation for the results of our two-photon interference experiments. In the framework of the incoherent good cavity regime, the feeding of the cavity through the fast decay channel generates photons with near-unity visibility [45]. The actual visibility in Fig. 5.6c is lower than unity (0.65 ± 0.24), most probably due to photons generated via the slow process with lifetimes exceeding the cavity coherence time of 20 ps, which renders them partly distinguishable. A reduction in visibility is also backed by our model for time-dependent NTD-cavity coupling, which predicts $v_{\mathrm{HOM}} = 0.3$. The deviation between measured and estimated value is consistent with operation of our experiment at wavelengths on the edge of the DBR stopband (see Fig. 5.1d). In this regime, small shifts towards larger resonance wavelength caused by cavity length drifts can decrease the cavity linewidth by a factor of up to two and in turn result in increased visibility, which is inversely proportional to κ [45].

The enhancement of indistinguishability by virtue of cavity-coupling in our system is benchmarked by computing the two-photon visibility expected for free-space NTD decay. To this end, we assume that fast and slow process have visibilities $v_{\mathrm{fast/slow}} = T_2/(2\tau_{\mathrm{fast/slow}})$, where the coherence time is given by the dephasing time as $T_2 \approx 1/\gamma^* = 80$ fs. With the values for decay timescales and amplitudes used in the computation of ρ_c as discussed above, we estimate v_{HOM} as a weighted sum of visibilities for fast and slow process, $v_{\mathrm{HOM}} = \tilde{A}_{\mathrm{fast}} v_{\mathrm{fast}} + \tilde{A}_{\mathrm{slow}} v_{\mathrm{slow}}$ to arrive at a vanishingly small free-space visibility $v_{\mathrm{HOM}} = 0.003$.

5.5. Summary and outlook

To summarize, we have presented a room-temperature source of telecom-band single photons based on microcavity-coupled carbon nanotube quantum defects. Emission efficiency and indistinguishability are greatly enhanced by operating the system in the regime of incoherent good cavity-coupling. In particular, the visibility in the two-photon interference data in Fig. 5.6c corresponds to a 217-fold enhancement of the value estimated for the free-space limit. For spectrally filtered free-space emission, the same visibility can be achieved in principle, yet at the cost of very low single photon efficiency. In the incoherent good cavity regime implemented here, the measured lower bound for the cavity-enhanced single photon efficiency is a factor of four larger than the estimated upper bound for spectrally filtered free-space decay, whose actual value we expect to be at least one order of magnitude smaller when taking into account the non-unity NTD quantum yield. Further benefit arises from the fiber-based design of our cavity, which in principle allows unity in-fiber coupling efficiency in contrast to free-space collection with inherent diffraction losses.

To our knowledge, our results represent the first demonstration of cavity-enhanced indistinguishability for a quantum emitter with room-temperature dephasing. We estimate that the current two-photon interference visibility of about 0.5 can be improved to near-unity values by increasing the cavity finesse to 35000, a feasible value with open fiber cavities [63]. Simultaneously, a further reduction of the mode volume to recently reported values [274] would yield an enhancement in emission efficiency by another order of magnitude. This would also result in a decrease of experimental uncertainties, which are currently limited by the low emitter count rates on the order of a few kHz in our setup. Even without these improvements, our results represent a step towards room-temperature quantum photonic devices for applications at telecom-wavelength in optical quantum computation [384] or long-distance communication relying on optical quantum repeaters [385].

6 Summary and outlook

This dissertation reported on the coupling of excitons in low-dimensional semiconductors to fiber-based Fabry-Pérot cavities [53–56], optical resonators in which one mirror was micromachined on the tip of an optical fiber. This platform was employed to achieve microscopic mode volumes at correspondingly large light-matter coupling strengths and full tunability of the relative mirror position, providing a straightforward way to place individual quantum emitters inside the cavity mode volume [60, 62, 274, 331] and to investigate light-matter coupling as a function of lateral cavity mode position [65].

In Chapter 4, we presented experiments on cavity-coupled excitons in a monolayer of molybdenum diselenide [36], a two-dimensional transition metal dichalcogenide semiconductor [33]. The large exciton binding energies and oscillator strengths in this material platform provided access to the regime of strong exciton-photon coupling [77], in which coherently hybridized light-matter quantum states called exciton-polaritons are formed [13]. We operated the cavity setup at cryogenic temperatures [328] to minimize phonon-induced broadening of the exciton linewidth, requiring a thorough investigation of vibrational fluctuations in the cavity length induced by the cryostat compressor.

In the framework of this dissertation, we developed a fabrication technique to locally control the properties of polaritons formed in our device via their excitonic fraction. TMDs are highly suitable for this purpose due to the large susceptibility of two-dimensional excitons to their dielectric environment [101], which can be tuned by incorporating monolayer semiconductors in tailored van der Waals heterostacks [68–70]. To harness these properties, we locally removed the hexagonal boron nitride layer used for TMD encapsulation [340] by etching, creating disk-shaped domains of excitons with modified resonance energies. Upon cavity-coupling, the local modulation of the exciton energy resulted in shifts of the polariton energies, with a magnitude of several meV and tunability via the cavity energy. In addition, we demonstrated operation of our system in the regime of dispersive cavity-coupling [71, 72], where an effective hopping was mediated between highly exciton-like polaritons localized to different domains in the device as defined by the nanostructured dielectric environment.

The ability to engineer polariton energy landscapes has enabled experiments in non-

equilibrium many-body physics [13, 42] and quantum simulation [41, 210] in established semiconductor platforms by defining lattice potentials for these intriguing light-matter quantum states [67], which inherit properties from both photon and exciton. TMDs promise to add novel and unique perspectives to this field, including spin-valley locking [193, 353] and the coupling to novel exciton states in moiré heterostructures [P3, 206], but flexible and scalable methods for polariton trapping have remained challenging despite recent efforts [355–358]. The fabrication approach developed in this work is expected to provide such a method, enabling large-scale TMD-based polariton lattices. The required two-dimensional cavity geometry, which contrasts the Gaussian mode of our fiber cavity, could be implemented with a recently demonstrated micro-mechanical assembly technique for microcavity-coupling of TMDs [366]. In addition, unintended local variations of polariton energies in the present devices, likely arising from strain induced during heterostack assembly, could be mitigated by an improved fabrication approach, including the cleaning of interfaces in the heterostack using atomic force microscopy [386]. Further improvements in the form of narrower polariton linewidths could be achieved by reducing photonic scattering loss at the etch site edges by optimizing the hBN thickness.

The results of this work also offer perspectives beyond straightforward improvements to the present device. The presented fabrication method could be used in novel sample geometries, with a first example provided by our recent implementation of a plasmonic lattice embedded in a van der Waals heterostack [P4]. Another example is provided by combining nanostructured hBN layers with graphene-based capacitors to realize spatially modulated electric fields for the trapping of excitons [37, 38, 387]. In addition, effective exciton hopping mediated by the cavity in the dispersive coupling regime as implemented here has scarcely been investigated for the case of bosonic excitons, motivating further investigations. Finally, it is exciting to risk a highly speculative look into future exciton-polariton devices. Here, a long-standing challenge is to engineer strong effective photon-photon interactions by dressing with interacting excitons [42, 186] to realize photonic quantum simulators [12] and nonlinearities on the single photon level [186]. One strategy towards enhanced polariton interactions is confinement to small quantum well areas [186]. While this is achieved in principle in the present device, small shifts in exciton resonance energy upon dielectric modulation lead to undesired hybridization of localized polaritons with excitons in the surrounding monolayer, adding to the challenge of insufficient exciton-exciton interaction strength in TMDs. However, novel van der Waals materials might emerge from ongoing research, in which excitons with increased interaction strength give rise to enhanced nonlinearities based on polaritons confined by engineered dielectric environments.

Chapter 5 reported on cavity-coupling of excitons in fluorescent carbon nanotube defects [31]. In these quantum emitters, a local modification of the nanotube lattice by the incorporation of molecular defects enables the localization of individual excitons, accompanied by a strong redshift in emission wavelengths to the technologically relevant telecom

band and room-temperature emission of single photons [73]. In our experiments, we implemented the regime of incoherent good cavity-coupling as motivated by a recent theoretical proposal [45]. In this regime, the emitter spectral linewidth which is broadened by strong dephasing greatly exceeds that of the cavity, resulting in a drastic spectral purification of the emitted photons. Operating a room-temperature fiber cavity setup, we demonstrated the emission of telecom-band single photons from cavity-coupled NTDs. We utilized the tunability of the cavity system to infer the emitter linewidth from cavity-based spectroscopy. Further, we demonstrated tunability of the emission intensity via the mode volume, consistent with an expected enhancement of the photon emission efficiency induced by the modified density of states in the cavity. The enhanced photon spectral purity enabled two-photon interference experiments in an imbalanced Mach-Zehnder interferometer, where we measured an interference visibility of around 0.5. The results of a theoretical model accounting for the presence of a dark NTD exciton reservoir are in qualitative agreement with the experimental results.

While NTDs are promising candidates for sources of quantum light operating at telecom wavelengths, strong room-temperature dephasing prevents the emission of indistinguishable single photons which are an important resource in photonic quantum technologies [10, 257, 368, 369]. The same challenge is faced in telecom-band sources based on different room-temperature emitters [229, 239]. The results presented in Chapter 5 demonstrate that incoherent good cavity-coupling constitutes an extremely promising strategy to overcome this limitation. The measured two-photon interference visibility, which is a direct measure for the indistinguishability, exceeds the one expected for free-space emission by an estimated two orders of magnitude. In addition, cavity-coupling enhances the single photon emission efficiency by at least a factor of four compared to the value expected for filtering at a spectral bandwidth similar to the cavity linewidth, a competing strategy to increase the indistinguishability. Our simulation results suggest that by increasing the cavity finesse to state of the art values, near unity two-photon visibilities could be achieved in our setup. An additional reduction of the mode volume via shallower fiber mirror profiles would yield a further enhancement in emission efficiency. A more speculative but highly interesting perspective towards increased source brightness is to combine cavity-coupled NTDs with nanoplasmonic emitters [388, 389]. The experimental scheme implemented here could straightforwardly be applied to different emitters or in different cavity geometries. Our results thus establish incoherent good cavity-coupling as a promising strategy for the development of optimized single photon sources operating at room-temperature and telecom wavelengths.

To conclude, it is worth noting that the experimental results presented in this thesis build on implementations of highly different regimes of cavity-coupling, highlighting the versatility of the fiber cavity platform. Our results add constructively to the large variety of experiments on solid-state emitters performed in this cavity geometry [60, 61, 64, 65, 294,

331, 390, 391], which are highly likely to see further stimulation by the recent developments and commercialization efforts of setups operating at cryogenic temperatures in closed-cycle cryostats [328–332]. Other exciting applications, already demonstrated or envisioned, include harnessing the large sensitivity of high finesse fiber cavities to optical extinction loss in sensing of gases [392] or nanoparticles and molecules in liquids [393, 394], as well as in cavity-enhanced microscopy [63, 159, 395, 396]. These highly promising implementations contribute to the large variety of research activities on platforms for tailored photonic environments, making it easy to imagine that the interaction between light and matter will continue to attract dedicated scientific interest.

Transfer matrix simulation of dielectric multilayer structures

A

Formalism

To compute the optical response of dielectric multilayer structures such as highly reflective distributed Bragg reflector coatings of the cavity mirrors, we employ a widely used transfer matrix formalism which we describe briefly in the following. We assume normal incidence on the multilayer structure, and describe the relation between the complex electric field amplitude of left- and right-traveling electromagnetic waves E_i^+ and E_i^- in neighboring elements of the structure, indexed by i and $i+1$, in terms of multiplication with a matrix M as

$$\begin{pmatrix} E_{i+1}^+ \\ E_{i+1}^- \end{pmatrix} = M \begin{pmatrix} E_i^+ \\ E_i^- \end{pmatrix}. \tag{A.1}$$

In our work, we adapt the convention of Refs. [108, 397]. The transfer matrices M_L for propagation in a layer of thickness d and refractive index n and M_I for an interface between media of different refractive indices n_1 and n_2 are given by

$$M_\mathrm{L} = \begin{pmatrix} \exp(i\frac{2\pi n d}{\lambda}) & 0 \\ 0 & \exp(-i\frac{2\pi n d}{\lambda}) \end{pmatrix} \quad \text{and} \quad M_\mathrm{I} = \frac{1}{2n_2}\begin{pmatrix} n_1+n_2 & n_2-n_1 \\ n_2-n_1 & n_1+n_2 \end{pmatrix} \tag{A.2}$$

where λ is the optical wavelength.

Based on Eq. (A.2), the total transfer matrix M_tot of the full structure is computed as the product of the matrices associated with subsequent elements, starting with the matrix of the first element. Amplitude reflection and transmission coefficients r_tot and t_tot, which determine the optical response of the structure, are obtained from the coefficients of the total transfer matrix as

$$r_\mathrm{tot} = -\frac{M_\mathrm{tot}^{21}}{M_\mathrm{tot}^{22}} \quad \text{and} \quad t_\mathrm{tot} = \frac{M_\mathrm{tot}^{11}M_\mathrm{tot}^{22} - M_\mathrm{tot}^{21}M_\mathrm{tot}^{12}}{M_\mathrm{tot}^{22}}\sqrt{\frac{n_\mathrm{l}}{n_\mathrm{f}}}, \tag{A.3}$$

in which n_l and n_f are the refractive indices of the first and last layer of the structure under consideration and indices j and k in the labeling of components M_tot^{jk} denote matrix row

and column, respectively. From these relations, the coefficients of reflected and transmitted power are computed as $R_{\mathrm{tot}} = |r_{\mathrm{tot}}|^2$ and $T_{\mathrm{tot}} = |t_{\mathrm{tot}}|^2$.

To obtain the optical intensity I at a position z_0 along the optical axis z of the structure, the full transfer matrix for propagation to this position $M_{\mathrm{tot}}(z_0)$ is calculated. Next, the electric field vector is obtained as $\left(E^+(z_0), E^-(z_0)\right)^T = M_{\mathrm{tot}}(z_0) \cdot (1, r_{\mathrm{tot}}(z_0))^T$, from which the intensity computes to $I(z_0) = \left|E^+(z_0) + E^-(z_0)\right|^2$.

Simulation of mirror coatings

For numerical analysis of the mirror coatings employed in the experiments presented in this work, we described the wavelength-dependent refractive index using the Sellmeier formula

$$n^2(\lambda) = 1 + \sum_i \frac{B_i \lambda^2}{\lambda^2 - C_i} \tag{A.4}$$

with the Sellmeier coefficients B_1, B_2, B_3 and C_1, C_2, C_3. To obtain the refractive indices of SiO_2, TiO_2 and Ta_2O_5, we fit Eq. (A.4) with the coefficients as free parameters to refractive index data [398] in the relevant wavelength range. The thicknesses of individual layers in commercial coatings were provided by the manufacturer. Thicknesses of the exemplary coating investigated in Fig. 2.8 were computed as $\lambda_s / (4n(\lambda_s))$ from the wavelength-dependent refractive index.

Semiclassical treatment of light-matter coupling

The transfer matrix formalism also allows for a numerical analysis of quantum well-cavity coupling in the semiclassical treatment introduced in Section 2.4. This is achieved by incorporating the quantum well transfer matrix [164, p. 162]

$$M_{\mathrm{QW}} = \frac{1}{t_{\mathrm{QW}}} \begin{pmatrix} t_{\mathrm{QW}}^2 - r_{\mathrm{QW}}^2 & r_{\mathrm{QW}} \\ -r_{\mathrm{QW}} & 1 \end{pmatrix}, \tag{A.5}$$

with r_{QW} and r_{QW} defined in Eq. (2.14), in the computation of the full transfer matrix of the structure. Using this approach, we numerically verified the agreement between the semiclassical and quantum mechanical treatment of quantum well-cavity coupling introduced in Section 2.4 for the experimental parameter regime relevant to this work.

Hong-Ou-Mandel coincidence histograms

B

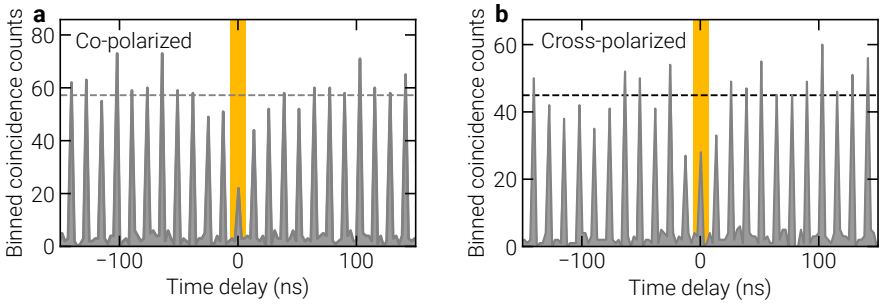

Figure B.1.: Hong-Ou-Mandel coincidence histograms for NTD 3. Coincidence histograms obtained in two-photon interference experiments for co- and cross-polarized configuration of the imbalanced Mach-Zehnder interferometer (**a** and **b**, respectively), performed on a cavity-coupled nanotube defect (NTD 3) as described in Chapter 5. The histograms were used to compute the Hong-Ou-Mandel (HOM) cross-correlation function $g^{(2)}_{\mathrm{HOM}}$ shown in Fig. 5.6b.

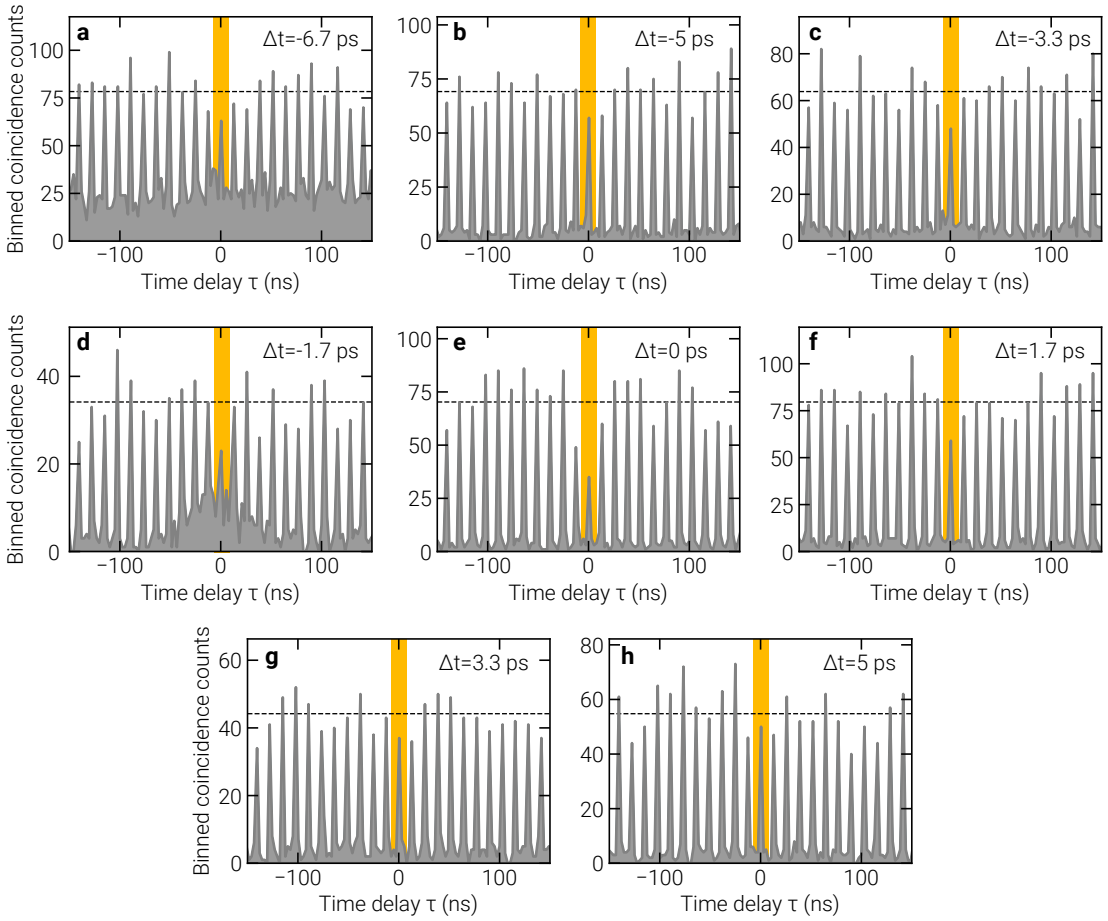

Figure B.2.: Hong-Ou-Mandel coincidence histograms for NTD 1. a-h, Coincidence histograms obtained in two-photon interference experiments for varying interferometer delay Δt, performed on a cavity-coupled nanotube defect (NTD 1) as described in Chapter 5. The histograms were used to compute the Hong-Ou-Mandel (HOM) cross-correlation function $g^{(2)}_{\mathrm{HOM}}(0)$, resulting in the HOM-Dip of Fig. 5.6c. The increased background in **a** and **d** as compared to all other histograms stems from incoherent room light and electronic noise caused by construction works, respectively, and was corrected for in the computation of $g^{(2)}_{\mathrm{HOM}}(0)$. For all other measurements, this background was absent.

List of Abbreviations

Term	Description	Page List
CCD	Charge-coupled device	56, 66, 73, 83, 85
CNT	Carbon nanotube	2, 3, 10–15, 29, 49
DBR	Distributed bragg reflector	17–20, 22, 23, 29, 38, 50, 51, 56, 65, 66, 74, 78, 103, 104, 118
FWHM	Full width at half maximum	9, 19, 22, 31, 37–39, 60, 71, 78, 85, 106
hBN	Hexagonal boron nitride	29, 30, 66, 71, 72, 74–78, 80–83, 85, 87, 88, 93, 122
HBT	Hanbury-Brown-Twiss experiment	31–33, 36, 56, 62, 105, 110, 112, 113
HOM	Hong-Ou-Mandel experiment	37, 45, 46, 110–114, 116, 118
HWHM	Half width at half maximum	23
LP	Lower polariton	25, 26
NTD	Carbon nanotube defect	13–15, 30, 31, 53–56, 58, 100–108, 110, 111, 113, 114, 116–119, 123
PCL	Polycaprolactone	77
PL	Photoluminescence	14, 54, 73, 77, 78, 89, 103–108, 110, 116, 118
PS	Polystyrene	54, 58
rms	Root mean square	68, 70
SEM	Scanning electron microscope	76, 77
SNSPD	Superconducting nanowire single photon detector	56, 61, 62
TEM	Transverse electromagnetic mode	52, 106

Term	Description	Page List
TMD	Transition metal dichalcogenide	2, 3, 5–7, 9, 22, 24, 27–30, 49, 63, 66, 71, 72, 74, 76, 80, 82, 85, 87, 88, 97, 121, 122
UP	Upper polariton	25, 26

References

[1] Einstein, A.: "Über einen die Erzeugung und Verwandlung des Lichtes betreffenden heuristischen Gesichtspunkt." *Annalen der Physik* **322**, 132–148 (1905).

[2] Lewis, G. N.: "The Conservation of Photons." *Nature* **118**, 874–875 (1926).

[3] Ekert, A. and Jozsa, R.: "Quantum computation and Shor's factoring algorithm." *Reviews of Modern Physics* **68**, 733–753 (1996).

[4] Ladd, T. D., Jelezko, F., Laflamme, R., Nakamura, Y., Monroe, C., and O'Brien, J. L.: "Quantum computers." *Nature* **464**, 45–53 (2010).

[5] Liu, J., Liu, M., Liu, J.-P., Ye, Z., Wang, Y., Alexeev, Y., Eisert, J., and Jiang, L.: "Towards provably efficient quantum algorithms for large-scale machine-learning models." *Nature Communications* **15**, 434 (2024).

[6] Gisin, N., Ribordy, G., Tittel, W., and Zbinden, H.: "Quantum cryptography." *Reviews of Modern Physics* **74**, 145–195 (2002).

[7] Pirandola, S., Andersen, U. L., Banchi, L., Berta, M., Bunandar, D., Colbeck, R., Englund, D., Gehring, T., Lupo, C., Ottaviani, C., Pereira, J. L., Razavi, M., Shamsul Shaari, J., Tomamichel, M., Usenko, V. C., Vallone, G., Villoresi, P., and Wallden, P.: "Advances in quantum cryptography." *Advances in Optics and Photonics* **12**, 1012 (2020).

[8] Kimble, H. J.: "The quantum internet." *Nature* **453**, 1023–1030 (2008).

[9] Wehner, S., Elkouss, D., and Hanson, R.: "Quantum internet: A vision for the road ahead." *Science* **362**, eaam9288 (2018).

[10] O'Brien, J. L.: "Optical Quantum Computing." *Science* **318**, 1567–1570 (2007).

[11] Aspuru-Guzik, A. and Walther, P.: "Photonic quantum simulators." *Nature Physics* **8**, 285–291 (2012).

[12] Hartmann, M. J.: "Quantum simulation with interacting photons." *Journal of Optics* **18**, 104005 (2016).

[13] Deng, H., Haug, H., and Yamamoto, Y.: "Exciton-polariton Bose-Einstein condensation." *Reviews of Modern Physics* **82**, 1489–1537 (2010).

[14] Jia, N., Schine, N., Georgakopoulos, A., Ryou, A., Clark, L. W., Sommer, A., and Simon, J.: "A strongly interacting polaritonic quantum dot." *Nature Physics* **14**, 550–554 (2018).

[15] Kroemer, H.: "A proposed class of hetero-junction injection lasers." *Proceedings of the IEEE* **51**, 1782–1783 (1963).

[16] Ivchenko, E. and Pikus, G.: "Superlattices and other heterostructures: Symmetry and optical phenomena." Springer series in solid-state sciences. Springer Berlin Heidelberg, 2012.

[17] Michler, P.: "Single Quantum Dots: Fundamentals, Applications, and New Concepts." Topics in Applied Physics. Springer Berlin Heidelberg, 2003.

[18] Petta, J. R., Johnson, A. C., Taylor, J. M., Laird, E. A., Yacoby, A., Lukin, M. D., Marcus, C. M., Hanson, M. P., and Gossard, A. C.: "Coherent Manipulation of Coupled Electron Spins in Semiconductor Quantum Dots." *Science* **309**, 2180–2184 (2005).

[19] Michler, P., Kiraz, A., Becher, C., Schoenfeld, W. V., Petroff, P. M., Zhang, L., Hu, E., and Imamoglu, A.: "A Quantum Dot Single-Photon Turnstile Device." *Science* **290**, 2282–2285 (2000).

[20] Michler, P., Imamoğlu, A., Mason, M. D., Carson, P. J., Strouse, G. F., and Buratto, S. K.: "Quantum correlation among photons from a single quantum dot at room temperature." *Nature* **406**, 968–970 (2000).

[21] Santori, C., Fattal, D., Vučković, J., Solomon, G. S., and Yamamoto, Y.: "Indistinguishable photons from a single-photon device." *Nature* **419**, 594–597 (2002).

[22] Mak, K. F., Lee, C., Hone, J., Shan, J., and Heinz, T. F.: "Atomically Thin MoS_2: A New Direct-Gap Semiconductor." *Physical Review Letters* **105**, 136805 (2010).

[23] Novoselov, K. S., Geim, A. K., Morozov, S. V., Jiang, D., Zhang, Y., Dubonos, S. V., Grigorieva, I. V., and Firsov, A. A.: "Electric Field Effect in Atomically Thin Carbon Films." *Science* **306**, 666–669 (2004).

[24] Wang, Q. H., Kalantar-Zadeh, K., Kis, A., Coleman, J. N., and Strano, M. S.: "Electronics and optoelectronics of two-dimensional transition metal dichalcogenides." *Nature Nanotechnology* **7**, 699–712 (2012).

[25] Mak, K. F. and Shan, J.: "Photonics and optoelectronics of 2D semiconductor transition metal dichalcogenides." *Nature Photonics* **10**, 216–226 (2016).

[26] Tan, T., Jiang, X., Wang, C., Yao, B., and Zhang, H.: "2D Material Optoelectronics for Information Functional Device Applications: Status and Challenges." *Advanced Science* **7**, 2000058 (2020).

[27] Wang, S., Liu, X., and Zhou, P.: "The Road for 2D Semiconductors in the Silicon Age." *Advanced Materials* **34**, 2106886 (2022).

[28] Iijima, S.: "Helical microtubules of graphitic carbon." *Nature* **354**, 56–58 (1991).

[29] De Volder, M. F. L., Tawfick, S. H., Baughman, R. H., and Hart, A. J.: "Carbon Nanotubes: Present and Future Commercial Applications." *Science* **339**, 535–539 (2013).

[30] Baydin, A., Tay, F., Fan, J., Manjappa, M., Gao, W., and Kono, J.: "Carbon Nanotube Devices for Quantum Technology." *Materials* **15**, 1535 (2022).

[31] He, X., Htoon, H., Doorn, S. K., Pernice, W. H. P., Pyatkov, F., Krupke, R., Jeantet, A., Chassagneux, Y., and Voisin, C.: "Carbon nanotubes as emerging quantum-light sources." *Nature Materials* **17**, 663–670 (2018).

[32] Avouris, P., Freitag, M., and Perebeinos, V.: "Carbon-nanotube photonics and optoelectronics." *Nature Photonics* **2**, 341–350 (2008).

[33] Wang, G., Chernikov, A., Glazov, M. M., Heinz, T. F., Marie, X., Amand, T., and Urbaszek, B.: "Colloquium: Excitons in atomically thin transition metal dichalcogenides." *Reviews of Modern Physics* **90**, 021001 (2018).

[34] Miyauchi, Y., Iwamura, M., Mouri, S., Kawazoe, T., Ohtsu, M., and Matsuda, K.: "Brightening of excitons in carbon nanotubes on dimensionality modification." *Nature Photonics* **7**, 715–719 (2013).

[35] Piao, Y., Meany, B., Powell, L. R., Valley, N., Kwon, H., Schatz, G. C., and Wang, Y.: "Brightening of carbon nanotube photoluminescence through the incorporation of sp^3 defects." *Nature Chemistry* **5**, 840–845 (2013).

[36] Li, Y., Ludwig, J., Low, T., Chernikov, A., Cui, X., Arefe, G., Kim, Y. D., van der Zande, A. M., Rigosi, A., Hill, H. M., Kim, S. H., Hone, J., Li, Z., Smirnov, D., and Heinz, T. F.: "Valley Splitting and Polarization by the Zeeman Effect in Monolayer $MoSe_2$." *Physical Review Letters* **113**, 266804 (2014).

[37] Thureja, D., Imamoglu, A., Smoleński, T., Amelio, I., Popert, A., Chervy, T., Lu, X., Liu, S., Barmak, K., Watanabe, K., Taniguchi, T., Norris, D. J., Kroner, M., and Murthy, P. A.: "Electrically tunable quantum confinement of neutral excitons." *Nature* **606**, 298–304 (2022).

[38] Hu, J., Lorchat, E., Chen, X., Watanabe, K., Taniguchi, T., Heinz, T. F., Murthy, P. A., and Chervy, T.: "Quantum control of exciton wave functions in 2D semiconductors." *Science Advances* **10**, eadk6369 (2024).

[39] Maiman, T. H.: "Stimulated Optical Radiation in Ruby." *Nature* **187**, 493–494 (1960).

[40] Siegman, A. E.: "Lasers." University Science Books, 1986.

[41] Boulier, T., Jacquet, M. J., Maître, A., Lerario, G., Claude, F., Pigeon, S., Glorieux, Q., Amo, A., Bloch, J., Bramati, A., and Giacobino, E.: "Microcavity Polaritons for Quantum Simulation." *Advanced Quantum Technologies* **3**, 2000052 (2020).

[42] Carusotto, I. and Ciuti, C.: "Quantum fluids of light." *Reviews of Modern Physics* **85**, 299–366 (2013).

[43] Purcell, E.: "Spontaneous emission probabilities at radio frequencies." *Physical Review* **69**, 681 (1946).

[44] Auffèves, A., Gérard, J.-M., and Poizat, J.-P.: "Pure emitter dephasing: A resource for advanced solid-state single-photon sources." *Physical Review A* **79**, 053838 (2009).

[45] Grange, T., Hornecker, G., Hunger, D., Poizat, J.-P., Gérard, J.-M., Senellart, P., and Auffèves, A.: "Cavity-Funneled Generation of Indistinguishable Single Photons from Strongly Dissipative Quantum Emitters." *Physical Review Letters* **114**, 193601 (2015).

[46] Weisbuch, C., Nishioka, M., Ishikawa, A., and Arakawa, Y.: "Observation of the coupled exciton-photon mode splitting in a semiconductor quantum microcavity." *Physical Review Letters* **69**, 3314–3317 (1992).

[47] Villeneuve, P. R., Fan, S., and Joannopoulos, J. D.: "Microcavities in photonic crystals: Mode symmetry, tunability, and coupling efficiency." *Physical Review B* **54**, 7837–7842 (1996).

[48] Chikkaraddy, R., de Nijs, B., Benz, F., Barrow, S. J., Scherman, O. A., Rosta, E., Demetriadou, A., Fox, P., Hess, O., and Baumberg, J. J.: "Single-molecule strong coupling at room temperature in plasmonic nanocavities." *Nature* **535**, 127–130 (2016).

[49] Kravets, V. G., Kabashin, A. V., Barnes, W. L., and Grigorenko, A. N.: "Plasmonic Surface Lattice Resonances: A Review of Properties and Applications." *Chemical Reviews* **118**, 5912–5951 (2018).

[50] Kuznetsov, A. I., Miroshnichenko, A. E., Brongersma, M. L., Kivshar, Y. S., and Luk'yanchuk, B.: "Optically resonant dielectric nanostructures." *Science* **354**, aag2472 (2016).

[51] Koshelev, K., Lepeshov, S., Liu, M., Bogdanov, A., and Kivshar, Y.: "Asymmetric Metasurfaces with High-Q Resonances Governed by Bound States in the Continuum." *Physical Review Letters* **121**, 193903 (2018).

[52] Weber, T., Kühner, L., Sortino, L., Ben Mhenni, A., Wilson, N. P., Kühne, J., Finley, J. J., Maier, S. A., and Tittl, A.: "Intrinsic strong light-matter coupling with self-hybridized bound states in the continuum in van der Waals metasurfaces." *Nature Materials* **22**, 970–976 (2023).

[53] Trupke, M., Hinds, E. A., Eriksson, S., Curtis, E. A., Moktadir, Z., Kukharenka, E., and Kraft, M.: "Microfabricated high-finesse optical cavity with open access and small volume." *Applied Physics Letters* **87**, 211106 (2005).

[54] Steinmetz, T., Colombe, Y., Hunger, D., Hänsch, T. W., Balocchi, A., Warburton, R. J., and Reichel, J.: "Stable fiber-based Fabry-Pérot cavity." *Applied Physics Letters* **89**, 111110 (2006).

[55] Muller, A., Flagg, E. B., Lawall, J. R., and Solomon, G. S.: "Ultrahigh-finesse, low-mode-volume Fabry-Perot microcavity." *Optics Letters* **35**, 2293 (2010).

[56] Hunger, D., Steinmetz, T., Colombe, Y., Deutsch, C., Hänsch, T. W., and Reichel, J.: "A fiber Fabry-Perot cavity with high finesse." *New Journal of Physics* **12**, 065038 (2010).

[57] Brekenfeld, M., Niemietz, D., Christesen, J. D., and Rempe, G.: "A quantum network node with crossed optical fibre cavities." *Nature Physics* **16**, 647–651 (2020).

[58] Steiner, M., Meyer, H. M., Deutsch, C., Reichel, J., and Köhl, M.: "Single Ion Coupled to an Optical Fiber Cavity." *Physical Review Letters* **110**, 043003 (2013).

[59] Brandstätter, B., McClung, A., Schüppert, K., Casabone, B., Friebe, K., Stute, A., Schmidt, P. O., Deutsch, C., Reichel, J., Blatt, R., and Northup, T. E.: "Integrated fiber-mirror ion trap for strong ion-cavity coupling." *Review of Scientific Instruments* **84**, 123104 (2013).

[60] Albrecht, R., Bommer, A., Deutsch, C., Reichel, J., and Becher, C.: "Coupling of a Single Nitrogen-Vacancy Center in Diamond to a Fiber-Based Microcavity." *Physical Review Letters* **110**, 243602 (2013).

[61] Benedikter, J., Kaupp, H., Hümmer, T., Liang, Y., Bommer, A., Becher, C., Krueger, A., Smith, J. M., Hänsch, T. W., and Hunger, D.: "Cavity-Enhanced Single-Photon Source Based on the Silicon-Vacancy Center in Diamond." *Physical Review Applied* **7**, 024031 (2017).

[62] Jeantet, A., Chassagneux, Y., Raynaud, C., Roussignol, P., Lauret, J. S., Besga, B., Estève, J., Reichel, J., and Voisin, C.: "Widely Tunable Single-Photon Source from a Carbon Nanotube in the Purcell Regime." *Physical Review Letters* **116**, 247402 (2016).

[63] Hümmer, T., Noe, J., Hofmann, M. S., Hänsch, T. W., Högele, A., and Hunger, D.: "Cavity-enhanced Raman microscopy of individual carbon nanotubes." *Nature Communications* **7**, 12155 (2016).

[64] Borel, A., Habrant-Claude, T., Rapisarda, F., Reichel, J., Doorn, S. K., Voisin, C., and Chassagneux, Y.: "Telecom Band Single-Photon Source Using a Grafted Carbon Nanotube Coupled to a Fiber Fabry-Perot Cavity in the Purcell Regime." *ACS Photonics* **10**, 2839–2845 (2023).

[65] Gebhardt, C., Förg, M., Yamaguchi, H., Bilgin, I., Mohite, A. D., Gies, C., Florian, M., Hartmann, M., Hänsch, T. W., Högele, A., and Hunger, D.: "Polariton hyperspectral imaging of two-dimensional semiconductor crystals." *Scientific Reports* **9**, 13756 (2019).

[66] Tan, L. B., Cotlet, O., Bergschneider, A., Schmidt, R., Back, P., Shimazaki, Y., Kroner, M., and İmamoğlu, A.: "Interacting Polaron-Polaritons." *Physical Review X* **10**, 021011 (2020).

[67] Schneider, C., Winkler, K., Fraser, M. D., Kamp, M., Yamamoto, Y., Ostrovskaya, E. A., and Höfling, S.: "Exciton-polariton trapping and potential landscape engineering." *Reports on Progress in Physics* **80**, 016503 (2016).

[68] Raja, A., Chaves, A., Yu, J., Arefe, G., Hill, H. M., Rigosi, A. F., Berkelbach, T. C., Nagler, P., Schüller, C., Korn, T., Nuckolls, C., Hone, J., Brus, L. E., Heinz, T. F., Reichman, D. R., and Chernikov, A.: "Coulomb engineering of the bandgap and excitons in two-dimensional materials." *Nature Communications* **8**, 15251 (2017).

[69] Peimyoo, N., Wu, H.-Y., Escolar, J., De Sanctis, A., Prando, G., Vollmer, F., Withers, F., Riis-Jensen, A. C., Craciun, M. F., Thygesen, K. S., and Russo, S.: "Engineering Dielectric Screening for Potential-well Arrays of Excitons in 2D Materials." *ACS Applied Materials & Interfaces* **12**, 55134–55140 (2020).

[70] Khestanova, E., Shahnazaryan, V., Kozin, V. K., Kondratyev, V. I., Krizhanovskii, D. N., Skolnick, M. S., Shelykh, I. A., Iorsh, I. V., and Kravtsov, V.: "Electrostatic control of nonlinear photonic-crystal polaritons in a monolayer semiconductor." *Nano Letters* **24**, 7350–7357 (2024).

[71] Blais, A., Huang, R.-S., Wallraff, A., Girvin, S. M., and Schoelkopf, R. J.: "Cavity quantum electrodynamics for superconducting electrical circuits: An architecture for quantum computation." *Physical Review A* **69**, 062320 (2004).

[72] Evans, R. E., Bhaskar, M. K., Sukachev, D. D., Nguyen, C. T., Sipahigil, A., Burek, M. J., Machielse, B., Zhang, G. H., Zibrov, A. S., Bielejec, E., Park, H., Lončar, M., and Lukin, M. D.: "Photon-mediated interactions between quantum emitters in a diamond nanocavity." *Science* **362**, 662–665 (2018).

[73] He, X., Hartmann, N. F., Ma, X., Kim, Y., Ihly, R., Blackburn, J. L., Gao, W., Kono, J., Yomogida, Y., Hirano, A., Tanaka, T., Kataura, H., Htoon, H., and Doorn, S. K.: "Tunable room-temperature single-photon emission at telecom wavelengths from sp^3 defects in carbon nanotubes." *Nature Photonics* **11**, 577–582 (2017).

[74] Lounis, B. and Orrit, M.: "Single-photon sources." *Reports on Progress in Physics* **68**, 1129–1179 (2005).

[75] Fox, A. M.: "Solid-State Quantum Emitters." *Advanced Quantum Technologies* 2300390 (2024).

[76] Geim, A. K. and Grigorieva, I. V.: "Van der Waals heterostructures." *Nature* **499**, 419–425 (2013).

[77] Schneider, C., Glazov, M. M., Korn, T., Höfling, S., and Urbaszek, B.: "Two-dimensional semiconductors in the regime of strong light-matter coupling." *Nature Communications* **9**, 2695 (2018).

[78] Mak, K. F., Xiao, D., and Shan, J.: "Light-valley interactions in 2D semiconductors." *Nature Photonics* **12**, 451–460 (2018).

[79] Mak, K. F. and Shan, J.: "Semiconductor moiré materials." *Nature Nanotechnology* **17**, 686–695 (2022).

[80] Novoselov, K. S., Jiang, D., Schedin, F., Booth, T. J., Khotkevich, V. V., Morozov, S. V., and Geim, A. K.: "Two-dimensional atomic crystals." *Proceedings of the National Academy of Sciences* **102**, 10451–10453 (2005).

[81] Wang, X., Gong, Y., Shi, G., Chow, W. L., Keyshar, K., Ye, G., Vajtai, R., Lou, J., Liu, Z., Ringe, E., Tay, B. K., and Ajayan, P. M.: "Chemical Vapor Deposition Growth of Crystalline Monolayer $MoSe_2$." *ACS Nano* **8**, 5125–5131 (2014).

[82] Liu, B., Fathi, M., Chen, L., Abbas, A., Ma, Y., and Zhou, C.: "Chemical Vapor Deposition Growth of Monolayer WSe_2 with Tunable Device Characteristics and Growth Mechanism Study." *ACS Nano* **9**, 6119–6127 (2015).

[83] Bilgin, I., Liu, F., Vargas, A., Winchester, A., Man, M. K. L., Upmanyu, M., Dani, K. M., Gupta, G., Talapatra, S., Mohite, A. D., and Kar, S.: "Chemical Vapor Deposition Synthesized Atomically Thin Molybdenum Disulfide with Optoelectronic-Grade Crystalline Quality." *ACS Nano* **9**, 8822–8832 (2015).

[84] Zhang, Y., Chang, T.-R., Zhou, B., Cui, Y.-T., Yan, H., Liu, Z., Schmitt, F., Lee, J., Moore, R., Chen, Y., Lin, H., Jeng, H.-T., Mo, S.-K., Hussain, Z., Bansil, A., and Shen, Z.-X.: "Direct observation of the transition from indirect to direct bandgap in atomically thin epitaxial $MoSe_2$." *Nature Nanotechnology* **9**, 111–115 (2014).

[85] Mattheiss, L. F.: "Band Structures of Transition-Metal-Dichalcogenide Layer Compounds." *Physical Review B* **8**, 3719–3740 (1973).

[86] Cheiwchanchamnangij, T. and Lambrecht, W. R. L.: "Quasiparticle band structure calculation of monolayer, bilayer, and bulk MoS_2." *Physical Review B* **85**, 205302 (2012).

[87] Splendiani, A., Sun, L., Zhang, Y., Li, T., Kim, J., Chim, C.-Y., Galli, G., and Wang, F.: "Emerging Photoluminescence in Monolayer MoS_2." *Nano Letters* **10**, 1271–1275 (2010).

[88] Xiao, D., Liu, G.-B., Feng, W., Xu, X., and Yao, W.: "Coupled Spin and Valley Physics in Monolayers of MoS_2 and Other Group-VI Dichalcogenides." *Physical Review Letters* **108**, 196802 (2012).

[89] Liu, G.-B., Shan, W.-Y., Yao, Y., Yao, W., and Xiao, D.: "Three-band tight-binding model for monolayers of group-VIB transition metal dichalcogenides." *Physical Review B* **88**, 085433 (2013).

[90] Zhu, Z. Y., Cheng, Y. C., and Schwingenschlögl, U.: "Giant spin-orbit-induced spin splitting in two-dimensional transition-metal dichalcogenide semiconductors." *Physical Review B* **84**, 153402 (2011).

[91] Kośmider, K., González, J. W., and Fernández-Rossier, J.: "Large spin splitting in the conduction band of transition metal dichalcogenide monolayers." *Physical Review B* **88**, 245436 (2013).

[92] Kormányos, A., Zólyomi, V., Drummond, N. D., and Burkard, G.: "Spin-Orbit Coupling, Quantum Dots, and Qubits in Monolayer Transition Metal Dichalcogenides." *Physical Review X* **4**, 011034 (2014).

[93] Glazov, M. M., Ivchenko, E. L., Wang, G., Amand, T., Marie, X., Urbaszek, B., and Liu, B. L.: "Spin and valley dynamics of excitons in transition metal dichalcogenide monolayers." *physica status solidi (b)* **252**, 2349–2362 (2015).

[94] Yao, W., Xiao, D., and Niu, Q.: "Valley-dependent optoelectronics from inversion symmetry breaking." *Physical Review B* **77**, 235406 (2008).

[95] Sallen, G., Bouet, L., Marie, X., Wang, G., Zhu, C. R., Han, W. P., Lu, Y., Tan, P. H., Amand, T., Liu, B. L., and Urbaszek, B.: "Robust optical emission polarization in MoS_2 monolayers through selective valley excitation." *Physical Review B* **86**, 081301 (2012).

[96] Cao, T., Wang, G., Han, W., Ye, H., Zhu, C., Shi, J., Niu, Q., Tan, P., Wang, E., Liu, B., and Feng, J.: "Valley-selective circular dichroism of monolayer molybdenum disulphide." *Nature Communications* **3**, 887 (2012).

[97] Ramasubramaniam, A.: "Large excitonic effects in monolayers of molybdenum and tungsten dichalcogenides." *Physical Review B* **86**, 115409 (2012).

[98] Komsa, H.-P. and Krasheninnikov, A. V.: "Effects of confinement and environment on the electronic structure and exciton binding energy of MoS_2 from first principles." *Physical Review B* **86**, 241201 (2012).

[99] He, K., Kumar, N., Zhao, L., Wang, Z., Mak, K. F., Zhao, H., and Shan, J.: "Tightly Bound Excitons in Monolayer WSe_2." *Physical Review Letters* **113**, 026803 (2014).

[100] Robert, C., Han, B., Kapuscinski, P., Delhomme, A., Faugeras, C., Amand, T., Molas, M. R., Bartos, M., Watanabe, K., Taniguchi, T., Urbaszek, B., Potemski, M., and Marie, X.: "Measurement of the spin-forbidden dark excitons in MoS_2 and $MoSe_2$ monolayers." *Nature Communications* **11**, 4037 (2020).

[101] Chernikov, A., Berkelbach, T. C., Hill, H. M., Rigosi, A., Li, Y., Aslan, B., Reichman, D. R., Hybertsen, M. S., and Heinz, T. F.: "Exciton Binding Energy and Nonhydrogenic Rydberg Series in Monolayer WS_2." *Physical Review Letters* **113**, 076802 (2014).

[102] Mak, K. F., He, K., Lee, C., Lee, G. H., Hone, J., Heinz, T. F., and Shan, J.: "Tightly bound trions in monolayer MoS_2." *Nature Materials* **12**, 207–211 (2013).

[103] Gao, F., Gong, Y., Titze, M., Almeida, R., Ajayan, P. M., and Li, H.: "Valley trion dynamics in monolayer $MoSe_2$." *Physical Review B* **94**, 245413 (2016).

[104] You, Y., Zhang, X.-X., Berkelbach, T. C., Hybertsen, M. S., Reichman, D. R., and Heinz, T. F.: "Observation of biexcitons in monolayer WSe_2." *Nature Physics* **11**, 477–481 (2015).

[105] Glazov, M. M., Amand, T., Marie, X., Lagarde, D., Bouet, L., and Urbaszek, B.: "Exciton fine structure and spin decoherence in monolayers of transition metal dichalcogenides." *Physical Review B* **89**, 201302 (2014).

[106] Selig, M., Berghäuser, G., Raja, A., Nagler, P., Schüller, C., Heinz, T. F., Korn, T., Chernikov, A., Malic, E., and Knorr, A.: "Excitonic linewidth and coherence lifetime in monolayer transition metal dichalcogenides." *Nature Communications* **7**, 13279 (2016).

[107] Jakubczyk, T., Delmonte, V., Koperski, M., Nogajewski, K., Faugeras, C., Langbein, W., Potemski, M., and Kasprzak, J.: "Radiatively Limited Dephasing and Exciton Dynamics in $MoSe_2$ Monolayers Revealed with Four-Wave Mixing Microscopy." *Nano Letters* **16**, 5333–5339 (2016).

[108] Fang, H. H., Han, B., Robert, C., Semina, M. A., Lagarde, D., Courtade, E., Taniguchi, T., Watanabe, K., Amand, T., Urbaszek, B., Glazov, M. M., and Marie, X.: "Control of the Exciton Radiative Lifetime in van der Waals Heterostructures." *Physical Review Letters* **123**, 067401 (2019).

[109] Polovnikov, B., Scherzer, J., Misra, S., Huang, X., Mohl, C., Li, Z., Göser, J., Förste, J., Bilgin, I., Watanabe, K., Taniguchi, T., Högele, A., and Baimuratov, A. S.: "Field-Induced Hybridization of Moiré Excitons in $MoSe_2/WS_2$ Heterobilayers." *Physical Review Letters* **132**, 076902 (2024).

[110] Ren, L., Robert, C., Urbaszek, B., Marie, X., Semina, M., and Glazov, M. M.: "Tuning absorption and emission in monolayer semiconductors: a brief survey." *Comptes Rendus. Physique* **22**, 43–52 (2022).

[111] Shree, S., Semina, M., Robert, C., Han, B., Amand, T., Balocchi, A., Manca, M., Courtade, E., Marie, X., Taniguchi, T., Watanabe, K., Glazov, M. M., and Urbaszek, B.: "Observation of exciton-phonon coupling in $MoSe_2$ monolayers." *Physical Review B* **98**, 035302 (2018).

[112] Mhenni, A. B., Van Tuan, D., Geilen, L., Petrić, M. M., Erdi, M., Watanabe, K., Taniguchi, T., Tongay, S., Müller, K., Wilson, N. P., Finley, J. J., Dery, H., and Barbone, M.: "Breakdown of the static dielectric screening approximation of Coulomb interactions in atomically thin semiconductors." *arXiv.org*, 2402.18639 (2024).

[113] Cho, Y. and Berkelbach, T. C.: "Environmentally sensitive theory of electronic and optical transitions in atomically thin semiconductors." *Physical Review B* **97**, 041409 (2018).

[114] Chaves, A., Azadani, J. G., Alsalman, H., da Costa, D. R., Frisenda, R., Chaves, A. J., Song, S. H., Kim, Y. D., He, D., Zhou, J., Castellanos-Gomez, A., Peeters, F. M., Liu, Z., Hinkle, C. L., Oh, S.-H., Ye, P. D., Koester, S. J., Lee, Y. H., Avouris, P., Wang, X., and Low, T.: "Bandgap engineering of two-dimensional semiconductor materials." *npj 2D Materials and Applications* **4**, 1–21 (2020).

[115] Borghardt, S., Tu, J.-S., Winkler, F., Schubert, J., Zander, W., Leosson, K., and Kardynał, B. E.: "Engineering of optical and electronic band gaps in transition metal dichalcogenide monolayers through external dielectric screening." *Physical Review Materials* **1**, 054001 (2017).

[116] Drüppel, M., Deilmann, T., Krüger, P., and Rohlfing, M.: "Diversity of trion states and substrate effects in the optical properties of an MoS_2 monolayer." *Nature Communications* **8**, 2117 (2017).

[117] Saito, R., Dresselhaus, G., and Dresselhaus, M. S.: "Physical Properties of Carbon Nanotubes." Imperial College Press, 1998.

[118] Hofmann, M.: "Spectroscopy of localized excitons in carbon nanotubes." PhD thesis, Ludwig-Maximilians-Universität München, 2016.

[119] Neto, A. H. C., Guinea, F., Peres, N. M. R., Novoselov, K. S., and Geim, A. K.: "The electronic properties of graphene." *Reviews of Modern Physics* **81**, 109–162 (2009).

[120] Saito, T.: "Multidimensional Aspects of Single-Wall Carbon Nanotube Synthesis." In: *Carbon Nanotubes and Graphene*, pp. 7–17. Elsevier, 2014.

[121] Saito, R., Fujita, M., Dresselhaus, G., and Dresselhaus, M. S.: "Electronic structure of chiral graphene tubules." *Applied Physics Letters* **60**, 2204–2206 (1992).

[122] Božović, I., Božović, N., and Damnjanović, M.: "Optical dichroism in nanotubes." *Physical Review B* **62**, 6971–6974 (2000).

[123] Miyauchi, Y., Oba, M., and Maruyama, S.: "Cross-polarized optical absorption of single-walled nanotubes by polarized photoluminescence excitation spectroscopy." *Physical Review B* **74**, 205440 (2006).

[124] Ichida, M., Mizuno, S., Tani, Y., Saito, Y., and Nakamura, A.: "Exciton Effects of Optical Transitions in Single-Wall Carbon Nanotubes." *Journal of the Physical Society of Japan* **68**, 3131–3133 (1999).

[125] Wang, F., Dukovic, G., Brus, L. E., and Heinz, T. F.: "The Optical Resonances in Carbon Nanotubes Arise from Excitons." *Science* **308**, 838–841 (2005).

[126] Maultzsch, J., Pomraenke, R., Reich, S., Chang, E., Prezzi, D., Ruini, A., Molinari, E., Strano, M. S., Thomsen, C., and Lienau, C.: "Exciton binding energies in carbon nanotubes from two-photon photoluminescence." *Physical Review B* **72**, 241402 (2005).

[127] Ando, T.: "Effects of Valley Mixing and Exchange on Excitons in Carbon Nanotubes with Aharonov-Bohm Flux." *Journal of the Physical Society of Japan* **75**, 024707 (2006).

[128] Mortimer, I. B. and Nicholas, R. J.: "Role of Bright and Dark Excitons in the Temperature-Dependent Photoluminescence of Carbon Nanotubes." *Physical Review Letters* **98**, 027404 (2007).

[129] Hertel, T., Himmelein, S., Ackermann, T., Stich, D., and Crochet, J.: "Diffusion Limited Photoluminescence Quantum Yields in 1-D Semiconductors: Single-Wall Carbon Nanotubes." *ACS Nano* **4**, 7161–7168 (2010).

[130] Shaver, J. and Kono, J.: "Temperature-dependent magneto-photoluminescence spectroscopy of carbon nanotubes: evidence for dark excitons." *Laser & Photonics Reviews* **1**, 260–274 (2007).

[131] Shaver, J., Crooker, S. A., Fagan, J. A., Hobbie, E. K., Ubrig, N., Portugall, O., Perebeinos, V., Avouris, P., and Kono, J.: "Magneto-optical spectroscopy of highly aligned carbon nanotubes: Identifying the role of threading magnetic flux." *Physical Review B* **78**, 081402 (2008).

[132] Zhou, W., Sasaki, T., Nakamura, D., Liu, H., Kataura, H., and Takeyama, S.: "Band-edge exciton states in a single-walled carbon nanotube revealed by magneto-optical spectroscopy in ultrahigh magnetic fields." *Physical Review B* **87**, 241406 (2013).

[133] Spataru, C. D., Ismail-Beigi, S., Capaz, R. B., and Louie, S. G.: "Theory and Ab Initio Calculation of Radiative Lifetime of Excitons in Semiconducting Carbon Nanotubes." *Physical Review Letters* **95**, 247402 (2005).

[134] Perebeinos, V., Tersoff, J., and Avouris, P.: "Radiative Lifetime of Excitons in Carbon Nanotubes." *Nano Letters* **5**, 2495–2499 (2005).

[135] Miyauchi, Y., Hirori, H., Matsuda, K., and Kanemitsu, Y.: "Radiative lifetimes and coherence lengths of one-dimensional excitons in single-walled carbon nanotubes." *Physical Review B* **80**, 081410 (2009).

[136] Hagen, A., Steiner, M., Raschke, M. B., Lienau, C., Hertel, T., Qian, H., Meixner, A. J., and Hartschuh, A.: "Exponential Decay Lifetimes of Excitons in Individual Single-Walled Carbon Nanotubes." *Physical Review Letters* **95**, 197401 (2005).

[137] Högele, A., Galland, C., Winger, M., and Imamoğlu, A.: "Photon Antibunching in the Photoluminescence Spectra of a Single Carbon Nanotube." *Physical Review Letters* **100**, 217401 (2008).

[138] Hofmann, M. S., Noé, J., Kneer, A., Crochet, J. J., and Högele, A.: "Ubiquity of Exciton Localization in Cryogenic Carbon Nanotubes." *Nano Letters* **16**, 2958–2962 (2016).

[139] Ghosh, S., Bachilo, S. M., Simonette, R. A., Beckingham, K. M., and Weisman, R. B.: "Oxygen Doping Modifies Near-Infrared Band Gaps in Fluorescent Single-Walled Carbon Nanotubes." *Science* **330**, 1656–1659 (2010).

[140] Ma, X., Adamska, L., Yamaguchi, H., Yalcin, S. E., Tretiak, S., Doorn, S. K., and Htoon, H.: "Electronic Structure and Chemical Nature of Oxygen Dopant States in Carbon Nanotubes." *ACS Nano* **8**, 10782–10789 (2014).

[141] Wang, P., Fortner, J., Luo, H., Kłos, J., Wu, X., Qu, H., Chen, F., Li, Y., and Wang, Y.: "Quantum Defects: What Pairs with the Aryl Group When Bonding to the sp^2 Carbon Lattice of Single-Wall Carbon Nanotubes?" *Journal of the American Chemical Society* **144**, 13234–13241 (2022).

[142] Saha, A., Gifford, B. J., He, X., Ao, G., Zheng, M., Kataura, H., Htoon, H., Kilina, S., Tretiak, S., and Doorn, S. K.: "Narrow-band single-photon emission through selective aryl functionalization of zigzag carbon nanotubes." *Nature Chemistry* **10**, 1089–1095 (2018).

[143] Kwon, H., Furmanchuk, A., Kim, M., Meany, B., Guo, Y., Schatz, G. C., and Wang, Y.: "Molecularly Tunable Fluorescent Quantum Defects." *Journal of the American Chemical Society* **138**, 6878–6885 (2016).

[144] Hartmann, N. F., Velizhanin, K. A., Haroz, E. H., Kim, M., Ma, X., Wang, Y., Htoon, H., and Doorn, S. K.: "Photoluminescence Dynamics of Aryl sp^3 Defect States in Single-Walled Carbon Nanotubes." *ACS Nano* **10**, 8355–8365 (2016).

[145] Kim, Y., Goupalov, S. V., Weight, B. M., Gifford, B. J., He, X., Saha, A., Kim, M., Ao, G., Wang, Y., Zheng, M., Tretiak, S., Doorn, S. K., and Htoon, H.: "Hidden Fine Structure of Quantum Defects Revealed by Single Carbon Nanotube Magneto-Photoluminescence." *ACS Nano* **14**, 3451–3460 (2020).

[146] Sykes, M. E., Kim, M., Wu, X., Wiederrecht, G. P., Peng, L., Wang, Y., Gosztola, D. J., and Ma, X.: "Ultrafast Exciton Trapping at sp^3 Quantum Defects in Carbon Nanotubes." *ACS Nano* **13**, 13264–13270 (2019).

[147] Luo, Y., He, X., Kim, Y., Blackburn, J. L., Doorn, S. K., Htoon, H., and Strauf, S.: "Carbon Nanotube Color Centers in Plasmonic Nanocavities: A Path to Photon Indistinguishability at Telecom Bands." *Nano Letters* **19**, 9037–9044 (2019).

[148] Fabry, C. and Perot, A.: "Theorie et applications d'une nouvelle methode de spectroscopie interferentielle." *Ann. Chim. Phys.* **16** (1899).

[149] Perot, A. and Fabry, C.: "On the Application of Interference Phenomena to the Solution of Various Problems of Spectroscopy and Metrology." *The Astrophysical Journal* **9**, 87 (1899).

[150] Vahala, K. J.: "Optical microcavities." *Nature* **424**, 839–846 (2003).

[151] Saleh, B. E. A. and Teich, M. C.: "Fundamentals of Photonics: Second Edition." John Wiley & Son, 2007.

[152] Ismail, N., Kores, C. C., Geskus, D., and Pollnau, M.: "Fabry-Pérot resonator: spectral line shapes, generic and related Airy distributions, linewidths, finesses, and performance at low or frequency-dependent reflectivity." *Optics Express* **24**, 16366 (2016).

[153] Husel, L.: "Ein optischer Bow-Tie-Resonator für ein photonisches Quantengatter." MSc thesis, Ludwig-Maximilians-Universität München, 2019.

[154] Rempe, G., Thompson, R. J., Kimble, H. J., and Lalezari, R.: "Measurement of ultralow losses in an optical interferometer." *Optics Letters* **17**, 363–365 (1992).

[155] Najer, D., Söllner, I., Sekatski, P., Dolique, V., Löbl, M. C., Riedel, D., Schott, R., Starosielec, S., Valentin, S. R., Wieck, A. D., Sangouard, N., Ludwig, A., and Warburton, R. J.: "A gated quantum dot strongly coupled to an optical microcavity." *Nature* **575**, 622–627 (2019).

[156] Thompson, R. J., Rempe, G., and Kimble, H. J.: "Observation of normal-mode splitting for an atom in an optical cavity." *Physical Review Letters* **68**, 1132–1135 (1992).

[157] Rempe, G., Thompson, R. J., Brecha, R. J., Lee, W. D., and Kimble, H. J.: "Optical bistability and photon statistics in cavity quantum electrodynamics." *Physical Review Letters* **67**, 1727–1730 (1991).

[158] Savona, V., Andreani, L., Schwendimann, P., and Quattropani, A.: "Quantum well excitons in semiconductor microcavities: Unified treatment of weak and strong coupling regimes." *Solid State Communications* **93**, 733–739 (1995).

[159] Mader, M., Reichel, J., Hänsch, T. W., and Hunger, D.: "A scanning cavity microscope." *Nature Communications* **6**, 7249 (2015).

[160] Basov, D. N., Asenjo-Garcia, A., Schuck, P. J., Zhu, X., and Rubio, A.: "Polariton panorama." *Nanophotonics* **10**, 549–577 (2021).

[161] Sidler, M., Back, P., Cotlet, O., Srivastava, A., Fink, T., Kroner, M., Demler, E., and Imamoglu, A.: "Fermi polaron-polaritons in charge-tunable atomically thin semiconductors." *Nature Physics* **13**, 255–261 (2017).

[162] Andreani, L., Savona, V., Schwendimann, P., and Quattropani, A.: "Polaritons in high reflectivity microcavities: semiclassical and full quantum treatment of optical properties." *Superlattices and Microstructures* **15**, 453–458 (1994).

[163] Savona, V.: "Linear optical properties of semiconductor microcavities with embedded quantum wells." In: *Confined Photon Systems*, pp. 173–242. Ed. by Benisty, H., Weisbuch, C., Polytechnique, É., Gérard, J.-M., Houdré, R., and Rarity, J. Springer Berlin Heidelberg, 1999, pp. 173–242.

[164] Kavokin, A., Baumberg, J., Malpuech, G., and Laussy, F.: "Microcavities." Oxford science publications. Oxford University Press, 2011.

[165] Flatten, L. C., He, Z., Coles, D. M., Trichet, A. a. P., Powell, A. W., Taylor, R. A., Warner, J. H., and Smith, J. M.: "Room-temperature exciton-polaritons with two-dimensional WS_2." *Scientific Reports* **6**, 1–7 (2016).

[166] Epstein, I., Terrés, B., Chaves, A. J., Pusapati, V.-V., Rhodes, D. A., Frank, B., Zimmermann, V., Qin, Y., Watanabe, K., Taniguchi, T., Giessen, H., Tongay, S., Hone, J. C., Peres, N. M. R., and Koppens, F. H. L.: "Near-Unity Light Absorption in a Monolayer WS_2 Van der Waals Heterostructure Cavity." *Nano Letters* **20**, 3545–3552 (2020).

[167] Andreani, L. C.: "Exciton-polaritons in superlattices." *Physics Letters A* **192**, 99–109 (1994).

[168] Zhu, Y., Gauthier, D. J., Morin, S. E., Wu, Q., Carmichael, H. J., and Mossberg, T. W.: "Vacuum Rabi splitting as a feature of linear-dispersion theory: Analysis and experimental observations." *Physical Review Letters* **64**, 2499–2502 (1990).

[169] Savona, V., Hradil, Z., Quattropani, A., and Schwendimann, P.: "Quantum theory of quantum-well polaritons in semiconductor microcavities." *Physical Review B* **49**, 8774–8779 (1994).

[170] Yamamoto, Y. and İmamoğlu, A.: "Mesoscopic quantum optics." Wiley-Interscience. Wiley, 1999.

[171] Hopfield, J. J.: "Theory of the Contribution of Excitons to the Complex Dielectric Constant of Crystals." *Physical Review* **112**, 1555–1567 (1958).

[172] Besga, B., Vaneph, C., Reichel, J., Estève, J., Reinhard, A., Miguel-Sánchez, J., Imamoğlu, A., and Volz, T.: "Polariton Boxes in a Tunable Fiber Cavity." *Physical Review Applied* **3**, 014008 (2015).

[173] Deng, H., Weihs, G., Santori, C., Bloch, J., and Yamamoto, Y.: "Condensation of Semiconductor Microcavity Exciton Polaritons." *Science* **298**, 199–202 (2002).

[174] Kasprzak, J., Richard, M., Kundermann, S., Baas, A., Jeambrun, P., Keeling, J. M. J., Marchetti, F. M., Szymańska, M. H., André, R., Staehli, J. L., Savona, V., Littlewood, P. B., Deveaud, B., and Dang, L. S.: "Bose-Einstein condensation of exciton polaritons." *Nature* **443**, 409–414 (2006).

[175] André, R., Heger, D., Dang, L. S., and Merle d'Aubigné, Y.: "Spectroscopy of polaritons in CdTe-based microcavities." *Journal of Crystal Growth* **184–185**, 758–762 (1998).

[176] Shimada, R., Xie, J., Avrutin, V., Özgür, Ü., and Morkoč, H.: "Cavity polaritons in ZnO-based hybrid microcavities." *Applied Physics Letters* **92**, 011127 (2008).

[177] Orfanakis, K., Rajendran, S. K., Walther, V., Volz, T., Pohl, T., and Ohadi, H.: "Rydberg exciton-polaritons in a Cu_2O microcavity." *Nature Materials* **21**, 767–772 (2022).

[178] Lidzey, D. G., Bradley, D. D. C., Skolnick, M. S., Virgili, T., Walker, S., and Whittaker, D. M.: "Strong exciton-photon coupling in an organic semiconductor microcavity." *Nature* **395**, 53–55 (1998).

[179] Kéna-Cohen, S., Davanço, M., and Forrest, S. R.: "Strong Exciton-Photon Coupling in an Organic Single Crystal Microcavity." *Physical Review Letters* **101**, 116401 (2008).

[180] Brehier, A., Parashkov, R., Lauret, J. S., and Deleporte, E.: "Strong exciton-photon coupling in a microcavity containing layered perovskite semiconductors." *Applied Physics Letters* **89**, 171110 (2006).

[181] Graf, A., Tropf, L., Zakharko, Y., Zaumseil, J., and Gather, M. C.: "Near-infrared exciton-polaritons in strongly coupled single-walled carbon nanotube microcavities." *Nature Communications* **7**, 13078 (2016).

[182] Möhl, C., Graf, A., Berger, F. J., Lüttgens, J., Zakharko, Y., Lumsargis, V., Gather, M. C., and Zaumseil, J.: "Trion-Polariton Formation in Single-Walled Carbon Nanotube Microcavities." *ACS Photonics* **5**, 2074–2080 (2018).

[183] Dirnberger, F., Bushati, R., Datta, B., Kumar, A., MacDonald, A. H., Baldini, E., and Menon, V. M.: "Spin-correlated exciton-polaritons in a van der Waals magnet." *Nature Nanotechnology* **17**, 1060–1064 (2022).

[184] Dirnberger, F., Quan, J., Bushati, R., Diederich, G. M., Florian, M., Klein, J., Mosina, K., Sofer, Z., Xu, X., Kamra, A., García-Vidal, F. J., Alù, A., and Menon, V. M.: "Magneto-optics in a van der Waals magnet tuned by self-hybridized polaritons." *Nature* **620**, 533–537 (2023).

[185] Wang, T., Zhang, D., Yang, S., Lin, Z., Chen, Q., Yang, J., Gong, Q., Chen, Z., Ye, Y., and Liu, W.: "Magnetically-dressed CrSBr exciton-polaritons in ultrastrong coupling regime." *Nature Communications* **14**, 5966 (2023).

[186] Verger, A., Ciuti, C., and Carusotto, I.: "Polariton quantum blockade in a photonic dot." *Physical Review B* **73**, 193306 (2006).

[187] Liu, X., Galfsky, T., Sun, Z., Xia, F., Lin, E.-c., Lee, Y.-H., Kéna-Cohen, S., and Menon, V. M.: "Strong light-matter coupling in two-dimensional atomic crystals." *Nature Photonics* **9**, 30–34 (2015).

[188] Dufferwiel, S., Schwarz, S., Withers, F., Trichet, A. a. P., Li, F., Sich, M., Del Pozo-Zamudio, O., Clark, C., Nalitov, A., Solnyshkov, D. D., Malpuech, G., Novoselov, K. S., Smith, J. M., Skolnick, M. S., Krizhanovskii, D. N., and Tartakovskii, A. I.: "Exciton-polaritons in van der Waals heterostructures embedded in tunable microcavities." *Nature Communications* **6**, 1–7 (2015).

[189] Gogna, R., Zhang, L., and Deng, H.: "Self-Hybridized, Polarized Polaritons in ReS_2 Crystals." *ACS Photonics* **7**, 3328–3332 (2020).

[190] Sun, Z., Gu, J., Ghazaryan, A., Shotan, Z., Considine, C. R., Dollar, M., Chakraborty, B., Liu, X., Ghaemi, P., Kéna-Cohen, S., and Menon, V. M.: "Optical control of room-temperature valley polaritons." *Nature Photonics* **11**, 491–496 (2017).

[191] Chen, Y.-J., Cain, J. D., Stanev, T. K., Dravid, V. P., and Stern, N. P.: "Valley-polarized exciton-polaritons in a monolayer semiconductor." *Nature Photonics* **11**, 431–435 (2017).

[192] Dufferwiel, S., Lyons, T. P., Solnyshkov, D. D., Trichet, A. a. P., Withers, F., Schwarz, S., Malpuech, G., Smith, J. M., Novoselov, K. S., Skolnick, M. S., Krizhanovskii, D. N., and Tartakovskii, A. I.: "Valley-addressable polaritons in atomically thin semiconductors." *Nature Photonics* **11**, 497–501 (2017).

[193] Lundt, N., Dusanowski, Ł., Sedov, E., Stepanov, P., Glazov, M. M., Klembt, S., Klaas, M., Beierlein, J., Qin, Y., Tongay, S., Richard, M., Kavokin, A. V., Höfling, S., and Schneider, C.: "Optical valley Hall effect for highly valley-coherent exciton-polaritons in an atomically thin semiconductor." *Nature Nanotechnology* **14**, 770–775 (2019).

[194] LaMountain, T., Nelson, J., Lenferink, E. J., Amsterdam, S. H., Murthy, A. A., Zeng, H., Marks, T. J., Dravid, V. P., Hersam, M. C., and Stern, N. P.: "Valley-selective optical Stark effect of exciton-polaritons in a monolayer semiconductor." *Nature Communications* **12**, 4530 (2021).

[195] Lyons, T. P., Gillard, D. J., Leblanc, C., Puebla, J., Solnyshkov, D. D., Klompmaker, L., Akimov, I. A., Louca, C., Muduli, P., Genco, A., Bayer, M., Otani, Y., Malpuech, G., and Tartakovskii, A. I.: "Giant effective Zeeman splitting in a monolayer semiconductor realized by spin-selective strong light-matter coupling." *Nature Photonics* **16**, 632–636 (2022).

[196] Anton-Solanas, C., Waldherr, M., Klaas, M., Suchomel, H., Harder, T. H., Cai, H., Sedov, E., Klembt, S., Kavokin, A. V., Tongay, S., Watanabe, K., Taniguchi, T., Höfling, S., and Schneider, C.: "Bosonic condensation of exciton-polaritons in an atomically thin crystal." *Nature Materials* **20**, 1233–1239 (2021).

[197] Gu, J., Chakraborty, B., Khatoniar, M., and Menon, V. M.: "A room-temperature polariton light-emitting diode based on monolayer WS_2." *Nature Nanotechnology* **14**, 1024–1028 (2019).

[198] Lundt, N., Klembt, S., Cherotchenko, E., Betzold, S., Iff, O., Nalitov, A. V., Klaas, M., Dietrich, C. P., Kavokin, A. V., Höfling, S., and Schneider, C.: "Room-temperature Tamm-plasmon exciton-polaritons with a WSe_2 monolayer." *Nature Communications* **7**, 13328 (2016).

[199] Wang, S., Li, S., Chervy, T., Shalabney, A., Azzini, S., Orgiu, E., Hutchison, J. A., Genet, C., Samorì, P., and Ebbesen, T. W.: "Coherent Coupling of WS_2 Monolayers with Metallic Photonic Nanostructures at Room Temperature." *Nano Letters* **16**, 4368–4374 (2016).

[200] Koshelev, K. L., Sychev, S. K., Sadrieva, Z. F., Bogdanov, A. A., and Iorsh, I. V.: "Strong coupling between excitons in transition metal dichalcogenides and optical bound states in the continuum." *Physical Review B* **98**, 161113 (2018).

[201] Liu, W., Ji, Z., Wang, Y., Modi, G., Hwang, M., Zheng, B., Sorger, V. J., Pan, A., and Agarwal, R.: "Generation of helical topological exciton-polaritons." *Science* **370**, 600–604 (2020).

[202] Li, M., Sinev, I., Benimetskiy, F., Ivanova, T., Khestanova, E., Kiriushechkina, S., Vakulenko, A., Guddala, S., Skolnick, M., Menon, V. M., Krizhanovskii, D., Alù, A., Samusev, A., and Khanikaev, A. B.: "Experimental observation of topological Z_2 exciton-polaritons in transition metal dichalcogenide monolayers." *Nature Communications* **12**, 4425 (2021).

[203] Kang, H., Ma, J., Li, J., Zhang, X., and Liu, X.: "Exciton Polaritons in Emergent Two-Dimensional Semiconductors." *ACS Nano* **17**, 24449–24467 (2023).

[204] Emmanuele, R. P. A., Sich, M., Kyriienko, O., Shahnazaryan, V., Withers, F., Catanzaro, A., Walker, P. M., Benimetskiy, F. A., Skolnick, M. S., Tartakovskii, A. I., Shelykh, I. A., and Krizhanovskii, D. N.: "Highly nonlinear trion-polaritons in a monolayer semiconductor." *Nature Communications* **11**, 3589 (2020).

[205] Gu, J., Walther, V., Waldecker, L., Rhodes, D., Raja, A., Hone, J. C., Heinz, T. F., Kéna-Cohen, S., Pohl, T., and Menon, V. M.: "Enhanced nonlinear interaction of polaritons via excitonic Rydberg states in monolayer WSe_2." *Nature Communications* **12**, 2269 (2021).

[206] Zhang, L., Wu, F., Hou, S., Zhang, Z., Chou, Y.-H., Watanabe, K., Taniguchi, T., Forrest, S. R., and Deng, H.: "Van der Waals heterostructure polaritons with moiré-induced nonlinearity." *Nature* **591**, 61–65 (2021).

[207] Datta, B., Khatoniar, M., Deshmukh, P., Thouin, F., Bushati, R., De Liberato, S., Cohen, S. K., and Menon, V. M.: "Highly nonlinear dipolar exciton-polaritons in bilayer MoS_2." *Nature Communications* **13**, 6341 (2022).

[208] Abbarchi, M., Amo, A., Sala, V. G., Solnyshkov, D. D., Flayac, H., Ferrier, L., Sagnes, I., Galopin, E., Lemaître, A., Malpuech, G., and Bloch, J.: "Macroscopic quantum self-trapping and Josephson oscillations of exciton polaritons." *Nature Physics* **9**, 275–279 (2013).

[209] Jacqmin, T., Carusotto, I., Sagnes, I., Abbarchi, M., Solnyshkov, D. D., Malpuech, G., Galopin, E., Lemaître, A., Bloch, J., and Amo, A.: "Direct Observation of Dirac Cones and a Flatband in a Honeycomb Lattice for Polaritons." *Physical Review Letters* **112**, 116402 (2014).

[210] Klembt, S., Harder, T. H., Egorov, O. A., Winkler, K., Ge, R., Bandres, M. A., Emmerling, M., Worschech, L., Liew, T. C. H., Segev, M., Schneider, C., and Höfling, S.: "Exciton-polariton topological insulator." *Nature* **562**, 552–556 (2018).

[211] Fontaine, Q., Squizzato, D., Baboux, F., Amelio, I., Lemaître, A., Morassi, M., Sagnes, I., Le Gratiet, L., Harouri, A., Wouters, M., Carusotto, I., Amo, A., Richard, M., Minguzzi, A., Canet, L., Ravets, S., and Bloch, J.: "Kardar-Parisi-Zhang universality in a one-dimensional polariton condensate." *Nature* **608**, 687–691 (2022).

[212] Bennenhei, C., Shan, H., Struve, M., Kunte, N., Eilenberger, F., Ohmer, J., Fischer, U., Schumacher, S., Ma, X., Schneider, C., and Esmann, M.: "Organic Room-Temperature Polariton Condensate in a Higher-Order Topological Lattice." *ACS Photonics* **11**, 3046–3054 (2024).

[213] Kim, N. Y., Kusudo, K., Wu, C., Masumoto, N., Löffler, A., Höfling, S., Kumada, N., Worschech, L., Forchel, A., and Yamamoto, Y.: "Dynamical d-wave condensation of exciton-polaritons in a two-dimensional square-lattice potential." *Nature Physics* **7**, 681–686 (2011).

[214] Tanaka, K., Nakamura, T., Takamatsu, W., Yamanishi, M., Lee, Y., and Ishihara, T.: "Cavity-Induced Changes of Spontaneous Emission Lifetime in One-Dimensional Semiconductor Microcavities." *Physical Review Letters* **74**, 3380–3383 (1995).

[215] Rogers, C., Gray, D., Bogdanowicz, N., Taniguchi, T., Watanabe, K., and Mabuchi, H.: "Coherent feedback control of two-dimensional excitons." *Physical Review Research* **2**, 012029 (2020).

[216] Horng, J., Martin, E. W., Chou, Y.-H., Courtade, E., Chang, T.-c., Hsu, C.-Y., Wentzel, M.-H., Ruth, H. G., Lu, T.-c., Cundiff, S. T., Wang, F., and Deng, H.: "Perfect Absorption by an Atomically Thin Crystal." *Physical Review Applied* **14**, 024009 (2020).

[217] DiVincenzo, D. P.: "The Physical Implementation of Quantum Computation." *Fortschritte der Physik* **48**, 771–783 (2000).

[218] Clauser, J. F.: "Experimental distinction between the quantum and classical field-theoretic predictions for the photoelectric effect." *Physical Review D* **9**, 853–860 (1974).

[219] Kimble, H. J., Dagenais, M., and Mandel, L.: "Photon Antibunching in Resonance Fluorescence." *Physical Review Letters* **39**, 691–695 (1977).

[220] Diedrich, F. and Walther, H.: "Nonclassical radiation of a single stored ion." *Physical Review Letters* **58**, 203–206 (1987).

[221] Basché, T., Moerner, W. E., Orrit, M., and Talon, H.: "Photon antibunching in the fluorescence of a single dye molecule trapped in a solid." *Physical Review Letters* **69**, 1516–1519 (1992).

[222] Kurtsiefer, C., Mayer, S., Zarda, P., and Weinfurter, H.: "Stable Solid-State Source of Single Photons." *Physical Review Letters* **85**, 290–293 (2000).

[223] Brouri, R., Beveratos, A., Poizat, J.-P., and Grangier, P.: "Photon antibunching in the fluorescence of individual color centers in diamond." *Optics Letters* **25**, 1294 (2000).

[224] Wang, C., Kurtsiefer, C., Weinfurter, H., and Burchard, B.: "Single photon emission from SiV centres in diamond produced by ion implantation." *Journal of Physics B: Atomic, Molecular and Optical Physics* **39**, 37 (2005).

[225] Iwasaki, T., Ishibashi, F., Miyamoto, Y., Doi, Y., Kobayashi, S., Miyazaki, T., Tahara, K., Jahnke, K. D., Rogers, L. J., Naydenov, B., Jelezko, F., Yamasaki, S., Nagamachi, S., Inubushi, T., Mizuochi, N., and Hatano, M.: "Germanium-Vacancy Single Color Centers in Diamond." *Scientific Reports* **5**, 12882 (2015).

[226] Iwasaki, T., Miyamoto, Y., Taniguchi, T., Siyushev, P., Metsch, M. H., Jelezko, F., and Hatano, M.: "Tin-Vacancy Quantum Emitters in Diamond." *Physical Review Letters* **119**, 253601 (2017).

[227] Ditalia Tchernij, S., Lühmann, T., Herzig, T., Küpper, J., Damin, A., Santonocito, S., Signorile, M., Traina, P., Moreva, E., Celegato, F., Pezzagna, S., Degiovanni, I. P., Olivero, P., Jakšić, M., Meijer, J., Genovese, P. M., and Forneris, J.: "Single-Photon Emitters in Lead-Implanted Single-Crystal Diamond." *ACS Photonics* **5**, 4864–4871 (2018).

[228] Berhane, A. M., Jeong, K.-Y., Bodrog, Z., Fiedler, S., Schröder, T., Triviño, N. V., Palacios, T., Gali, A., Toth, M., Englund, D., and Aharonovich, I.: "Bright Room-Temperature Single-Photon Emission from Defects in Gallium Nitride." *Advanced Materials* **29**, 1605092 (2017).

[229] Wang, J., Zhou, Y., Wang, Z., Rasmita, A., Yang, J., Li, X., von Bardeleben, H. J., and Gao, W.: "Bright room temperature single photon source at telecom range in cubic silicon carbide." *Nature Communications* **9**, 4106 (2018).

[230] Bishop, S. G., Hadden, J. P., Alzahrani, F. D., Hekmati, R., Huffaker, D. L., Langbein, W. W., and Bennett, A. J.: "Room-Temperature Quantum Emitter in Aluminum Nitride." *ACS Photonics* **7**, 1636–1641 (2020).

[231] Senichev, A., Martin, Z. O., Peana, S., Sychev, D., Xu, X., Lagutchev, A. S., Boltasseva, A., and Shalaev, V. M.: "Room-temperature single-photon emitters in silicon nitride." *Science Advances* **7**, eabj0627 (2021).

[232] Udvarhelyi, P., Somogyi, B., Thiering, G., and Gali, A.: "Identification of a Telecom Wavelength Single Photon Emitter in Silicon." *Physical Review Letters* **127**, 196402 (2021).

[233] Zhao, S., Lavie, J., Rondin, L., Orcin-Chaix, L., Diederichs, C., Roussignol, P., Chassagneux, Y., Voisin, C., Müllen, K., Narita, A., Campidelli, S., and Lauret, J.-S.: "Single photon emission from graphene quantum dots at room temperature." *Nature Communications* **9**, 3470 (2018).

[234] He, Y.-M., Clark, G., Schaibley, J. R., He, Y., Chen, M.-C., Wei, Y.-J., Ding, X., Zhang, Q., Yao, W., Xu, X., Lu, C.-Y., and Pan, J.-W.: "Single quantum emitters in monolayer semiconductors." *Nature Nanotechnology* **10**, 497–502 (2015).

[235] Koperski, M., Nogajewski, K., Arora, A., Cherkez, V., Mallet, P., Veuillen, J.-Y., Marcus, J., Kossacki, P., and Potemski, M.: "Single photon emitters in exfoliated WSe_2 structures." *Nature Nanotechnology* **10**, 503–506 (2015).

[236] Srivastava, A., Sidler, M., Allain, A. V., Lembke, D. S., Kis, A., and Imamoğlu, A.: "Optically active quantum dots in monolayer WSe_2." *Nature Nanotechnology* **10**, 491–496 (2015).

[237] Zhao, H., Pettes, M. T., Zheng, Y., and Htoon, H.: "Site-controlled telecom-wavelength single-photon emitters in atomically-thin $MoTe_2$." *Nature Communications* **12**, 6753 (2021).

[238] Tran, T. T., Bray, K., Ford, M. J., Toth, M., and Aharonovich, I.: "Quantum emission from hexagonal boron nitride monolayers." *Nature Nanotechnology* **11**, 37–41 (2016).

[239] Zhong, T., Kindem, J. M., Bartholomew, J. G., Rochman, J., Craiciu, I., Verma, V., Nam, S. W., Marsili, F., Shaw, M. D., Beyer, A. D., and Faraon, A.: "Optically Addressing Single Rare-Earth Ions in a Nanophotonic Cavity." *Physical Review Letters* **121**, 183603 (2018).

[240] Ourari, S., Dusanowski, Ł., Horvath, S. P., Uysal, M. T., Phenicie, C. M., Stevenson, P., Raha, M., Chen, S., Cava, R. J., de Leon, N. P., and Thompson, J. D.: "Indistinguishable telecom band photons from a single Er ion in the solid state." *Nature* **620**, 977–981 (2023).

[241] Wu, C.-J., Riedel, D., Ruskuc, A., Zhong, D., Kwon, H., and Faraon, A.: "Near-infrared hybrid quantum photonic interface for $^{171}Yb^{3+}$ solid-state qubits." *Physical Review Applied* **20**, 044018 (2023).

[242] Utzat, H., Sun, W., Kaplan, A. E. K., Krieg, F., Ginterseder, M., Spokoyny, B., Klein, N. D., Shulenberger, K. E., Perkinson, C. F., Kovalenko, M. V., and Bawendi, M. G.: "Coherent single-photon emission from colloidal lead halide perovskite quantum dots." *Science* **363**, 1068–1072 (2019).

[243] Aharonovich, I., Englund, D., and Toth, M.: "Solid-state single-photon emitters." *Nature Photonics* **10**, 631–641 (2016).

[244] Lee, J., Leong, V., Kalashnikov, D., Dai, J., Gandhi, A., and Krivitsky, L. A.: "Integrated single photon emitters." *AVS Quantum Science* **2**, 031701 (2020).

[245] Castelletto, S. and Boretti, A.: "Perspective on Solid-State Single-Photon Sources in the Infrared for Quantum Technology." *Advanced Quantum Technologies* **6**, 2300145 (2023).

[246] MohammadNejad, S., Nosratkhah, P., and Arab, H.: "Recent advances in room temperature single-photon emitters." *Quantum Information Processing* **22**, 360 (2023).

[247] Esmann, M., Wein, S. C., and Antón-Solanas, C.: "Solid-State Single-Photon Sources: Recent Advances for Novel Quantum Materials." *Advanced Functional Materials* **34**, 2315936 (2024).

[248] Loudon, R.: "The Quantum Theory of Light." Third Edition. Oxford University Press, 2000.

[249] Hanbury Brown, R. and Twiss, R. Q.: "Correlation between Photons in two Coherent Beams of Light." *Nature* **177**, 27–29 (1956).

[250] Hanbury Brown, R. and Twiss, R. Q.: "A Test of a New Type of Stellar Interferometer on Sirius." *Nature* **178**, 1046–1048 (1956).

[251] Kiraz, A., Atatüre, M., and Imamoğlu, A.: "Quantum-dot single-photon sources: Prospects for applications in linear optics quantum-information processing." *Physical Review A* **69**, 032305 (2004).

[252] Bylander, J., Robert-Philip, I., and Abram, I.: "Interference and correlation of two independent photons." *The European Physical Journal D - Atomic, Molecular, Optical and Plasma Physics* **22**, 295–301 (2003).

[253] Santori, C., Fattal, D., Vuckovic, J., Solomon, G. S., and Yamamoto, Y.: "Single-photon generation with InAs quantum dots." *New Journal of Physics* **6**, 89 (2004).

[254] Khan, S., Agarwalla, B. K., and Jain, S.: "Quantum regression theorem for multi-time correlators: A detailed analysis in the Heisenberg picture." *Physical Review A* **106**, 022214 (2022).

[255] Gies, C., Wiersig, J., and Jahnke, F.: "Quantum Statistical Properties of the Light Emission from Quantum Dots in Microcavities." In: *Single Semiconductor Quantum Dots*, pp. 1–30. Ed. by Michler, P. Springer Berlin Heidelberg, 2009.

[256] Michler, P.: "Quantum Dot Single-Photon Sources." In: *Single Semiconductor Quantum Dots*, pp. 185–225. Ed. by Michler, P. Springer Berlin Heidelberg, 2009.

[257] Bouchard, F., Sit, A., Zhang, Y., Fickler, R., Miatto, F. M., Yao, Y., Sciarrino, F., and Karimi, E.: "Two-photon interference: the Hong-Ou-Mandel effect." *Reports on Progress in Physics* **84**, 012402 (2020).

[258] Hong, C. K., Ou, Z. Y., and Mandel, L.: "Measurement of subpicosecond time intervals between two photons by interference." *Physical Review Letters* **59**, 2044–2046 (1987).

[259] Shih, Y. H. and Alley, C. O.: "New Type of Einstein-Podolsky-Rosen-Bohm Experiment Using Pairs of Light Quanta Produced by Optical Parametric Down Conversion." *Physical Review Letters* **61**, 2921–2924 (1988).

[260] Rarity, J. G. and Tapster, P. R.: "Fourth-order interference in parametric downconversion." *Journal of the Optical Society of America B* **6**, 1221 (1989).

[261] Fischer, K. A., Müller, K., Lagoudakis, K. G., and Vučković, J.: "Dynamical modeling of pulsed two-photon interference." *New Journal of Physics* **18**, 113053 (2016).

[262] Oxborrow, M. and Sinclair, A. G.: "Single-photon sources." *Contemporary Physics* **46**, 173–206 (2005).

[263] Trivedi, R., Fischer, K. A., Vučković, J., and Müller, K.: "Generation of Non-Classical Light Using Semiconductor Quantum Dots." *Advanced Quantum Technologies* **3**, 1900007 (2020).

[264] Thoma, A., Schnauber, P., Gschrey, M., Seifried, M., Wolters, J., Schulze, J.-H., Strittmatter, A., Rodt, S., Carmele, A., Knorr, A., Heindel, T., and Reitzenstein, S.: "Exploring Dephasing of a Solid-State Quantum Emitter via Time- and Temperature-Dependent Hong-Ou-Mandel Experiments." *Physical Review Letters* **116**, 033601 (2016).

[265] Ollivier, H., Thomas, S. E., Wein, S. C., de Buy Wenniger, I. M., Coste, N., Loredo, J. C., Somaschi, N., Harouri, A., Lemaitre, A., Sagnes, I., Lanco, L., Simon, C., Anton, C., Krebs, O., and Senellart, P.: "Hong-Ou-Mandel Interference with Imperfect Single Photon Sources." *Physical Review Letters* **126**, 063602 (2021).

[266] Schofield, R. C., Clear, C., Hoggarth, R. A., Major, K. D., McCutcheon, D. P. S., and Clark, A. S.: "Photon indistinguishability measurements under pulsed and continuous excitation." *Physical Review Research* **4**, 013037 (2022).

[267] Kiraz, A., Ehrl, M., Hellerer, T., Müstecaplıoğlu, Ö. E., Bräuchle, C., and Zumbusch, A.: "Indistinguishable Photons from a Single Molecule." *Physical Review Letters* **94**, 223602 (2005).

[268] Rezai, M., Wrachtrup, J., and Gerhardt, I.: "Coherence Properties of Molecular Single Photons for Quantum Networks." *Physical Review X* **8**, 031026 (2018).

[269] Jaynes, E. and Cummings, F.: "Comparison of quantum and semiclassical radiation theories with application to the beam maser." *Proceedings of the IEEE* **51**, 89–109 (1963).

[270] Shore, B. W. and Knight, P. L.: "The Jaynes-Cummings Model." *Journal of Modern Optics* **40**, 1195–1238 (1993).

[271] Fox, M.: "Quantum optics: an introduction." Oxford master series in physics Atomic, optical, and laser physics 15. Oxford University Press, 2013.

[272] Karrai, K. and J. Warburton, R.: "Optical transmission and reflection spectroscopy of single quantum dots." *Superlattices and Microstructures* **33**, 311–337 (2003).

[273] Toninelli, C., Delley, Y., Stöferle, T., Renn, A., Götzinger, S., and Sandoghdar, V.: "A scanning microcavity for *in situ* control of single-molecule emission." *Applied Physics Letters* **97**, 021107 (2010).

[274] Kaupp, H., Hümmer, T., Mader, M., Schlederer, B., Benedikter, J., Haeusser, P., Chang, H.-C., Fedder, H., Hänsch, T. W., and Hunger, D.: "Purcell-Enhanced Single-Photon Emission from Nitrogen-Vacancy Centers Coupled to a Tunable Microcavity." *Physical Review Applied* **6**, 054010 (2016).

[275] Merkel, B., Ulanowski, A., and Reiserer, A.: "Coherent and Purcell-Enhanced Emission from Erbium Dopants in a Cryogenic High-Q Resonator." *Physical Review X* **10**, 041025 (2020).

[276] Pyatkov, F., Fütterling, V., Khasminskaya, S., Flavel, B. S., Hennrich, F., Kappes, M. M., Krupke, R., and Pernice, W. H. P.: "Cavity-enhanced light emission from electrically driven carbon nanotubes." *Nature Photonics* **10**, 420–427 (2016).

[277] Sipahigil, A., Evans, R. E., Sukachev, D. D., Burek, M. J., Borregaard, J., Bhaskar, M. K., Nguyen, C. T., Pacheco, J. L., Atikian, H. A., Meuwly, C., Camacho, R. M., Jelezko, F., Bielejec, E., Park, H., Lončar, M., and Lukin, M. D.: "An integrated diamond nanophotonics platform for quantum-optical networks." *Science* **354**, 847–850 (2016).

[278] Faraon, A., Santori, C., Huang, Z., Acosta, V. M., and Beausoleil, R. G.: "Coupling of Nitrogen-Vacancy Centers to Photonic Crystal Cavities in Monocrystalline Diamond." *Physical Review Letters* **109**, 033604 (2012).

[279] Gritsch, A., Ulanowski, A., and Reiserer, A.: "Purcell enhancement of single-photon emitters in silicon." *Optica* **10**, 783 (2023).

[280] Laucht, A., Pütz, S., Günthner, T., Hauke, N., Saive, R., Frédérick, S., Bichler, M., Amann, M.-C., Holleitner, A. W., Kaniber, M., and Finley, J. J.: "A Waveguide-Coupled On-Chip Single-Photon Source." *Physical Review X* **2**, 011014 (2012).

[281] Wang, H., He, Y.-M., Chung, T.-H., Hu, H., Yu, Y., Chen, S., Ding, X., Chen, M.-C., Qin, J., Yang, X., Liu, R.-Z., Duan, Z.-C., Li, J.-P., Gerhardt, S., Winkler, K., Jurkat, J., Wang, L.-J., Gregersen, N., Huo, Y.-H., Dai, Q., Yu, S., Höfling, S., Lu, C.-Y., and Pan, J.-W.: "Towards optimal single-photon sources from polarized microcavities." *Nature Photonics* **13**, 770–775 (2019).

[282] Sortino, L., Gale, A., Kühner, L., Li, C., Biechteler, J., Wendisch, F. J., Kianinia, M., Ren, H., Toth, M., Maier, S. A., Aharonovich, I., and Tittl, A.: "Optically addressable spin defects coupled to bound states in the continuum metasurfaces." *Nature Communications* **15**, 2008 (2024).

[283] Akimov, A. V., Mukherjee, A., Yu, C. L., Chang, D. E., Zibrov, A. S., Hemmer, P. R., Park, H., and Lukin, M. D.: "Generation of single optical plasmons in metallic nanowires coupled to quantum dots." *Nature* **450**, 402–406 (2007).

[284] Huck, A., Kumar, S., Shakoor, A., and Andersen, U. L.: "Controlled Coupling of a Single Nitrogen-Vacancy Center to a Silver Nanowire." *Physical Review Letters* **106**, 096801 (2011).

[285] Tame, M. S., McEnery, K. R., Özdemir, Ş. K., Lee, J., Maier, S. A., and Kim, M. S.: "Quantum plasmonics." *Nature Physics* **9**, 329–340 (2013).

[286] Bozhevolnyi, S. I. and Khurgin, J. B.: "The case for quantum plasmonics." *Nature Photonics* **11**, 398–400 (2017).

[287] Lodahl, P., Mahmoodian, S., and Stobbe, S.: "Interfacing single photons and single quantum dots with photonic nanostructures." *Reviews of Modern Physics* **87**, 347–400 (2015).

[288] Schröder, T., Mouradian, S. L., Zheng, J., Trusheim, M. E., Walsh, M., Chen, E. H., Li, L., Bayn, I., and Englund, D.: "Quantum nanophotonics in diamond." *Journal of the Optical Society of America B* **33**, B65 (2016).

[289] Auffèves, A., Gerace, D., Gérard, J.-M., Santos, M. F., Andreani, L. C., and Poizat, J.-P.: "Controlling the dynamics of a coupled atom-cavity system by pure dephasing." *Physical Review B* **81**, 245419 (2010).

[290] Cui, G. and Raymer, M. G.: "Emission spectra and quantum efficiency of single-photon sources in the cavity-QED strong-coupling regime." *Physical Review A* **73**, 053807 (2006).

[291] Laussy, F. P., Del Valle, E., and Tejedor, C.: "Strong Coupling of Quantum Dots in Microcavities." *Physical Review Letters* **101**, 083601 (2008).

[292] Cui, G. and Raymer, M. G.: "Quantum efficiency of single-photon sources in the cavity-QED strong-coupling regime." *Optics Express* **13**, 9660 (2005).

[293] Del Valle, E., Laussy, F. P., and Tejedor, C.: "Luminescence spectra of quantum dots in microcavities. II. Fermions." *Physical Review B* **79**, 235326 (2009).

[294] Muñoz-Matutano, G., Wood, A., Johnsson, M., Vidal, X., Baragiola, B. Q., Reinhard, A., Lemaître, A., Bloch, J., Amo, A., Nogues, G., Besga, B., Richard, M., and Volz, T.: "Emergence of quantum correlations from interacting fibre-cavity polaritons." *Nature Materials* **18**, 213–218 (2019).

[295] Delteil, A., Fink, T., Schade, A., Höfling, S., Schneider, C., and İmamoğlu, A.: "Towards polariton blockade of confined exciton-polaritons." *Nature Materials* **18**, 219–222 (2019).

[296] Kuhn, A., Hennrich, M., and Rempe, G.: "Deterministic Single-Photon Source for Distributed Quantum Networking." *Physical Review Letters* **89**, 067901 (2002).

[297] Duan, L.-M. and Kimble, H. J.: "Scalable Photonic Quantum Computation through Cavity-Assisted Interactions." *Physical Review Letters* **92**, 127902 (2004).

[298] Hacker, B., Welte, S., Rempe, G., and Ritter, S.: "A photon-photon quantum gate based on a single atom in an optical resonator." *Nature* **536**, 193–196 (2016).

[299] Birnbaum, K. M., Boca, A., Miller, R., Boozer, A. D., Northup, T. E., and Kimble, H. J.: "Photon blockade in an optical cavity with one trapped atom." *Nature* **436**, 87–90 (2005).

[300] Hamsen, C., Tolazzi, K. N., Wilk, T., and Rempe, G.: "Two-Photon Blockade in an Atom-Driven Cavity QED System." *Physical Review Letters* **118**, 133604 (2017).

[301] Takahashi, H., Kassa, E., Christoforou, C., and Keller, M.: "Strong Coupling of a Single Ion to an Optical Cavity." *Physical Review Letters* **124**, 013602 (2020).

[302] Reithmaier, J. P., Sęk, G., Löffler, A., Hofmann, C., Kuhn, S., Reitzenstein, S., Keldysh, L. V., Kulakovskii, V. D., Reinecke, T. L., and Forchel, A.: "Strong coupling in a single quantum dot-semiconductor microcavity system." *Nature* **432**, 197–200 (2004).

[303] Yoshie, T., Scherer, A., Hendrickson, J., Khitrova, G., Gibbs, H. M., Rupper, G., Ell, C., Shchekin, O. B., and Deppe, D. G.: "Vacuum Rabi splitting with a single quantum dot in a photonic crystal nanocavity." *Nature* **432**, 200–203 (2004).

[304] Faraon, A., Fushman, I., Englund, D., Stoltz, N., Petroff, P., and Vučković, J.: "Coherent generation of non-classical light on a chip via photon-induced tunnelling and blockade." *Nature Physics* **4**, 859–863 (2008).

[305] Kasprzak, J., Reitzenstein, S., Muljarov, E. A., Kistner, C., Schneider, C., Strauss, M., Höfling, S., Forchel, A., and Langbein, W.: "Up on the Jaynes-Cummings ladder of a quantum-dot/microcavity system." *Nature Materials* **9**, 304–308 (2010).

[306] Hinds, E.: "Cavity Quantum Electrodynamics." In: *Advances In Atomic, Molecular, and Optical Physics* **28**, pp. 237–289. Elsevier, 1990.

[307] Benedikter, J.: "Microcavity enhancement of silicon vacancy centres in diamond and europium ions in yttria." PhD thesis, Ludwig-Maximilians-Universität München, 2019.

[308] Kaupp, H., Deutsch, C., Chang, H.-C., Reichel, J., Hänsch, T. W., and Hunger, D.: "Scaling laws of the cavity enhancement for nitrogen-vacancy centers in diamond." *Physical Review A* **88**, 053812 (2013).

[309] Meldrum, A., Bianucci, P., and Marsiglio, F.: "Modification of ensemble emission rates and luminescence spectra for inhomogeneously broadened distributions of quantum dots coupled to optical microcavities." *Optics Express* **18**, 10230 (2010).

[310] Liu, F., Brash, A. J., O'Hara, J., Martins, L. M. P. P., Phillips, C. L., Coles, R. J., Royall, B., Clarke, E., Bentham, C., Prtljaga, N., Itskevich, I. E., Wilson, L. R., Skolnick, M. S., and Fox, A. M.: "High Purcell factor generation of indistinguishable on-chip single photons." *Nature Nanotechnology* **13**, 835–840 (2018).

[311] Somaschi, N., Giesz, V., De Santis, L., Loredo, J. C., Almeida, M. P., Hornecker, G., Portalupi, S. L., Grange, T., Antón, C., Demory, J., Gómez, C., Sagnes, I., Lanzillotti-Kimura, N. D., Lemaítre, A., Auffeves, A., White, A. G., Lanco, L., and Senellart, P.: "Near-optimal single-photon sources in the solid state." *Nature Photonics* **10**, 340–345 (2016).

[312] Tomm, N., Javadi, A., Antoniadis, N. O., Najer, D., Löbl, M. C., Korsch, A. R., Schott, R., Valentin, S. R., Wieck, A. D., Ludwig, A., and Warburton, R. J.: "A bright and fast source of coherent single photons." *Nature Nanotechnology* **16**, 399–403 (2021).

[313] Holewa, P., Vajner, D. A., Zięba-Ostój, E., Wasiluk, M., Gaál, B., Sakanas, A., Burakowski, M., Mrowiński, P., Krajnik, B., Xiong, M., Yvind, K., Gregersen, N., Musiał, A., Huck, A., Heindel, T., Syperek, M., and Semenova, E.: "High-throughput quantum photonic devices emitting indistinguishable photons in the telecom C-band." *Nature Communications* **15**, 3358 (2024).

[314] Vajner, D. A., Holewa, P., Zięba-Ostój, E., Wasiluk, M., Von Helversen, M., Sakanas, A., Huck, A., Yvind, K., Gregersen, N., Musiał, A., Syperek, M., Semenova, E., and Heindel, T.: "On-Demand Generation of Indistinguishable Photons in the Telecom C-Band Using Quantum Dot Devices." *ACS Photonics* **11**, 339–347 (2024).

[315] Komza, L., Samutpraphoot, P., Odeh, M., Tang, Y.-L., Mathew, M., Chang, J., Song, H., Kim, M.-K., Xiong, Y., Hautier, G., and Sipahigil, A.: "Indistinguishable photons from an artificial atom in silicon photonics." *Nature Communications* **15**, 6920 (2024).

[316] Hunger, D., Deutsch, C., Barbour, R. J., Warburton, R. J., and Reichel, J.: "Laser microfabrication of concave, low-roughness features in silica." *AIP Advances* **2**, 012119 (2012).

[317] Pfeifer, H., Ratschbacher, L., Gallego, J., Saavedra, C., Faßbender, A., von Haaren, A., Alt, W., Hofferberth, S., Köhl, M., Linden, S., and Meschede, D.: "Achievements and perspectives of optical fiber Fabry-Perot cavities." *Applied Physics B* **128**, 29 (2022).

[318] Uphoff, M., Brekenfeld, M., Rempe, G., and Ritter, S.: "Frequency splitting of polarization eigenmodes in microscopic Fabry-Perot cavities." *New Journal of Physics* **17**, 013053 (2015).

[319] Greuter, L., Starosielec, S., Najer, D., Ludwig, A., Duempelmann, L., Rohner, D., and Warburton, R. J.: "A small mode volume tunable microcavity: Development and characterization." *Applied Physics Letters* **105**, 121105 (2014).

[320] Takahashi, H., Morphew, J., Oručević, F., Noguchi, A., Kassa, E., and Keller, M.: "Novel laser machining of optical fibers for long cavities with low birefringence." *Optics Express* **22**, 31317 (2014).

[321] Hessenauer, J., Weber, K., Benedikter, J., Gissibl, T., Höfer, J., Giessen, H., and Hunger, D.: "Laser written mirror profiles for open-access fiber Fabry-Perot microcavities." *Optics Express* **31**, 17380 (2023).

[322] Benedikter, J., Hümmer, T., Mader, M., Schlederer, B., Reichel, J., Hänsch, T. W., and Hunger, D.: "Transverse-mode coupling and diffraction loss in tunable Fabry-Pérot microcavities." *New Journal of Physics* **17**, 053051 (2015).

[323] Trapp, J.: "Cavity-Enhanced Room Temperature Single-Photon Emission at Telecom-Wavelength from Single-Walled Carbon Nanotubes." MSc thesis, Ludwig-Maxilimians-Universität München, 2022.

[324] An, K., Yang, C., Dasari, R. R., and Feld, M. S.: "Cavity ring-down technique and its application to the measurement of ultraslow velocities." *Optics Letters* **20**, 1068 (1995).

[325] Lawrence, M. J., Willke, B., Husman, M. E., Gustafson, E. K., and Byer, R. L.: "Dynamic response of a Fabry-Perot interferometer." *Journal of the Optical Society of America B* **16**, 523 (1999).

[326] Loredo, J. C., Zakaria, N. A., Somaschi, N., Anton, C., De Santis, L., Giesz, V., Grange, T., Broome, M. A., Gazzano, O., Coppola, G., Sagnes, I., Lemaitre, A., Auffeves, A., Senellart, P., Almeida, M. P., and White, A. G.: "Scalable performance in solid-state single-photon sources." *Optica* **3**, 433 (2016).

[327] Ruelle, T., Jaeger, D., Fogliano, F., Braakman, F., and Poggio, M.: "A tunable fiber Fabry-Perot cavity for hybrid optomechanics stabilized at 4 K." *Review of Scientific Instruments* **93**, 095003 (2022).

[328] Vadia, S., Scherzer, J., Thierschmann, H., Schäfermeier, C., Dal Savio, C., Taniguchi, T., Watanabe, K., Hunger, D., Karraï, K., and Högele, A.: "Open-Cavity in Closed-Cycle Cryostat as a Quantum Optics Platform." *PRX Quantum* **2**, 040318 (2021).

[329] Ruf, M., Weaver, M., van Dam, S., and Hanson, R.: "Resonant Excitation and Purcell Enhancement of Coherent Nitrogen-Vacancy Centers Coupled to a Fabry-Perot Microcavity." *Physical Review Applied* **15**, 024049 (2021).

[330] Fontana, Y., Zifkin, R., Janitz, E., Rodríguez Rosenblueth, C. D., and Childress, L.: "A mechanically stable and tunable cryogenic Fabry-Pérot microcavity." *Review of Scientific Instruments* **92**, 053906 (2021).

[331] Casabone, B., Deshmukh, C., Liu, S., Serrano, D., Ferrier, A., Hümmer, T., Goldner, P., Hunger, D., and de Riedmatten, H.: "Dynamic control of Purcell enhanced emission of erbium ions in nanoparticles." *Nature Communications* **12**, 3570 (2021).

[332] Pallmann, M., Eichhorn, T., Benedikter, J., Casabone, B., Hümmer, T., and Hunger, D.: "A highly stable and fully tunable open microcavity platform at cryogenic temperatures." *APL Photonics* **8**, 046107 (2023).

[333] Scherzer, J.: "Light-matter interactions in semiconductor moiré heterostructures." PhD thesis, Ludwig-Maximilians-Universität München, 2024.

[334] Vadia, S.: "Controlling light-matter interactions with two-dimensional semiconductors at cryogenic temperatures." PhD thesis, Ludwig-Maximilians-Universität München, 2021.

[335] Shree, S., Paradisanos, I., Marie, X., Robert, C., and Urbaszek, B.: "Guide to optical spectroscopy of layered semiconductors." *Nature Reviews Physics* **3**, 39–54 (2021).

[336] Cao, Y., Fatemi, V., Fang, S., Watanabe, K., Taniguchi, T., Kaxiras, E., and Jarillo-Herrero, P.: "Unconventional superconductivity in magic-angle graphene superlattices." *Nature* **556**, 43–50 (2018).

[337] Yankowitz, M., Chen, S., Polshyn, H., Zhang, Y., Watanabe, K., Taniguchi, T., Graf, D., Young, A. F., and Dean, C. R.: "Tuning superconductivity in twisted bilayer graphene." *Science* **363**, 1059–1064 (2019).

[338] Lu, X., Stepanov, P., Yang, W., Xie, M., Aamir, M. A., Das, I., Urgell, C., Watanabe, K., Taniguchi, T., Zhang, G., Bachtold, A., MacDonald, A. H., and Efetov, D. K.: "Superconductors, orbital magnets and correlated states in magic-angle bilayer graphene." *Nature* **574**, 653–657 (2019).

[339] Krelle, L.: "Plasmon-Exciton-Polaritons in Two-Dimensional Semiconductors Strongly Coupled to Gold Nanoparticle Arrays." MSc thesis, Ludwig-Maxilimians-Universität München, 2022.

[340] Cadiz, F., Courtade, E., Robert, C., Wang, G., Shen, Y., Cai, H., Taniguchi, T., Watanabe, K., Carrere, H., Lagarde, D., Manca, M., Amand, T., Renucci, P., Tongay, S., Marie, X., and Urbaszek, B.: "Excitonic Linewidth Approaching the Homogeneous Limit in MoS_2-Based van der Waals Heterostructures." *Physical Review X* **7**, 021026 (2017).

[341] Kotsakidis, J. C., Zhang, Q., Vazquez de Parga, A. L., Currie, M., Helmerson, K., Gaskill, D. K., and Fuhrer, M. S.: "Oxidation of Monolayer WS_2 in Ambient Is a Photoinduced Process." *Nano Letters* **19**, 5205–5215 (2019).

[342] Rupp, A.: "Characterisation of Layered Semiconductors with Scanning Electron Microscopy Techniques." MSc thesis, Ludwig-Maxilimians-Universität München, 2022.

[343] Funk, V.: "Cryogenic confocal spectroscopy of few-layer transition metal dichalcogenides." PhD thesis, Ludwig-Maximilians-Universität München, 2024.

[344] Zotev, P. G., Wang, Y., Andres-Penares, D., Severs-Millard, T., Randerson, S., Hu, X., Sortino, L., Louca, C., Brotons-Gisbert, M., Huq, T., Vezzoli, S., Sapienza, R., Krauss, T. F., Gerardot, B. D., and Tartakovskii, A. I.: "Van der Waals Materials for Applications in Nanophotonics." *Laser & Photonics Reviews* **17**, 2200957 (2023).

[345] Grenadier, S., Li, J., Lin, J., and Jiang, H.: "Dry etching techniques for active devices based on hexagonal boron nitride epilayers." *Journal of Vacuum Science & Technology A* **31**, 061517 (2013).

[346] Quincke, M., Lehnert, T., Keren, I., Moses Badlyan, N., Port, F., Goncalves, M., Mohn, M. J., Maultzsch, J., Steinberg, H., and Kaiser, U.: "Transmission-Electron-Microscopy-Generated Atomic Defects in Two-Dimensional Nanosheets and Their Integration in Devices for Electronic and Optical Sensing." *ACS Applied Nano Materials* **5**, 11429–11436 (2022).

[347] Pizzocchero, F., Gammelgaard, L., Jessen, B. S., Caridad, J. M., Wang, L., Hone, J., Bøggild, P., and Booth, T. J.: "The hot pick-up technique for batch assembly of van der Waals heterostructures." *Nature Communications* **7**, 11894 (2016).

[348] Frisenda, R., Navarro-Moratalla, E., Gant, P., Lara, D. P. D., Jarillo-Herrero, P., Gorbachev, R. V., and Castellanos-Gomez, A.: "Recent progress in the assembly of nanodevices and van der Waals heterostructures by deterministic placement of 2D materials." *Chemical Society Reviews* **47**, 53–68 (2018).

[349] Son, S., Shin, Y. J., Zhang, K., Shin, J., Lee, S., Idzuchi, H., Coak, M. J., Kim, H., Kim, J., Kim, J. H., Kim, M., Kim, D., Kim, P., and Park, J.-G.: "Strongly adhesive dry transfer technique for van der Waals heterostructure." *2D Materials* **7**, 041005 (2020).

[350] Shin, M. J. and Shin, Y. J.: "Stacking of 2D materials containing a thin layer of hexagonal boron nitride using polycaprolactone." *Journal of the Korean Physical Society* **78**, 1089–1094 (2021).

[351] Purdie, D. G., Pugno, N. M., Taniguchi, T., Watanabe, K., Ferrari, A. C., and Lombardo, A.: "Cleaning interfaces in layered materials heterostructures." *Nature Communications* **9**, 5387 (2018).

[352] Ajayi, O. A., Ardelean, J. V., Shepard, G. D., Wang, J., Antony, A., Taniguchi, T., Watanabe, K., Heinz, T. F., Strauf, S., Zhu, X.-Y., and Hone, J. C.: "Approaching the intrinsic photoluminescence linewidth in transition metal dichalcogenide monolayers." *2D Materials* **4**, 031011 (2017).

[353] Qiu, L., Chakraborty, C., Dhara, S., and Vamivakas, A. N.: "Room-temperature valley coherence in a polaritonic system." *Nature Communications* **10**, 1513 (2019).

[354] Wurdack, M., Estrecho, E., Todd, S., Yun, T., Pieczarka, M., Earl, S. K., Davis, J. A., Schneider, C., Truscott, A. G., and Ostrovskaya, E. A.: "Motional narrowing, ballistic transport, and trapping of room-temperature exciton polaritons in an atomically-thin semiconductor." *Nature Communications* **12**, 5366 (2021).

[355] Rupprecht, C., Klaas, M., Knopf, H., Taniguchi, T., Watanabe, K., Qin, Y., Tongay, S., Schröder, S., Eilenberger, F., Höfling, S., and Schneider, C.: "Demonstration of a polariton step potential by local variation of light-matter coupling in a van-der-Waals heterostructure." *Optics Express* **28**, 18649–18657 (2020).

[356] Wurdack, M., Estrecho, E., Todd, S., Schneider, C., Truscott, A. G., and Ostrovskaya, E. A.: "Enhancing Ground-State Population and Macroscopic Coherence of Room-Temperature WS_2 Polaritons through Engineered Confinement." *Physical Review Letters* **129**, 147402 (2022).

[357] Li, D., Shan, H., Knopf, H., Watanabe, K., Taniguchi, T., Qin, Y., Tongay, S., Eilenberger, F., Höfling, S., Schneider, C., and Brixner, T.: "Trapping-induced quantum beats in a van-der-Waals heterostructure microcavity observed by two-dimensional microspectroscopy." *Optical Materials Express* **13**, 2798–2807 (2023).

[358] Zhao, J., Su, R., Fieramosca, A., Zhao, W., Du, W., Liu, X., Diederichs, C., Sanvitto, D., Liew, T. C. H., and Xiong, Q.: "Ultralow Threshold Polariton Condensate in a Monolayer Semiconductor Microcavity at Room Temperature." *Nano Letters* **21**, 3331–3339 (2021).

[359] Majer, J., Chow, J. M., Gambetta, J. M., Koch, J., Johnson, B. R., Schreier, J. A., Frunzio, L., Schuster, D. I., Houck, A. A., Wallraff, A., Blais, A., Devoret, M. H., Girvin, S. M., and Schoelkopf, R. J.: "Coupling superconducting qubits via a cavity bus." *Nature* **449**, 443–447 (2007).

[360] Ritsch, H., Domokos, P., Brennecke, F., and Esslinger, T.: "Cold atoms in cavity-generated dynamical optical potentials." *Reviews of Modern Physics* **85**, 553–601 (2013).

[361] Vijayan, J., Piotrowski, J., Gonzalez-Ballestero, C., Weber, K., Romero-Isart, O., and Novotny, L.: "Cavity-mediated long-range interactions in levitated optomechanics." *Nature Physics* **20**, 859–864 (2024).

[362] Tan, L. B., Diessel, O. K., Popert, A., Schmidt, R., Imamoglu, A., and Kroner, M.: "Bose Polaron Interactions in a Cavity-Coupled Monolayer Semiconductor." *Physical Review X* **13**, 031036 (2023).

[363] Walls, D. and Milburn, G. J.: "Input-Output Formulation of Optical Cavities." In: *Quantum Optics*, pp. 127–141. Ed. by Walls, D. and Milburn, G. J. Springer Berlin Heidelberg, 2008.

[364] Schmidt, R., Niehues, I., Schneider, R., Drüppel, M., Deilmann, T., Rohlfing, M., Vasconcellos, S. M. de, Castellanos-Gomez, A., and Bratschitsch, R.: "Reversible uniaxial strain tuning in atomically thin WSe_2." *2D Materials* **3**, 021011 (2016).

[365] Thureja, D.: "Electrically tunable quantum confinement of neutral excitons." Doctoral Thesis, ETH Zurich, 2023.

[366] Rupprecht, C., Lundt, N., Wurdack, M., Stepanov, P., Estrecho, E., Richard, M., Ostrovskaya, E. A., Höfling, S., and Schneider, C.: "Micro-mechanical assembly and characterization of high-quality Fabry-Pérot microcavities for the integration of two-dimensional materials." *Applied Physics Letters* **118** (2021).

[367] Gu, L., Zhang, L., Ni, R., Xie, M., Wild, D. S., Park, S., Jang, H., Taniguchi, T., Watanabe, K., Hafezi, M., and Zhou, Y.: "Giant optical nonlinearity of Fermi polarons in atomically thin semiconductors." *Nature Photonics* **18**, 816–822 (2024).

[368] Bennett, C. H., Brassard, G., Crépeau, C., Jozsa, R., Peres, A., and Wootters, W. K.: "Teleporting an unknown quantum state via dual classical and Einstein-Podolsky-Rosen channels." *Physical Review Letters* **70**, 1895–1899 (1993).

[369] Dowling, J. P.: "Quantum optical metrology - the lowdown on high-N00N states." *Contemporary Physics* **49**, 125–143 (2008).

[370] Senellart, P., Solomon, G., and White, A.: "High-performance semiconductor quantum-dot single-photon sources." *Nature Nanotechnology* **12**, 1026–1039 (2017).

[371] Arakawa, Y. and Holmes, M. J.: "Progress in quantum-dot single photon sources for quantum information technologies: A broad spectrum overview." *Applied Physics Reviews* **7**, 021309 (2020).

[372] Zhou, Y., Wang, Z., Rasmita, A., Kim, S., Berhane, A., Bodrog, Z., Adamo, G., Gali, A., Aharonovich, I., and Gao, W.-b.: "Room temperature solid-state quantum emitters in the telecom range." *Science Advances* **4**, eaar3580 (2018).

[373] Settele, S., Berger, F. J., Lindenthal, S., Zhao, S., El Yumin, A. A., Zorn, N. F., Asyuda, A., Zharnikov, M., Högele, A., and Zaumseil, J.: "Synthetic control over the binding configuration of luminescent sp^3-defects in single-walled carbon nanotubes." *Nature Communications* **12**, 2119 (2021).

[374] Li, M.-K., Riaz, A., Wederhake, M., Fink, K., Saha, A., Dehm, S., He, X., Schöppler, F., Kappes, M. M., Htoon, H., Popov, V. N., Doorn, S. K., Hertel, T., Hennrich, F., and Krupke, R.: "Electroluminescence from Single-Walled Carbon Nanotubes with Quantum Defects." *ACS Nano* **16**, 11742–11754 (2022).

[375] Ishii, A., He, X., Hartmann, N. F., Machiya, H., Htoon, H., Doorn, S. K., and Kato, Y. K.: "Enhanced Single-Photon Emission from Carbon-Nanotube Dopant States Coupled to Silicon Microcavities." *Nano Letters* **18**, 3873–3878 (2018).

[376] Sun, F. W. and Wong, C. W.: "Indistinguishability of independent single photons." *Physical Review A* **79**, 013824 (2009).

[377] Dusanowski, Ł., Köck, D., Shin, E., Kwon, S.-H., Schneider, C., and Höfling, S.: "Purcell-Enhanced and Indistinguishable Single-Photon Generation from Quantum Dots Coupled to On-Chip Integrated Ring Resonators." *Nano Letters* **20**, 6357–6363 (2020).

[378] Sharma, L. and Tripathi, L. N.: "Deterministic coupling of quantum emitter to surface plasmon polaritons, Purcell enhanced generation of indistinguishable single photons and quantum information processing." *Optics Communications* **496**, 127139 (2021).

[379] Fagan, J. A., Hároz, E. H., Ihly, R., Gui, H., Blackburn, J. L., Simpson, J. R., Lam, S., Hight Walker, A. R., Doorn, S. K., and Zheng, M.: "Isolation of >1 nm Diameter Single-Wall Carbon Nanotube Species Using Aqueous Two-Phase Extraction." *ACS Nano* **9**, 5377–5390 (2015).

[380] Weisman, R. B. and Bachilo, S. M.: "Dependence of Optical Transition Energies on Structure for Single-Walled Carbon Nanotubes in Aqueous Suspension: An Empirical Kataura Plot." *Nano Letters* **3**, 1235–1238 (2003).

[381] ITU-T: "Optical system design and engineering considerations." Tech. rep. ITU-T G Suppl. 39. International Telecommunication Union, 2016.

[382] Hartschuh, A., Pedrosa, H. N., Novotny, L., and Krauss, T. D.: "Simultaneous Fluorescence and Raman Scattering from Single Carbon Nanotubes." *Science* **301**, 1354–1356 (2003).

[383] Gokus, T., Cognet, L., Duque, J. G., Pasquali, M., Hartschuh, A., and Lounis, B.: "Mono- and Biexponential Luminescence Decays of Individual Single-Walled Carbon Nanotubes." *The Journal of Physical Chemistry C* **114**, 14025–14028 (2010).

[384] Knill, E., Laflamme, R., and Milburn, G. J.: "A scheme for efficient quantum computation with linear optics." *Nature* **409**, 46–52 (2001).

[385] Azuma, K., Tamaki, K., and Lo, H.-K.: "All-photonic quantum repeaters." *Nature Communications* **6**, 6787 (2015).

[386] Chen, S., Son, J., Huang, S., Watanabe, K., Taniguchi, T., Bashir, R., Van Der Zande, A. M., and King, W. P.: "Tip-Based Cleaning and Smoothing Improves Performance in Monolayer MoS_2 Devices." *ACS Omega* **6**, 4013–4021 (2021).

[387] Shanks, D. N., Mahdikhanysarvejahany, F., Muccianti, C., Alfrey, A., Koehler, M. R., Mandrus, D. G., Taniguchi, T., Watanabe, K., Yu, H., LeRoy, B. J., and Schaibley, J. R.: "Nanoscale Trapping of Interlayer Excitons in a 2D Semiconductor Heterostructure." *Nano Letters* **21**, 5641–5647 (2021).

[388] Setaro, A.: "Advanced carbon nanotubes functionalization." *Journal of Physics: Condensed Matter* **29**, 423003 (2017).

[389] Amirjani, A., Tsoulos, T. V., Sajjadi, S. H., Antonucci, A., Wu, S.-J., Tagliabue, G., Haghshenas, D. F., and Boghossian, A. A.: "Plasmon-induced near-infrared fluorescence enhancement of single-walled carbon nanotubes." *Carbon* **194**, 162–175 (2022).

[390] Miguel-Sánchez, J., Reinhard, A., Togan, E., Volz, T., Imamoglu, A., Besga, B., Reichel, J., and Estève, J.: "Cavity quantum electrodynamics with charge-controlled quantum dots coupled to a fiber Fabry-Perot cavity." *New Journal of Physics* **15**, 045002 (2013).

[391] Häußler, S., Bayer, G., Waltrich, R., Mendelson, N., Li, C., Hunger, D., Aharonovich, I., and Kubanek, A.: "Tunable Fiber-Cavity Enhanced Photon Emission from Defect Centers in hBN." *Advanced Optical Materials* **9**, 2002218 (2021).

[392] Saavedra, C., Pandey, D., Alt, W., Meschede, D., and Pfeifer, H.: "Spectroscopic Gas Sensor Based on a Fiber Fabry-Perot Cavity." *Physical Review Applied* **18**, 044039 (2022).

[393] Kohler, L., Mader, M., Kern, C., Wegener, M., and Hunger, D.: "Tracking Brownian motion in three dimensions and characterization of individual nanoparticles using a fiber-based high-finesse microcavity." *Nature Communications* **12**, 6385 (2021).

[394] Needham, L.-M., Saavedra, C., Rasch, J. K., Sole-Barber, D., Schweitzer, B. S., Fairhall, A. J., Vollbrecht, C. H., Wan, S., Podorova, Y., Bergsten, A. J., Mehlenbacher, B., Zhang, Z., Tenbrake, L., Saimi, J., Kneely, L. C., Kirkwood, J. S., Pfeifer, H., Chapman, E. R., and Goldsmith, R. H.: "Label-free detection and profiling of individual solution-phase molecules." *Nature* **629**, 1062–1068 (2024).

[395] Sigger, F., Amersdorffer, I., Hötger, A., Nutz, M., Kiemle, J., Taniguchi, T., Watanabe, K., Förg, M., Noe, J., Finley, J. J., Högele, A., Holleitner, A. W., Hümmer, T., Hunger, D., and Kastl, C.: "Ultra-Sensitive Extinction Measurements of Optically Active Defects in Monolayer MoS_2." *The Journal of Physical Chemistry Letters* **13**, 10291–10296 (2022).

[396] Noé, J., Förg, M., Nutz, M., Steiner, F., Fernandes, R., Amersdorffer, I., Hunger, D., and Hümmer, T.: "Seeing the Unseen - Boosted Absorption Imaging and Spectroscopy Using a Scanning Microresonator." *arXiv.org,* 2212.11590 (2022).

[397] Robert, C., Semina, M. A., Cadiz, F., Manca, M., Courtade, E., Taniguchi, T., Watanabe, K., Cai, H., Tongay, S., Lassagne, B., Renucci, P., Amand, T., Marie, X., Glazov, M. M., and Urbaszek, B.: "Optical spectroscopy of excited exciton states in MoS_2 monolayers in van der Waals heterostructures." *Physical Review Materials* **2**, 011001 (2018).

[398] Polyanskiy, M. N.: "Refractiveindex.info database of optical constants." *Scientific Data* **11**, 94 (2024).

List of Publications

Manuscripts related to this dissertation are labeled [P1–P4].

[P1] Husel, L., Tabataba-Vakili, F., Scherzer, J., Krelle, L., Bilgin, I., Vadia, S., Watanabe, K., Taniguchi, T., Carusotto, I., and Högele, A.: "Cavity-mediated exciton hopping in a dielectrically engineered polariton system." *arXiv.org*, 2506.05561 (2025).

[P2] Husel, L., Trapp, J., Scherzer, J., Wu, X., Wang, P., Fortner, J., Nutz, M., Hümmer, T., Polovnikov, B., Förg, M., Hunger, D., Wang, Y., and Högele, A.: "Cavity-enhanced photon indistinguishability at room temperature and telecom wavelengths." *Nature Communications* **15**, 1–7 (2024).

[P3] Scherzer, J., Lackner, L., Han, B., Polovnikov, B., Husel, L., Göser, J., Li, Z., Drawer, J.-C., Esmann, M., Bennenhei, C., Eilenberger, F., Watanabe, K., Taniguchi, T., Baimuratov, A. S., Schneider, C., and Högele, A.: "Correlated magnetism of moiré exciton-polaritons on a triangular electron-spin lattice." *arXiv.org*, 2405.12698 (2024).

[P4] Tabataba-Vakili, F., Krelle, L., Husel, L., Nguyen, H. P. G., Li, Z., Bilgin, I., Watanabe, K., Taniguchi, T., and Högele, A.: "Metasurface of Strongly Coupled Excitons and Nanoplasmonic Arrays." *Nano Letters* **24**, 10090–10097 (2024).

[P5] Mader, M., Benedikter, J., Husel, L., Hänsch, T. W., and Hunger, D.: "Quantitative determination of the complex polarizability of individual nanoparticles by scanning cavity microscopy." *ACS Photonics* **9**, 466–473 (2022).

[P6] Stolz, T., Hegels, H., Winter, M., Röhr, B., Hsiao, Y.-F., Husel, L., Rempe, G., and Dürr, S.: "Quantum-Logic Gate between Two Optical Photons with an Average Efficiency above 40%." *Physical Review X* **12**, 021035 (2022).

Acknowledgements

Scientific work is a collaborative process and this thesis is certainly no exception. I would like to express my deepest gratitude to everyone who has made this project possible, by directly contributing to the experiments and data analysis, as well as by accompanying and supporting me during the memorable time of my PhD.

First of all, I would like to thank Alex Högele for giving me the opportunity to be a part of his research group. Thank you Alex for entrusting me to work independently, for the support that helped to keep pressure out of the PhD, and for giving me the opportunity and freedom to pursue many of my interests. Thank you also for the inspiring attention to detail in data and experiments in our discussions, and for the lessons in spectroscopy and scientific writing.

What made working on the PhD highly enjoyable and contributed massively to keeping the motivation high was being a part of the Nanophotonics Group over the last few years. I would like to thank all the members, past and present, who have contributed to making this a friendly, collaborative and supportive environment which was fun to work in. I am also very grateful for all the direct contributions that many of you have made to the experiments, the data analysis, the publications and this document. In addition to these broad statements, there is an enormous list of individual acknowledgments that forms in my mind as I look back over the past few years. Due to limitations in time and space (of the document), I will only list a subset of them below. Julian Trapp, thank you for the exceptional teamwork on the nanotube project, for sharing the thrill and the pain of counting photon coincidences, for bringing your hands-on attitude and optimism to the lab and for the refreshing perspectives on physics and everything else. Johannes Scherzer, thank you for being passionate about the cavity and for making it work as a team, for the willingness to discuss any kind of question, for your inspiring approach of trying things instead of overthinking, and for your support in times of crisis, in the lab and in the Colombian jungle. Farsane Tabataba-Vakili and Lukas Krelle, thanks for the successful teamwork on sample fabrication and confocal spectroscopy. Manuel Nutz, for a thorough introduction to optical spectroscopy, in which I should have taken notes, and for your support in all kinds of questions. Samarth Vadia, for help with the cavity setup, the motivating optimism, and a crucial hint regarding a job offer. Jonathan Förste and Victor Funk, for the constant supply of great coffee. Jonathan Förste, for the helpfulness and support with various problems and questions. Victor Funk, for sharing your vast knowledge of climbing. Jonas Göser, for the crystals and all the good memories of our

common physics education since the first semester of the bachelor. I also thank Johannes Scherzer for this last point. Subhradeep Misra, thank you for your helpfulness and for bringing your immense knowledge of physics to every discussion. Anna Rupp, for your motivating enthusiasm for physics and for sharing all your insights on excitons, magnets, and diamond pressure cells. Xin Huang, for a meditative lesson on stamping. Borislav Polovnikov, for enriching discussions about physics and life. Tim Wedl, for enriching discussions about physics, life, and hip-hop. Shen Zhao, for sharing some of your knowledge about carbon nanotubes and spectroscopy. Ismail Bilgin and Zhijie Li, for your high quality crystals. Sarah Rößle and Julius Kleusberg, for the motivated contributions during your bachelor and internship projects. Anvar Baimuratov, for the introduction to Russian subculture. Anyone not yet on this list, including Christian Mohl, Huy Nguyen, Patrick Pertsch, and Lukas Aicher, for contributing to the friendly and positive atmosphere in the group. I am also very grateful to the staff of the former Kotthaus chair for keeping things running and thereby enabling the experiments. Bert Lorenz, thank you for all your support and advice. Dayse Ferreira e Silva, for all the administrative support and helpfulness. Anton Heindl, for providing solutions to all kinds of technical problems. Philipp Altpeter and Christian Obermayer, for mastering the clean room and your tireless support during fabrication. Stephan Manus, thank you for making many experiments possible by providing reliable devices and for all the lessons on bicycles and electronics.

Beyond the Nanophotonics Group, I am very grateful for the numerous collaborations and scientific interactions during my PhD and for all the support I received from different sides. I would like to thank Fabian Grusdt for the excellent thesis co-supervision and for all the advice and motivation. I am grateful to David Hunger for the advice and the great collaboration on the nanotube project. David and team, thank you also for providing high quality fibers and mirrors. A big thank you to the team at Qlibri, Michael Förg, Thomas Hümmer, Manuel Nutz, Jonathan Noé and Max Huber, for the shared interest in fiber cavities and for designing and building a wonderful machine and supporting its operation. Excellent nanotube samples provided by Yu-Huang Wang and his team at the University of Maryland, especially James Wu, were also greatly appreciated. I am grateful to Iacopo Carusotto for taking the time to collaborate on the polariton project, which led to many valuable insights. A discussion on Hong-Ou Mandel experiments with Lukas Knips proved very relevant, thank you. I also wish to thank Sonya Gzyl for the support through IMPRS, and Barbara Tautz for her dedication in putting together a great workshop program at MCQST. To close this certainly incomplete list, I would like to thank Thibault Chervy for the opportunity to spend an exciting time in his group in Sunnyvale, which included a lot of valuable learning, and for showing me around California. I would also like to thank Etienne Lorchat, Jenny Hu, Ouri Karni and the team at NTT Research as well as Tony Heinz and his group at Stanford for all the support and the scientific and personal exchange that made my time in California highly memorable.

Finally, I am privileged to be accompanied and supported by extraordinary people in my life outside the university, and it is hard to put into words how grateful I am for that. Rebekka, thank you for all your invaluable support and encouragement, and for constantly motivating me to discover new and interesting things and places together. All my friends, I hope you know that you are the best, thank you for all the precious time we spent together, in the cities, in the mountains and at the lake. And to my family, thank you for a lifetime of memories, big and small, your understanding and your constant and unconditional support.